



U.S. DEPARTMENT OF
ENERGY

PNNL-23257

Prepared for the U.S. Department of Energy
under Contract DE-AC05-76RL01830

Preliminary Three-Dimensional Simulation of Sediment and Cesium Transport in the Ogi Dam Reservoir using FLESCOT – Task 6, Subtask 2

Y Onishi
H Kurikami
ST Yokuda

March 2014



Pacific Northwest
NATIONAL LABORATORY

*Proudly Operated by **Battelle** Since 1965*

DISCLAIMER

This report was prepared as an account of work sponsored by an agency of the United States Government. Neither the United States Government nor any agency thereof, nor Battelle Memorial Institute, nor any of their employees, makes **any warranty, express or implied, or assumes any legal liability or responsibility for the accuracy, completeness, or usefulness of any information, apparatus, product, or process disclosed, or represents that its use would not infringe privately owned rights.** Reference herein to any specific commercial product, process, or service by trade name, trademark, manufacturer, or otherwise does not necessarily constitute or imply its endorsement, recommendation, or favoring by the United States Government or any agency thereof, or Battelle Memorial Institute. The views and opinions of authors expressed herein do not necessarily state or reflect those of the United States Government or any agency thereof.

PACIFIC NORTHWEST NATIONAL LABORATORY
operated by
BATTELLE
for the
UNITED STATES DEPARTMENT OF ENERGY
under Contract DE-AC05-76RL01830

Printed in the United States of America

Available to DOE and DOE contractors from the
Office of Scientific and Technical Information,
P.O. Box 62, Oak Ridge, TN 37831-0062;
ph: (865) 576-8401
fax: (865) 576-5728
email: reports@adonis.osti.gov

Available to the public from the National Technical Information Service
5301 Shawnee Rd., Alexandria, VA 22312
ph: (800) 553-NTIS (6847)
email: orders@ntis.gov <<http://www.ntis.gov/about/form.aspx>>
Online ordering: <http://www.ntis.gov>



This document was printed on recycled paper.

(8/2010)

Preliminary Three-Dimensional Simulation of Sediment and Cesium Transport in the Ogi Dam Reservoir using FLESCOT – Task 6, Subtask 2

Y Onishi
H Kurikami*
ST Yokuda

March 2014

Prepared for
the U.S. Department of Energy
under Contract DE-AC05-76RL01830

Pacific Northwest National Laboratory
Richland, Washington 99352

*Japan Atomic Energy Agency

Executive Summary

After the accident at the Fukushima Daiichi Nuclear Power Plant in March 2011, the Japan Atomic Energy Agency and the Pacific Northwest National Laboratory initiated a collaborative project on environmental restoration. In October 2013, the collaborative team started a task of three-dimensional modeling of sediment and cesium transport in the Fukushima environment using the FLESCOT (Flow, Energy, Salinity, Sediment Contaminant Transport) code. As the first trial, we applied it to the Ogi Dam Reservoir that is one of the reservoirs in the Japan Atomic Energy Agency's (JAEA's) investigation project.

Three simulation cases under the following different temperature conditions were studied:

- incoming rivers and the Ogi Dam Reservoir have the same water temperature
- incoming rivers have lower water temperature than that of the reservoir
- incoming rivers have higher water temperature than that of the reservoir.

The preliminary simulations suggest that seasonal temperature changes influence the sediment and cesium transport. The preliminary results showed the following:

- Suspended sand, and cesium adsorbed by sand, coming into the reservoirs from upstream rivers is deposited near the reservoir entrance.
- Suspended silt, and cesium adsorbed by silt, is deposited farther in the reservoir.
- Suspended clay, and cesium adsorbed by clay, travels the farthest into the reservoir.

With sufficient time, the dissolved cesium reaches the downstream end of the reservoir. This preliminary modeling also suggests the possibility of a suitable dam operation to control the cesium migration farther downstream from the dam.

JAEA has been sampling in the Ogi Dam Reservoir, but these data were not yet available for the current model calibration and validation for this reservoir. Nonetheless these preliminary FLESCOT modeling results were qualitatively valid and confirmed the applicability of the FLESCOT code to the Ogi Dam Reservoir, and in general to other reservoirs in the Fukushima environment.

The issues to be addressed in future are the following:

- Validate the simulation results by comparison with the investigation data.
- Confirm the applicability of the FLESCOT code to Fukushima coastal areas.
- Increase computation speed by parallelizing the FLESCOT code.

Acknowledgments

This work was based on the collaborative project between the Japan Atomic Energy Agency (JAEA) and the Pacific Northwest National Laboratory (PNNL) funded by JAEA. The second author has been assigned from JAEA to PNNL as a visiting scientist from April 2013 to March 2014.

Acronyms and Abbreviations

Bq	becquerel(s); Standard International (SI) unit for radioactivity, defined as the activity of a quantity of radioactive material in which one nucleus decays per second
F-TRACE	long-term assessment of Transport of RAdioactive Contaminant in the Environment of Fukushima
FLESCOT	Flow, Energy, Salinity, Sediment Contaminant Transport
JAEA	Japan Atomic Energy Agency
kg	kilogram(s)
km	kilometer(s)
m	meter(s)
m ³ /s	cubic meter(s) per second
PNNL	Pacific Northwest National Laboratory
s	second(s)
TEMPEST	Transient Energy, Momentum, and Pressure Equation Solution in Three Dimensions

Nomenclature

c	specific heat	G_X	body force per unit mass in X direction
C_i	i^{th} sediment concentration per unit volume	G_Z	body force per unit mass in Z direction
$C_{\varepsilon 1}$	constant	H	flow depth
$C_{\varepsilon 2}$	constant	K	thermal conductivity
$C_{\varepsilon 3}$	constant	k	turbulent kinetic energy per unit mass
C_μ	constant	K_{Bi}	transfer rate of species for adsorption with the i^{th} non-moving sediment in the bed
D_i	particle diameter of the i^{th} sediment	K_{Di}	distribution (or partition) coefficient between dissolved species and particulate species associated with the i^{th} sediment for adsorption
D_{Mi}	molecular diffusion coefficient of the i^{th} component	K_i	transfer rate of species with the i^{th} moving sediment for adsorption
D_ω	$D_{Mi} + \mu_T/Sc_T$	K_{ke}	$K + K_T$
$F_R(U)$	flow drag in R direction	K_T	turbulent (eddy) thermal conductivity
F_U	$2\Omega_E U \sin(\phi)$	K'_{Bi}	transfer rate of species for desorption with the i^{th} non-moving sediment in the bed
F_W	$2\Omega_E U \cos(\phi)$	K'_{Di}	distribution (or partition) coefficient between dissolved species and particulate species associated with the i^{th} sediment for desorption
$F_X(W)$	flow drag in X direction	K'_i	transfer rate of species with the i^{th} moving sediment for desorption
$F_Z(V)$	flow drag in Z direction	P	static pressure
G	dissolved species concentration per unit volume (radionuclide activity or weight of species per unit volume)	P_k	turbulent kinetic energy shear production
G_{Bi}	particulate species concentration per unit weight of sediment in the i^{th} sediment size fraction in the bed	POR	porosity of bed sediment
G_i	particulate species concentration associated with the i^{th} sediment (radionuclide activity or weight of species per unit volume)	Q_{Ci}	source of the i^{th} sediment
G_k	turbulent kinetic energy buoyant production	Q_i	source of particulate species G_i
G_R	body force per unit mass in R direction		

\dot{Q}	volumetric heat generation rate	λ	radionuclide decay, or first-order chemical and biological degradation rates of species
R	R direction for Cartesian and cylindrical coordinates	μ	dynamic viscosity
S	salinity	μ_k	$\mu + \mu_T/\sigma_k$
Sc_T	turbulent Schmidt number	$\mu_{k\varepsilon}$	$\mu + \mu_T$
S_{Di}	i^{th} sediment deposition rate per unit surface area	μ_T	turbulent (eddy) viscosity ($\mu_T = C_\mu \rho k^2/\varepsilon$)
S_k	$P_k + G_k$	μ_ε	$\mu + \mu_T/\sigma_\varepsilon$
S_{Ri}	i^{th} sediment erosion rate per unit surface area	ρ	local density obtained from Boussinesq approximation
S_ε	$C_{\varepsilon 1} P_k + C_{\varepsilon 3} G_k$	ρ_i	partial density of the i^{th} component
T	temperature	ρ_0	fluid density
U	velocity in R direction	σ_k	constant
V	velocity in Z direction	σ_T	constant
V_{Si}	settling velocity of the i^{th} sediment	σ_ε	constant
W	velocity in X direction	ϕ	planetary latitude
X	X direction for Cartesian and cylindrical coordinates	Ω_E	planetary angular velocity ($7.29 \times 10^{-5} [\text{sec}^{-1}]$)
Z	Z direction for Cartesian and cylindrical coordinates	$\dot{\Omega}_i$	mass fraction source of the i^{th} component
β	0 for Cartesian coordinates and 1 for cylindrical coordinates	ω_i	mass fraction of the i^{th} component ($\omega_i = \rho_i/\rho$)
γ_i	specific weight of the i^{th} sediment		
ε	turbulent kinetic energy dissipation per unit mass		
ε_R	dispersion coefficient in R direction		
ε_X	dispersion coefficient in X direction		
ε_Z	dispersion coefficient in Z direction		

Contents

Executive Summary	iii
Acknowledgments.....	v
Acronyms and Abbreviations	vii
Nomenclature.....	ix
1.0 Introduction	1.1
2.0 FLESCOT Model Description.....	2.3
2.1 Coordinate Systems.....	2.4
2.2 Conservation of Mass.....	2.4
2.3 Conservation of Momentum in R Direction.....	2.5
2.4 Conservation of Momentum in X Direction.....	2.6
2.5 Conservation of Momentum in Z Direction	2.6
2.6 Conservation of Turbulent Kinetic Energy	2.7
2.7 Conservation of Turbulent Kinetic Energy Dissipation	2.8
2.8 Turbulent Viscosity	2.8
2.9 Conservation of Thermal Energy	2.8
2.10 Transport Equation for the i^{th} Component in a Mixture of n Species.....	2.9
2.11 Transport in the Surface Water Environment.....	2.10
2.11.1 Sediment Transport Equation for i^{th} Sediment in Cartesian Coordinates.....	2.10
2.11.2 Dissolved Species Transport Equation for Dissolved Species G in Cartesian Coordinates.....	2.11
2.11.3 Transport Equation for the i^{th} Particulate Species in Cartesian Coordinates.....	2.12
2.11.4 Transport Equation for Salinity in Cartesian Coordinates	2.12
3.0 Ogi Dam Reservoir Modeling	3.1
3.1 Description of the Ogi Dam Reservoir	3.1
3.2 Simulation Results.....	3.2
3.2.1 Modeling Conditions.....	3.2
3.2.2 Preliminary Simulation Results.....	3.3
4.0 Conclusions	4.1
5.0 References	5.1

Figures

2.1 Cartesian Coordinates	2.4
2.2 Cylindrical Coordinates	2.4
3.1 Location of the Ogi Dam Reservoir (bottom right) and Images of the Area	3.1
3.2 Contours of the Bottom Elevation in the Ogi Dam Reservoir	3.2
3.3 The Ogi Dam Reservoir Model Setup	3.3
3.4 Ogi Dam Reservoir Simulation Results for an Isothermal Condition Case.....	3.4
3.5 Ogi Dam Reservoir Simulation Results for the Colder Water Inflow Case	3.5
3.6 Ogi Dam Reservoir Simulation Results for the Warmer Water Inflow Case	3.6

1.0 Introduction

The nuclear accident at the Fukushima Daiichi Nuclear Power Plant (NPP) in March 2011 caused widespread environmental contamination. To understand the contaminant transport behavior in the environment, the Japan Atomic Energy Agency (JAEA) initiated the F-TRACE (long-term assessment of Transport of RAdioactive Contaminant in the Environment of Fukushima) project (Iijima et al. 2013) in the fall of 2012. In the project, several rivers and reservoirs near the Fukushima Daiichi NPP have been investigated.

JAEA and the Pacific Northwest National Laboratory initiated a task of three-dimensional modeling of sediment and cesium transport in the Fukushima environment using the FLESCOT (Flow, Energy, Salinity, Sediment Contaminant Transport) code in October 2013. This report presents preliminary results of the simulations applied to the Ogi Dam Reservoir of the Oginosawa River, Fukushima that is one of the target reservoirs of the F-TRACE project.

2.0 FLESCOT Model Description

FLESCOT (Onishi et al. 1993) is a finite-volume code developed by PNNL to predict time-varying three-dimensional distributions of the following:

- flow (velocity and depth) resulting from a river flow, tide, wind, waves, and water density variations
- turbulent kinetic energy and its dissipation
- water temperature
- salinity
- sediment concentrations of
 - suspended sand
 - suspended silt
 - suspended clay
- dissolved radionuclide concentration
- particulate radionuclide concentrations adsorbed by
 - suspended sand
 - suspended silt
 - suspended clay
- within the water bottom at any given location,
 - bed elevation change caused by sediment erosion and deposition
 - sediment fractions of
 - bottom sand
 - bottom silt
 - bottom clay
 - radionuclide concentrations adsorbed by
 - bottom sand
 - bottom silt
 - bottom clay

FLESCOT is applicable to various contaminants, e.g., radionuclides, heavy metals, and toxic organic chemicals, including ^{137}Cs moving and depositing in the Hudson River Estuary with ^{137}Cs adsorption/desorption changing with salinity (Onishi and Trent 1985, Onishi et al. 1987, Onishi and Trent 1992, Onishi et al. 1993). It has been applied to river mouths/estuaries, coastal water, seas, and deep oceans.

FLESCOT solves the differential equations based on the following principles:

- conservation of mass (continuity)
- conservation of momentum (Newton's second law)
- conservation of energy (first law of thermodynamics)
- conservation of turbulent kinetic energy, κ
- conservation of turbulent kinetic energy dissipation, ϵ
- conservation of mass constituents, C_i

These conservation equations are described in the following subsections.

FLESCOT is the marine version of the TEMPEST (Transient Energy, Momentum, and Pressure Equation Solution in Three Dimensions) computer code. The code assessment and validation of TEMPEST is presented in the appendix, "TEMPEST – Assessment and Verification Results."

2.1 Coordinate Systems

FLESCOT uses two coordinate systems, Cartesian and cylindrical coordinates, as shown in Figure 2.1 and Figure 2.2, respectively.

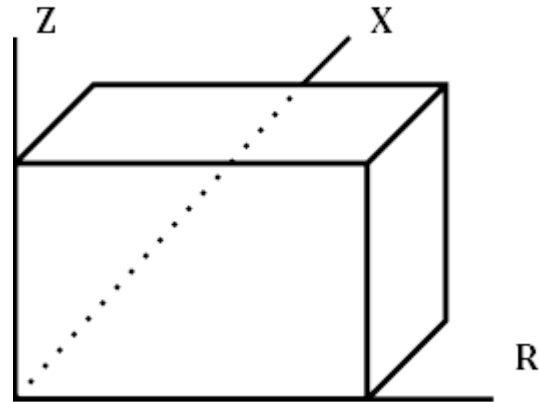


Figure 2.1. Cartesian Coordinates

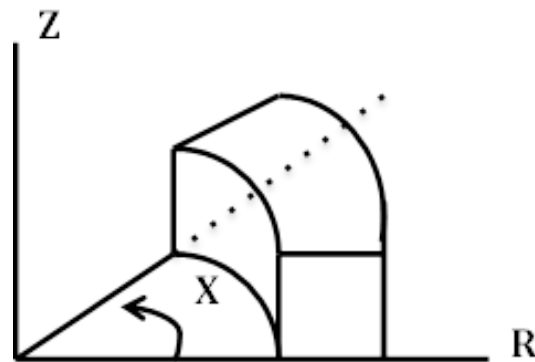


Figure 2.2. Cylindrical Coordinates

2.2 Conservation of Mass (Continuity of Incompressible Fluid)

The equation for conservation of mass used in FLESCOT is Equation (2.1):

$$\frac{1}{R^\beta} \frac{\partial R^\beta U}{\partial R} + \frac{1}{R^\beta} \frac{\partial W}{\partial X} + \frac{\partial V}{\partial Z} = 0 \quad (2.1)$$

where

U = velocity in R direction

W = velocity in X direction

V = velocity in Z direction

$\beta = 1$ for cylindrical coordinates

$\beta = 0$ for Cartesian coordinates

2.3 Conservation of Momentum in R Direction

FLESCOT uses Equations (2.2) and (2.3) for conservation of momentum in the R direction:

$$\begin{aligned} & \rho_0 \left[\frac{\partial U}{\partial t} + \frac{1}{R^\beta} \frac{\partial}{\partial R} (R^\beta U U) + \frac{1}{R^\beta} \frac{\partial}{\partial X} (W U) + \frac{\partial}{\partial Z} (V U) - \beta \left(\frac{\rho}{\rho_0} \right) \frac{W^2}{R} - F_U \right] \\ & = - \frac{\partial P}{\partial R} + \rho G_R + \frac{1}{R^\beta} \frac{\partial}{\partial R} \left(R^\beta \mu_{ke} \frac{\partial U}{\partial R} \right) + \frac{1}{R^{2\beta}} \frac{\partial}{\partial X} \left(\mu_{ke} \frac{\partial U}{\partial X} \right) + \frac{\partial}{\partial Z} \left(\mu_{ke} \frac{\partial U}{\partial Z} \right) + S_R \end{aligned} \quad (2.2)$$

$$S_R = - \beta \mu_{ke} \left(\frac{U}{R^2} + \frac{2}{R^2} \frac{\partial W}{\partial X} \right) + \frac{\partial \mu_{ke}}{\partial R} \frac{\partial U}{\partial R} + \frac{\partial \mu_{ke}}{\partial X} \frac{\partial}{\partial R} \left(\frac{W}{R^\beta} \right) + \frac{\partial \mu_{ke}}{\partial Z} \frac{\partial V}{\partial R} - F_R(U) \quad (2.3)$$

where

ρ_0 = fluid density

ρ = local density obtained from the Boussinesq approximation

$\mu_{ke} = \mu + \mu_T$

μ = dynamic viscosity

μ_T = turbulent (eddy) viscosity calculated as $\mu_T = C_\mu \rho k^2 / \varepsilon$ from the Prandtl-Kolmogorov hypothesis

k = turbulent kinetic energy per unit mass

ε = turbulent kinetic energy dissipation per unit mass

C_μ = constant

$F_R(U)$ = flow drag in R direction

$F_U = 2\Omega_E U \sin(\phi)$

ϕ = planetary latitude

$\Omega_E = 7.29 \times 10^{-5} [\text{sec}^{-1}]$ (Planetary angular velocity)

G_R = body force per unit mass in R direction

P = static pressure

2.4 Conservation of Momentum in X Direction

FLESCOT uses Equations (2.4) and (2.5) for conservation of momentum in the X direction:

$$\begin{aligned} & \rho_0 \left[\frac{\partial W}{\partial t} + \frac{1}{R^\beta} \frac{\partial}{\partial R} (R^\beta U W) + \frac{1}{R^\beta} \frac{\partial}{\partial X} (W W) + \frac{\partial}{\partial Z} (V W) + \beta \left(\frac{\rho}{\rho_0} \right) \frac{U W}{R} + F_w \right] \\ & = - \frac{1}{R^\beta} \frac{\partial P}{\partial X} + \rho G_x + \frac{1}{R^\beta} \frac{\partial}{\partial R} \left(R^\beta \mu_{ke} \frac{\partial W}{\partial R} \right) + \frac{1}{R^{2\beta}} \frac{\partial}{\partial X} \left(\mu_{ke} \frac{\partial W}{\partial X} \right) + \frac{\partial}{\partial Z} \left(\mu_{ke} \frac{\partial W}{\partial Z} \right) + S_x \end{aligned} \quad (2.4)$$

$$\begin{aligned} S_x & = \frac{\beta \mu_{ke}}{R^2} \left(2 \frac{\partial U}{\partial X} - W \right) + \frac{1}{R^\beta} \frac{\partial \mu_{ke}}{\partial R} \left(\frac{\partial U}{\partial X} - \beta W \right) + \frac{1}{R^{2\beta}} \frac{\partial \mu_{ke}}{\partial X} \left(\frac{\partial W}{\partial X} + 2\beta U \right) \\ & + \frac{1}{R^\beta} \frac{\partial \mu_{ke}}{\partial Z} \frac{\partial V}{\partial X} - F_x(W) \end{aligned} \quad (2.5)$$

where

$F_x(W)$ = flow drag in X direction

$F_w = 2\Omega_E U \cos(\phi)$

G_x = body force per unit mass in X direction

2.5 Conservation of Momentum in Z Direction

FLESCOT uses Equations (2.6) and (2.7) for conservation of momentum in the Z direction:

$$\begin{aligned} & \rho_0 \left[\frac{\partial V}{\partial t} + \frac{1}{R^\beta} \frac{\partial}{\partial R} (R^\beta U V) + \frac{1}{R^\beta} \frac{\partial}{\partial X} (W V) + \frac{\partial}{\partial Z} (V V) \right] \\ & = - \frac{\partial P}{\partial Z} + \rho G_z + \frac{1}{R^\beta} \frac{\partial}{\partial R} \left(R^\beta \mu_{ke} \frac{\partial V}{\partial R} \right) + \frac{1}{R^{2\beta}} \frac{\partial}{\partial X} \left(\mu_{ke} \frac{\partial V}{\partial X} \right) + \frac{\partial}{\partial Z} \left(\mu_{ke} \frac{\partial V}{\partial Z} \right) + S_z \end{aligned} \quad (2.6)$$

$$S_z = \frac{\partial \mu_{ke}}{\partial R} \frac{\partial U}{\partial Z} + \frac{1}{R^\beta} \frac{\partial \mu_{ke}}{\partial X} \frac{\partial W}{\partial Z} + \frac{\partial \mu_{ke}}{\partial Z} \frac{\partial V}{\partial Z} - F_z(V) \quad (2.7)$$

where

$F_z(V)$ = flow drag in Z direction

G_z = body force per unit mass in Z direction

2.6 Conservation of Turbulent Kinetic Energy (k-ε Model)

The equation for conservation of turbulent kinetic energy used in FLESCOT is Equation (2.8):

$$\begin{aligned} & \rho_0 \left[\frac{\partial k}{\partial t} + \frac{1}{R^\beta} \frac{\partial}{\partial R} (R^\beta U k) + \frac{1}{R^\beta} \frac{\partial}{\partial X} (W k) + \frac{\partial}{\partial Z} (V k) \right] \\ &= \frac{1}{R^\beta} \frac{\partial}{\partial R} \left(R^\beta \mu_k \frac{\partial k}{\partial R} \right) + \frac{1}{R^{2\beta}} \frac{\partial}{\partial X} \left(\mu_k \frac{\partial k}{\partial X} \right) + \frac{\partial}{\partial Z} \left(\mu_k \frac{\partial k}{\partial Z} \right) - \rho \varepsilon + S_k \end{aligned} \quad (2.8)$$

where

k = turbulent kinetic energy per unit mass

ε = turbulent kinetic energy dissipation per unit mass

$\mu_k = \mu + \mu_T / \sigma_k$

$\sigma_k = \text{constant}$

$S_k = P_k + G_k$

For the shear production,

$$\begin{aligned} P_k = \mu_T \left\{ 2 \left[\left(\frac{\partial U}{\partial R} \right)^2 + \left(\frac{1}{R^\beta} \frac{\partial W}{\partial X} + \beta \frac{U}{R} \right)^2 + \left(\frac{\partial V}{\partial Z} \right)^2 \right] + \left(\frac{1}{R^\beta} \frac{\partial U}{\partial X} + \frac{\partial W}{\partial R} - \beta \frac{W}{R} \right)^2 \right. \\ \left. + \left(\frac{\partial U}{\partial Z} + \frac{\partial V}{\partial R} \right)^2 + \left(\frac{\partial W}{\partial Z} + \frac{1}{R^\beta} \frac{\partial V}{\partial X} \right)^2 \right\} \end{aligned} \quad (2.9)$$

For the buoyant production,

$$G_k = \frac{\mu_T}{\rho_0 \sigma_T} \left(\frac{\partial p}{\partial R} G_R + \frac{1}{R^\beta} \frac{\partial p}{\partial X} G_X + \frac{\partial p}{\partial Z} G_Z \right) \quad (2.10)$$

where $\sigma_T = \text{constant}$

2.7 Conservation of Turbulent Kinetic Energy Dissipation (k-ε Model)

FLESCOT uses Equation (2.11) for conservation of turbulent kinetic energy dissipation:

$$\begin{aligned} & \rho_0 \left[\frac{\partial \varepsilon}{\partial t} + \frac{1}{R^\beta} \frac{\partial}{\partial R} (R^\beta U \varepsilon) + \frac{1}{R^\beta} \frac{\partial}{\partial X} (W \varepsilon) + \frac{\partial}{\partial Z} (V \varepsilon) \right] \\ &= \frac{1}{R^\beta} \frac{\partial}{\partial R} \left(R^\beta \mu_\varepsilon \frac{\partial \varepsilon}{\partial R} \right) + \frac{1}{R^{2\beta}} \frac{\partial}{\partial X} \left(\mu_\varepsilon \frac{\partial \varepsilon}{\partial X} \right) + \frac{\partial}{\partial Z} \left(\mu_\varepsilon \frac{\partial \varepsilon}{\partial Z} \right) + \frac{1}{k} (S_\varepsilon - \rho C_{\varepsilon 2} \varepsilon) \varepsilon \end{aligned} \quad (2.11)$$

where

ε = turbulent kinetic energy dissipation per unit mass

$$\mu_\varepsilon = \mu + \mu_T / \sigma_\varepsilon$$

$$S_\varepsilon = C_{\varepsilon 1} P_k + C_{\varepsilon 3} G_k$$

$\sigma_\varepsilon, C_{\varepsilon 1}, C_{\varepsilon 2},$ and $C_{\varepsilon 3}$ = constants

2.8 Turbulent Viscosity

The turbulent viscosity, μ_T , is computed using the Prandtl-Kolmogorov hypothesis:

$$\mu_T = C_\mu \rho k^2 / \varepsilon \quad (2.12)$$

Recommended turbulent model constants (Jones and Launder 1973) are:

$$\begin{array}{lll} \sigma_k = 1.0 & C_{\varepsilon 1} = 1.44 & C_\mu = 0.09 \\ \sigma_T = 0.9 & C_{\varepsilon 2} = 1.92 & \\ \sigma_\varepsilon = 1.3 & C_{\varepsilon 3} = 1.44 & \end{array}$$

2.9 Conservation of Thermal Energy

The equation for conservation of thermal energy used in FLESCOT is Equation (2.13):

$$\begin{aligned} & \rho_0 c \left[\frac{\partial T}{\partial t} + \frac{1}{R^\beta} \frac{\partial}{\partial R} (R^\beta U T) + \frac{1}{R^\beta} \frac{\partial}{\partial X} (W T) + \frac{\partial}{\partial Z} (V T) \right] \\ &= \frac{1}{R^\beta} \frac{\partial}{\partial R} \left(R^\beta K_{k\varepsilon} \frac{\partial T}{\partial R} \right) + \frac{1}{R^{2\beta}} \frac{\partial}{\partial X} \left(K_{k\varepsilon} \frac{\partial T}{\partial X} \right) + \frac{\partial}{\partial Z} \left(K_{k\varepsilon} \frac{\partial T}{\partial Z} \right) + \dot{Q} \end{aligned} \quad (2.13)$$

where

T = temperature

$$K_{ke} = K + K_T$$

K = thermal conductivity

K_T = turbulent (eddy) thermal conductivity

c = specific heat

\dot{Q} = volumetric heat generation rate

2.10 Transport Equation for the i^{th} Component in a Mixture of n Species ($i=1,2,\dots,n$)

The transport equation for the i^{th} component in a mixture of n species in FLESCOT is Equation (2.14):

$$\begin{aligned} \frac{\partial \omega_i}{\partial t} + \frac{1}{R^\beta} \frac{\partial}{\partial R} (R^\beta U \omega_i) + \frac{1}{R^\beta} \frac{\partial}{\partial X} (W \omega_i) + \frac{\partial}{\partial Z} (V \omega_i) \\ = \frac{1}{R^\beta} \frac{\partial}{\partial R} \left(R^\beta D_\omega \frac{\partial \omega_i}{\partial R} \right) + \frac{1}{R^{2\beta}} \frac{\partial}{\partial X} \left(D_\omega \frac{\partial \omega_i}{\partial X} \right) + \frac{\partial}{\partial Z} \left(D_\omega \frac{\partial \omega_i}{\partial Z} \right) + \dot{\Omega}_i \end{aligned} \quad (2.14)$$

where

ω_i = mass fraction of the i^{th} component defined as $\omega_i = \rho_i / \rho$

ρ_i = partial density of the i^{th} component

$$D_\omega = D_{Mi} + \mu_T / Sc_T$$

D_{Mi} = molecular diffusion coefficient of the i^{th} component

Sc_T = turbulent Schmidt number

$\dot{\Omega}_i$ = mass fraction source of the i^{th} component

$|\Delta \rho / \rho|$ is assumed to be small for the Boussinesq approximation.

2.11 Transport in the Surface Water Environment

FLESCOT has the capability of predicting the transport and fate of chemical, biological, radiological, and suspended solid material species in marine and surface water environments. The transport equations can be applied for up to nine species involving the following three types:

- sediment
- dissolved species
- particulate species attached to or detached from sediments

Although FLESCOT can use both Cartesian and cylindrical coordinates for transport modeling in the surface water environment, the transport equations for the surface water environment are described with Cartesian coordinates for the sake of simplicity.

2.11.1 Sediment Transport Equation for i^{th} Sediment in Cartesian Coordinates (R,X,Z)

The equation for transport of the i^{th} sediment used in FLESCOT is Equation (2.15):

$$\begin{aligned} & \frac{\partial C_i}{\partial t} + \frac{\partial}{\partial R}(UC_i) + \frac{\partial}{\partial X}(WC_i) + \frac{\partial}{\partial Z}[(V - V_{si})C_i] \\ & = \frac{\partial}{\partial R}\left(\varepsilon_R \frac{\partial C_i}{\partial R}\right) + \frac{\partial}{\partial X}\left(\varepsilon_X \frac{\partial C_i}{\partial X}\right) + \frac{\partial}{\partial Z}\left(\varepsilon_Z \frac{\partial C_i}{\partial Z}\right) + \left(\frac{S_{Ri}}{H} - \frac{S_{Di}}{H}\right) + Q_{Ci} \end{aligned} \quad (2.15)$$

where

C_i = i^{th} sediment concentration per unit volume

ε_R = dispersion coefficient in R direction

ε_X = dispersion coefficient in X direction

ε_Z = dispersion coefficient in Z direction

H = flow depth

Q_{Ci} = source of i^{th} sediment

S_{Di} = i^{th} sediment deposition rate per unit surface area

S_{Ri} = i^{th} sediment erosion rate per unit surface area

V_{si} = settling velocity of the i^{th} sediment

2.11.2 Dissolved Species Transport Equation for Dissolved Species G in Cartesian Coordinates (R,X,Z)

FLESCOT uses Equations (2.16) and (2.17) for transport of dissolved species “G”:

$$\begin{aligned} & \frac{\partial G}{\partial t} + \frac{\partial}{\partial R}(UG) + \frac{\partial}{\partial X}(WG) + \frac{\partial}{\partial Z}(VG) \\ &= \frac{\partial}{\partial R} \left(\epsilon_R \frac{\partial G}{\partial R} \right) + \frac{\partial}{\partial X} \left(\epsilon_X \frac{\partial G}{\partial X} \right) + \frac{\partial}{\partial Z} \left(\epsilon_Z \frac{\partial G}{\partial Z} \right) + \dot{G} \end{aligned} \quad (2.16)$$

$$\begin{aligned} \dot{G} = & -\lambda G - \sum_{i=1}^3 K_i (C_i K_{Di} G - G_i) - \sum_{i=1}^3 K'_i (C_i K'_{Di} G - G_i) \\ & - \frac{1}{H} \sum_{i=1}^3 \gamma_i (1 - \text{POR}) D_i K_{Bi} (K_{Di} G - G_{Bi}) \\ & - \frac{1}{H} \sum_{i=1}^3 \gamma_i (1 - \text{POR}) D_i K'_{Bi} (K_{Di} G - G_{Bi}) \end{aligned} \quad (2.17)$$

where

G = dissolved species concentration per unit volume (radionuclide activity or weight of species per unit volume)

G_i = particulate species concentration associated with the i^{th} sediment (radionuclide activity or weight of species per unit volume)

G_{Bi} = particulate species concentration per unit weight of sediment in the i^{th} sediment size fraction in the bed

K_i, K'_i = transfer rate of species with the i^{th} moving sediment for adsorption and desorption, respectively

K_{Bi}, K'_{Bi} = transfer rate of species for adsorption and desorption with the i^{th} non-moving sediment in the bed, respectively

K_{Di}, K'_{Di} = distribution (or partition) coefficient between dissolved species and particulate species associated with the i^{th} sediment for adsorption and desorption, respectively.

D_i = particle diameter of the i^{th} sediment

λ = radionuclide decay or, first-order chemical and biological degradation rates of species

γ_i = specific weight of the i^{th} sediment

POR = porosity of bed sediment

Note that, in Equation (2.17), adsorption and desorption do not occur simultaneously.

2.11.3 Transport Equation for the i^{th} Particulate Species in Cartesian Coordinates (R,X,Z)

FLESCOT uses Equations (2.18) and (2.19) for transport of the i^{th} particulate species:

$$\begin{aligned} \frac{\partial G_i}{\partial t} + \frac{\partial}{\partial R}(UG_i) + \frac{\partial}{\partial X}(WG_i) + \frac{\partial}{\partial Z}[(V - V_{si})G_i] \\ = \frac{\partial}{\partial R}\left(\epsilon_R \frac{\partial G_i}{\partial R}\right) + \frac{\partial}{\partial X}\left(\epsilon_X \frac{\partial G_i}{\partial X}\right) + \frac{\partial}{\partial Z}\left(\epsilon_Z \frac{\partial G_i}{\partial Z}\right) + \dot{G}_i \end{aligned} \quad (2.18)$$

$$\dot{G}_i = -\lambda G_i - \frac{S_{Di}}{H} G_i + K_i (C_i K_{Di} G - G_i) + K'_i (C_i K'_{Di} G - G_i) + \frac{G_{Bi} S_{Ri}}{H} + Q_i \quad (2.19)$$

where Q_i = source of particulate species G_i .

2.11.4 Transport Equation for Salinity in Cartesian Coordinates (R,X,Z)

The transport equation for salinity used in FLESCOT is Equation (2.20):

$$\begin{aligned} \frac{\partial S}{\partial t} + \frac{\partial}{\partial R}(US) + \frac{\partial}{\partial X}(WS) + \frac{\partial}{\partial Z}(VS) \\ = \frac{\partial}{\partial R}\left(\epsilon_R \frac{\partial S}{\partial R}\right) + \frac{\partial}{\partial X}\left(\epsilon_X \frac{\partial S}{\partial X}\right) + \frac{\partial}{\partial Z}\left(\epsilon_Z \frac{\partial S}{\partial Z}\right) \end{aligned} \quad (2.20)$$

where S = salinity.

3.0 Ogi Dam Reservoir Modeling

3.1 Description of the Ogi Dam Reservoir

The Ogi Dam and its reservoir on the Oginosawa River are located in a mountainous area near Kawauchi Village about 15 km southwest of the Fukushima Daiichi NPP, as shown in Figure 3.1. The reservoir is marked by a small red circle in the bottom-right image, which is a cesium contamination level map. The Ogi Dam Reservoir had supplied irrigation water to local rice paddy fields before the nuclear accident. It is a small but a typical reservoir in the Fukushima area. Figure 3.2 shows the contours of the reservoir bottom elevation measured by Funaki et al. (2013). The volume of the reservoir is approximately $5 \times 10^5 \text{ m}^3$ and the maximum water depth is about 12 m. River water enters at three places; the main entrance is at the southwestern end. The water level was 362 m above sea level before the Fukushima accident. It was lowered to 358 m after the accident to avoid collapse of the dam structure due to any aftershocks because it is located in an evacuation area and cannot be actively managed. Because the upstream area is relatively contaminated, the contamination of the reservoir is a concern of the local community.

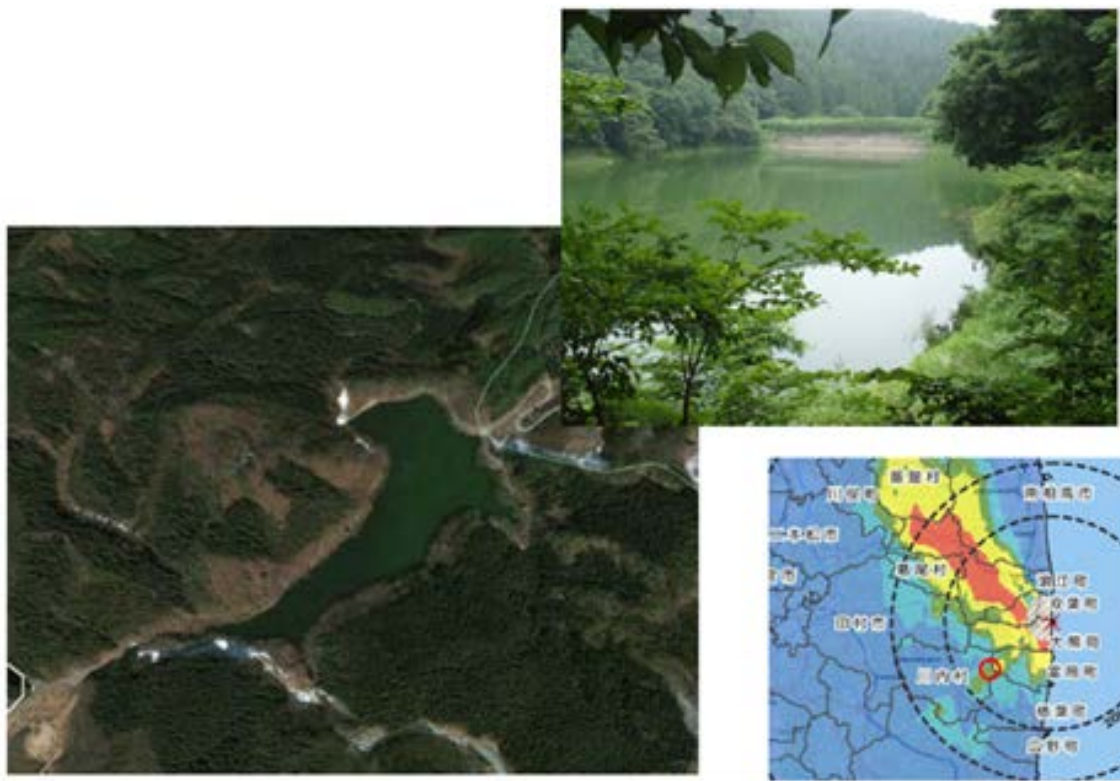


Figure 3.1. Location of the Ogi Dam Reservoir (bottom right) and Images of the Area

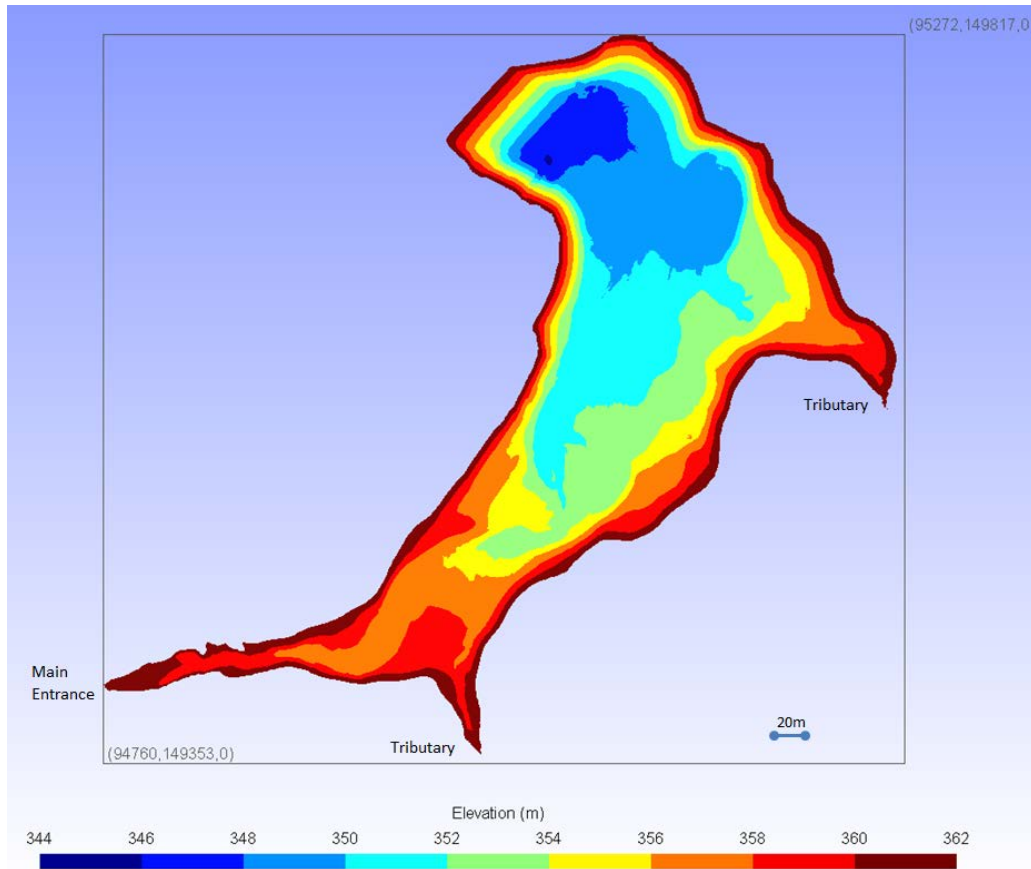


Figure 3.2. Contours of the Bottom Elevation in the Ogi Dam Reservoir

3.2 Simulation Results

3.2.1 Modeling Conditions

The domain was divided into 49,140 computation cells (resolution: 52 in the longitudinal direction \times 27 in the vertical-direction \times 35 in the lateral direction) as shown in Figure 3.3, where the number of fluid cells is 9,595. As boundary conditions, constant water fluxes were applied to the Oginosawa River and two other small streams at the upstream end of the reservoir. They were $1.0 \text{ m}^3/\text{s}$ for the Oginosawa River and $0.1 \text{ m}^3/\text{s}$ for the two small streams. Suspended sand, silt and clay concentrations at these three boundary locations were assigned to be 0.02 , 0.02 and $0.01 \text{ kg}/\text{m}^3$, and concentrations of dissolved cesium, sand-sorbed cesium, silt-sorbed cesium and clay-sorbed cesium were set to be $1,000 \text{ Bq}/\text{m}^3$, $3 \times 10^4 \text{ Bq}/\text{kg}$, $5 \times 10^5 \text{ Bq}/\text{kg}$, and $1 \times 10^5 \text{ Bq}/\text{kg}$, respectively. Distribution coefficients of sand, silt and clay to cesium were assigned to be 30, 500, and $100 \text{ m}^3/\text{kg}$, respectively, for these preliminary simulations. For thermal conditions, three cases were simulated: an isothermal condition, river inflows of colder water, and river inflows of warmer water. The simulation time was $10 \times 10^5 \text{ s}$ (about a day).

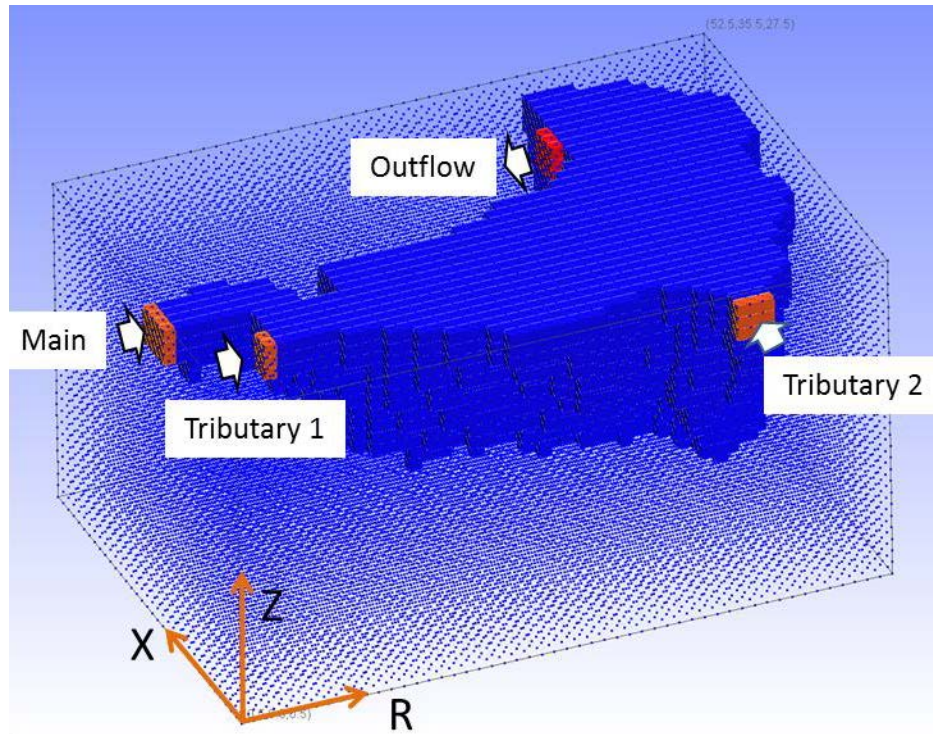


Figure 3.3. The Ogi Dam Reservoir Model Setup

3.2.2 Preliminary Simulation Results

Figure 3.4, Figure 3.5, and Figure 3.6 show the simulation results. Under the isothermal condition shown in Figure 3.4, the velocity field was almost uniform in the cross section perpendicular to the flow direction. On the other hand, large-scale flow circulations occur due to thermal convection in the colder and warmer river inflow cases.

In the colder water inflow case (Figure 3.5), the river water flows sink into the deeper part of the reservoir, causing a reverse flow moving toward the reservoir entrance near the water surface. On the other hand, for the warmer river inflow case (Figure 3.6), the river inflow spread over the reservoir near the water surface, causing a reverse flow near the reservoir bottom moving toward the reservoir entrance.

The simulated distributions of suspended sediment and cesium concentrations generally reflect these differences of the flow distributions with each case. This suggests that seasonal temperature changes influence the sediment and cesium transport.

Regarding the bed conditions, sand settled near the entrance, then silt deposited, and clay traveled far from the entrance. In these simulations, all sand and silt deposited. Since the distribution coefficient of silt was higher than those for sand and clay, the bed contamination was strongly affected by the deposition of silt.

With these preliminary simulations, we confirmed the applicability of the FLESCOT code to reservoirs in the Fukushima environment. In the next step, we need to calibrate and validate the simulation results with the Ogi Dam Reservoir field data being collected by JAEA.

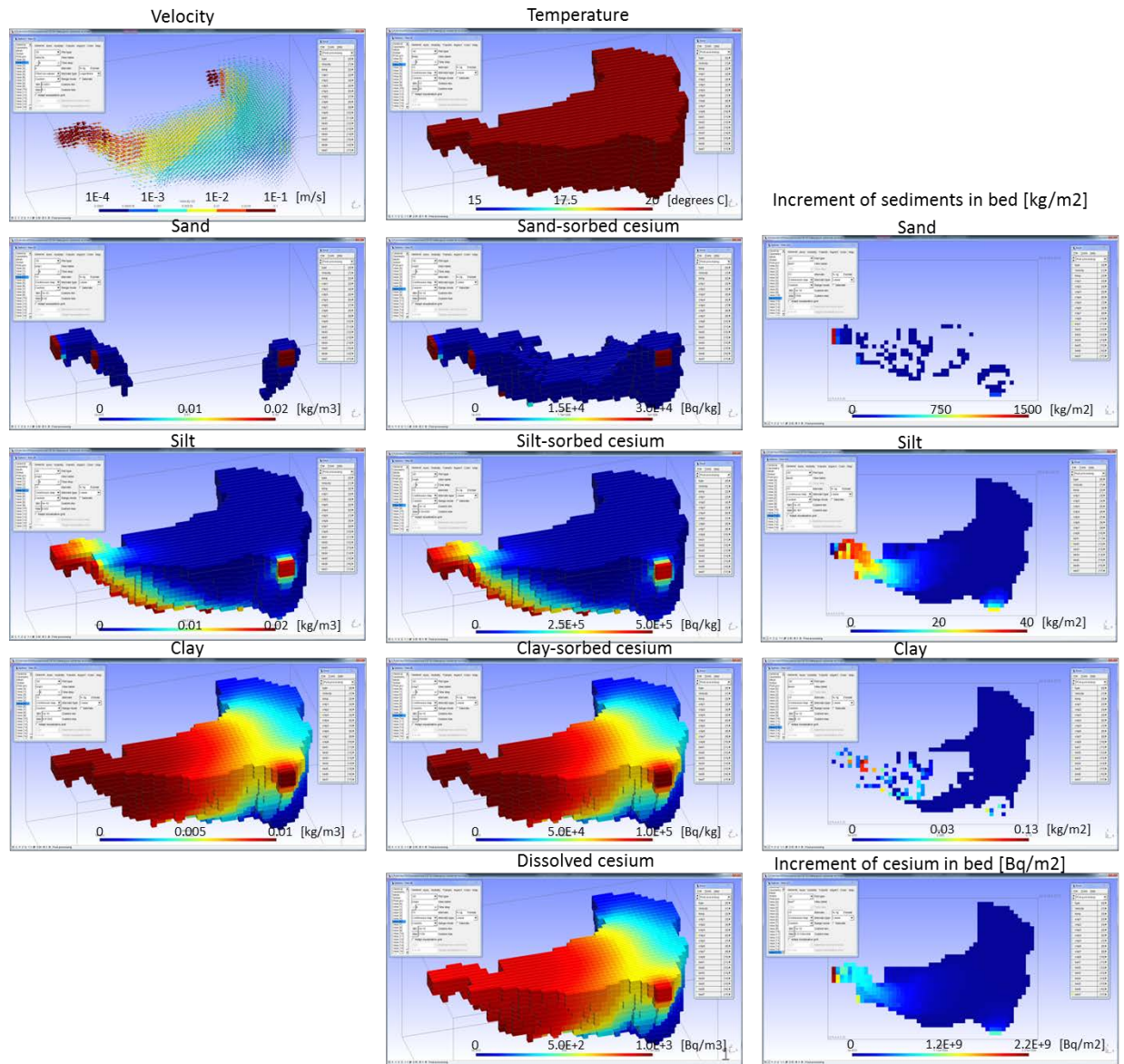


Figure 3.4. Ogi Dam Reservoir Simulation Results for an Isothermal Condition Case

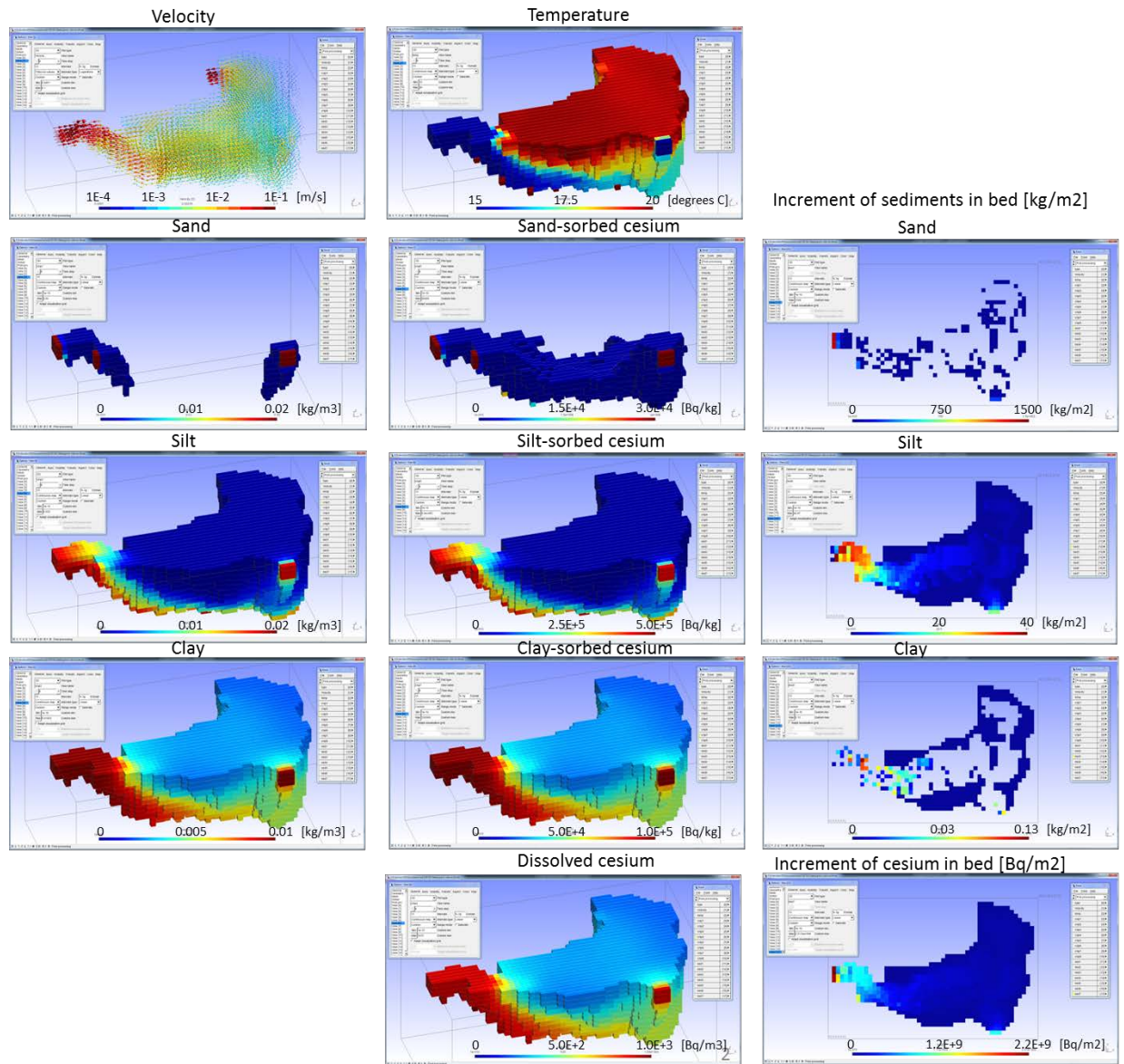


Figure 3.5. Ogi Dam Reservoir Simulation Results for the Colder Water Inflow Case

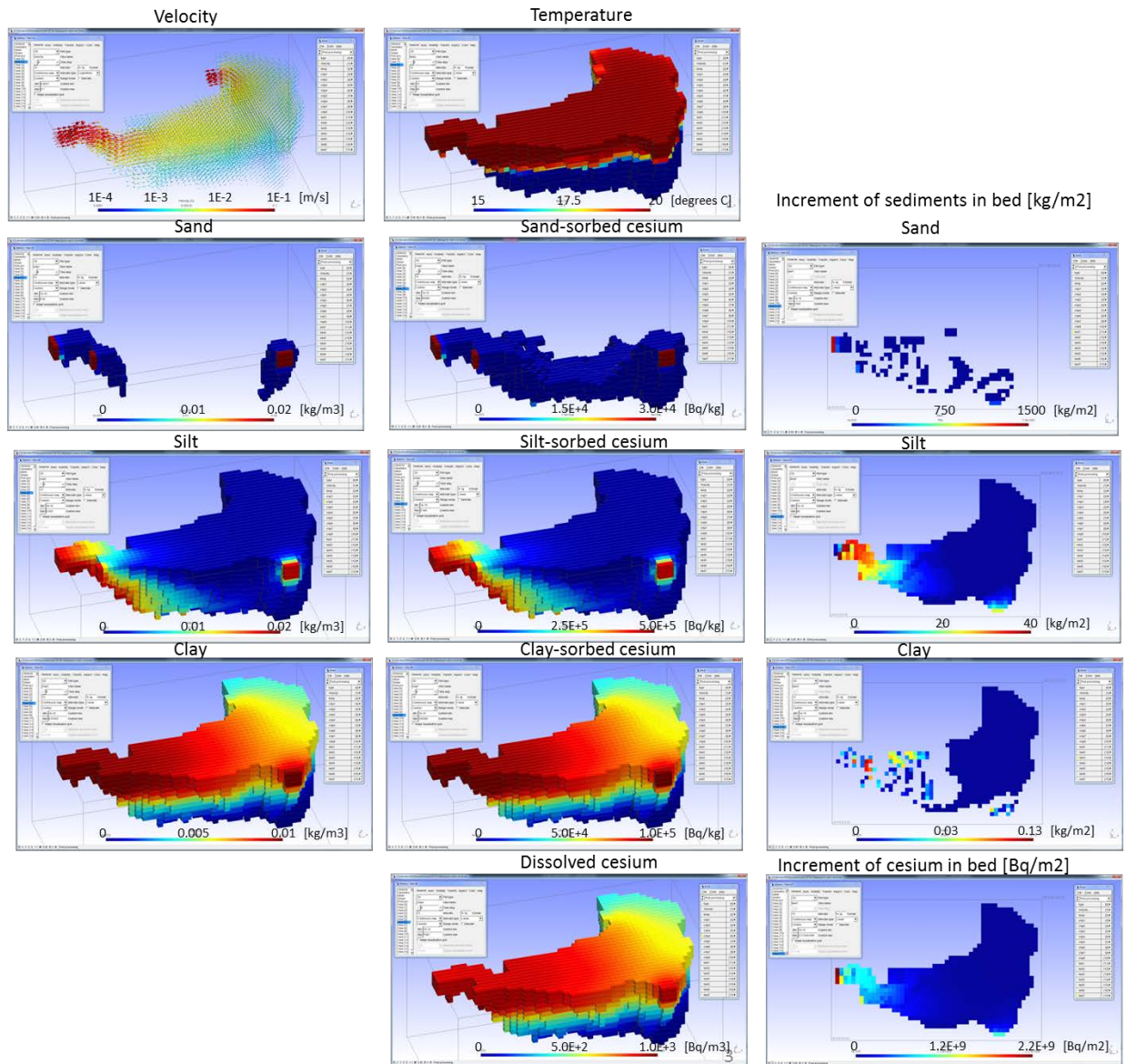


Figure 3.6. Ogi Dam Reservoir Simulation Results for the Warmer Water Inflow Case

4.0 Conclusions

We initiated simulation of the sediment and cesium transport and deposition in the Ogi Dam Reservoir in the Fukushima area using the FLESCOT code. JAEA has been sampling in the Ogi Dam Reservoir, but these data are not yet available for the current model calibration and validation for this reservoir.

The preliminary results showed that suspended sand, and cesium adsorbed by sand, coming into the reservoirs from upstream rivers deposit near the reservoir entrance; suspended silt, and cesium adsorbed by silt, deposit farther into the reservoir; and suspended clay and cesium adsorbed by clay travel the farthest into the reservoir. With sufficient time, the dissolved cesium reaches the downstream end of the reservoir. The current preliminary simulations suggest that seasonal temperature changes influence the sediment and cesium transport. This preliminary modeling also suggests the possibility of a suitable dam operation to control cesium migration farther downstream from the dam.

Future issues to be addressed are the following:

- Validate the simulation results by comparison with the investigation data.
- Confirm the applicability of the code to coastal areas in Fukushima.
- Increase computation speed by parallelizing the FLESCOT code.

5.0 References

- Funaki H, H Hagiwara, and T Tsuruta. 2013. “The Behavior of Radiocesium Deposited in an Upland Reservoir after the Fukushima Nuclear Power Plant Accident.” *Proceedings of the International Symposium “Scientific Basis for Nuclear Waste Management”* (MRS 2013), September 30–October 4, 2013, Barcelona, Spain. (In press).
- Iijima K, T Niizato, A Kitamura, H Sato and M Yui. 2013. *Long-term Assessment of Transport of Radioactive Contaminant in the Environment of Fukushima (F-TRACE)*. Japan Atomic Energy Agency, Fukushima, Japan. Accessed February 17, 2014 at http://fukushima.jaea.go.jp/initiatives/cat01/pdf00/20_Iijima.pdf.
- Jones WP and BE Launder. 1973. “The Calculation of Low-Reynolds-Number Phenomena with a Two-Equation Model of Turbulence.” *Int. J. Heat Mass Transfer* 16:1119–1130.
- Onishi Y and DS Trent. 1985. “Three-Dimensional Simulation of Flow, Salinity, Sediment, Radionuclide Movements in the Hudson River Estuary.” In *Proceedings of the 1985 Specialty Conference of the Hydraulics Division*, , pp. 1095–1100. American Society of Civil Engineers, August 12–17, 1985, Lake Buena Vista, Florida.
- Onishi Y and DS Trent. 1992. “Turbulence Modeling for Deep Ocean Radionuclide.” *International Journal for Numerical Methods in Fluids* 15(9):1059–1071.
- Onishi Y, HC Graber and DS Trent. 1993. “Preliminary Modeling of Wave-Enhanced Sediment and Contaminant Transport in New Bedford Harbor.” In Book Series 42 of *Estuarine and Coastal Water Cohesive Sediment Transport*, pp. 541–557, AJ Mehta (Ed.), American Geophysical Union.
- Onishi Y, DS Trent and AS Koontz. 1987. “Three-Dimensional Hydrodynamic and Transport Modeling of Sequim Bay, Washington.” In *Abstract Proceedings of the Workshop on Modeling Physical Oceanography of Puget Sound*, pp. 32–33, November 4–5, 1987, Seattle, Washington.

Appendix

TEMPEST

Assessment and Verification Results

APPLIED TECHNOLOGY

Any further distribution by any holder of this document or of the data therein to third parties representing foreign interests, foreign governments, foreign companies, and foreign subsidiaries or foreign divisions of U.S. companies should be coordinated with the Deputy Assistant Secretary for Breeder Reactor Programs, Department of Energy.

TEMPEST

A THREE-DIMENSIONAL TIME-
DEPENDENT COMPUTER PROGRAM FOR
HYDROTHERMAL ANALYSIS

VOLUME II: ASSESSMENT AND VERIFICATION
RESULTS

L. L. Eyer
D. S. Trent
M. J. Budden

September 1983

Prepared for
the U.S. Department of Energy
under Contract DE-AC06-76RLO 1830

Pacific Northwest Laboratory
Richland, Washington 99352

CONTENTS

FOREWORD	iii
ACKNOWLEDGEMENTS.....	v
1.0 INTRODUCTION.....	1.1
1.1 TEMPEST DEVELOPMENT SCOPE.....	1.2
1.2 TEMPEST ASSESSMENT AND VALIDATION PHILOSOPHY.....	1.6
1.3 STATUS OF TEMPEST ASSESSMENT AND VALIDATION.....	1.8
2.0 CONCLUSIONS AND RECOMMENDATIONS.....	2.1
3.0 CONDUCTION HEAT TRANSFER SIMULATION RESULTS.....	3.1
3.1 TRANSIENT HEAT CONDUCTION IN CARTESIAN GEOMETRY.....	3.1
3.2 TRANSIENT HEAT CONDUCTION IN A CYLINDRICAL GEOMETRY.....	3.2
3.3 COMPUTATIONAL EFFICIENCY OF TEMPEST COMPARED TO OTHER CONDUCTION CODES.....	3.8
4.0 CONVECTION SIMULATION RESULTS: LAMINAR FLOW.....	4.1
4.1 LAMINAR ISOTHERMAL FLOW.....	4.1
4.4.1 One-Dimensional Testing.....	4.2
4.1.2 Two-Dimensional Testing: Cartesian Coordinates.....	4.3
4.1.3 Two-Dimensional Testing: Cylindrical Coordinates.....	4.11
4.1.4 Three-Dimensional Testing.....	4.15
4.2 CONVECTION FLOW AND HEAT TRANSFER.....	4.17
4.2.1 Flat-Plate Convection Heat Transfer.....	4.18
4.2.2 Plane Channel Flow with Variable Viscosity.....	4.21
4.2.3 Buoyancy-Driven Cartesian Cavity Convection.....	4.23
4.2.4 Combined Free- and Forced-Convection Pipe Flow (Morton's Problem).....	4.29

4.2.5	Natural-Convection Heat Transfer in a Cylindrical Annulus.....	4.31
4.2.6	Time-Step Testing in Internal Wave Flow with Stable and Unstable Stratification.....	4.34
4.3	THERMALLY COUPLED FLOW AND SOLID-WALL HEAT CONDUCTION.....	4.40
4.3.1	Steady-State Heat Transfer Between Two Flow Cavities....	4.40
5.0	CONVECTION SIMULATION RESULTS: TURBULENT FLOW.....	5.1
5.1	TURBULENT ISOTHERMAL FLOW.....	5.2
5.1.1	One-Dimensional Diffusion of Turbulence Variables.....	5.2
5.1.2	Free Shear Decay.....	5.2
5.1.3	Combined Grid Generation and Decay.....	5.3
5.1.4	Momentum Jets.....	5.5
5.1.5	Two-Dimensional Plane Channel Flow.....	5.10
5.1.6	Two-Dimensional Pipe Flow.....	5.14
5.1.7	Three-Dimensional Scaled Breeder Reactor Upper Plenum Model.....	5.19
5.2	TURBULENT FLOW WITH HEAT TRANSFER.....	5.38
5.2.1	Buoyant, Turbulent Jets and Plumes.....	5.39
5.2.2	Turbulent Heat Transfer Boundary Condition Model and Pipe Flow Results.....	5.42
5.2.3	Fluid and Thermal Mixing in a Model Cold Leg and Downcomer.....	5.50
6.0	ADDITIONAL SIMULATIONS.....	6.1
6.1	LAMINAR CONVECTION.....	6.1
6.1.1	Vertical, Closed-End Thermal Siphon.....	6.1
6.1.2	Natural Convection About a Horizontal Cylinder.....	6.3
6.1.3	Natural Convection in a Full-Polar, Cylindrical Region.....	6.3

6.1.4	Transient, Two-Region, Coupled Convection in Cylindrical Coordinates.....	6.6
6.2	TURBULENT CONVECTION.....	6.10
6.2.1	Cooling Tower Inlet Structure with Flow Diverter Vaness.....	6.10
6.2.2	Positively Buoyant Thermal Outfall Plume Injected at the River Bottom.....	6.13
6.2.3	Large-Scale Prototype Breeder Inlet Torus B10-A Transient.....	6.14

FIGURES

3.1	TEMPEST Predictions and Analytical Solutions for Transient Conduction in One, Two, and Three Dimensions in Cartesian Coordinates.....	3.3
3.2	Transient One-dimensional Heat Conduction in Cylindrical Coordinates.....	3.5
3.3	Steady-State One-dimensional Radial Conduction with Heat Generation and Surface Film Coefficient.....	3.6
3.4	Transient, Two-Dimensional Heat Conduction in Cylindrical Coordinates.....	3.7
3.5	Schematic of the Two-Region, Steady-State Test Problem for Conduction Code Comparison (Problem 1).....	3.9
3.6	Schematic of the Transient Test Problem for Conduction Code Comparison (Problem 2).....	3.9
3.7	Comparison of Computation Speed for Conduction Problem 1.....	3.12
3.8	Comparison of Computation Speed for Conduction Problem 2.....	3.13
4.1	Schematic of Form and Friction Drag Application.....	4.3
4.2	Schematic Showing Slip Factor Application.....	4.4
4.3	Velocity Profiles for a Two-Dimensional Planar Channel, with Uniform Inlet Velocity and Constant Cell Spacing, $Re = 500$ Case.....	4.5
4.4	Velocity Profiles for a Two-Dimensional Planar Channel with Uniform Inlet Velocity and Constant Cell Spacing, $Re = 50$ Case.....	4.6
4.5	Velocity Profiles for a Two-Dimensional Cartesian Channel with Uniform Inlet Velocity and Variable Cell Spacing, $Re = 200$ Case.....	4.7
4.6	Comparison of Computed Centerline Velocity for a Two-Dimensional Planar Channel with Uniform Inlet Velocity.....	4.9
4.7	Variable Cell Spacing Nodalization Pattern for a Two-Dimensional Cartesian Channel with an Inlet Plenum.....	4.10
4.8	Velocity Profiles for a Two-Dimensional Planar Channel.....	4.11

4.9	Velocity Profiles for a Two-Dimensional, Cylindrical-Channel Flow with Uniform Inlet Velocity and Constant Cell Spacing, Re = 100 Case.....	4.13
4.10	Velocity Profile for a Two-Dimensional, Cylindrical-Channel Flow with Uniform Inlet Velocity and Variable Cell Spacing, Re = 100 Case.....	4.14
4.11	Comparison of Computed Centerline Velocity for Two-Dimensional Pipe Flow with Uniform Inlet Velocity.....	4.15
4.12	Velocity Profiles for a Three-Dimensional Cartesian Square Channel with Uniform Inlet Velocity and Constant Cell Spacing, Re = 200 Case.....	4.16
4.13	Centerline Velocity Profile for a Square Channel with Uniform Inlet Velocity and Constant Cell Spacing, Re = 200 Case.....	4.16
4.14	Schematic of the Flat-Plate Heat Transfer Problem.....	4.19
4.15	Comparison of Predicted and Theoretical Local Film Coefficients on a Flat Plate.....	4.20
4.16	Plane Channel Velocity Profile Comparison for Temperature Dependent Viscosity.....	4.22
4.17	Plane Channel Velocity Profile Comparison for Concentration-Dependent Viscosity.....	4.22
4.18	Natural Convection in a Two-Dimensional Cavity.....	4.24
4.19	Nondimensional, Square-Cavity Convection Simulation.....	4.26
4.20	Comparison of Predicted and Analytical Vertical Velocity Results in Bouyancy-Affected Laminar Pipe Flow.....	4.30
4.21	Cylinder Geometry and Node Structure for Annular Convection.....	4.32
4.22	Equivalent Thermal Conductivity Comparison for Annular Convection between Cylinders.....	4.32
4.23	Comparison of Predicted and Measured Isotherms at a Rayleigh Number of 5×10^4	4.33
4.24	Predicted Isotherms at a Rayleigh Number of 6×10^8	4.33
4.25	Internal Wave Type Oscillations in a Stably Stratified Adiabatic Box.....	4.36
4.26	Implicitly Damped Density Perturbation in a Stable Stratification.....	4.36

4.27	Vertical Velocity in an Unstable Density Gradient Turnover.....	4.38
4.28	Temperature in Unstable Density Gradient Turnover.....	4.38
4.29	Initial Unstable Temperature Gradient and Final Stable Gradient After Turnover.....	4.39
4.30	Schematic of Apparatus for a Two-Cavity Convection Experiment.....	4.41
4.31	Schematic of the Cell Structure in the Vicinity of the Conducting Wall.....	4.42
4.32	Temperature Profile at Midplane of Glass Wall.....	4.42
4.33	Comparison of Predicted and Measured Dimensionless Wall Surface Temperatures.....	4.43
4.34	Comparison of Surface Heat Flux for Coupled-Cavity Convection.....	4.46
5.1	Square-Rod, Square-Mesh Grid and Computational Structure - Full Square.....	5.4
5.2	Square Rod, Square Mesh Grid and Computational Structure - Quarter-Section Symmetry.....	5.5
5.3	Comparison of TEMPEST-Predicted, Grid-Generated Turbulence with Data.....	5.6
5.4	Momentum Jet Centerline Velocity.....	5.8
5.5	Momentum Jet Axial Velocity Profiles.....	5.9
5.6	Decay of Centerplane Velocity Comparison.....	5.10
5.7	Axial Distribution of Turbulence Intensity in a Round Jet.....	5.11
5.8	Radial Distribution of Turbulence Intensity in a Round Jet.....	5.11
5.9	Comparison of Two-Dimensional, Turbulent-Plane-Channel Data and Predictions.....	5.13
5.10	Two-Dimensional, Plane-Channel Velocity Profiles.....	5.15
5.11	Comparison of Turbulent Air Flow in a Pipe at $Re_0 = 5 \times 10^4$ and 5×10^5	5.16
5.12	Turbulent Pipe Flow, Comparison of TEMPEST and TEACH Results.....	5.18
5.13	Schematic of FFTF Test Geometry.....	5.20
5.14	FFTF Scaled Model with Constant-Mesh Noding Structure.....	5.21

5.15	Variable-Mesh Noding Structure: A) 2D and 3D Centerplane, B) 3D Depth Plane.....	5.22
5.16	Mean Vertical Velocity at Two Horizontal Planes.....	5.23
5.17	Mean Horizontal Velocity at Two Vertical Planes.....	5.24
5.18	Comparison of Experimental and Predicted Data for Centerplane Kinetic Energy with Constant Grid Spacing.....	5.26
5.19	Vertical Profile of Kinetic Energy at the Centerline Above the Inlet Chimney.....	5.29
5.20	Vertical Profile of Kinetic Energy at the Centerline Above the Inlet Chimney.....	5.30
5.21	Vertical Profile of Mean Vertical Velocity at the Centerline Above the Inlet Chimney.....	5.33
5.22	Comparison of 2D and 3D Kinetic Energy Predictions for Constant and Variable Mesh Spacing at Horizontal Plane $Z = 10$	5.34
5.23	Comparison of 2D and 3D Kinetic Energy Predictions at Horizontal Planes $Z = 6.2$ and 18.1	5.36
5.24	Comparison of Vertical Predictions and Data for 3D Flow.....	5.37
5.25	Centerline Temperature Results for Buoyant, Turbulent Jets.....	5.40
5.26	Centerline Velocity Results for Buoyant, Turbulent Jets.....	5.41
5.27	Velocity and Temperature Spread in a Buoyant, Turbulent Jet at $Z/D_0 = 35$	5.42
5.28	Heated Air Flow Temperature and Turbulence Profiles.....	5.45
5.29	Mercury Pipe Flow Temperature Profile.....	5.46
5.30	Dimensionless Mercury Pipe Flow Temperature Profiles.....	5.47
5.31	Experimental and Predicted Sodium Temperature Profiles.....	5.48
5.32	Experimental and Predicted Profiles of Dimensionless Sodium Temperature.....	5.49
5.33	Schematic of Cold Leg and Downcomer Mixing Test Model.....	5.51
5.34	Cold Leg Pipe Noding Structure.....	5.54
5.35	Downcomer Noding and Relative Thermocouple Locations.....	5.55

5.36	Transient Cold Leg Pipe Temperatures.....	5.57
5.37	Data and Predictions for Cold-Leg Temperatures in Creare Test Number 61.....	5.58
5.38	Downcomer Vessel Wall Temperatures.....	5.59
5.39	Downcomer Core Barrel Wall Temperatures.....	5.60
5.40	Temperature Contours at 200 sec.....	5.61
6.1	Vertical, Closed-end Thermal Siphon.....	6.2
6.2	Natural Convection about a Heated Horizontal Cylinder Located in a Free Environment, Isotherm and Velocity Vectors.....	6.4
6.3	Grid Structure for Full-Polar, Cylindrical Pipe Convection.....	6.5
6.4	Vertical Velocity Profiles for Full Polar, Cylindrical Pipe Convection.....	6.7
6.5	Description of the Heat-Transfer-Coupled Two-Region Model.....	6.8
6.6	Temperature History of the Two-Region Problem.....	6.9
6.7	Cooling Tower Inlet Structure with Turning Vanes.....	6.11
6.8	Cooling Tower Inlet Structure with No Turning Vanes.....	6.12
6.9	Predicted River Bottom Excess Temperature as a Function of Distance from Outfall Centerline.....	6.15
6.10	Predicted River Surface Excess Temperature as a Function of Distance from Outfall Centerline.....	6.16
6.11	B10-A Transient Torus Temperatures.....	6.17
6.12	B10-A Torus Temperatures at $t = 1000$ sec.....	6.17

TABLES

3.1	Mesh Schemes for Computational Efficiency Comparison of Conduction Problems 1 and 2.....	3.11
4.1	Square Cavity Nusselt Number Results.....	4.28
5.1	Summary of Two-Dimensional, Plane-Channel Test Cases.....	5.12
5.2	FFTF Scale Model Flow and Simulation Parameters.....	5.19
5.3	Friction Velocity Comparison in Heated Pipe Flows.....	5.49
5.4	Conditions for Creare Test No. 61.....	5.52

TEMPEST--A THREE-DIMENSIONAL TIME-DEPENDENT COMPUTER PROGRAM FOR HYDROTHERMAL ANALYSIS

1.0 INTRODUCTION

TEMPEST (a) is a transient, three-dimensional, finite-difference hydrothermal code designed to analyze a rather broad range of coupled fluid dynamic and heat transfer systems. It was developed for the U.S. Department of Energy, Division of Reactor Research and Technology, at the Pacific Northwest Laboratory. The primary objective of the code development program was to develop a state-of-the-art computer code which could be used for design analysis of fast breeder reactor component thermal hydraulics.

In TEMPEST, the full three-dimensional, time-dependent equations of motion, continuity, and heat transport are solved for either laminar or turbulent flow. Heat diffusion in both solid and liquid materials is included. Turbulence is modeled using a two-equation $k-\epsilon$ model. Because TEMPEST has been constructed with reasonable generality, it has considerable application outside the intended reactor design applications.

This report presents results computed with TEMPEST for the purpose of code assessment and validation during the course of the code's development. The objective of this report is to document these results. This objective is accomplished by comparison of TEMPEST predictions with experimental data, analytical solutions, and predictions of other computer codes which are less general or designed for specific applications. A wide spectrum of physical flow phenomena, geometrical configurations, and testing simulations are included. A separate report (Trent, Eyster and Budden 1983) presents the numerical basis for the code and describes user input.

(a) Transient Energy Momentum, and Pressure Equation Solution in Three Dimensions

1.1 TEMPEST DEVELOPMENT SCOPE

The primary objective of the TEMPEST code development effort is to provide a user-oriented hydrothermal analysis tool that is capable of resolving a wide range of hydrothermal flow problems. To satisfy this objective, TEMPEST was developed with several basic feature requirements. These included:

- fully three-dimensional with one- and two-dimensional capabilities included
- time-dependent coupled heat transfer and fluid dynamics
- capability for steady-state heat transfer only
- capability to predict spatial- and time-varying turbulent effects on transport processes over a wide range of flow conditions and geometry
- self-contained FORTRAN code operational on a CDC-7600 computer but modifiable to run on other computers with minimal effort.

In addition to these basic features, particular emphasis was placed on:

- single-phase flow and geometries typical of conditions in fast breeder reactor designs
- ease of use through input specification and the consequent elimination of the need for internal coding changes
- minimization of computation time
- validation of numerics and modeled physics.

Development of the TEMPEST computer code under these general guidelines has resulted in a finite-difference code with rather extensive capabilities. These are summarized by categories as follows:

- Modeling Capabilities
 - full three-dimensional with one- or two-dimensional options
 - time-dependent with transient approach to steady state
 - turbulence models (k- ϵ model)

- Cartesian or cylindrical coordinates
- heat diffusion in solid regions
- full implicit solution to the thermal energy equation and all scalar equations
- direct solution for thermal steady state
- multiple flow regions (may be connected through conduction heat transfer)
- arbitrary orientation of solution coordinate system (with respect to gravity)
- variable grid spacing along all or any coordinate direction(s)
- use of specified or precomputed flow regions
- internal heat generation (20 time-dependent tables possible on a node-by-node or material-by-material basis)
- fifty different material types
- inflow/outflow boundaries specified or computed
- time-dependent flow and thermal boundary condition tables (20 tables possible)
- variable materials properties (thermal conductivity, density, specific heat, and viscosity)
- single-cell width or zero-width wall logic
- drag coefficient correlations for each direction of each cell (98 different coefficient types available from input specification)
- film coefficient for each direction of each cell
- partial material properties table built in
- wind shear
- planetary Coriolis effects.

- Program Control

- hydrodynamics only
- solids heat transfer only
- decoupled hydrodynamics (no buoyancy effects)
- fully coupled hydrodynamics and heat transfer
- inviscid hydrodynamics
- variable eddy transport coefficients (e.g., two-equation turbulence model)
- steady-state thermal solution
- ability to obtain steady-state thermal solution at each hydrodynamic time step
- internal wave stability control
- automatic time stepping and stability control
- restart at any filed time
- computation in either the U.S. Customary System of engineering units or the International System (SI) of units.

- I/O Control

- input debug output and control (limited)
- internal bookkeeping debug output options
- cell type/material type maps
- intermediate output including heat transfer connectors, cell continuity, density, thermal conductivity, molecular viscosity, eddy viscosity, turbulence quantities, heat flux map, numerical stability map and heat generation
- all primary variables with either R-Z, R-X, or Z-X arrays on output page
- ability to specify print/file time

- choice of either the Engineering or SI system of units for input data supplied for the same run
- partial skip of printing
- result and execution time monitoring
- postprocessing graphics (including contours, vectors, and line plots).
- Limitations of the code are as follows:
 - Flow is incompressible only.
 - Computational cell structure must be in rows/columns/tiers.
 - Cartesian or cylindrical coordinate are allowed (regions cannot have mixed coordinates).
 - Hydrodynamic solution is explicit in time--no direct solution for steady state.
 - Pressure boundary conditions are not available.
 - Curved boundaries (except circular) must be stair-stepped.

The TEMPEST code simulates flow and thermal fields subject to the following assumptions and/or restrictions:

- The fluid is single phase and incompressible (insofar as sonic effects are not considered).
- The body forces other than gravity are not considered. Forces resulting from an accelerating reference frame are included.
- The fluid is Newtonian (for laminar situations, Navier-Stokes equations apply).
- The turbulent flow conservation equations are time averaged, and Reynolds stresses are incorporated through appropriate eddy viscosity models.
- The viscous dissipation is eliminated.
- The Boussinesq approximation holds.

For low-speed flows that involve small density variations (i.e., $|\Delta\rho/\rho| \ll 1$), the well-known Boussinesq approximation is valid. This approximation is commonly used in natural convection simulations involving either liquids or gases. While the approximation is consistent with the accuracy of other approximations required for numerical simulation, its validity is questionable if density changes considered are large compared to local fluid density. Whereas most simulations involving liquid systems are within the valid range of this approximation, care should be exercised in gaseous systems, where temporal and spatial temperature changes may be large. The obvious reason for involving the Boussinesq approximation in TEMPEST is that some simplification of the governing equations is possible by treating density as constant in all terms except the body force terms of the momentum equations.

1.2 TEMPEST ASSESSMENT AND VALIDATION PHILOSOPHY

Assessment and validation of the TEMPEST computer code has been based on the premise, "A computer code whose ultimate use is for simulating integrated phenomena in complex engineering systems must first be able to accurately simulate a wide range of similar phenomena in simple systems." The code assessment and validation process should begin with simulating simple phenomena in simple geometries and proceed systematically to the complexities of engineered systems.

The premise of "simple problem correctness" is the foundation of TEMPEST assessment and validation philosophy. The approach used to support the premise is two-fold. The first step has been to verify coding. The second step has been to validate the modeled physics. These two steps, however, are not completely independent.

There are numerous approaches to verification of coding logic. The basic approach which has been used in the TEMPEST development is summarized as follows:

- Critical coding has been double checked by cognizant personnel who did not do the programming; however, it is not economically practical to check the entire program in this manner.

- Code logic has been extensively exercised to ensure that input, set-up, and other bookkeeping phases work correctly.
- Printing of intermediate computation debugging output has been made available by input command for hand checking.

Coding verification and logic flow checking have been continuous processes throughout development of TEMPEST.

Validating modeled physics is a more involved process. TEMPEST predictions have variously been compared to analytical results, results predicted by other codes, and experimental data. Each case has provided incremental support to conclusions concerning the correctness and accuracy of TEMPEST predictions.

There are a number of analytical solutions available in technical journals and text books which are readily available for code validation. Most of these, however, are analytical conduction heat transfer solutions. Analytical solutions for hydrodynamics are more limited. Several, such as laminar plane channel, pipe, and duct flow have been used.

There is a wealth of information published in technical literature regarding computed results which have been compared to experimental data. These results are invaluable because they are most often simple separate effects simulations, and both code results and data are already compared. It is also useful to obtain and use other computer codes to run side-by-side simulations of identical problems. This has been done using TEACH (Gosman et al. 1976). This code has considerably less capability than does TEMPEST, but TEMPEST can simulate problems within the capabilities of the TEACH. In this respect TEACH has been very valuable in assessing the TEMPEST turbulence model.

Comparison of predicted results with experimental data is, perhaps, the best test of modeled physics. Data for separate effects and small-scale experiments are readily available in open literature. While data for large-scale experiments are less available, sufficient large-scale data are available to test the more pertinent aspects of numerically modeled flows. Actual operating data in fast reactor components would be the best test of a code's

computation, but such data are rare, especially data sufficiently accurate and with sufficient spatial resolution to assess predictions.

1.3 STATUS OF TEMPEST ASSESSMENT AND VALIDATION

A large amount of testing assessment and validation has been done with TEMPEST as demonstrated by results in Sections 3.0, 4.0, and 5.0 of this report. The testing results are presented in a systematic manner beginning with the simpler and ending with the more complex. There are, however, so many features to the code and so many important features to the testing simulations, that not all of the details of each simulation have been presented herein. In most cases, only pertinent results are presented.

Numerous code logic tests have been performed. They have been done to assure that solution procedures are working correctly, that input data and problem set-up are handled correctly, that boundary condition logic is correct, that critical logic paths are decisioned correctly, that restart and postprocessing input/output are working, etc. Itemizing all of these tests would be an extremely lengthy task. The solution algorithms and ancillary bookkeeping code logic have been shown to perform as expected in the operational modes tested, but the process of encountering "bugs" will undoubtedly continue as TEMPEST use continues.

Conduction heat transfer tests are reported in Section 3.0 of this report. One-, two-, and three-dimensional transient and steady-state tests have been completed in both Cartesian and cylindrical geometries using various initial and boundary conditions. These tests indicate that the thermal solution algorithm is working properly in its various user-selectable modes, and that accurate temperatures are predicted.

Extensive laminar flow simulation tests are presented in Section 4.0 of this report. Results are variously compared to data and to analytical and computed results. Both isothermal and nonisothermal results have been assessed along with various code operational modes. These results have led to the conclusion that the basic finite differencing and solution algorithms for hydrodynamics are correct.

Turbulent flow model testing results are presented in Section 5.0. Solution algorithms for the two-equation $k-\epsilon$ model have been confirmed as working correctly. Basic physics of turbulent flows inherent to the $k-\epsilon$ modeling assumptions such as free shear decay, shear production, etc., have been tested and compared to data and other results. Applied boundary conditions for the turbulence transport equations have been extensively checked and confirmed to be working correctly within limits of assumptions applied.

All of the testing results, when considered in totality, represent an extensive assessment and validation of the TEMPEST code. They satisfy the objective of the code validation: to demonstrate that the coding logic is working correctly, that the physics are modeled properly, and that the code operates as advertised. Certainly, additional validation could be done and will be done as the code is used for more application-oriented analysis of large-scale and actual operating reactor systems.

2.0 CONCLUSIONS AND RECOMMENDATIONS

The principal objective of TEMPEST assessment and validation has been to assure correctness of the code's computation capabilities and modeled physics. This has been done through extensive verification of critical coding logic and analysis of computed results. Because of the code's generality, a multiplicity of operational modes are available. An extensive number of these modes have been exercised to assure proper operation of user-selectable options. Results presented in this report support the conclusion that the basic features of the TEMPEST computer code work correctly and that the numerics are capable of accurately predicting the modeled physics.

Solution of the thermal energy equation was confirmed with several tests of conduction heat transfer. Transient and steady-state temperature distributions were compared to analytical solutions in one-, two-, and three-dimensional conduction problems in Cartesian and cylindrical coordinate systems. Fixed temperature and modeled constant heat flux boundary conditions were tested as were spatial distribution of initial conditions and heat generation. Predicted temperature differences are typically less than 1°C out of a total temperature difference of 100°C. Computational efficiency was concluded to be very good when compared to conduction heat transfer codes designed specifically for that purpose.

Simulation of laminar flows were used to confirm correctness of hydrodynamic solution algorithms and differencing approximations. Results were used to conclude that basic finite-difference approximations for the governing equations were correct. Features of variable grid spacing, coordinate system, boundary conditions, drag coefficient specification, etc., were confirmed as working correctly. Comparison of predictions of plane channel flow, duct flow, and pipe flow with analytical velocity profiles, experimental results, and other code predictions further confirmed that the numerics were programmed correctly and that the physics were modeled correctly.

Heated laminar flows were tested to assess computation of thermally coupled flows. Coupling was tested for flow over a flat plate, buoyancy-

induced single-cavity convection, double-cavity convection, and combined convection in a vertical pipe. Comparison of results with data and analytical results was very good. Other simulations--of buoyancy-induced oscillations (internal waves) and full polar convection in a horizontal pipe--tested features of time-stepping logic and coordinate systems and orientation. In all cases, results led to conclusions that a particular capability or capabilities were computing correctly. Temperature-dependent viscosity was modeled to assure that spatially varying variable viscosity differencing logic was correct. This was done preparatory to testing spatial variations of turbulent viscosity.

The turbulence model incorporated in TEMPEST is a two-equation $k-\epsilon$ model. Basic phenomena inherent to the modeled transport equations were tested in simple one- and two-dimensional problems. These included diffusion, grid generation, and free shear decay. Turbulent momentum jets and plume simulations were computed, and results were compared to data. Agreement was satisfactory and well within ranges of previous numerical predictions of other less general $k-\epsilon$ turbulence codes which have been well tested. Buoyancy affects on turbulence were found to suppress turbulence in stably stratified flows, which is in agreement with expected physical phenomena.

Wall boundary conditions for the turbulence model were determined to be working correctly within the basis of the modified law-of-the-wall model incorporated. This was concluded based on numerous simple simulations and on comparison with hand calculations of turbulent-induced wall shear and pressure drop. The turbulent heat transfer wall boundary condition that is incorporated utilizes a modified universal temperature law-of-the-wall model. Modifications were made to handle low- and high-Prandtl-number fluids. The model was confirmed by comparison of heated turbulent flows in pipes with air, water, mercury, and sodium as test fluids.

When considered in totality, the assessment and validation results are extensive. However, because of the multiplicity of the code's operational modes and modeling capabilities, not all features have been explicitly confirmed; nor have all of the features been documented herein. Additional assessment and validation should be done, particularly through the use of

larger-scale experiments and operating reactor applications. While basic physics and coding logic have been extensively tested in simple simulation configurations relatively few large-scale simulations of complex flows have been assessed through comparison with data. Thus, the computational accuracy of such simulations must be assessed individually and separately.

There are several portions of the assessment and validation results which could benefit from additional work. Two principal ones are related to the turbulence modeling and include turbulence effects in stratified flows and turbulent wall heat transfer.

The buoyancy effect model which is built into the $k-\epsilon$ model in TEMPEST is most specifically applicable to stably stratified flow. In this configuration, turbulence is diminished by the stable density gradient, and associated transport mechanisms parallel to the density gradient are correspondingly diminished. Lateral transport mechanisms are not affected correctly in this treatment. Similarly, the reciprocal effect on turbulence in an unstable gradient has not been fully evaluated. The stable gradient effect is predominant for principal design application analysis in fast reactor components, which is why buoyancy effects on turbulence have not been more extensively evaluated.

The turbulent wall heat transfer model in TEMPEST should be further evaluated. It has only been tested in detail for pipe flows. Secondary effects such as buoyancy are not treated explicitly in the model. Thus applications of the model in flows such as free convection from a vertical flat plate or in a stably stratified pool have not been completely evaluated. However, an important point to keep in mind for low-Prandtl-number fluids is that at low turbulence levels (caused by stable density gradients, for example), the model reverts to a conduction boundary condition. This reversion is smooth at the transition point and is quite often more than adequate for sodium flows.

3.0 CONDUCTION HEAT TRANSFER SIMULATION RESULTS

The TEMPEST computer code includes a user input option for computing conduction in solids. When this option is used, the momentum equations and the continuity equation are not solved. The energy equation is solved in either a transient or steady-state mode, depending upon the user input options exercised.

The numerical procedure by which the energy equation is solved is a modification of the Douglas and Gunn three-step algorithm described by Richtmeyer and Morton (1967). Application of the algorithm in the TEMPEST code is described in the TEMPEST users' manual (Trent, Eyster and Budden 1983).

Various conduction heat transfer problems have been simulated to determine the correctness of the conduction heat transfer solution mode of the TEMPEST code. These include simulations in one, two, and three dimensions using the transient and steady-state implicit algorithms. Results are compared with analytical solutions.

3.1 TRANSIENT HEAT CONDUCTION IN CARTESIAN GEOMETRY

Transient heat conduction through one, two, and three dimensions in Cartesian geometry was simulated using constant cell widths. Ten computational cells were used in each coordinate direction. Results were compared to analytical solutions presented by Carslaw and Jaeger (1959). In the problem simulated, one surface of a solid material initially at 100°F was set to 0° at $t = 0$. The opposite surface is insulated. The transient temperature in the solid was then computed for $t > 0$.

The analytical solution for this problem in one dimension is:

$$\theta_x(t) = \sum_{n=0}^{\infty} (-1)^n \left[\operatorname{erfc} \left(\frac{2n + 1 - x/L}{2 \sqrt{F_0}} \right) + \operatorname{erfc} \left(\frac{2n + 1 + x/L}{2 \sqrt{F_0}} \right) \right] \quad (3.1)$$

where

$$\theta_x = \frac{T - T_L}{T_0 - T_L}$$

$$F_0 = \frac{at}{L^2}$$

In two dimensions, the analytical solution takes the form of

$$\theta_{xy} = \theta_x(t)\theta_y(t)$$

where $\theta_y(t)$ is identical to Equation (3.1) with y replacing x . Likewise, in three dimensions, the solution takes the form

$$\theta_{xyz} = \theta_x(t)\theta_y(t)\theta_z(t)$$

Results of the TEMPEST predictions as well as further description of the nomenclature are shown in Figure 3.1. All three simulations agreed excellently with the analytical solutions. This agreement shows that the conduction-only mode of TEMPEST is working correctly in all three Cartesian coordinates.

3.2 TRANSIENT HEAT CONDUCTION IN A CYLINDRICAL GEOMETRY

A solution for transient, one-dimensional heat conduction in the radial direction was performed. In the problem simulated, a cylindrical segment that was initially at temperature $T_0 = 100^\circ\text{F}$ was subjected to a step change in surface temperature at $t = 0$. Both ends of the cylindrical segment were insulated. Temperature was computed as a function of radius and time.

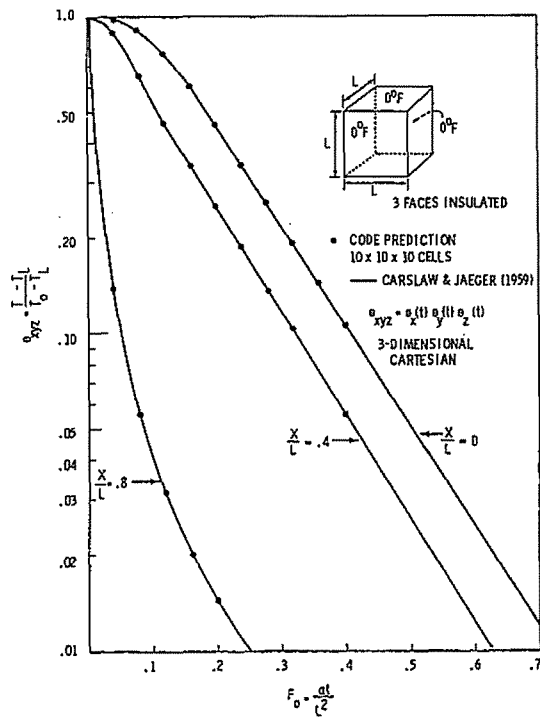
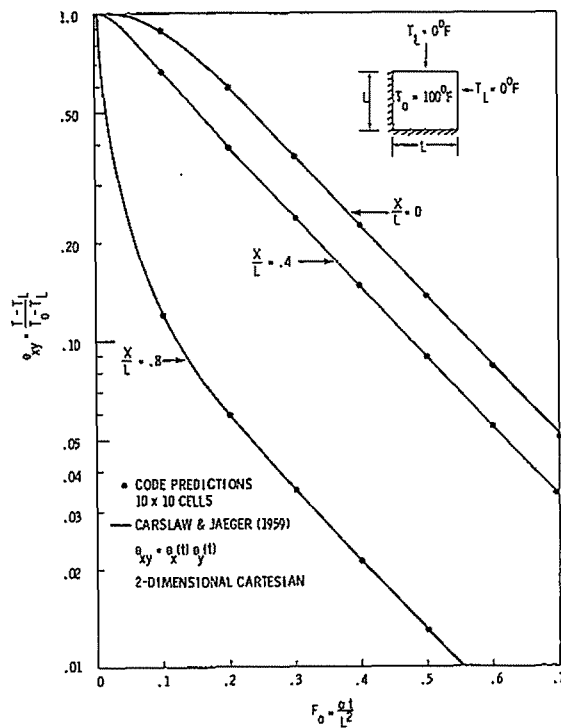
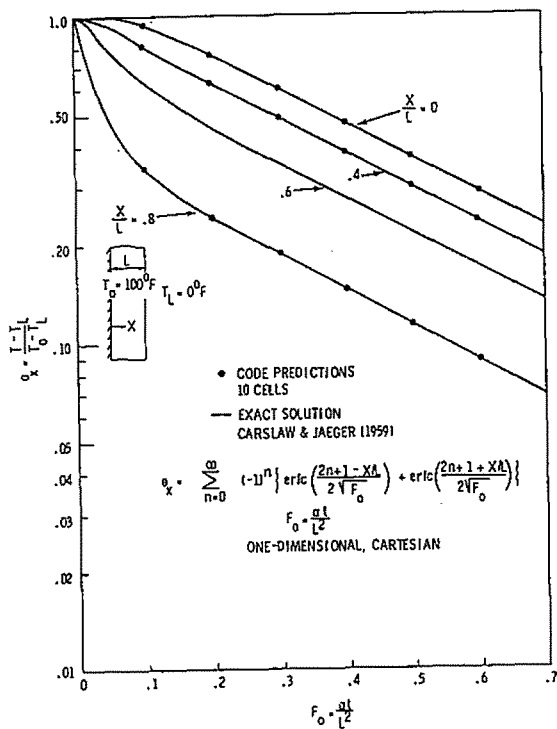


FIGURE 3.1. TEMPEST Predictions and Analytical Solutions for Transient Conduction in One, Two, and Three Dimensions in Cartesian Coordinates

The analytical result (Carslaw and Jaeger 1959) for this problem is:

$$\theta_r(t) = 1 - 2 \sum_{n=1}^{\infty} [(e^{-F_0 \beta_n^2}) \left(\frac{J_0(r\beta_n/L)}{\beta_n J_1(\beta_n)} \right)] \quad (3.2)$$

where

$$\theta_r = \frac{T - T_L}{T_0 - T_L}$$

$$F_0 = \frac{\alpha t}{L^2}$$

and J_0 and J_1 are Bessel functions.

The TEMPEST-computed results are compared to the analytical solution in Figure 3.2 as a function of time and radial position. Agreement with the analytical results is excellent.

A problem was simulated for steady-state heat conduction through one dimension in cylindrical coordinate geometry. The problem included uniform heat generation in the material and a surface film coefficient prescribed for the surface. The problem and its parameters are shown in Figure 3.3. The analytical solution for the steady-state temperature profile in the cylinder is

$$T(r) = T_s + \frac{\dot{Q} R_0^2}{4k} \left[1 - \left(\frac{r}{R_0} \right)^2 \right] \quad (3.3)$$

where T_s is the surface temperature at steady state. The quantity $(T_s - T_0)$ is equal to 36°F for the parameters and film coefficient prescribed for this problem.

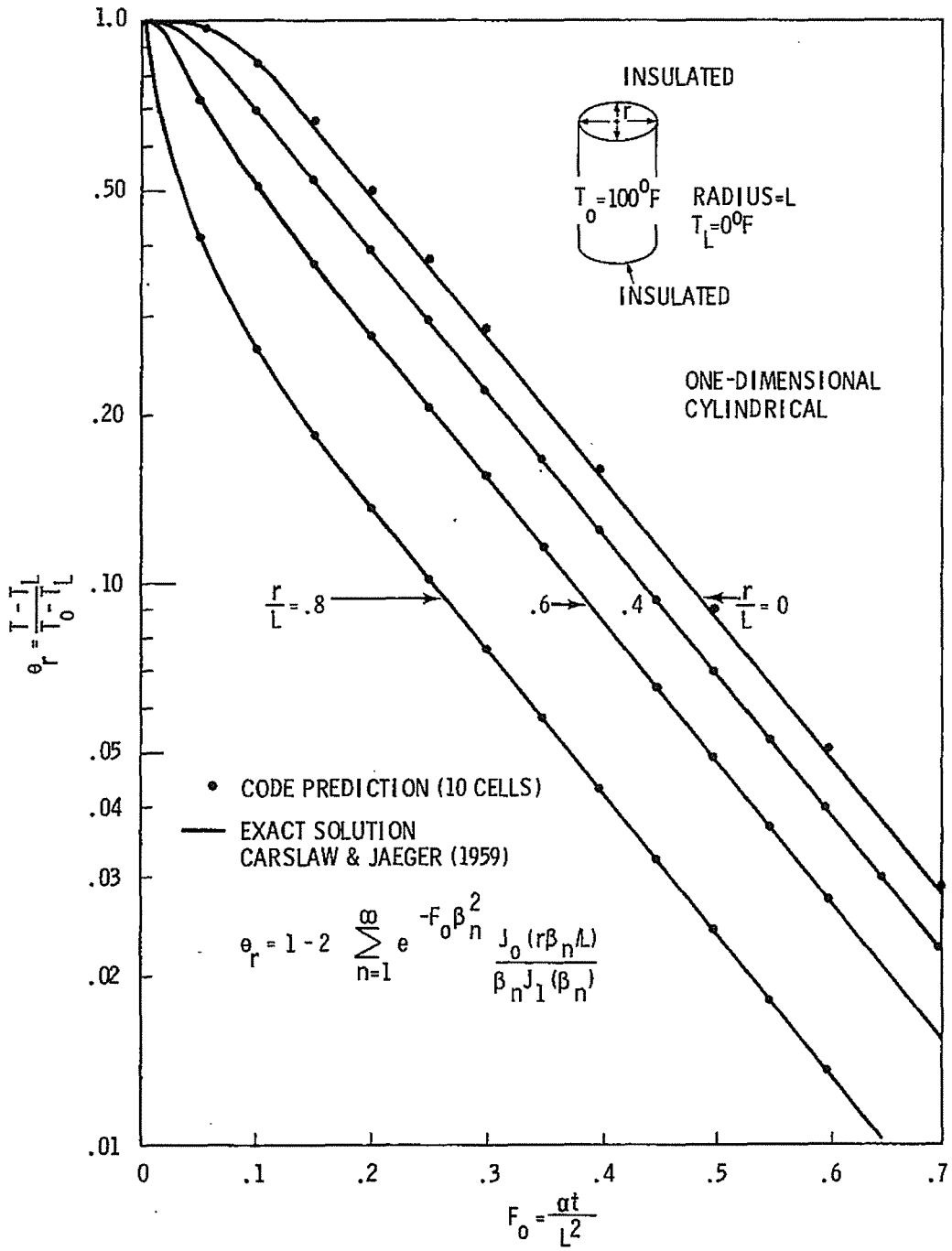


FIGURE 3.2. Transient One-dimensional Heat Conduction in Cylindrical Coordinates

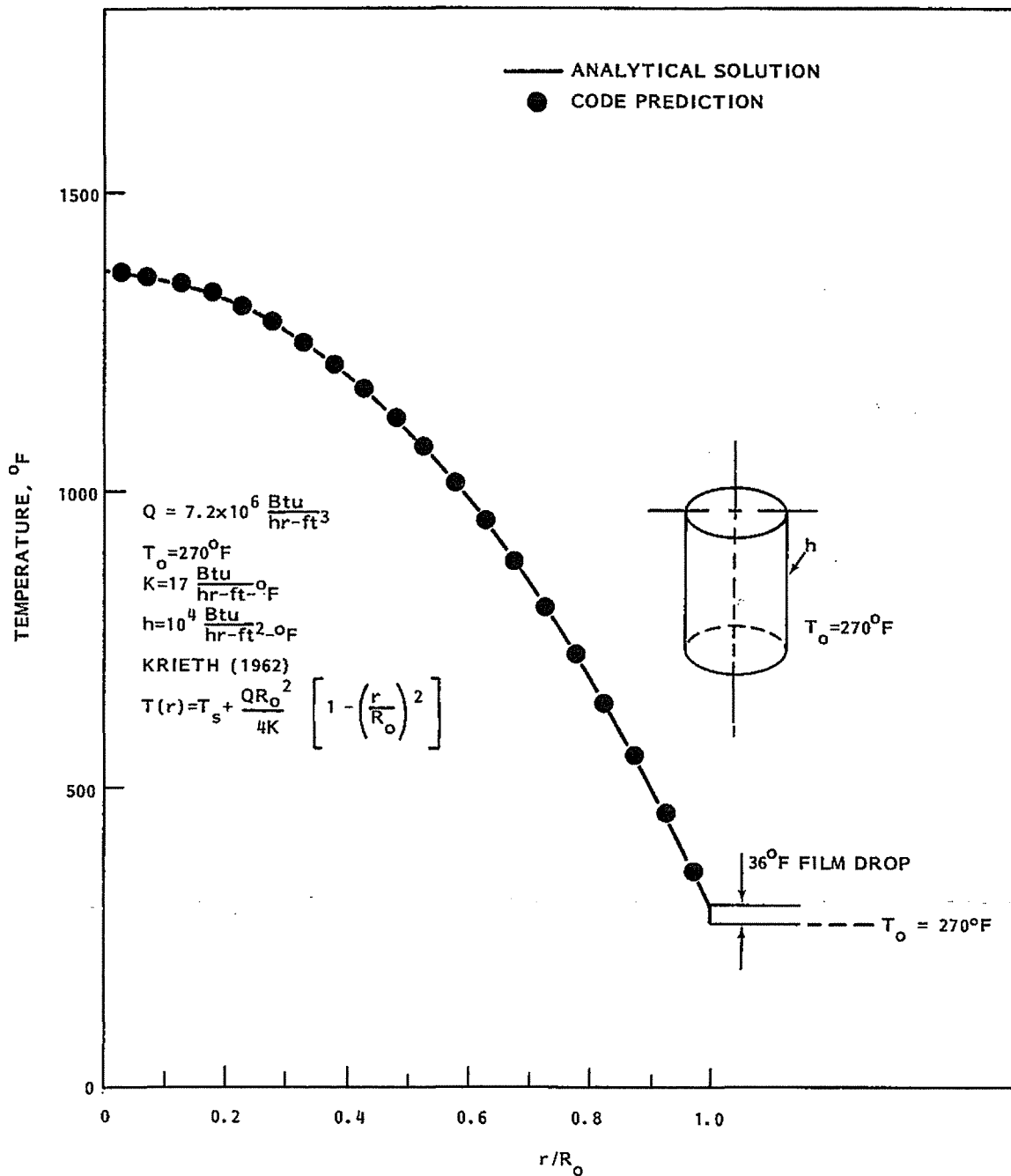


FIGURE 3.3. Steady-State One-dimensional Radial Conduction with Heat Generation and Surface Film Coefficient

The TEMPEST-computed results using 20 computational cells in the radial direction are in excellent agreement with the analytical solution. This indicates that the steady-state solution procedure works properly, including the film coefficient logic.

A transient, two-dimensional heat conduction problem with polar coordinates was simulated. In this problem, one-half of a circle initially at $T_0 = 100^\circ$ was subjected to a step change of surface temperature to $T_0 = 0^\circ$ at $t = 0$. The analytical solution for this problem was reported by Jaeger (1942).

The predicted TEMPEST results for temperature as a function of time, radius, and angle are illustrated in Figure 3.4. The agreement with the analytical model is excellent for this case in which ten radial and ten angular computational nodes are used. These results indicate that the angular conduction logic in TEMPEST is working properly.

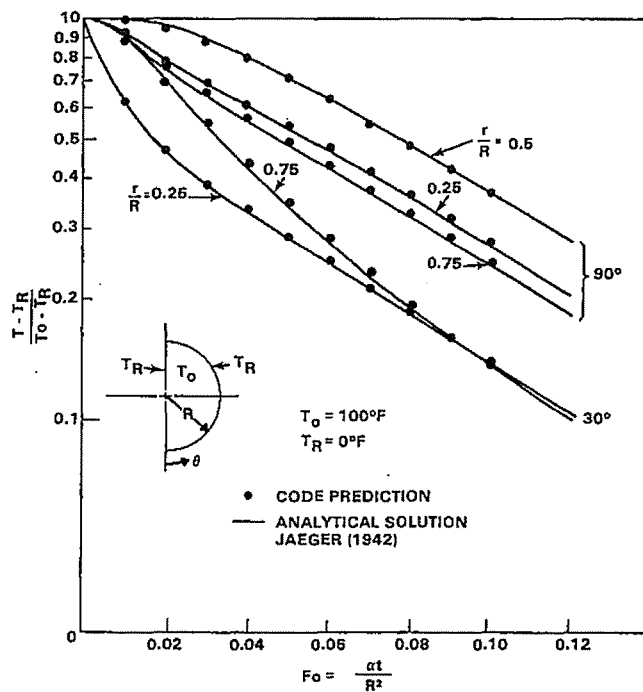


FIGURE 3.4. Transient, Two-Dimensional Heat Conduction in Cylindrical Coordinates

3.3 COMPUTATIONAL EFFICIENCY OF TEMPEST COMPARED TO OTHER CONDUCTION CODES

The computational efficiency of TEMPEST in the conduction-only mode compares very favorably to other computer codes designed specifically for that purpose. Two such codes are HEATING-5 (Turner et al. 1977) and TRUMP (Edwards 1972). To document the efficiency of TEMPEST relative to these codes, two model problems were set up and run. Computed results and execution times for each of the three codes were compared.

The first problem is shown schematically in Figure 3.5. It is a two-region, steady-state, cylindrical conduction problem. Region 1 has a constant heat generation rate. The exterior boundary for region 2 has a natural-convection film coefficient.

The second problem is shown schematically in Figure 3.6. It is a one-region, transient, cylindrical conduction problem. Region 1 is initially at a uniform temperature. At time $t = 0$, a uniform heat flux boundary condition is applied to the exterior surface. Temperatures in the conducting material were computed as a function of time and position.

Analytical solutions for these two problems exist (Carslaw and Jaeger 1959). Comparing the computed solutions of HEATING-5, TRUMP, and TEMPEST to the analytical solutions provides a direct means of comparing the computational efficiency of the codes. This eliminates the effect of code input parameters such as "maximum number of iterations" on the overall computation time.

The computed results of the three codes for these two problems are not presented here. It is sufficient to say that each code predicted results which compared very well to the analytical solution. TEMPEST accuracy has already been documented in previous sections of this report.

Aside from level of accuracy, other principal parameters which affect code computational speed are related directly to node structure. These include total number of mesh points, relative mesh locations, computational cell aspect ratio, etc. To normalize the computational speed, each problem was discretized the same for each code. Additionally, the total number of temperature points were varied ranging from a minimum of 100 to a maximum of 1600. The cell aspect ratios were affected accordingly, e.g., a 10x10x1 grid has a cell aspect

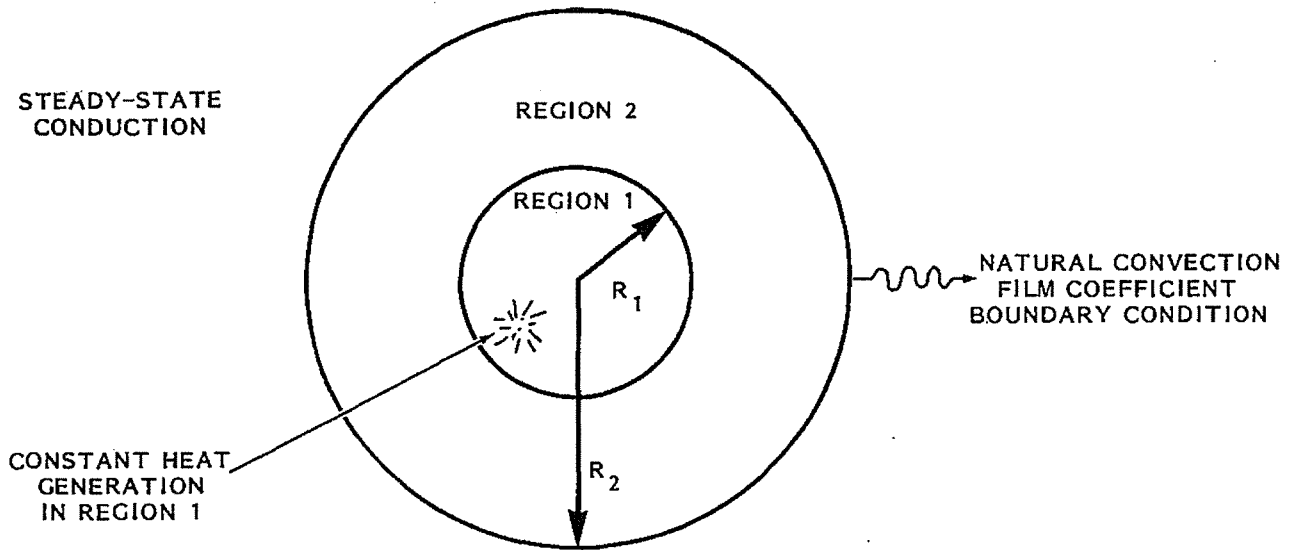


FIGURE 3.5. Schematic of the Two-Region, Steady-State Test Problem for Conduction Code Comparison (Problem 1)

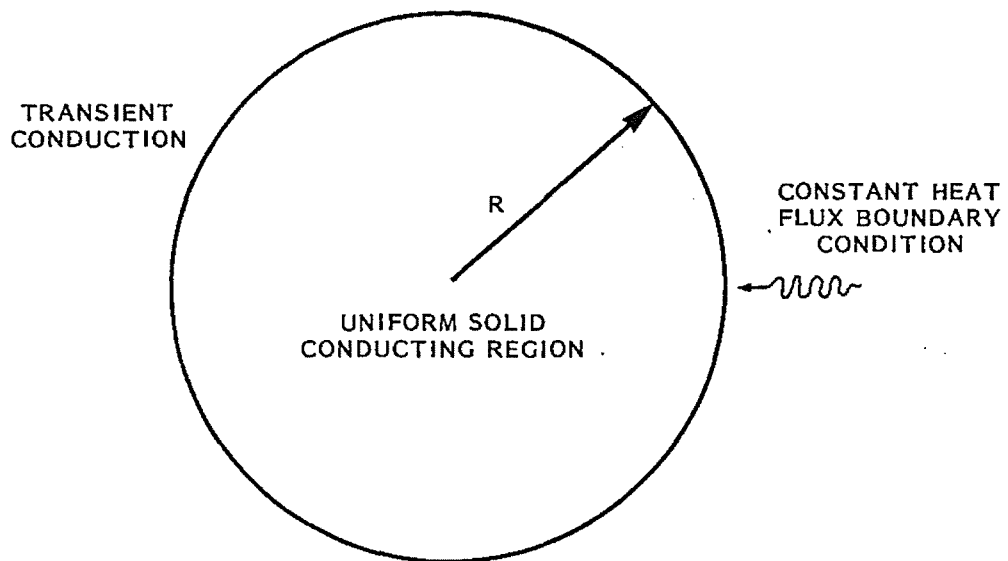


FIGURE 3.6. Schematic of the Transient Test Problem for Conduction Code Comparison (Problem 2)

ratio typically one-eighth of that in an 80x10x1 grid. Table 3.1 summarizes the number of computational cells used in each coordinate direction for each of the two problems.

Other input parameters required for each code were chosen as default values or as recommended values based on the code's users' manual. For the mesh cases run, default parameters usually provided acceptable accuracy. For problem 1, however, a significant reduction in the convergence criterion was necessary with HEATING-5 to obtain accuracy comparable to TRUMP and TEMPEST as mesh spacing was refined.

Total execution time on a CDC-7600 was recorded for each code's solution to a specified accuracy level for each mesh case listed in Table 3.1. Figure 3.7 compares the computation speed results for the steady-state problem 1 as a function of total mesh points. Figure 3.8 shows similar results for the transient problem 2.

In Figure 3.7, approximate trend curves are drawn for the different mesh cases. In all of the two-dimensional cases (one axial node), TEMPEST execution times are considerably less than those of the other two codes. For the three-dimensional case, execution time is typically the same. These results indicate that the steady-state thermal solution algorithm in TEMPEST performs very well.

In Figure 3.8, approximate trend curves indicate similar execution times for all three codes. For this transient problem, both TEMPEST and HEATING-5 show improved computation time for the three-dimensional case. For the two-dimensional cases, TEMPEST shows a marked improvement in execution time as the total number of cells increase. This observation demonstrates TEMPEST's efficiency in computing high-aspect ratio simulations.

These two conduction test problems further show that logic for the conduction-only mode of TEMPEST is working correctly. This was concluded based on the accuracy of the computed results compared to the analytical solution. These two problems also show that TEMPEST is an efficient conduction solver even with the attendant bookkeeping logic necessary for optional hydrodynamic solution.

TABLE 3.1. Mesh Schemes for Computational Efficiency Comparison of Conduction Problems 1 and 2

Problem 1. (Figure 3.5)			Problem 2. (Figure 3.6)		
<u>R-nodes (a)</u>	<u>θ-nodes (a)</u>	<u>Z-nodes (a)</u>	<u>R-nodes (a)</u>	<u>θ-nodes (a)</u>	<u>Z-nodes (a)</u>
10	10	1	10	10	1
20	10	1	10	10	1
40	10	1	10	10	1
80	10	1	10	10	1
20	20	1			
40	20	1			
10	10	10	10	10	10

(a) Due to logic differences, HEATING-5 requires one additional node in each coordinate direction. Spacing between the nodes and the temperature computation location were maintained the same in each simulation for each code, however.

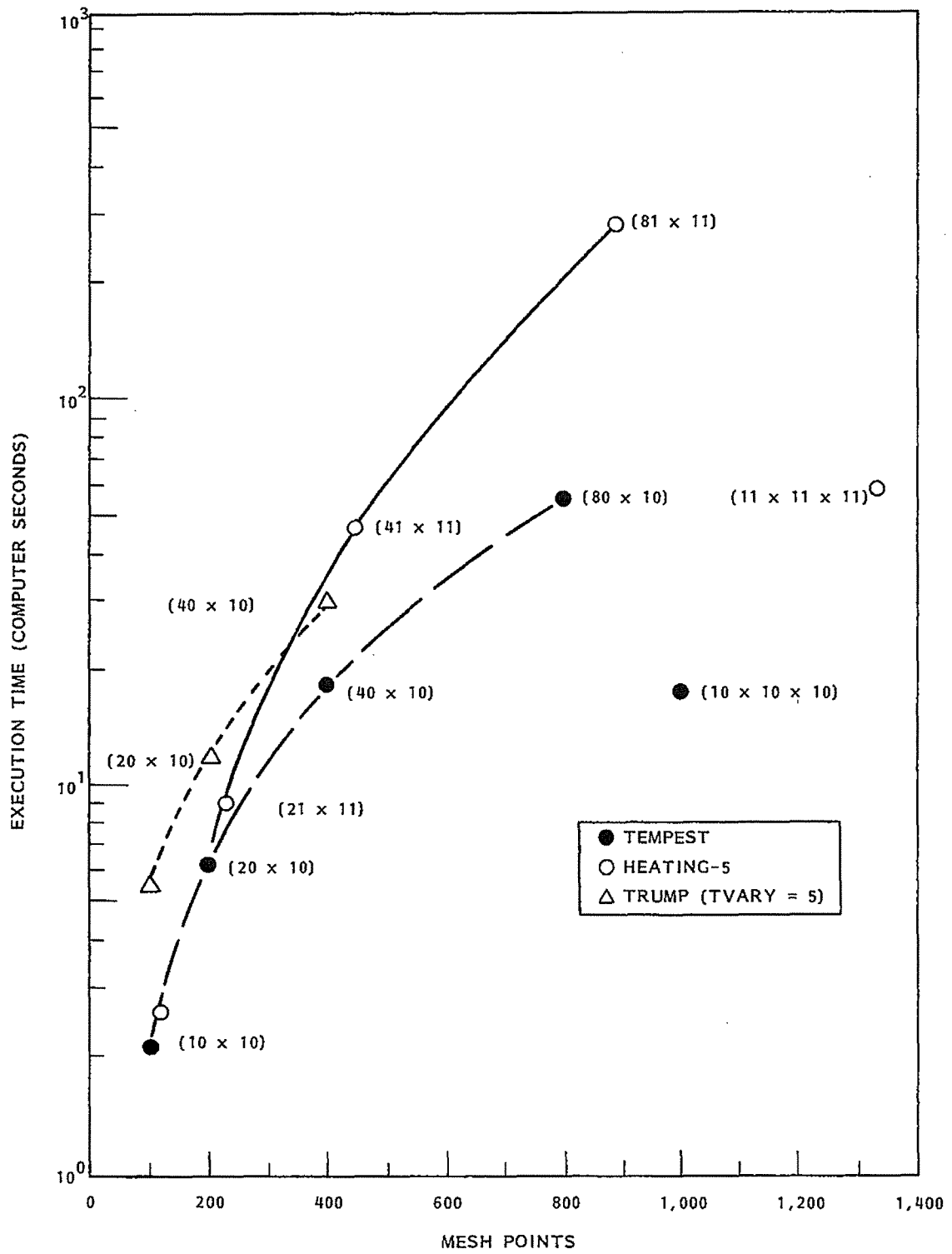


FIGURE 3.8. Comparison of Computation Speed for Conduction Problem 2

4.0 CONVECTION SIMULATION RESULTS: LAMINAR FLOW

This section presents results of laminar flow simulations performed with the TEMPEST computer code. Results are compared to analytical solutions, experimental data, and the predictions of other hydrodynamic codes. Isothermal simulations are presented first, followed by nonisothermal flows, and then convection flows coupled to solid-wall heat conduction.

Laminar flow of a fluid is very basic to the study of fluid mechanics. It is one of the few areas of fluid mechanics where simplified assumptions can be made which allow analytical solutions to be derived. While truly laminar flow does not occur regularly in nature, it can be produced and studied in the laboratory. For that reason, numerous data are available to which computer code predictions can be compared.

The Reynolds equations for turbulent flow can be written in the same form as the Navier-Stokes equations for laminar flow when a gradient-type turbulent viscosity assumption is made. Solving these equations for constant turbulent viscosity supports turbulence simulations by verifying that the numerics and solution procedures are correct before incorporation of a time- and space-dependent turbulence model.

Numerous laminar flow computer codes have been developed. They use the primitive variable approach such as in TEMPEST or, alternatively, a vorticity stream function approach. Results of several codes which are much less general than TEMPEST are used for comparison with TEMPEST predictions.

4.1 LAMINAR ISOTHERMAL FLOW

Laminar isothermal flow simulations were performed in one-, two-, and three-dimensional geometries. Included were plane channels, pipes, and ducts with a variety of node structures and inflow boundary conditions. Comparison of TEMPEST predictions with entry length and fully developed velocity profiles were made to assure the correctness of finite-differencing logic, boundary condition logic, and solution algorithm.

4.1.1 One-Dimensional Testing

Testing of the TEMPEST computer code in one-dimensional laminar flow was limited to demonstrating drag coefficient specification and slip factors. Both form drag and frictional drag relations can be accommodated. Wall slip factors ranging from -1 (no slip) to +1 (full slip) may be specified.

For form drag, TEMPEST is programmed to accept a drag coefficient satisfying the relation

$$\Delta P = K_i \left[\frac{\rho V}{2g} \right]^{N_i} \quad (4.1)$$

The form drag coefficient is K_i and the velocity dependence is N_i . Up to 48 different values of K and N may be used in any one simulation. They may be selectively applied to individual velocity components in user-specified locations.

Friction drag is accommodated in the relationship

$$\Delta P = \left(\frac{f}{D} \right)_i \left(\frac{L \rho V}{2g} \right)^{N_i} \quad (4.2)$$

where f is the Darcy friction factor and D is a characteristic length. The friction factor input is $(f/D)_i$, and L is the distance over which it is applied.

Up to 48 different friction factors may be selectively applied in addition to the form drag coefficients. These relationships are shown schematically in Figure 4.1 as applied to the R-coordinate direction. Other directions are treated similarly. One-dimensional flows were run to verify use of these expressions. Resulting pressure drops were verified by corresponding hand calculations.

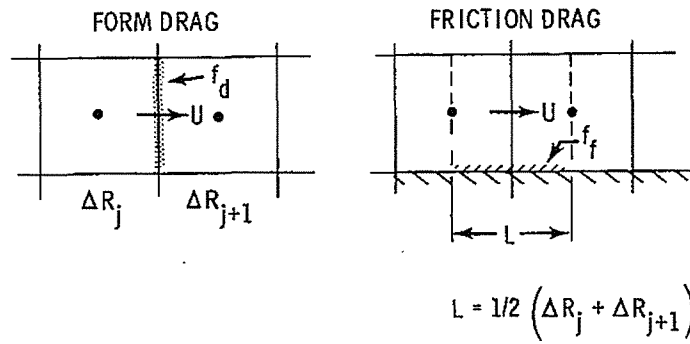


FIGURE 4.1. Schematic of Form and Friction Drag Application

Several one-dimensional laminar flow simulations were conducted to verify the slip factor logic. Figure 4.2 shows a schematic of wall slip factor application. Up to nine different slip factors may be used. Both Cartesian and cylindrical coordinate directions have been tested using constant and variable cell spacing.

4.1.2 Two-Dimensional Testing: Cartesian Coordinates

Numerous simulations of two-dimensional, forced-convection laminar flow have been conducted. These simulations tested the code's behavior regarding Reynolds number, grid spacing, and geometry. Four Cartesian geometry simulations using a uniform entry boundary condition are reported here:

- Constant cell spacing, $Re = 500$, 40×10 grid
- Constant cell spacing, $Re = 50$, 40×10 grid
- Variable cell spacing, $Re = 200$, 40×10 grid
- Variable cell spacing, $Re = 200$, 29×20 grid (including inlet plenum)

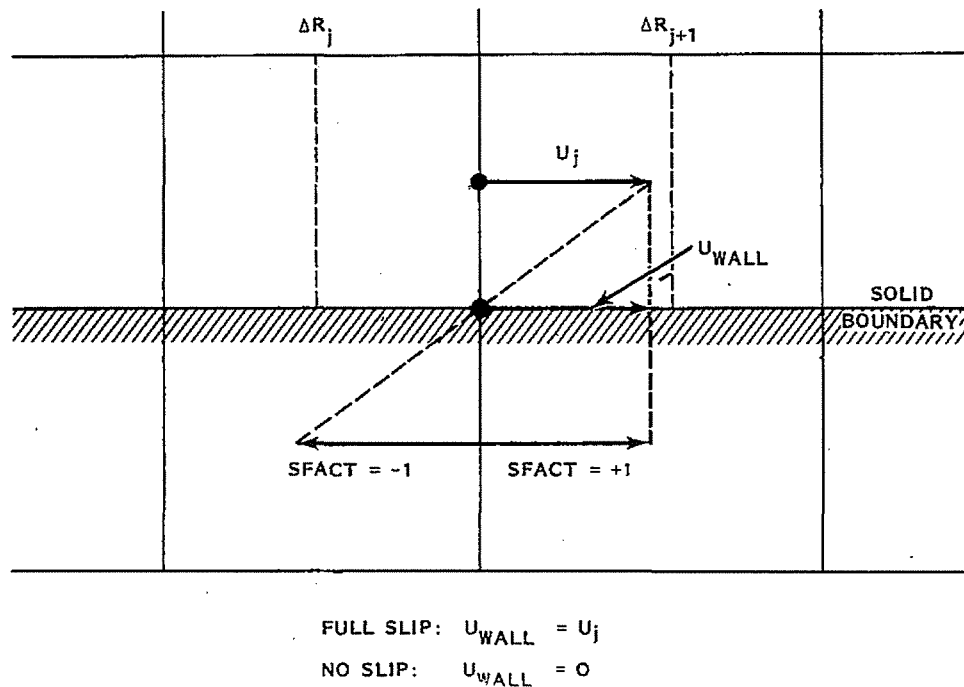


FIGURE 4.2. Schematic Showing Slip Factor Application

The predicted cross channel velocity profiles and centerline velocity for the uniform inlet flow case at $Re = 500$ is shown in Figure 4.3. This simulation did not assume symmetry with respect to the centerline but used a full-channel-width noding structure. Predicted results were symmetric. The analytical solution in a plane channel is a parabolic velocity profile with the centerline velocity being 1.5 times the bulk velocity. The predictions show this analytical centerline value being approached asymptotically.

Figure 4.4 presents similar results for the constant cell spacing case in which $Re = 50$. These results show a quicker asymptotic approach to the analytical solution, which is in agreement with boundary layer development theory. The coarseness of only five nodes on either side of the centerline, however, cannot be expected to exactly replicate the theoretical development of the boundary layer and entry length.

Noding structure, cross-stream velocity profiles, and centerline velocity are given in Figure 4.5 for the variable spacing, planar channel case in which $Re = 200$. For this case, half-plane symmetry was assumed, which concentrated more computational nodes in the flow region. The overall channel aspect ratio

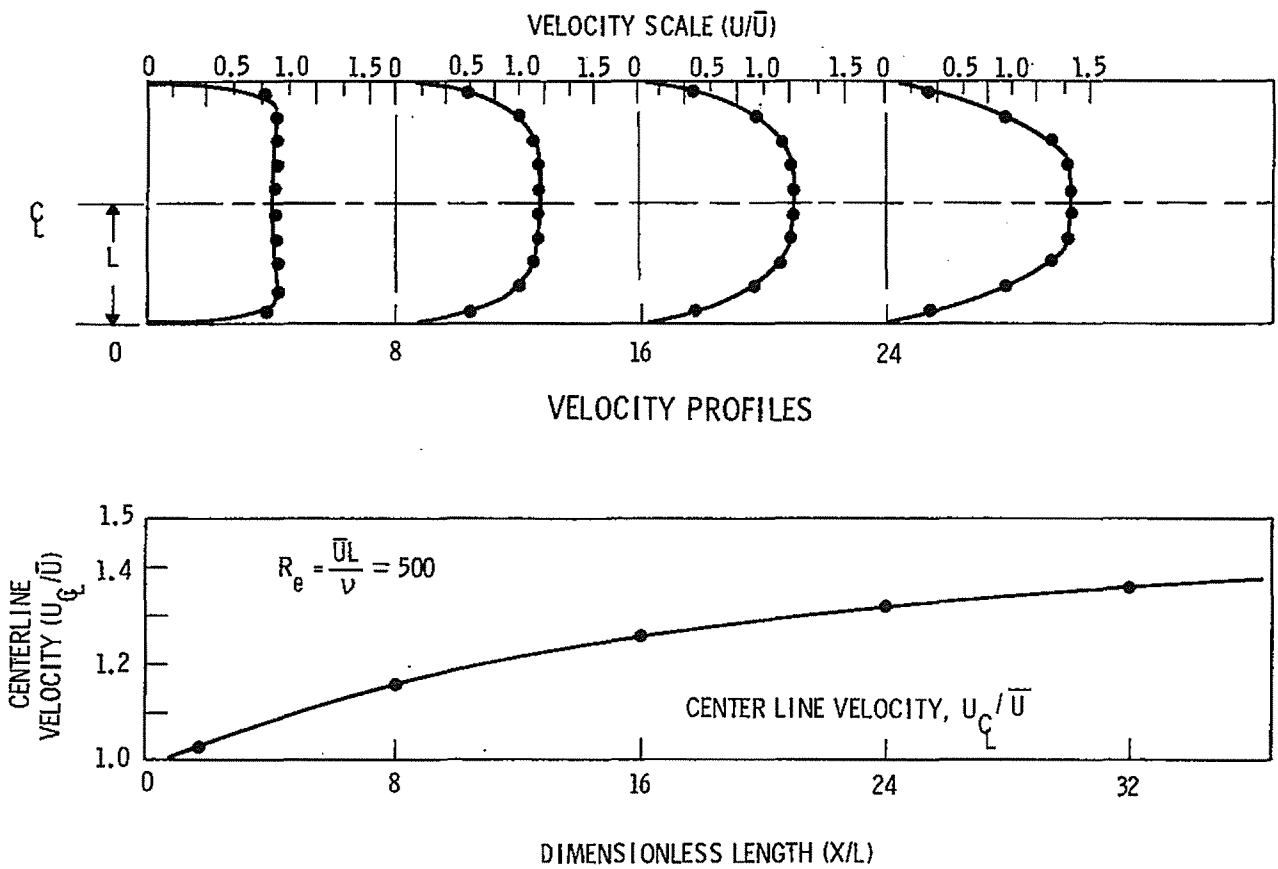


FIGURE 4.3. Velocity Profiles for a Two-Dimensional Planar Channel, with Uniform Inlet Velocity and Constant Cell Spacing, $Re = 500$ Case.

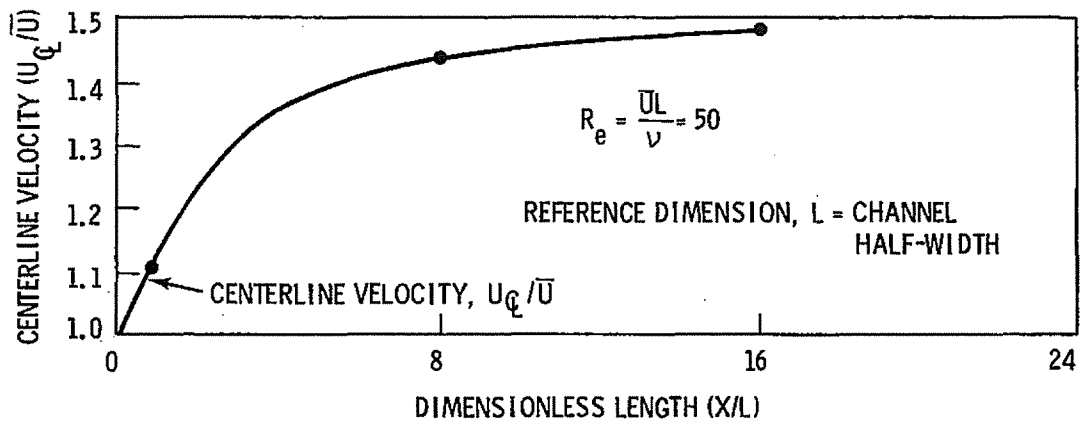
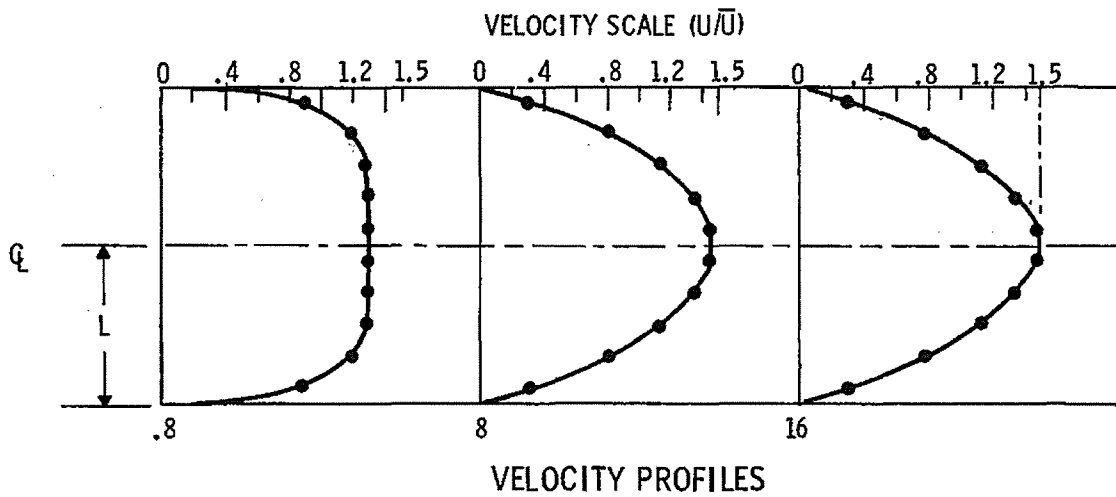


FIGURE 4.4. Velocity Profiles for a Two-Dimensional Planar Channel with Uniform Inlet Velocity and Constant Cell Spacing, $Re = 50$ Case.

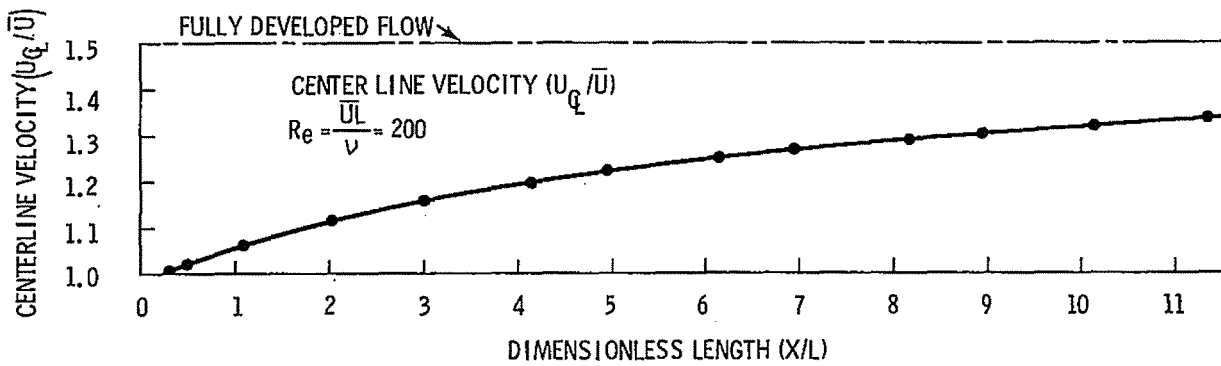
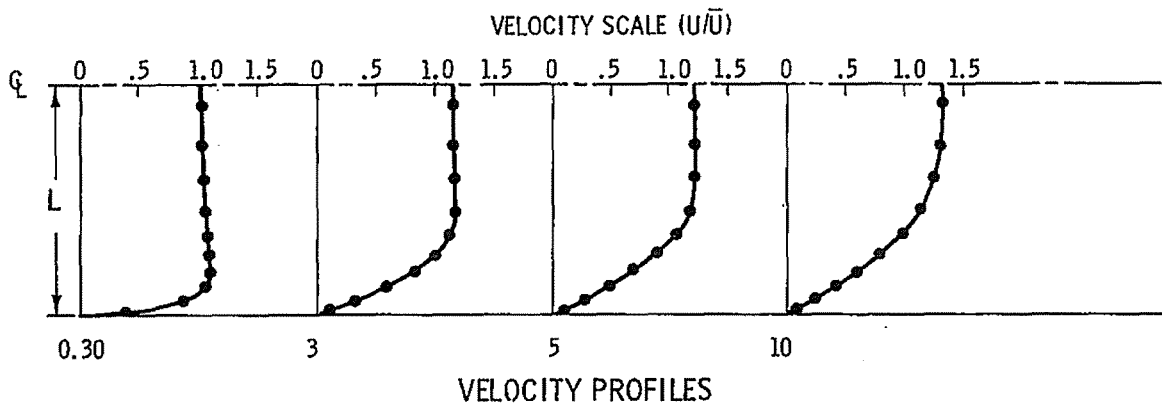
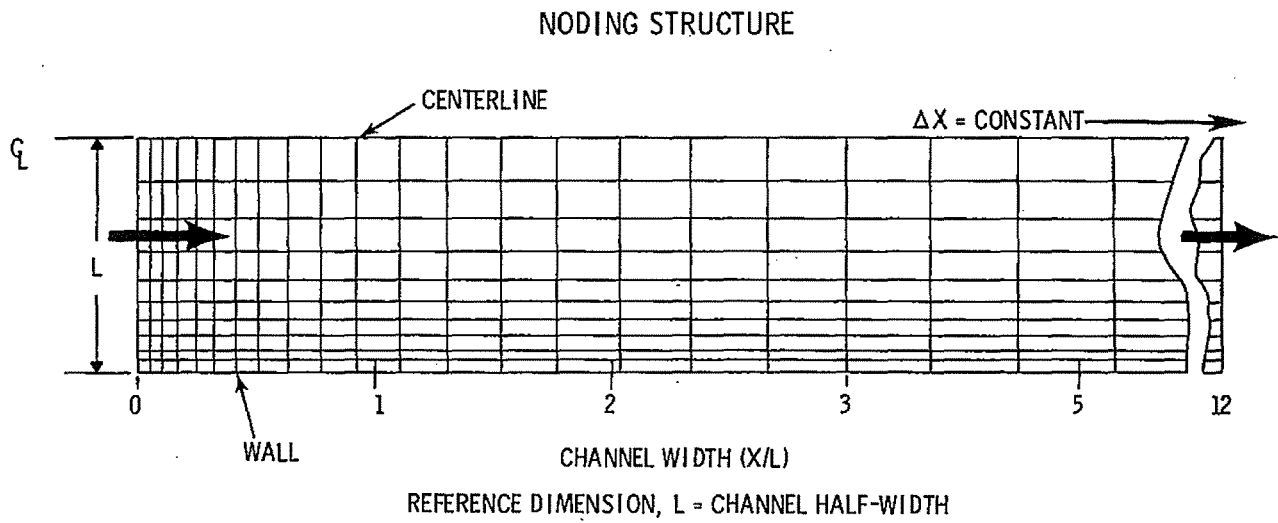


FIGURE 4.5. Velocity Profiles for a Two-Dimensional Cartesian Channel with Uniform Inlet Velocity and Variable Cell Spacing, $Re = 200$ Case.

was only 6:1. The length of the channel was not long enough for the solution to reach the fully developed parabolic result.

Figure 4.6 is a composite comparison of centerline velocities predicted by the TEMPEST code and by other computer codes. Included are the predicted results of McDonald et al. (1972) (which are vorticity/stream function results), and the VECTRA code, which is vorticity/stream function code (Trent 1973, and Hjelm and Donovan 1979).

There is scatter in the predictions, which may be due to a number of factors such as noding resolution (total number and location) or specified inlet conditions. The vorticity transport method is sensitive to the inlet conditions as referenced in Figure 4.6. Testing with the VECTRA code indicated it to be sensitive to the number of cross-stream nodes (Hjelm and Donovan 1979).

Use of a uniform entrance velocity profile raises certain questions about comparing computed results with experimental data in this geometry. Experiments will, of course, use an upstream plenum, and the channel entrance geometry will affect flow development. For a square-edged entrance one might expect a "Vena Contracta" behavior. In spite of attempts to minimize entrance losses, the velocity profile will begin to develop upstream from the entrance. An "apparent" shortening of the entrance length will necessarily occur when compared to results of boundary layer theory and of full numerical computations that utilize a uniform entrance boundary condition.

The variable-spacing, $Re = 200$ case with an inlet plenum was designed to investigate the effects of an upstream plenum and sharp-edged entrance. The cell structure for the computational region for this case is presented in Figure 4.7, and results are illustrated in Figure 4.8. Channel profiles are compared with results obtained with no inlet plenum. These results illustrate that the sharp-edge entry has a dramatic affect on both the entrance condition and flow development. Specifically, the velocity profile is partially developed upon entry. With the inlet plenum, a small eddy forms at the wall just downstream from the entry plane, and flow development is considerably different.

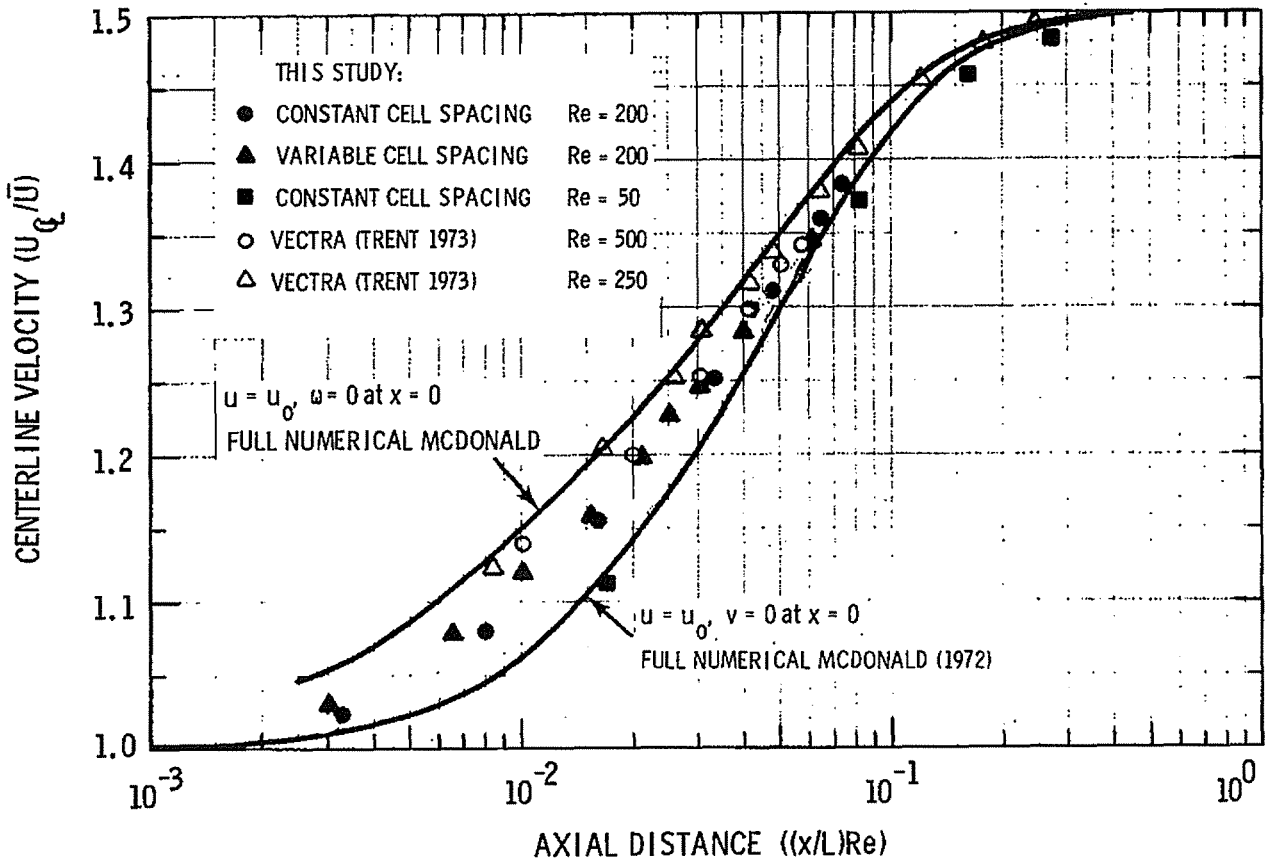


FIGURE 4.6. Comparison of Computed Centerline Velocity for a Two-Dimensional Planar Channel with Uniform Inlet Velocity

The four laminar flow cases presented here were designed primarily to test TEMPEST against other proven computational models. Results were found to be consistent, both for constant and variable spacing, and at different Reynolds numbers.

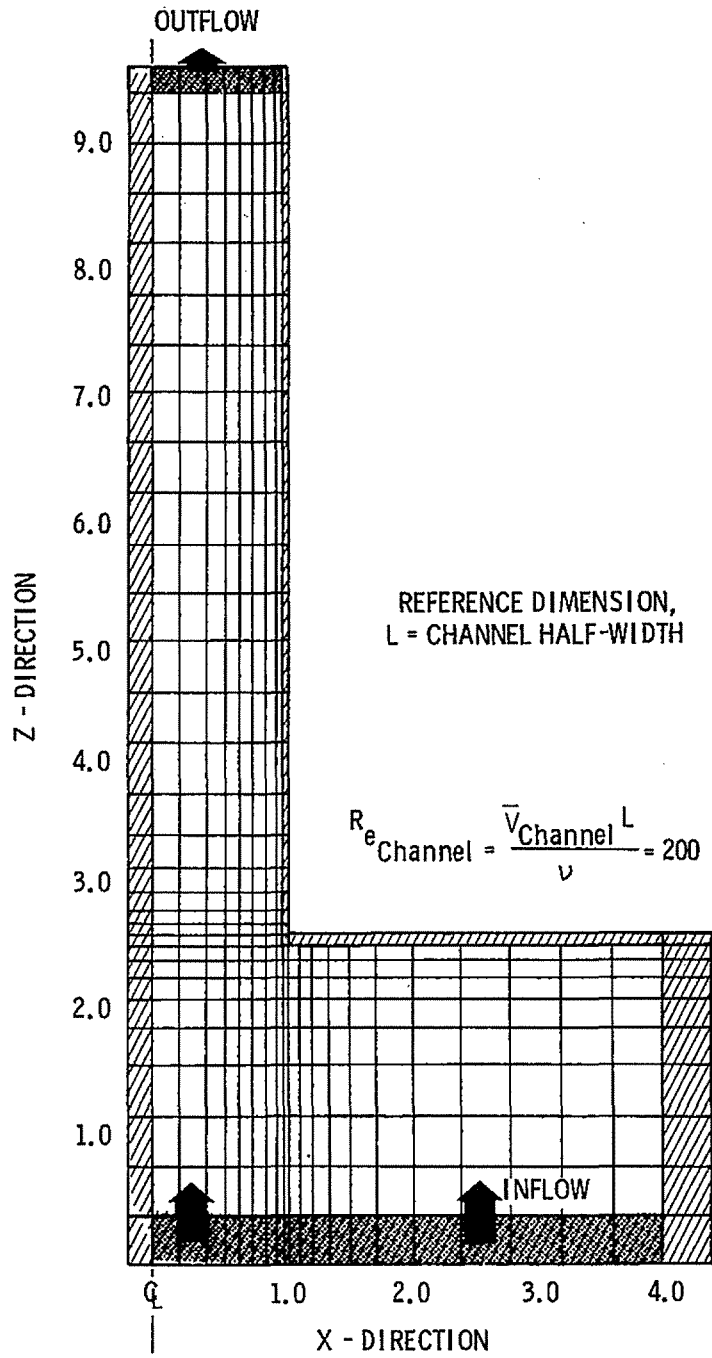


FIGURE 4.7. Variable Cell Spacing Nodalization Pattern for a Two-Dimensional Cartesian Channel with an Inlet Plenum

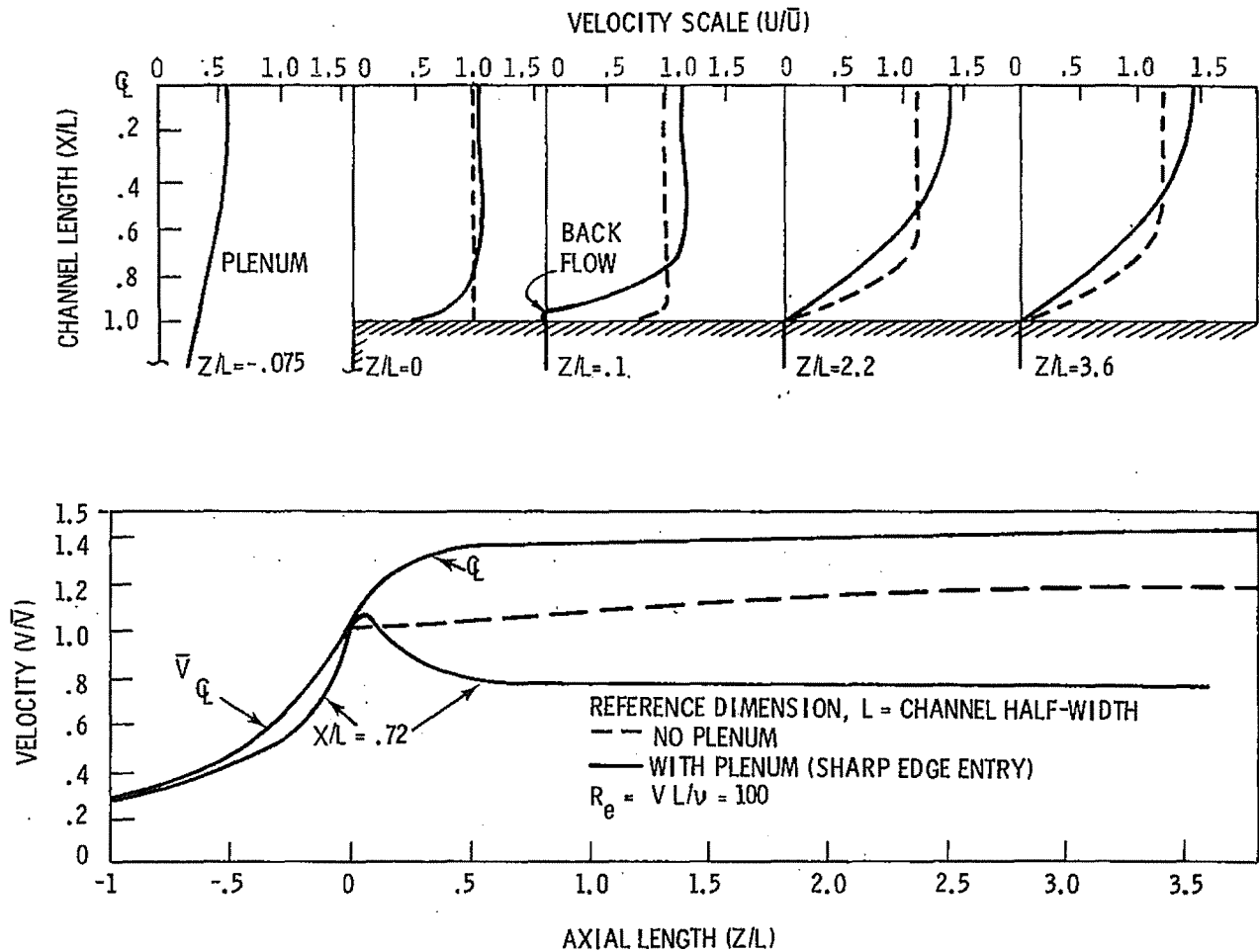


FIGURE 4.8. Velocity Profiles for a Two-Dimensional Planar Channel

4.1.3 Two-Dimensional Testing: Cylindrical Coordinates

Two-dimensional test cases showing the development of channel entry flow were performed using cylindrical coordinates:

- Constant cell spacing, $Re = 100$, 8×15 grid
- Variable cell spacing, $Re = 100$, 8×15 grid
- Constant cell spacing, $Re = 100$, $8 \times 15 \times 3$ grid

The first two cases were for comparing results for cell spacing consistency and variable cell spacing logic in cylindrical coordinates. The third case was identical to the first except that a three-dimensional cell structure was used. The cell structure and boundary conditions were such that azimuthal variations were eliminated, thus making it a three-dimensional computation of a two-dimensional problem.

Cross-stream velocity development and centerline velocity are shown in Figure 4.9. Results of the two constant-cell-spacing cases were identical. The fully developed, analytical velocity profile for this geometry is a parabolic profile given by

$$\frac{U}{\bar{U}} = 2 \left[1 - \left(\frac{r}{R} \right)^2 \right] \quad (4.3)$$

The analytical centerline value of $U_{CL}/\bar{U} = 2$ is asymptotically approached.

The variable-cell-spacing test case results and noding structure are presented in Figure 4.10. Again the analytical, fully developed solution is being asymptotically approached. Near the entrance, the variable-cell-spacing case shows greater resolution than the constant-cell-spacing case. In the entrance region, the deviation between the two cases is thus to be expected. Beyond $X/R = 10$, the results are very consistent.

In the variable-cell-spacing case, cell aspect ratios from 5:1 up to 33:1 were used. No undue computational difficulties were encountered because of these large aspect ratios.

A synopsis of computed centerline velocity results for a cylindrical channel is given in Figure 4.11. The present results are compared with those of Friedman et al. (1968), Lavan and Fejer (1966), McDonald et al. (1972), and the VECTRA code (Trent 1973; Hjelm and Donovan 1979). There is significant scatter in the predictions in the developing region for $(X/R)Re < 0.1$, but the analytical results of $U_{CL}/\bar{U} = 2.0$ is approached very consistently.

Additional tests were performed to determine the effect of cell aspect ratio on computation in a two-dimensional, cylindrical geometry. Constant-cell-spacing aspect ratios of 100:1, 1000:1, and 10,000:1 were used for constant inlet flow. At the largest ratio (10,000:1), execution time was 0.32 msec/time-step-cell with a maximum cellwise divergence of less than 10^{-5} ft³/ft³-sec. This problem was also run with a severe transient inlet boundary velocity which ramped linearly from +1 ft/sec to -1 ft/sec over 2 sec and then back to +1 ft/sec over 2 sec. Computational speed for this transient

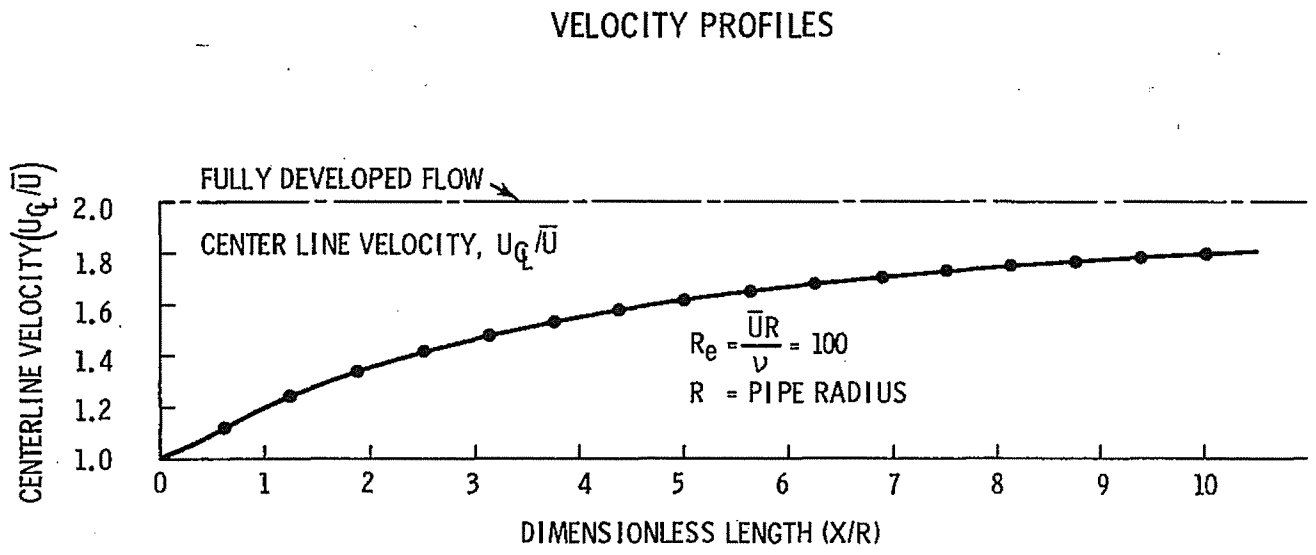
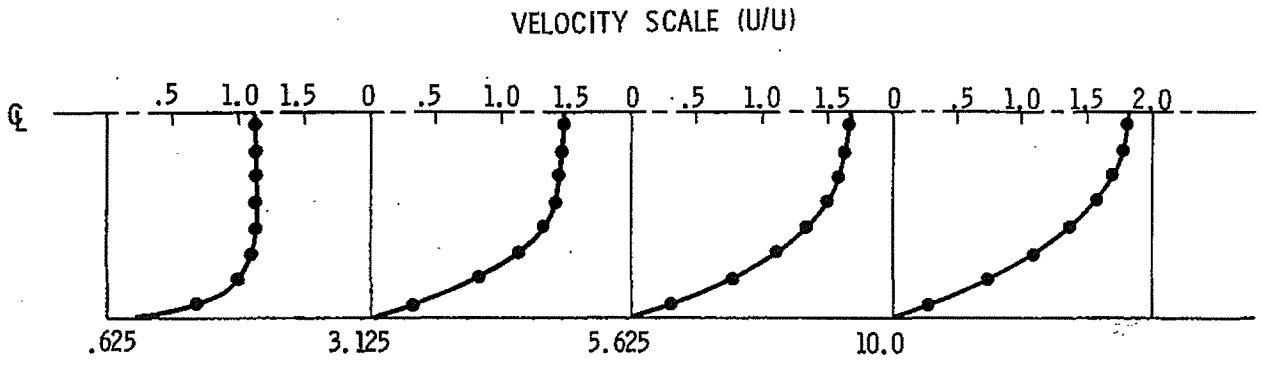
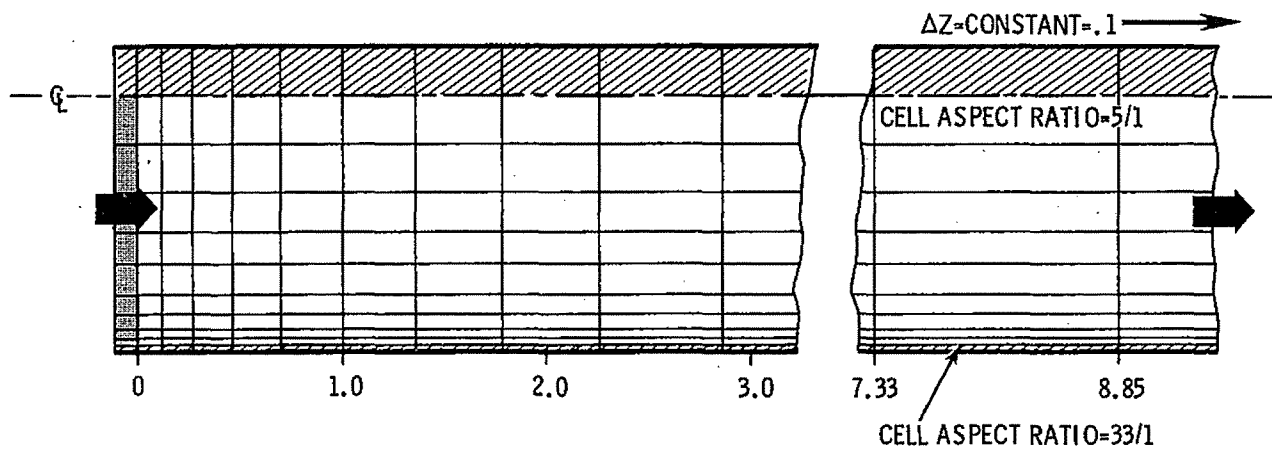
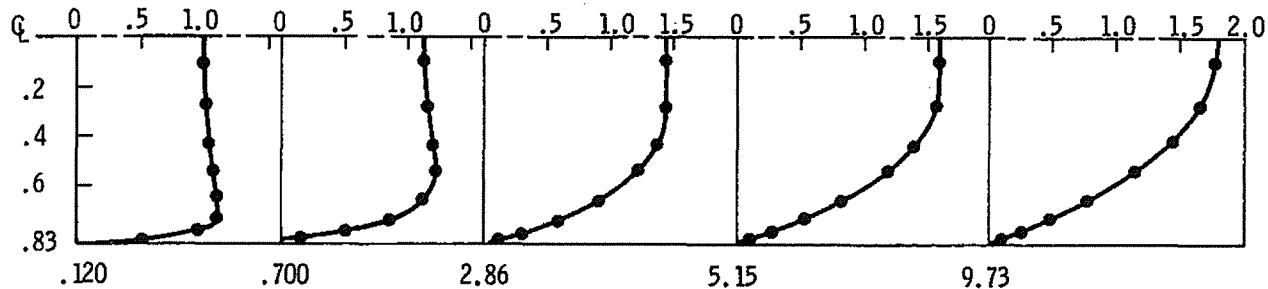


FIGURE 4.9. Velocity Profiles for a Two-Dimensional, Cylindrical-Channel Flow with Uniform Inlet Velocity and Constant Cell Spacing, $Re = 100$ Case

NODING STRUCTURE



VELOCITY SCALE (U/ \bar{U})



VELOCITY PROFILES

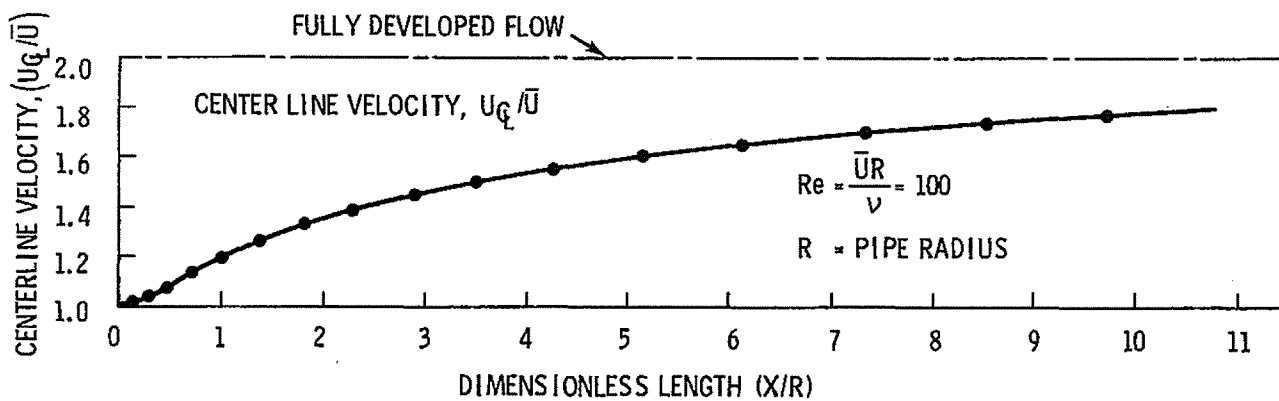


FIGURE 4.10. Velocity Profile for a Two-Dimensional, Cylindrical-Channel Flow with Uniform Inlet Velocity and Variable Cell Spacing, $Re = 100$ Case

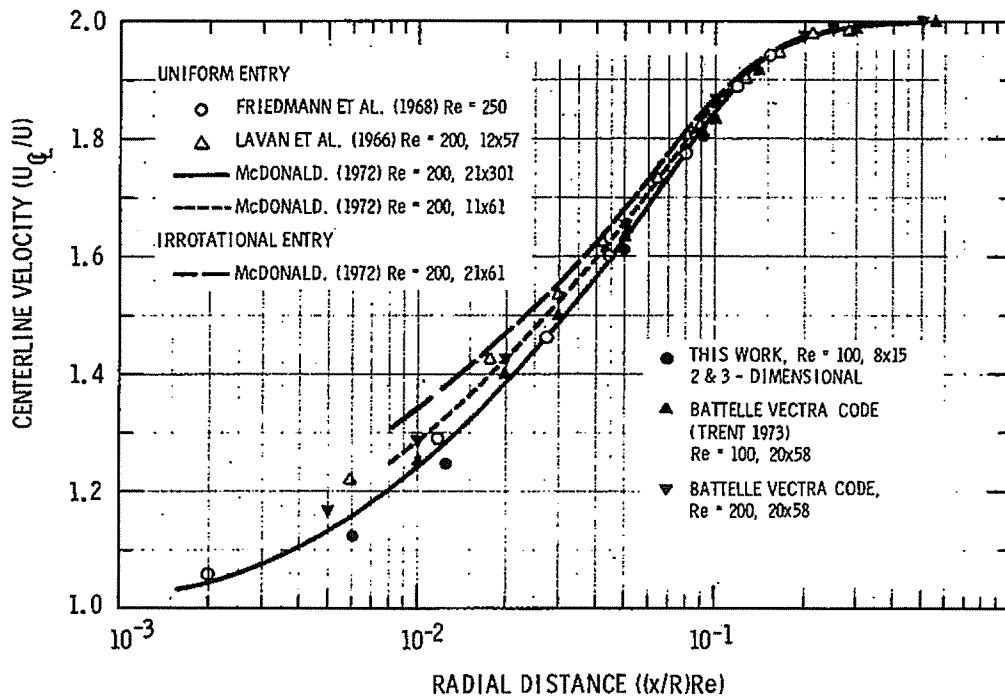


FIGURE 4.11. Comparison of Computed Centerline Velocity for Two-Dimensional Pipe Flow with Uniform Inlet Velocity

problem averaged 0.9 msec/time-step-cell for a cellwise divergence less than 10^{-9} ft³/ft³-sec. This test verified TEMPEST's transient velocity boundary condition logic and the code's ability to handle large cell aspect ratios without large degradation of computational speed.

4.1.4 Three-Dimensional Testing

Entry flow development in a square duct was chosen for testing because a reliable data base for centerline velocity is available and because this problem has been the subject of analytical studies. The test case was a 1/4-segment-of-symmetry model using a 40x5x5 grid with flow at Re = 200. Constant cell spacing with a cell aspect ratio ($\Delta R/\Delta X$ or ΔZ) of 5/1 was used. Cross-stream velocity profile results are shown in Figure 4.12, and the centerline flow development profile is compared to the experimental data of Kreid (1967) and Goldstein and Kreid (1967) in Figure 4.13.

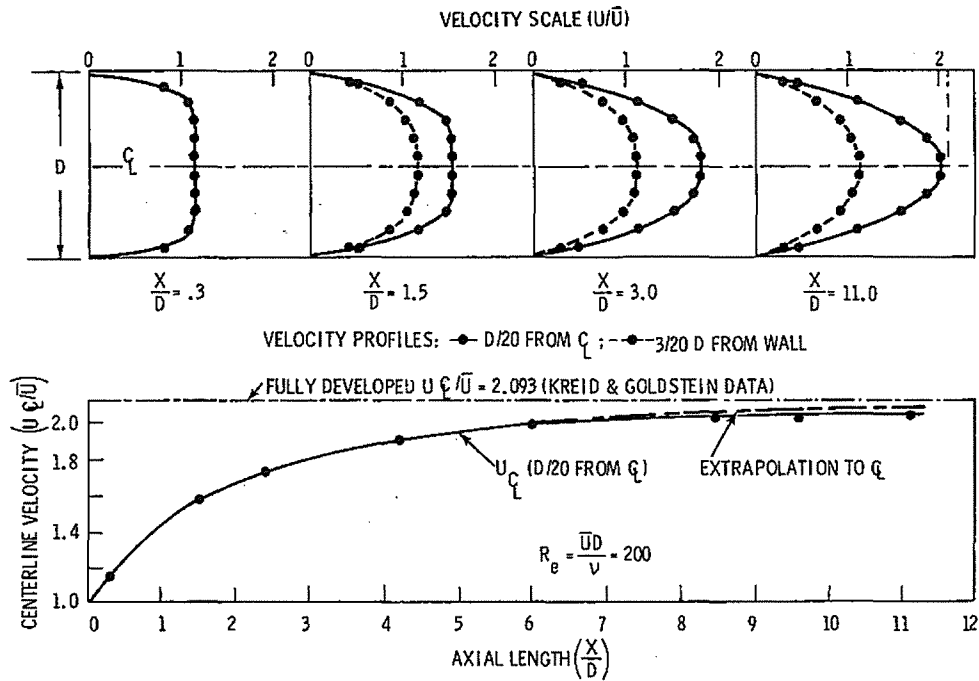


FIGURE 4.12. Velocity Profiles for a Three-Dimensional Cartesian Square Channel with Uniform Inlet Velocity and Constant Cell Spacing, $Re = 200$ Case

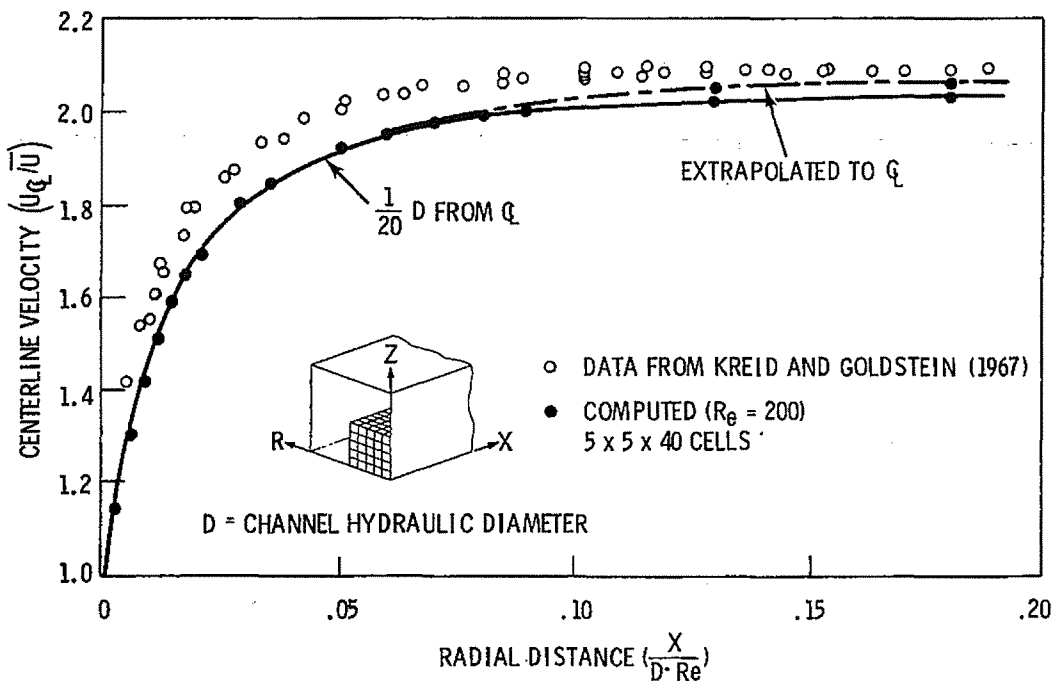


FIGURE 4.13. Centerline Velocity Profile for a Square Channel with Uniform Inlet Velocity and Constant Cell Spacing, $Re = 200$ Case

Because the code computes velocity at the cell face center, it is impossible to obtain velocity at the channel center using segment symmetry modeling. Thus both Figures 4.12 and 4.13 show velocity extrapolated to the centerline as the flow attains a near-parabolic cross-stream profile upon full development. Figure 4.12 reveals that the computed results underpredict the centerline velocity by a maximum of 5% to 7% during the early stages of development and 1% to 3% at full development. This underprediction may be caused by the assumed uniform velocity entrance condition.

Kreid's (1967) experiment used a glass channel fused to an upstream glass plenum. The fusing process resulted in a rounded rather than sharp-edge entry condition. A laser-Doppler anemometer was used to obtain the data, and Kreid indicated (private communication) that he was not able to obtain data at the entrance plane. Previous results for the two-dimensional computations with a plenum indicated that velocity profile begins to develop upstream from the entry. Thus it is reasonable to expect the computer code to underpredict the experimental results in the developing region when a uniform velocity profile is assumed at entry. A plenum was not modeled for this case to test this hypothesis.

The computational speed effect of large cell aspect ratios was determined by running this 40x5x5, three-dimensional channel problem with downstream cell aspect ratios of 50:1, 100:1, and 1000:1. To obtain a cellwise divergence of less than 10^{-5} ft³/ft³-sec, approximately 0.26 msec/time-step-cell were required for execution at the 50:1 ratio. The larger aspect ratios increased this speed by approximately 1 to 2 percent. These tests further indicated TEMPEST's ability to handle large-aspect-ratio problems without severe computational speed penalties.

4.2 CONVECTION FLOW AND HEAT TRANSFER

Numerous simulations involving laminar flows and heat transfer have been conducted during the TEMPEST code development. These simulations have been designed to verify certain code logic, document results by comparison to data or analytical solutions, and/or demonstrate an application.

Results of several of these simulations are presented in this section. These include:

- flat-plate convection heat transfer
- plane channel flow with variable viscosity
- buoyancy-driven Cartesian cavity convection
- buoyancy-affected vertical pipe flow (Morton's Problem)
- buoyancy-driven horizontal annulus flow

Results from these simulations have been used to draw conclusions as to the code's ability to couple laminar hydrodynamics with heat transfer and to compute basic flow phenomena predicted by analytical solutions or measured by experimental techniques.

4.2.1 Flat-Plate Convection Heat Transfer

To test TEMPEST's capability to accurately predict surface heat transfer coefficients, a simple flat-plate heat transfer case was chosen. For a uniform flow over a constant temperature flat plate, an analytical solution for the local Nusselt number is available for the case of no axial conduction. The limiting solution at a low Prandtl number (Schlichting 1968) is

$$Nu_x = 0.565 \sqrt{Re_x Pr} \quad (4.4)$$

where Re_x is the Reynolds number (based on distance from the leading edge) and Pr is the fluid Prandtl number.

Figure 4.14 shows a schematic of the problem simulated. The exterior flow field is uniform with a constant velocity, V_∞ . At the leading edge and far from the plate, the fluid temperature is T_∞ . The plate has a constant wall temperature, T_w .

The TEMPEST solution of this problem utilized a fixed-velocity-field mode, so that the problem was reduced to solution of the energy equation. Three simulations were conducted using 10 cross-stream nodes and 10, 20, and 30 axial nodes, respectively. Axial conduction was eliminated in the former two cases (by user input) by employing contact coefficients equal to zero ($h_c = 0$) between

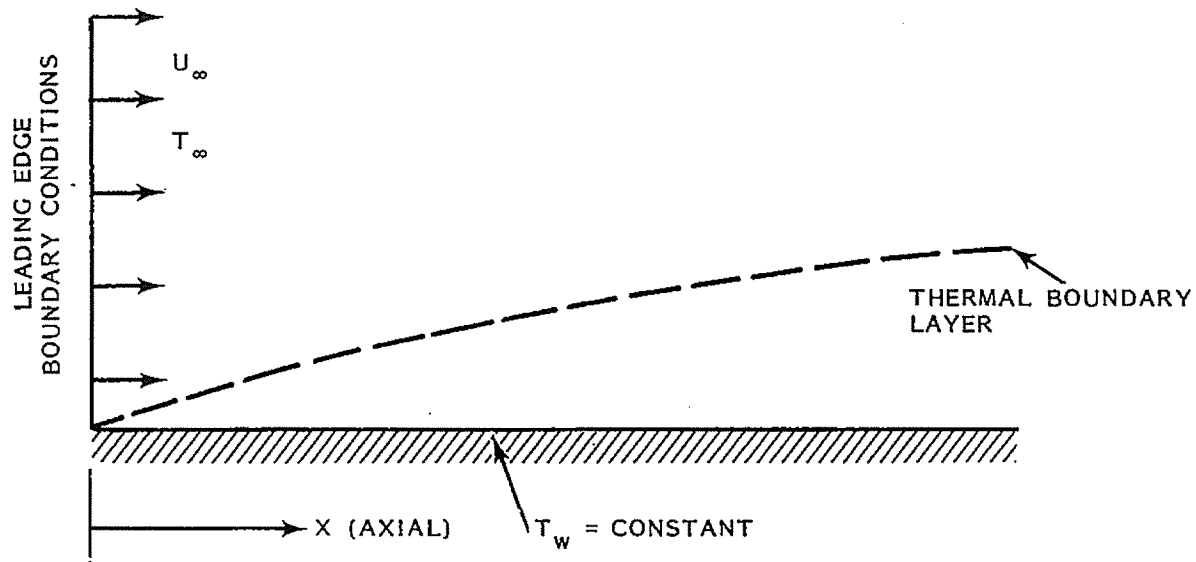


FIGURE 4.14. Schematic of the Flat-Plate Heat Transfer Problem

each level of downstream cells. Energy is thus transported downstream by advection alone. For the latter case, axial conduction was allowed and variable noding was used to resolve steep temperature gradients occurring near the leading edge.

The steady-state thermal solution option in TEMPEST was used. Convergence was accomplished in 5 to 24 iterations, achieving a total heat balance error of less than 10^{-5} Btu/sec. Five iterations were required for the case of no axial conduction, 24 iterations for the case with axial conduction. Computation time ranged correspondingly from 0.18 sec to 0.6 sec total CPU time on a CDC-7600 computer.

Sodium was the fluid simulated ($Pr \approx 0.005$) with the following properties:

$$\begin{aligned} \rho &= 50 \text{ lb/ft}^3 \\ C_p &= 0.3 \text{ Btu/lb-}^\circ\text{F} \\ k &= 40 \text{ Btu/hr-ft-}^\circ\text{F} \end{aligned}$$

With a velocity of $V_\infty = 1.0$ ft/sec the heat transfer coefficient from Equation (4.4) becomes

$$h = \frac{830}{\sqrt{x}} \quad (4.5)$$

This result is compared to TEMPEST predictions in Figure 4.15.

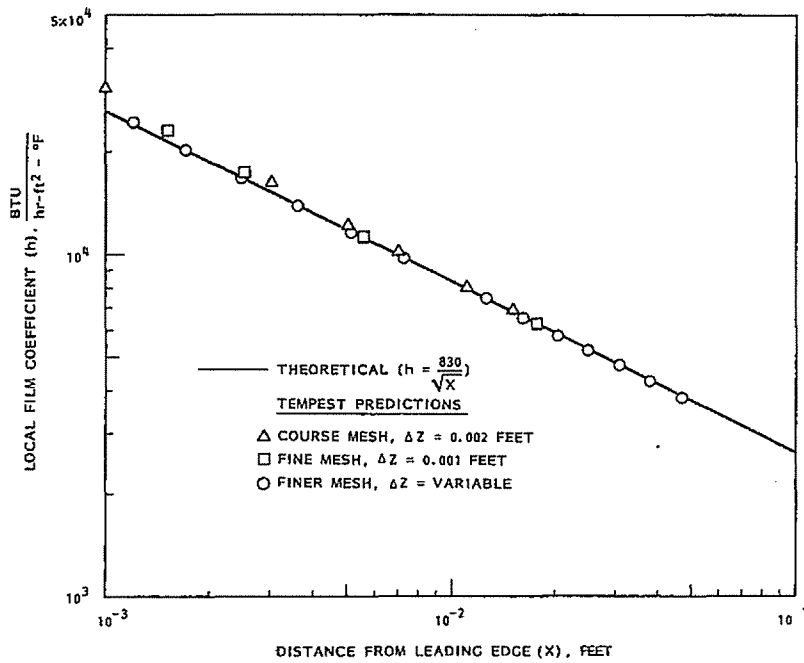


FIGURE 4.15. Comparison of Predicted and Theoretical Local Film Coefficients on a Flat Plate

The agreement is good except very near the leading edge. The constant-cell-spacing cases were incapable of resolving the large temperature gradients near the leading edge. The assumption of no axial conduction in this region was also invalid. The variable-grid-spacing case, which allowed axial conduction and concentrated smaller cells in the leading edge region and next to the wall, improved the overall prediction, particularly at the leading edge region.

The results of this simulation point out that the (convected) energy equation solution procedure is working properly and that the code is capable of accurately calculating local heat transfer coefficients. The level of accuracy is, of course, dependent on grid structure.

4.2.2 Plane Channel Flow with Variable Viscosity

To confirm that the variable viscosity logic was working correctly, two horizontal plane channel test problems were computed. One used temperature-dependent viscosity and the other used mixture concentration. In both cases, a linear viscosity function was used. The theoretical velocity profile for constant viscosity is

$$U(z) = 6 \bar{U} \left[\left(\frac{z}{D} \right) - \left(\frac{z}{D} \right)^2 \right]$$

where \bar{U} is the average velocity, z is measured from the bottom of the channel, and D is the channel width. For a linear viscosity distribution

$$\mu(z) = \mu(0) \left(1 + b \frac{z}{D} \right)$$

The velocity profile can be derived as

$$\mu(z) = \bar{U} \left[\frac{z}{bD} - \frac{\ln(1 + \frac{z}{D} b)}{b \ln(1 + b)} \right] \left[-\frac{1}{2b} - \frac{1}{2} + \frac{1}{b \ln(1 + b)} \right]^{-1}$$

The results for the two test cases are presented in Figures 4.16 and 4.17. The linear temperature case was obtained by imposing constant temperature boundary conditions on the channel walls, and theoretical results for two values of b (26.9 and 14.96) are given. The agreement of the TEMPEST results with the latter value is very good, as seen in Figure 4.16. The second case simulated was one in which a linear concentration distribution was imposed on the channel. The value determined for b was 22.5. The predicted TEMPEST results are in excellent agreement with the analytical solution as presented in Figure 4.17.

These two test simulations provided confirmation that the TEMPEST logic to account for variable viscosity as a function of local fluid conditions is working correctly.

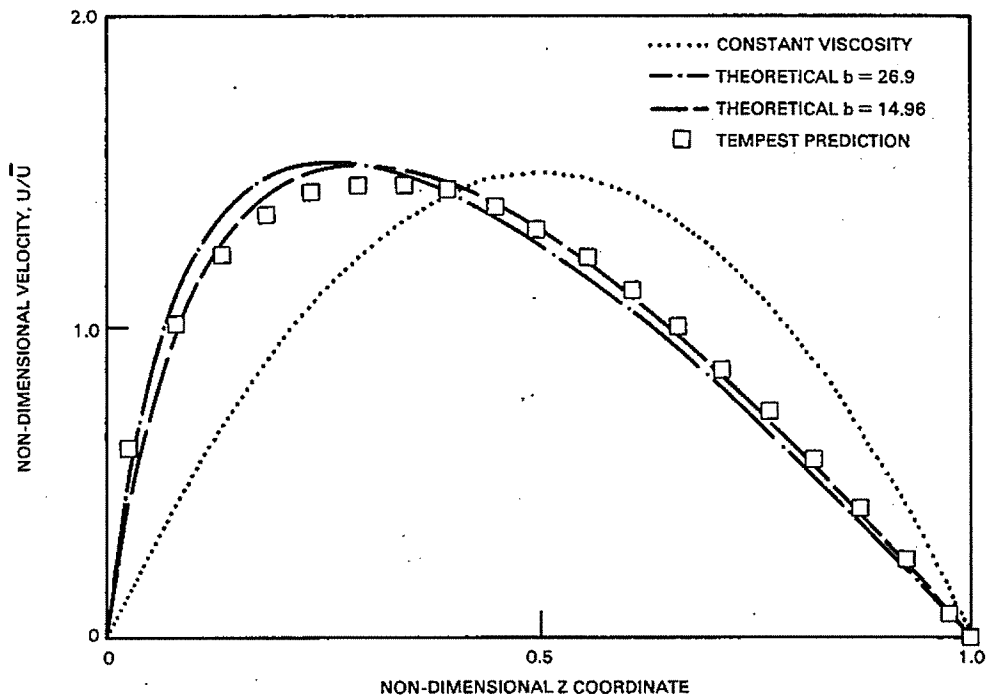


FIGURE 4.16. Plane Channel Velocity Profile Comparison for Temperature-Dependent Viscosity

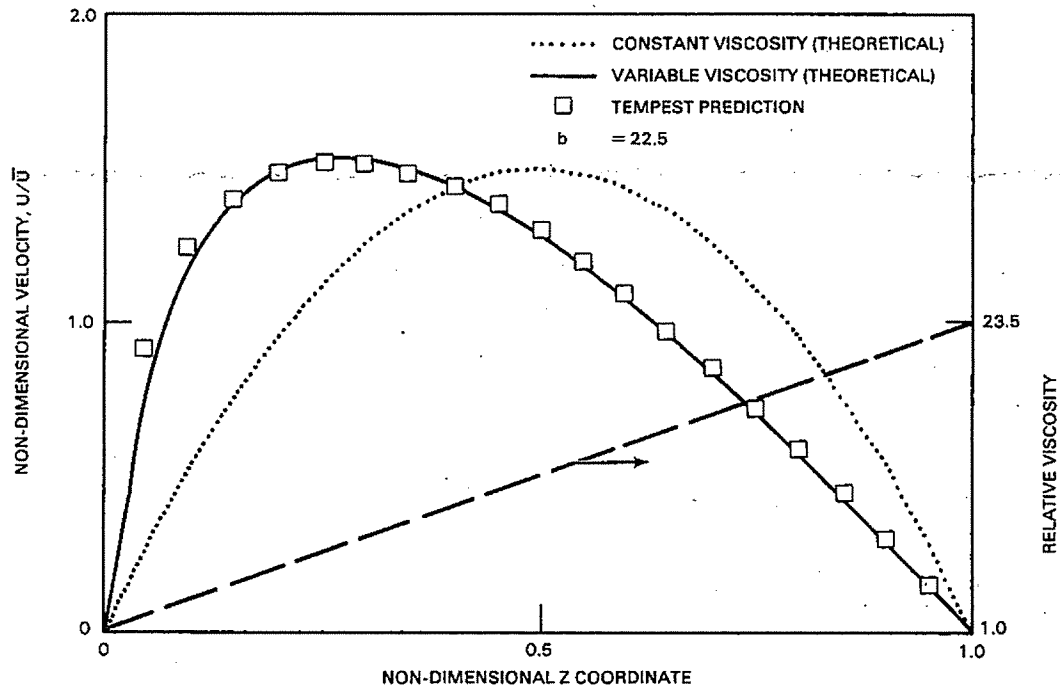


FIGURE 4.17. Plane Channel Velocity Profile Comparison for Concentration-Dependent Viscosity

4.2.3 Buoyancy-Driven Cartesian Cavity Convection

Buoyant convection flow in a cavity involves coupling between hydrodynamics and thermal energy transport. The experimental results of Eckert and Carlson (1961) in a 10:1-aspect-ratio cavity were chosen to test TEMPEST's ability to predict a buoyancy-driven convection flow.

The test simulation geometry is shown in Figure 4.18 along with results predicted with the TEMPEST code and the VECTRA code. Both vertical walls are constant-temperature boundaries with one being hot, the other cold. The top and bottom walls are adiabatic. The simulation was run with constant cell spacing (10 cells in the horizontal direction and 28 cells in the vertical direction). Constant-temperature vertical walls were modeled with air being the convecting medium.

The agreement between the data of Eckert and Carlson and the TEMPEST predictions using constant properties is excellent. Additional simulations were also run using variable cell spacing and the steady-state thermal solution algorithm. In each case, computed results were in excellent agreement with the data. Variable fluid properties were also used to test coding logic and their effect on the accuracy of the predictions. For this cavity case, the variable fluid properties logic was shown to work correctly. No significant difference in the temperature distribution was predicted.

Additional experimental results for convection in a square cavity have been reported by Sernas and Lee (1978). Also, deVahl Davies and Jones (1983) have compiled extensive numerical results of closed-square cavity convection obtained with several computer codes and present what they believe to be a very accurate answer to the problem. To further document TEMPEST's computational efficiency and accuracy, several simulations of a square cavity were run. Results were compared to Sernas and Lee's experimental results and deVahl Davis and Jones' numerical results.

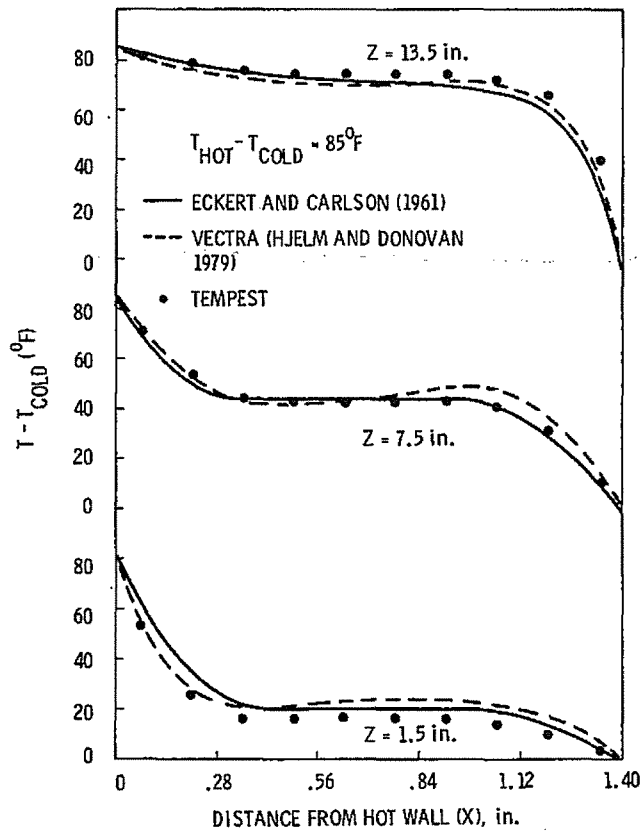
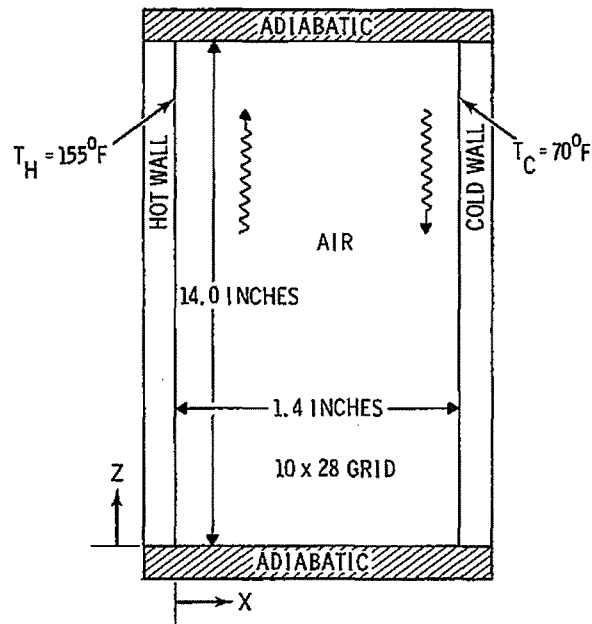


FIGURE 4.18. Natural Convection in a Two-Dimensional Cavity (Eckert and Carlson problem)

The square-cavity simulation geometry is shown schematically in Figure 4.19. For this simulation, dimensionless parameters were defined for both the geometry and the thermal hydraulics. The dimensionless quantities modeled are:

$$\text{Height: } H = 1$$

$$\text{Width: } W = 1$$

$$\text{Dimensionless Temperature: } \theta = \frac{T - T_c}{T_h - T_c}$$

$$\text{Dimensionless Velocities: } U = \frac{u(x,y) H}{\alpha}$$

$$V = \frac{v(x,y) W}{\alpha}$$

$$\text{Prandtl Number: } Pr = \frac{\nu}{\alpha}$$

$$\text{Rayleigh Number: } Ra = \frac{\beta g \Delta T W^3}{\nu \alpha}$$

$$\text{Average Nusselt Number: } \bar{Nu} = \int_0^1 \frac{\partial \theta}{\partial X} dZ \text{ at } X = 0 \text{ or } 1$$

The pseudo fluid properties were specified by tabular input:

Temperature:	$\theta = 0.0^0$	1.0^0
Density:	$\rho = 1.00$	$0.99 (\beta = 0.01/^0)$
Dynamic Viscosity:	$\mu = 0.10$	0.10
Specific Heat:	$C_p = 7.10$	7.10
Thermal Conductivity:	$k = 1.00$	1.00

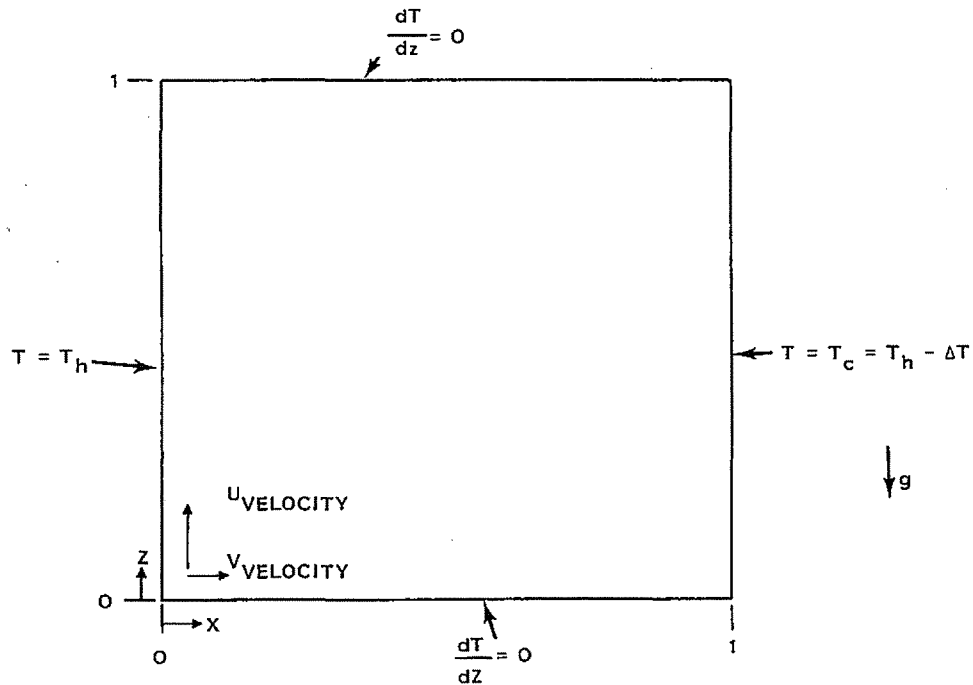


FIGURE 4.19. Nondimensional, Square-Cavity Convection Simulation

These properties result in a fluid with $Pr = 0.71$. Rayleigh numbers from 10^3 to 10^6 were obtained by changing the gravitational acceleration from 1.394 to 1.394×10^3 , respectively.

The boundary conditions were:

$$\theta = 1 \text{ at } X = 0$$

$$\theta = 0 \text{ at } X = 1$$

$$\frac{\partial \theta}{\partial Z} = 0 \text{ at } Z = 0 \text{ and } 1$$

Simulations at four Rayleigh numbers were run with four cell spacing configurations. These were:

$$Ra = 10^3, 10^4, 10^5, \text{ and } 10^6$$

with cell spacing configurations of:

- 5x5 grid, constant spacing
- 15x15 grid, constant spacing
- 25x25 grid, constant spacing
- 25x25 grid, variable spacing

For the latter case, smaller cell spacings were concentrated near the walls.

Results of these simulations are summarized in Table 4.1. The TEMPEST results are compared to the results from the deVahl Davies and Jones (1983) report, which represent the most accurate solutions.

The TEMPEST results obtained with the 25x25 grid with variable cell spacing are in best agreement with the deVahl Davies and Jones results. At $Ra = 10^6$, the maximum error in predicted Nusselt number is 5 percent, whereas at $Ra = 10^3$ it is less than 1 percent. For velocity, TEMPEST predictions of the maximum vertical and horizontal velocities are typically 2 to 5 percent different, with the exception of the horizontal velocity at $Ra = 10^6$. For this case, a large eddy-like structure was being predicted by TEMPEST not unlike development of a multicellular structure. The simulation was not carried to steady state to verify the realness of this predicted structure.

These simulations took less than 2 min of computer time on a CDC-7600 to achieve solutions at $Ra = 10^6$ using the uniform 25x25 cell structure. This time betters the most accurate solution presented by deVahl Davies and Jones by almost an order of magnitude.

One additional cavity simulation was conducted to compare TEMPEST predictions with the square-cavity experimental results of Sernas and Lee. For this case, real fluid properties for air were used in a cavity with an aspect ratio of 2.5:1 at $Ra = 3.86 \times 10^6$. Using a nonuniform 25x25 node structure, TEMPEST predicted local and average heat transfer coefficients within 10 percent of experimental results.

The results of these cavity simulations demonstrate both TEMPEST's efficiency and accuracy as well as support the correctness of solution algorithms. They also demonstrate the ease with which multiparameter simulations can be run directly through use of input card specification of parameters.

TABLE 4.1. Square Cavity Nusselt Number Results

Grid	Ra = 10 ³				
	Nu	Nu _{max}	Nu _{min}	U _{max}	V _{max}
5x5 constant	1.27	1.80	.80	3.39	3.57
15x15 constant	1.14	1.54	.72	3.52	3.58
25x25 constant	1.29	1.51	.71	3.55	3.57
25x25 variable	1.12	1.48	.73	3.44	3.48
deVahl Davis & Jones	1.11	1.50	.69	3.65	3.70

Grid	Ra = 10 ⁴				
	Nu	Nu _{max}	Nu _{min}	U _{max}	V _{max}
5x5 constant	2.58	3.95	1.26	15.01	18.00
15x15 constant	2.36	3.91	.68	15.95	18.93
25x25 constant	2.27	2.70	.63	15.78	18.91
25x25 variable	2.23	3.56	.65	15.68	19.08
deVahl Davis & Jones	2.23	3.52	.58	16.17	19.64

Grid	Ra = 10 ⁵				
	Nu	Nu _{max}	Nu _{min}	U _{max}	V _{max}
5x5 constant	3.94	5.14	2.67	40.7	50.92
15x15 constant	5.26	9.07	1.12	42.0	67.27
25x25 constant	4.83	8.75	.92	42.3	68.93
25x25 variable	4.57	7.92	.94	42.9	68.10
deVahl Davis & Jones	4.50	7.17	.72	34.7	68.25

Grid	Ra = 10 ⁶				
	Nu	Nu _{max}	Nu _{min}	U _{max}	V _{max}
5x5 constant	4.58	5.27	3.80	94.71	119.07
15x15 constant	9.94	15.66	3.67	75.40	221.09
25x25 constant	10.40	19.88	1.76	109.13	225.00
25x25 variable	7.2	19.69	1.55	113.29	224.29
deVahl Davis & Jones	8.90	18.56	1.00	64.95	221.29

4.2.4 Combined Free- and Forced-Convection Pipe Flow (Morton's Problem)

Code testing with combined free- and forced-convection flow has been done in several simulations. The case of a uniformly heated vertical pipe flow was chosen as a test case because an analytical solution exists (Morton 1960).

In the case of upward, heated flow in a pipe, the buoyancy effect of the fluid causes velocities near the wall to increase and velocities near the centerline to decrease as heat flux increases. At sufficiently high Rayleigh numbers, the velocity maximum may shift away from the centerline, resulting in a so-called "camel hump" profile.

TEMPEST was used to simulate the fully developed, upward-flowing case with constant heat flux at the wall. Flows with Rayleigh numbers of 10, 50, 100, and 400, based on the channel width, were computed. A two-dimensional simulation was conducted using the centerline as a symmetry boundary. At the lower Rayleigh numbers, 20 nodes were used in the radial direction. At the higher Rayleigh number, only 10 radial nodes were used. Axial noding was varied for the different Rayleigh numbers to ensure that a fully developed flow existed at the outlet of the modeled region.

Figure 4.20 presents a comparison of predicted velocity profiles and the analytical solution for a bulk velocity of 1 ft/sec. The analytical results were obtained from results presented by Morton (1960) at the same radial location as the TEMPEST results. At $Ra = 10$, where buoyancy is minimal, a nearly parabolic, laminar Poiseuille profile is predicted which would have a centerline value of 2.0. At higher Rayleigh numbers the buoyancy becomes significant until a camel hump profile results. In all four Rayleigh number cases, the TEMPEST predictions are in excellent agreement with the analytical results.

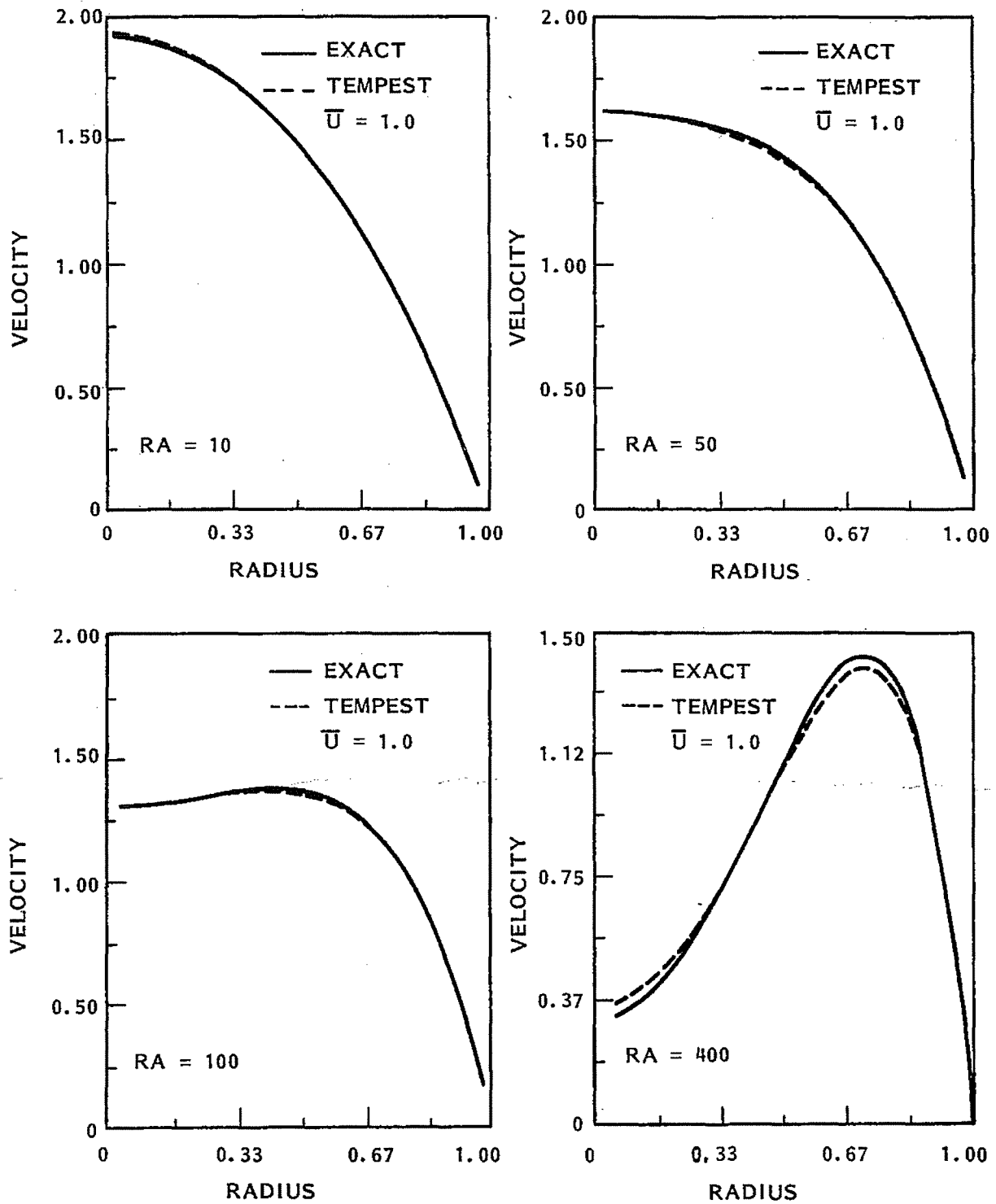


FIGURE 4.20. Comparison of Predicted and Analytical Vertical Velocity Results in Bouyancy-Affected Laminar Pipe Flow (Morton's Problem)

4.2.5 Natural-Convection Heat Transfer in a Cylindrical Annulus

Simulations of heat transfer in the annular region between two concentric cylinders was modeled. Eighteen evenly spaced radial nodes and 28 angular nodes were computed. Vertical centerline symmetry was assumed. Pseudo material properties were input to TEMPEST, and parameters were varied to span a gap width Rayleigh number range from 6×10^2 to 7×10^8 . Based on experimental observations of Kuehn and Goldstein (1976), this range spans flow regions from pseudo-conductive to laminar to turbulent. For $Ra > 10^7$, the k- ϵ turbulence model in TEMPEST was used.

A schematic of Kuehn's experimental test annulus and TEMPEST node structure is shown in Figure 4.21. The diameter of the inner cylinder is 3.56 cm, and the diameter of the outside cylinder is 9.25 cm. The gap width is the characteristic dimension used in the Rayleigh number. Kuehn used pressurized air and nitrogen as test fluids. His experimental results span $5 \times 10^2 \leq Ra_L \leq 8 \times 10^8$.

A comparison of the equivalent gap thermal conductivity, \bar{k}_{eq} , which is defined as the ratio of heat transfer by convection to the heat transfer by conduction, is presented in Figure 4.22. The TEMPEST predictions lie within the span of experimental data reported by Kuehn over the whole Rayleigh-number range simulated. TEMPEST results are also in good agreement with the Güçeri empirical correlation of Lis (1966) and numerical predictions presented by Farouk and Güçeri (1982). They used a steady-state stream function vorticity code and performed predictions up to $Ra = 10^7$.

A comparison of predicted isotherms and Kuehn's measured data in the form of fringe patterns at $Ra = 5 \times 10^4$ is illustrated in Figure 4.23. Very good agreement between the isotherm patterns is evident. At this Ra , the flow is in the region of fully laminar flow. At higher Rayleigh numbers, particularly for $Ra > 10^7$, experimental observations have shown that boundary layers near each cylinder became much thinner and that a very stably stratified region developed in the lower portion. Figure 4.24 shows TEMPEST results which exhibit these experimentally observed characteristics.

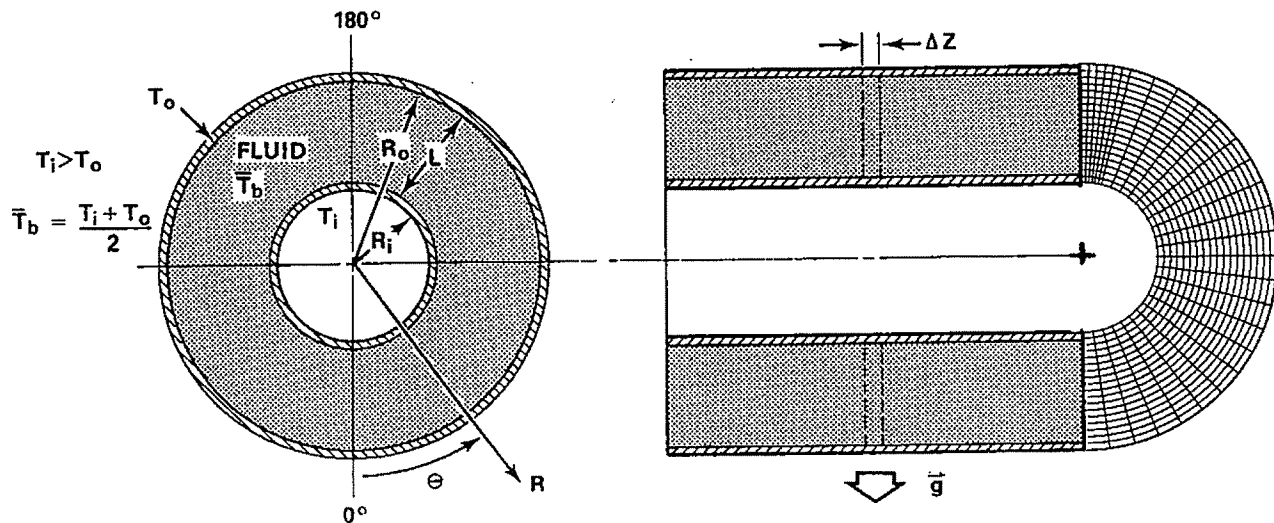


FIGURE 4.21. Cylinder Geometry and Node Structure for Annular Convection

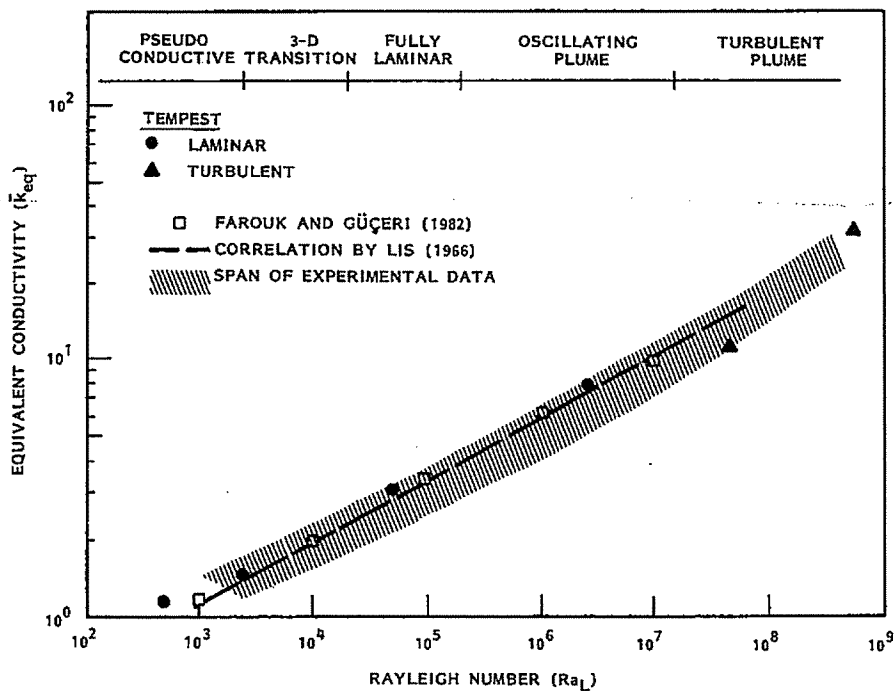


FIGURE 4.22. Equivalent Thermal Conductivity Comparison for Annular Convection Between Cylinders

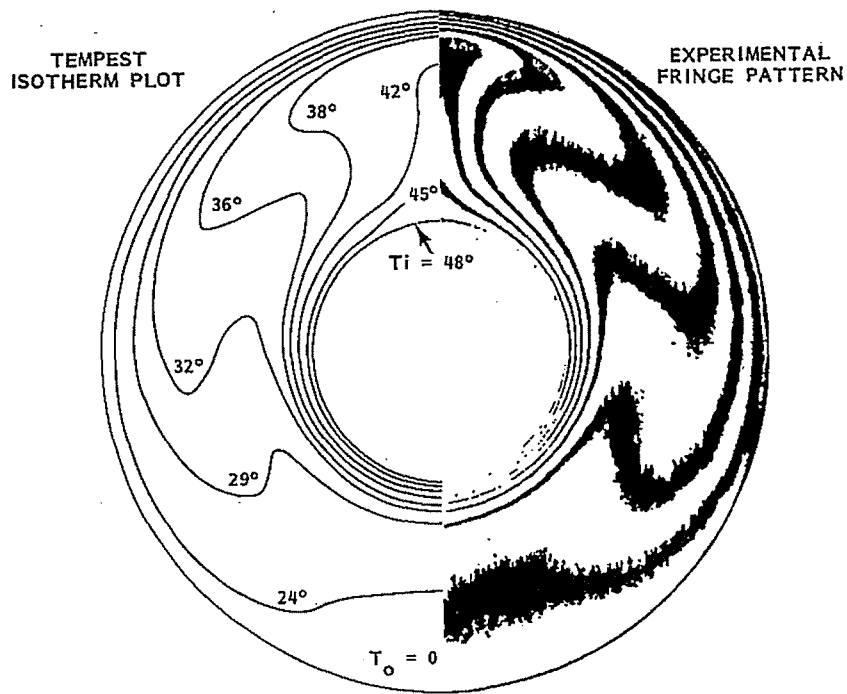


FIGURE 4.23. Comparison of Predicted and Measured Isotherms at a Rayleigh Number of 5×10^4

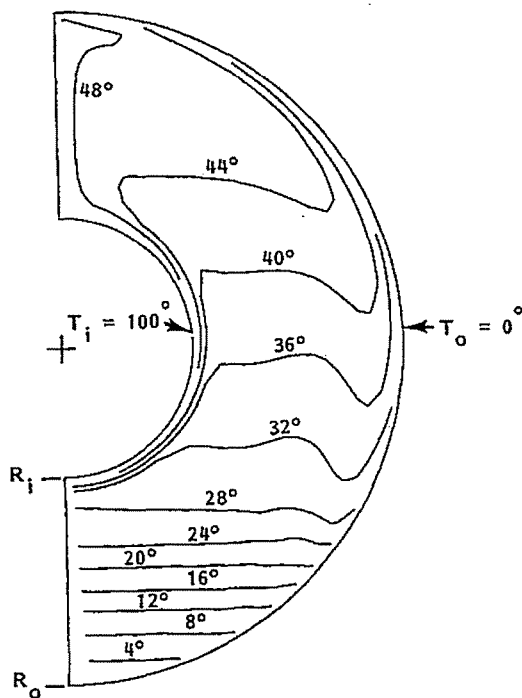


FIGURE 4.24. Predicted Isotherms at a Rayleigh Number of 6×10^8

4.2.6 Time-Step Testing in Internal Wave Flow with Stable and Unstable Stratification

Flow in an adiabatic box was simulated for both stable and unstable initial conditions. The objective of these tests was to check TEMPEST's automatic time-stepping logic and to determine the code's ability to predict internal waves and turnover in stably and unstably stratified fluids.

The simulations were conducted using a 10x10 computational grid in two dimensions. Constant node spacing was used with a 1-ft cell size. Adiabatic boundary conditions were used on all four sides. Temperatures were initialized in each horizontal row of cells to set up a 10°F/ft temperature gradient. Perturbations were imposed to initiate motion by setting the temperature in two central cells at a value 10°F above the ambient temperature of the other cells in that horizontal row. Both stable and unstable initial temperature gradients were tested.

For the initial temperature gradient that was stably stratified, simulations were run for perturbations which were both positively and negatively buoyant. Results were identical except for exactly opposite flow directions. For the unstable initial stratification, only a positively buoyant initial perturbation was simulated.

TEMPEST can be operated in a number of time-step-controlling modes. Briefly, these include:

- A fixed time-step mode. In this mode, a fixed input time step will be used as long as the time step is less than explicit stability requires. If it is not, TEMPEST will reduce the time step to a stable value and return to the constant input value subsequently.
- An automatic time-step mode. Several modes are available and depend on selected user input. The Courant number and diffusion criteria are the most commonly used. Additionally, the Brunt-Väisälä frequency limitation may be selected if flow oscillations induced by an internal density gradient are to be considered. Implicit damping may also be selected if internal waves may be present but resolving the wave form is not a consideration.

These time-step modes were tested in the stratification simulations.

Stable Stratification

For stable stratification with a $10^{\circ}\text{F}/\text{ft}$ temperature gradient in water, the period corresponding to the Brunt-Väisälä frequency is 26.4 sec. Thus the maximum time step that can be taken to resolve an oscillation caused by a density perturbation is 6.6 sec. Without implicit damping in a constant, fixed time-step mode, TEMPEST computes the oscillatory flow very well for time step increments less than 6.6 sec. Figure 4.25 shows results obtained at fixed time step increments of 1, 2, and 6 sec. At any time step increments over 6.6 sec, the solution becomes unstable without implicit damping. It is apparent from the results in Figure 4.25 that the larger the time step, the less the resolution of the oscillation. The envelope character of the oscillations is due to the computational grid not exactly matching the wave length of the oscillation.

When implicit damping is enabled, time steps larger than the oscillation quarter period can be used. In this mode, however, details of the oscillations caused by the density perturbation are damped out as shown in Figure 4.26. With implicit damping, stable solutions were predicted using time steps as large as 100 sec.

When the option for limiting the density gradient time step is used, the implicit damping is disabled. Computed results were virtually identical to the those obtained with the fixed-time-step results in Figure 4.25. In this mode, the user has the option of specifying the fraction of the quarter-period time that should be used. The smaller the fraction of the quarter-period time, the better the wave form is resolved.

Unstable Stratification

Simulations of unstable density gradient were also conducted. For these cases, initial temperature conditions were imposed such that the cold fluid was initially on top of the warm fluid. Again, a density perturbation was imposed by setting temperatures at two central cells 10°F above the other cells on that horizontal row.

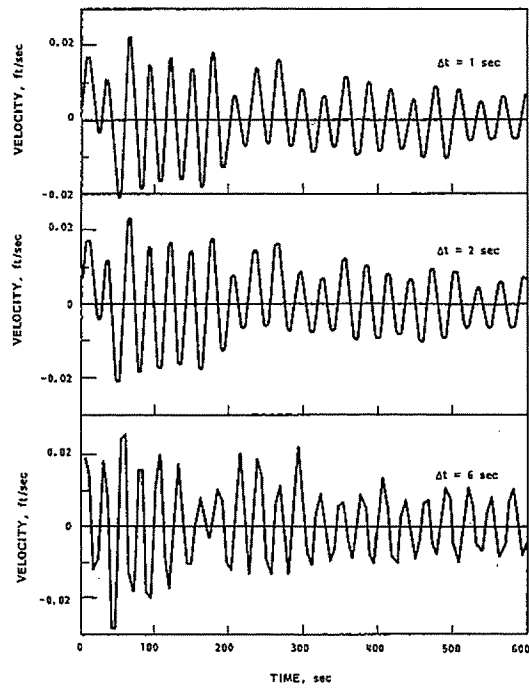


FIGURE 4.25. Internal Wave Type Oscillations in a Stably Stratified Adiabatic Box

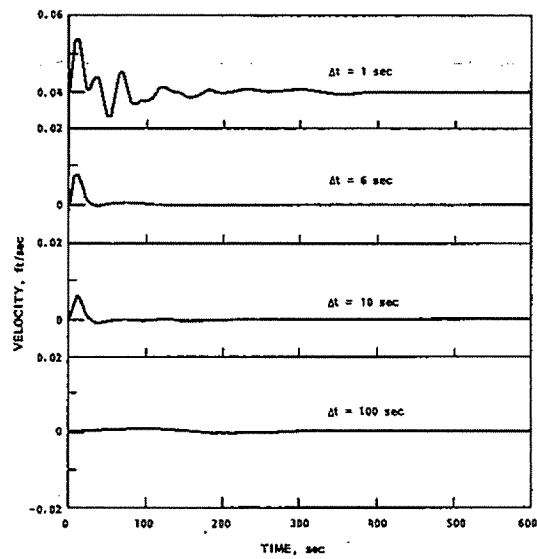


FIGURE 4.26. Implicitly Damped Density Perturbation in a Stable Stratification

Figure 4.27 shows a composite of the computed vertical velocity component at a central cell, and Figure 4.28 shows the corresponding temperature results for two of the test cases.

The four cases run were:

- Case 1: Automatic time stepping with specified initial time step - Implicit damping was enabled.
- Case 2: Constant fixed time step of 0.40 sec - Implicit damping was enabled.
- Case 3: Fixed-time-step ($\Delta t = 2.0$ sec) mode - A required stability at each time step resulted in a time step reduction through the steepest parts of the turnover transient.
- Case 4: Automatic time stepping controlled by density gradient criterion

In Case 1, the Courant limitation computes a stable but very large second time step before it senses the accelerating effect of the buoyancy perturbation. That is why the results appear to be shifted over about 100 sec. During the turnover transient, the minimum time step computed is 0.42 sec. After the turnover, the flow re-establishes a quiescent stable stratification, and the automatic time stepping increased Δt up to a value of about 100 sec.

Case 2 was run with a constant $\Delta t = 0.40$ sec, which is smaller than the minimum Δt in Case 1. This case shows very good resolution with turnover commencing immediately. The residual oscillations after turnover are very slowly being damped out by viscous effects.

Case 3 shows results obtained using the constant time step option with $\Delta t = 2.0$ sec. Because this value is larger than the minimum stable value encountered during the transient ($\Delta t_{\min} = 0.42$ sec), time-step reduction is performed by the code where necessary and again uses the 2-sec step after the turnover.

For Case 4, the option for limiting the density gradient time stepping was used. In this mode, implicit damping is not applied. The results look very similar to Case 2 results, although considerably larger time steps were taken after the turnover. These latter case results were also computed with a maximum time step limitation of 0.25 of the quarter-period time step. Better resolution of the oscillations resulted.

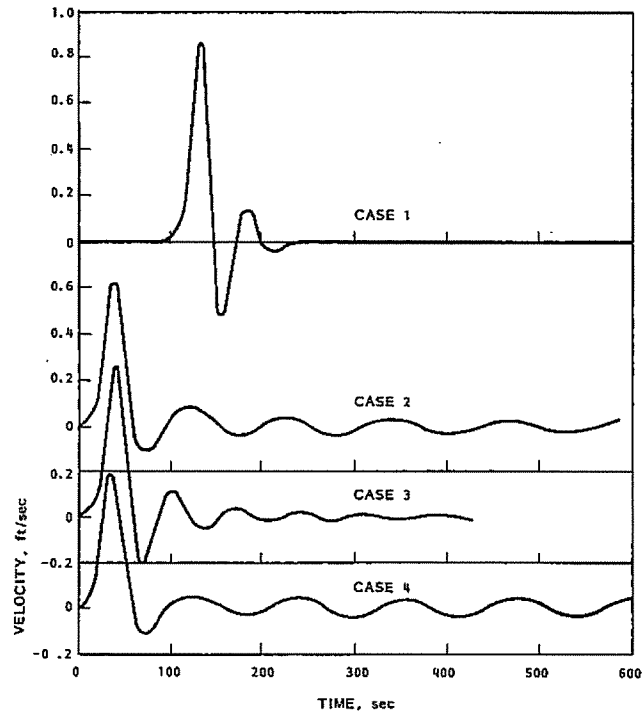


FIGURE 4.27. Vertical Velocity in an Unstable Density Gradient Turnover

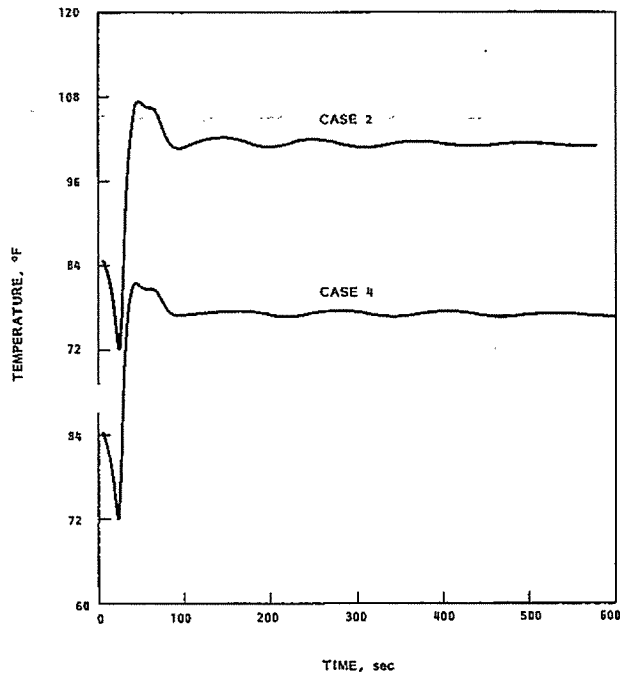


FIGURE 4.28. Temperature in Unstable Density Gradient Turnover

Figure 4.29 shows the initial unstable gradient and the final stable gradient after the turnover. During the turnover, significant thermal mixing has occurred, which results in a much lessened gradient.

These simulations of both perturbed stable and unstable gradient flows show that the time-stepping logic works correctly. The automatic mode, the fixed mode with and without backstepping, the implicit damping, and the density gradient limitation mode have been tested. Other tests in which buoyancy is not the dominant driving force have also been used to test the time-stepping logic.

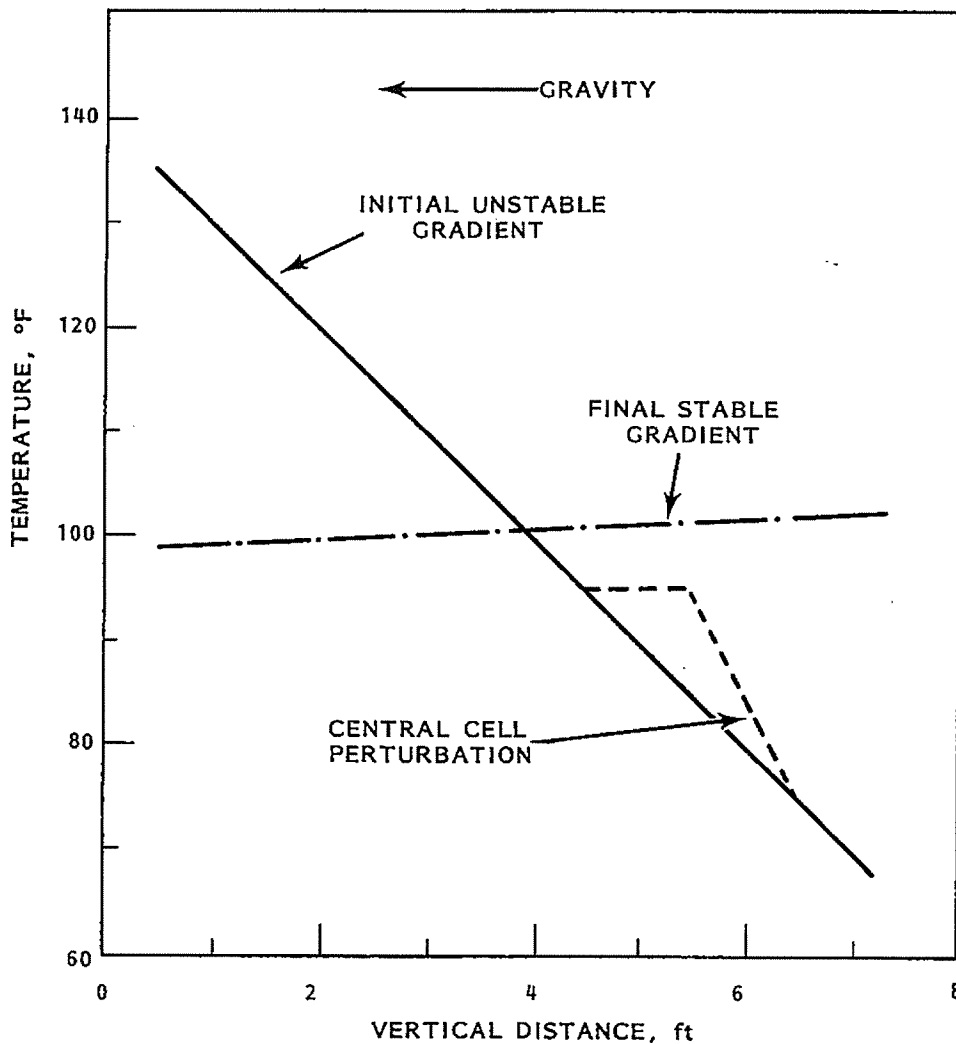


FIGURE 4.29. Initial Unstable Temperature Gradient and Final Stable Gradient After Turnover

4.3 THERMALLY COUPLED FLOW AND SOLID-WALL HEAT CONDUCTION

The TEMPEST computer code has the capability of computing thermal hydraulics in flow regions that are coupled by conduction heat transfer through solid walls. This capability enhances the code's ability to model complex flows which may be governed by the thermal characteristic of bounding or connecting solid material. In Section 3, results were presented which showed the code's ability to compute in the conduction-only mode. In this section, results of simulations are presented for coupled convection and conduction heat transfer.

Steady-state thermal characteristics are predicted for a coupled two-cavity geometry. The coupling is heat conduction through a thin layer of solid material separating two fluid cavities. The Cartesian cavities have a constant-temperature external wall boundary. The results are compared to experimental data.

4.3.1 Steady-State Heat Transfer Between Two Flow Cavities

A simulation of the coupled, two-cavity convection experiment reported by Viskanta and Lankford (1981) was set up and run. A schematic of the experimental apparatus is shown in Figure 4.30. It consisted of two 70-cm x 34-cm x 38-cm cavities thermally connected by a centrally located conduction wall. Brass, copper, and glass were used as conduction walls in the experiment. Balsa wood was used for the adiabatic section of the separating wall. Constant-temperature boundary conditions on the cold and warm sides were obtained by a water jacket and insulation assembly. Boundary condition temperature differences ranged from 10 to 40°C between the cavities in the experiments.

For the TEMPEST simulation, constant-temperature boundary conditions were imposed on the exterior walls of the warm and cold cavities. The warm side was 40°C and the cold side was 20°C. A coarse mesh was used with nine computation cells in each cavity in the horizontal coordinate direction and with twenty-three cells in the vertical coordinate direction. Variable cell spacing was used. The smallest cells were concentrated near the central conducting wall region. Two conduction cells were located in the horizontal direction of the conducting wall, and nine were located in the vertical

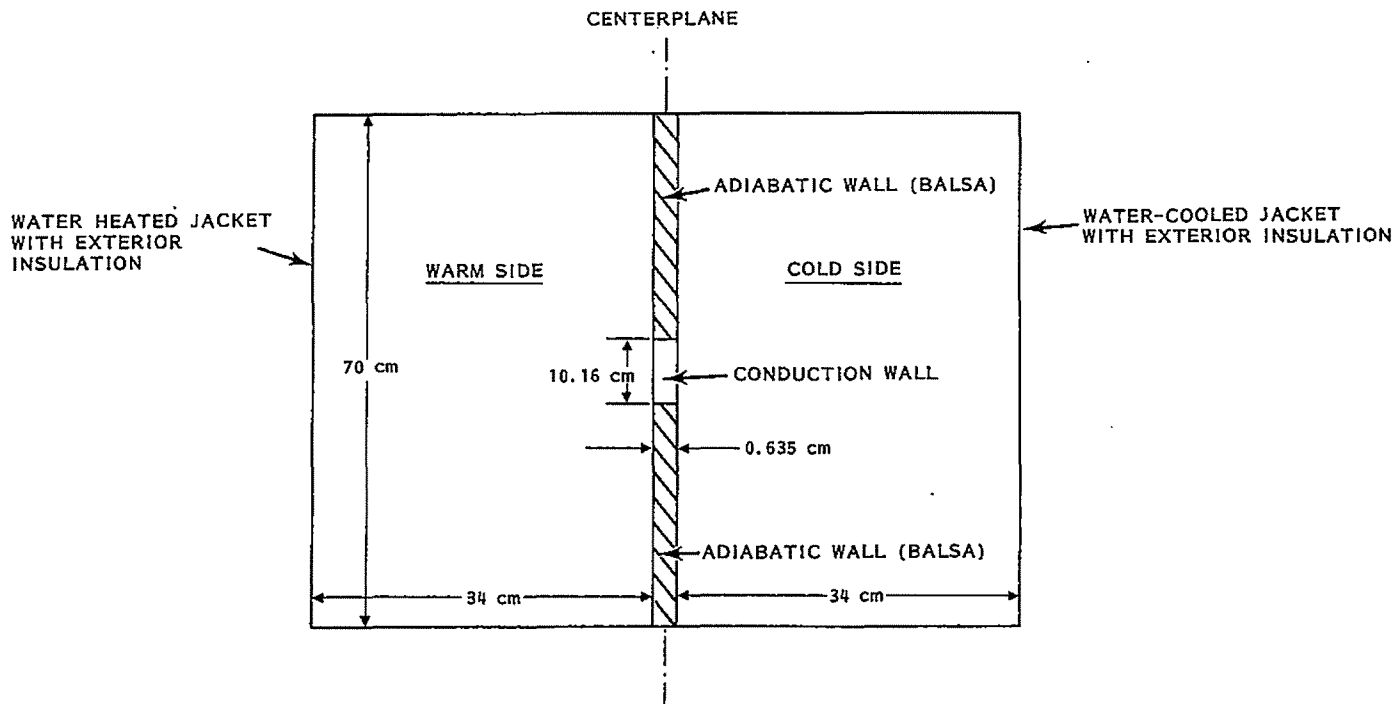


FIGURE 4.30. Schematic of Apparatus for a Two-Cavity Convection Experiment

direction of the conducting wall. Noding structure was maintained symmetric about the centerplane and about the horizontal midplane. A schematic of the noding structure in the vicinity of the conducting wall is shown in Figure 4.31.

The cell widths next to the conducting wall were reduced by a factor of two and then by a factor of two again to determine the cell spacing effect on predicted wall surface temperatures. Results are shown in Figure 4.32 for glass as the conducting wall. Varying the near-wall cell widths had little effect on the predicted steady-state wall temperatures. It did have an effect on the temperature profile in the free convecting boundary layer on both sides of the glass. The predicted bulk temperature of the fluid in the cavities was also unaffected.

Figure 4.33 compares predicted temperatures on the surface of the conducting wall on the hot cavity side with data presented by Viskanta and Lankford (1981). The dimensionless temperature is defined as

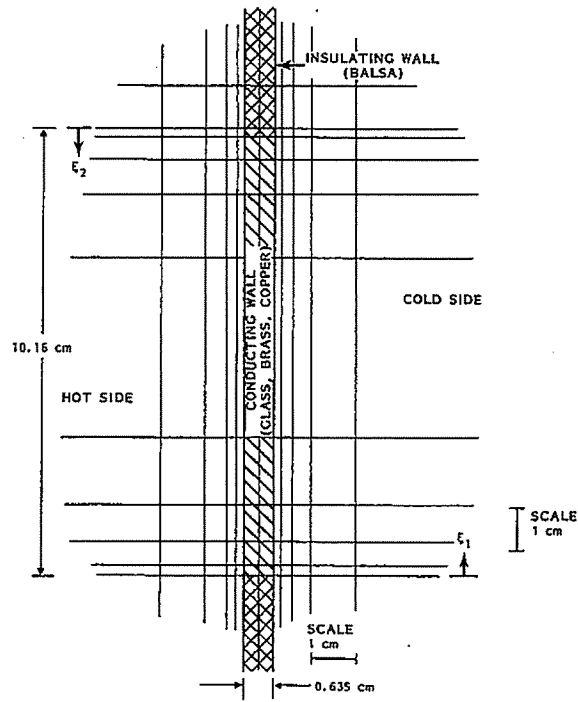


FIGURE 31. Schematic of the Cell Structure in the Vicinity of the Conducting Wall

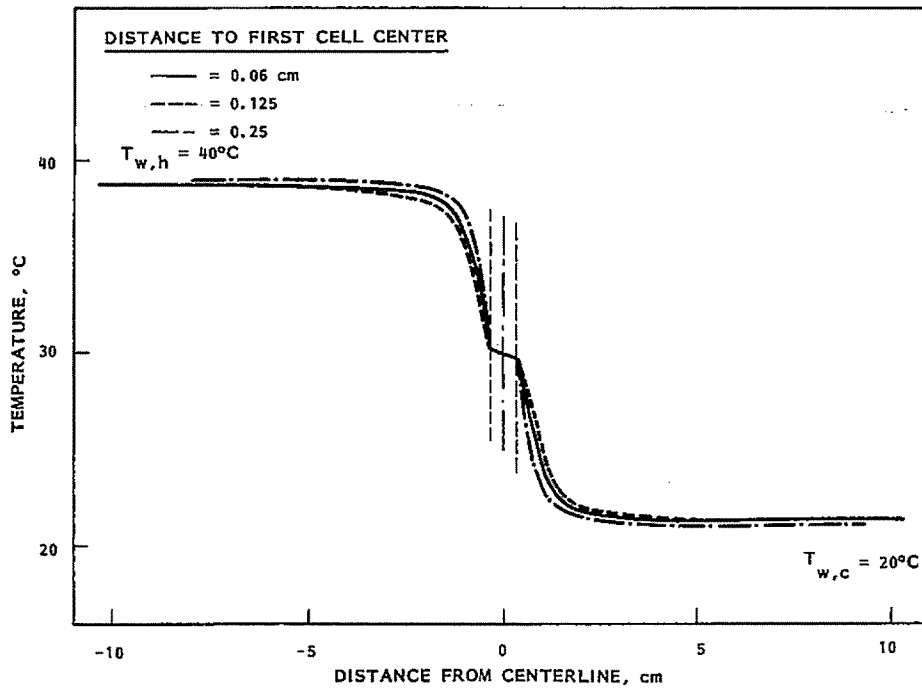


FIGURE 4.32. Temperature Profile at Midplane of Glass Wall ($k = 0.519 \text{ W/m}^{\circ}\text{C}$)

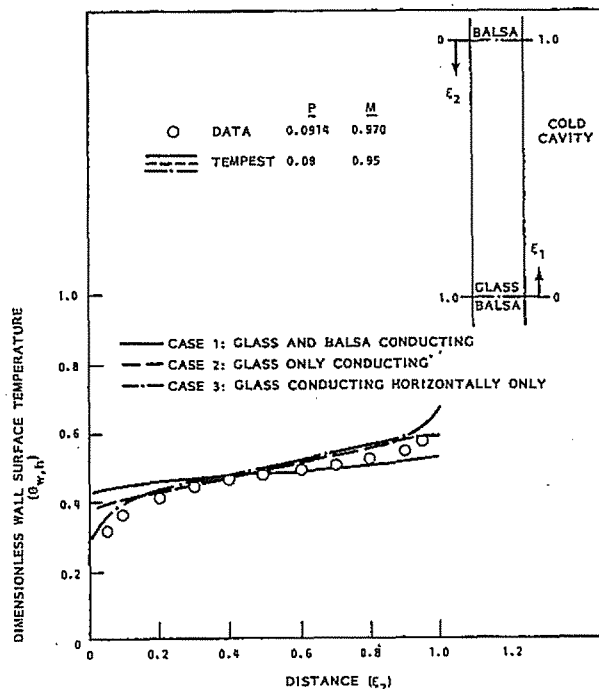


FIGURE 4.33. Comparison of Predicted and Measured Dimensionless Wall Surface

$$\theta_{wh} = \frac{T_{h,\infty} - T_{h,w}}{T_{h,\infty} - T_{c,\infty}}$$

where $T_{h,\infty}$ is the bulk fluid temperature in the hot cavity
 $T_{c,\infty}$ is the bulk fluid temperature in the cold cavity
 $T_{h,w}$ is the wall surface temperature on the hot side.

Three sets of predicted results included in Figure 4.33 were obtained with the smallest near-wall computational cell width of 0.12 cm. These are:

- Case 1. Glass ($k = 519 \text{ W/m-}^\circ\text{C}$) and balsa ($k = 0.055 \text{ W/m-}^\circ\text{C}$) walls with both materials conducting
- Case 2. Glass with the balsa wall treated as adiabatic
- Case 3. Glass conducting horizontally only (i.e., no axial conduction in the glass wall) with the adiabatic balsa wall.

The first case shows a fairly constant surface temperature gradient but does not follow the data trend very well, particularly in the leading edge ($\epsilon_2 = 0$) developing region. The second case also predicts a fairly constant surface temperature gradient that is more closely in agreement with the data. The third case, however, shows good agreement with slopes of the wall temperature data in the leading and trailing edge regions. An additional simulation of case 2 was also run with a coarser constant cell mesh in the vertical direction (as compared to the variable spacing in the vertical direction shown in Figure 4.31). These results were virtually identical to the variable-spacing temperature results. They indicated that resolving the conduction effect in the conducting wall for this simulation is as important as resolving the convecting cavity flows.

Other data reported by Viskanta and Lankford for brass and copper walls also showed significant nonlinearity of surface temperature profiles. Data reported by Anderson and Bejan (1981) in a similar experiment, however, showed a very linear temperature profile in an aluminum partition between cavities, and they concluded that axial conduction in their partition was significant in linearizing the wall temperature.

Neglecting axial conduction in the wall, Viskanta and Lankford developed an analytical model to predict the wall surface temperatures, heat fluxes, and corresponding Nusselt numbers. Anderson and Bejan developed a similar model. They found that the surface temperature and heat flux results depended on the parameters P and M where

$$P = \left(\frac{k_h}{k_w}\right) \left(\frac{W}{H}\right) Ra_h^{1/2}$$

and

$$M = \left(\frac{h_h}{k_c}\right) \left(\frac{Ra_h}{Ra_c}\right)^{1/4}$$

Subscripts h and c refer to the hot cavity fluids and cold cavity fluids, respectively. The parameter W is the width, and H is the height of the conducting section of the wall. The parameter P relates the relative thermal properties of the convecting fluid to that of the conducting wall. The parameter M relates the relative thermal properties of the convecting fluids in each cavity.

Figure 4.34 compares the results of predicted, dimensionless surface heat flux. The dimensionless heat flux is defined as

$$q^*_h = \frac{q''_{w,h}}{\left(\frac{k_w}{W}\right) (T_{h,\infty} - T_{c,\infty})} .$$

The TEMPEST results for case 3 (no axial conduction in the glass) are in good agreement with Viskanta's and Lankford's results that were obtained analytically assuming no axial conduction. Nusselt numbers computed from the heat flux and surface temperatures also agreed similarly.

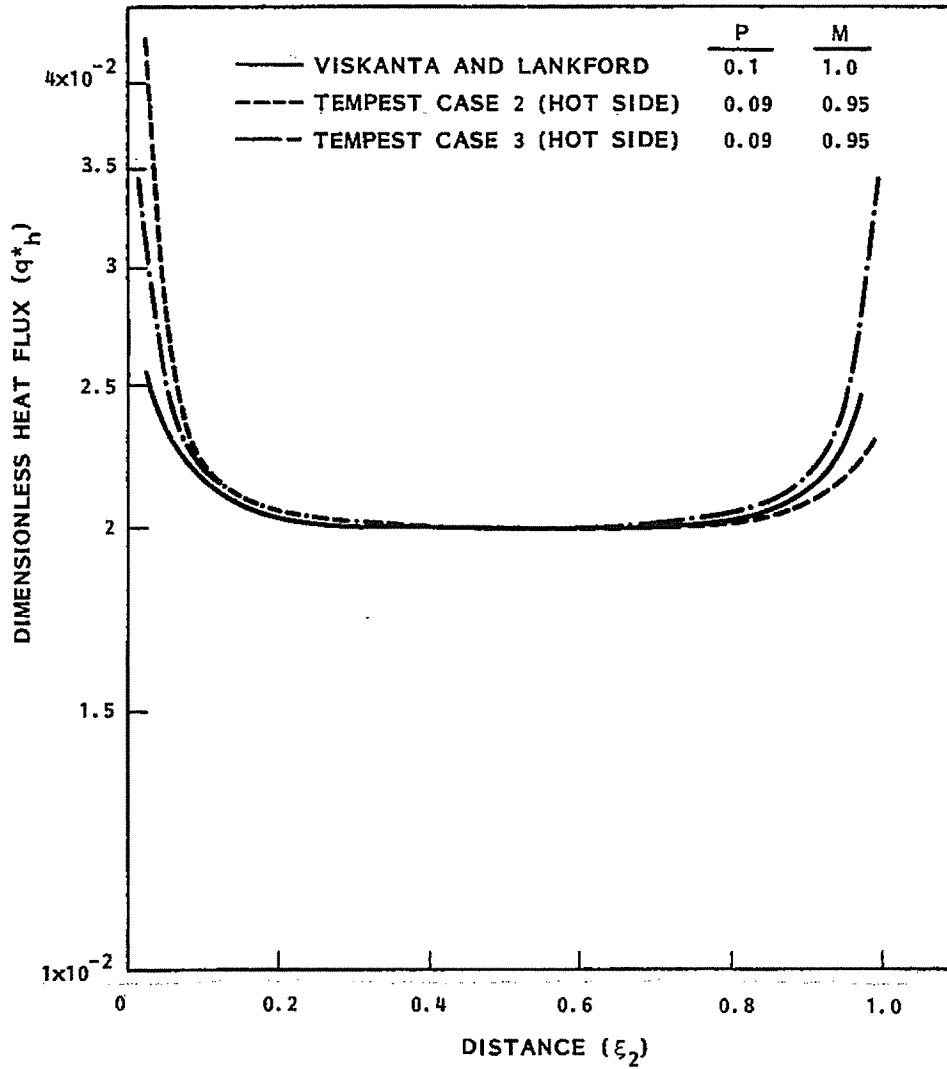


FIGURE 4.34. Comparison of Surface Heat Flux for Coupled-Cavity Convection

5.0 CONVECTION SIMULATION RESULTS: TURBULENT FLOW

Turbulence is a common occurrence in most flows of practical interest. Modeling turbulence in thermal-hydraulic analysis is a complex problem and one that can only be treated through appropriate assumptions that reduce the problem to a workable level.

Various levels of assumptions can be made concerning a modeling approach to turbulence. At one of the lowest levels, turbulent shear stresses which result from Reynolds' assumption applied to the Navier-Stokes equations (see Hinze 1975, for example) can be modeled as gradient-diffusion-type stress. The resulting turbulent or effective viscosity is then determined from empirical correlations or other available means. At one of the highest levels for which current technological capability for solution exists, the turbulent shear stresses are determined directly from modeled shear stress transport equations. Between these two levels are numerous other levels or models for determining the turbulent shear stresses.

The model which has been incorporated in TEMPEST is the two-equation $k-\epsilon$ model. It is one that has received significant attention and usage in the past 10 years or so. The model's complexity lies roughly halfway between full shear stress modeling and constant-turbulent-viscosity, gradient-diffusion modeling. It represents a tradeoff between computational complexity and physical modeling.

Numerous reports demonstrate the wide range of applicability of the two-equation $k-\epsilon$ level of turbulence modeling. A good review is provided by Kollmann (1981). In this section, results obtained with the $k-\epsilon$ model in TEMPEST are presented. The objectives of presenting these results are to demonstrate that the logic is correct and to demonstrate that the physical model is applicable to reactor design analysis. This is done through comparison with computed results of other codes, with experimental data, and with empirical information.

The developmental basis for the $k-\epsilon$ model can be found in Jones and Launder (1972), Launder (1975), and Kollmann (1981). Application of this model in TEMPEST and a discussion of the numerical solution scheme are presented by

Trent, Eyster and Budden (1983). Details of the $k-\epsilon$ model development and solution scheme are not included here.

5.1 TURBULENT ISOTHERMAL FLOW

To test the logic incorporated in TEMPEST for solution of the $k-\epsilon$ turbulence model, several simulations of isothermal flows were conducted. These included diffusion of turbulent kinetic energy and dissipation, free shear decay, and grid generation and decay. Plane and round jets were simulated, and comparisons were made to data. Isothermal wall-bounded simulations included plane channel flows, pipe flows, and pipe expansion flows. Analysis of these simulation results and comparison with data and other code results provide a basis for assessing the correctness of the solution scheme logic, boundary conditions, and numerical transport equations.

5.1.1 One-Dimensional Diffusion of Turbulence Variables

Correctness of the logic for the diffusion terms in the kinetic energy equation and the dissipation equations were determined by numerically modeling simple, one-dimensional boundary condition problems in Cartesian and cylindrical coordinates. A $10 \times 1 \times 1$ noding structure was used, and prescribed boundary values were set on each end of the region. Different initial values for k and ϵ were used for the interior cells. TEMPEST then was used to compute the steady-state distribution between the boundary values.

Results of these simple simulations showed excellent agreement with analytical distributions derived from the transport equations with no convection in both coordinate systems. Diffusion flux terms across individual cell faces were also computed by hand calculation to be in agreement with the code predictions. Thus, it was concluded that the logic for diffusion terms was correct.

5.1.2 Free Shear Decay

In the absence of shear production, turbulence is known to decay according to a uniform power law. Such a uniform decay rate has been measured in experiments downstream of a grid (Hinze 1976). The $k-\epsilon$ model uses this decay law to determine one of the constants in the modeled transport equations (Jones and Launder 1972).

To test the logic in TEMPEST, a free-shear decay simulation was run, modeling the far-downstream flows behind a grid. For this case, both one-dimensional and two-dimensional node structures were used. Dimensions in one of the coordinate directions in the latter case was modeled identically in the former case and showed the correctness of TEMPEST predictions of zero cross-stream gradients.

For this case, a uniform and constant velocity field was specified for the region. Turbulent kinetic energy and dissipation were prescribed at the inflow boundary only. The rest of the field was initialized to 10^{-30} to model no initial turbulence. The simulation was computed to a point in time equivalent to two advected throughputs. At this point, the TEMPEST-predicted distribution of turbulent kinetic energy and dissipation was steady in time. The same problem was set up and run with the TEACH code (Gosman 1976), which is a two-dimensional, steady-state code with a $k-\epsilon$ model.

Comparison of the TEMPEST and the TEACH results showed them to be in almost exact agreement over the whole flow domain. The decay rate predicted by both codes was very close to the decay rate ($-3/2$) reported by Hinze (1976). These results further confirmed the correctness of logic in TEMPEST.

5.1.3 Combined Grid Generation and Decay

To further test TEMPEST logic, the experimental results obtained by Warhaft and Lumley (1978) for flow downstream of a square-rod, square-mesh grid were simulated. Two models of the experiment were simulated with TEMPEST. Both were three-dimensional simulations.

In the first case, a $5 \times 5 \times 12$ computational node structure simulating one square of the turbulence-generating grid was modeled. A schematic of this segment is shown in Figure 5.1 along with the computational mesh used. The upstream boundary was as a constant velocity plane with no turbulence. Free-shear boundaries were modeled on the axial surfaces.

In the second case, additional detail was obtained by using $7 \times 7 \times 12$ computational mesh and assuming quarter-section symmetry within the one-square segment. Figure 5.2 shows schematically this geometry and the computational

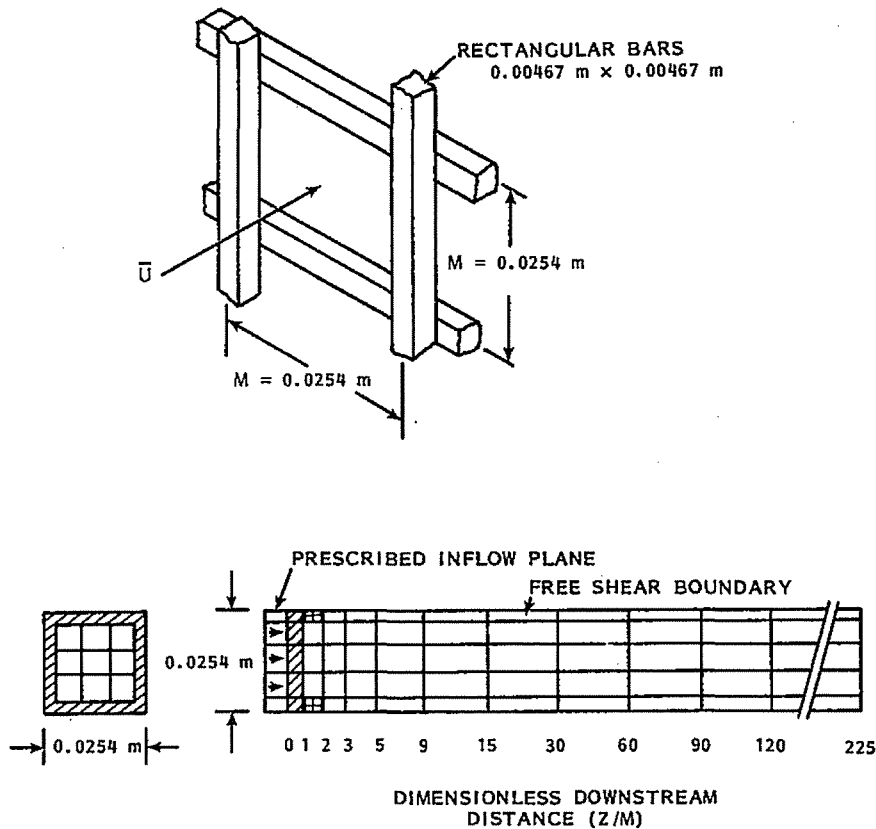


FIGURE 5.1. Square-Rod, Square-Mesh Grid and Computational Structure - Full Square

structure. Again, a constant inflow velocity was specified, corresponding to Warhaft and Lumley (1978) data, and no upstream or initial turbulence was specified. Turbulence is produced by shearing past the square grid bars.

A comparison of the TEMPEST prediction of the kinetic energy with the turbulence intensity data of Warhaft and Lumley is shown in Figure 5.3. The results are in good agreement. Although the magnitude of the kinetic energy is underpredicted, the characteristic decay slope is in very close agreement with a reported curve fit of the data which showed a -1.34 power law decay. The one point for which dissipation was reported ($z/M = 80$) is also predicted quite well.

This simulation provided a good test of TEMPEST's computation of both production and decay of turbulence. The production is a direct consequence of the

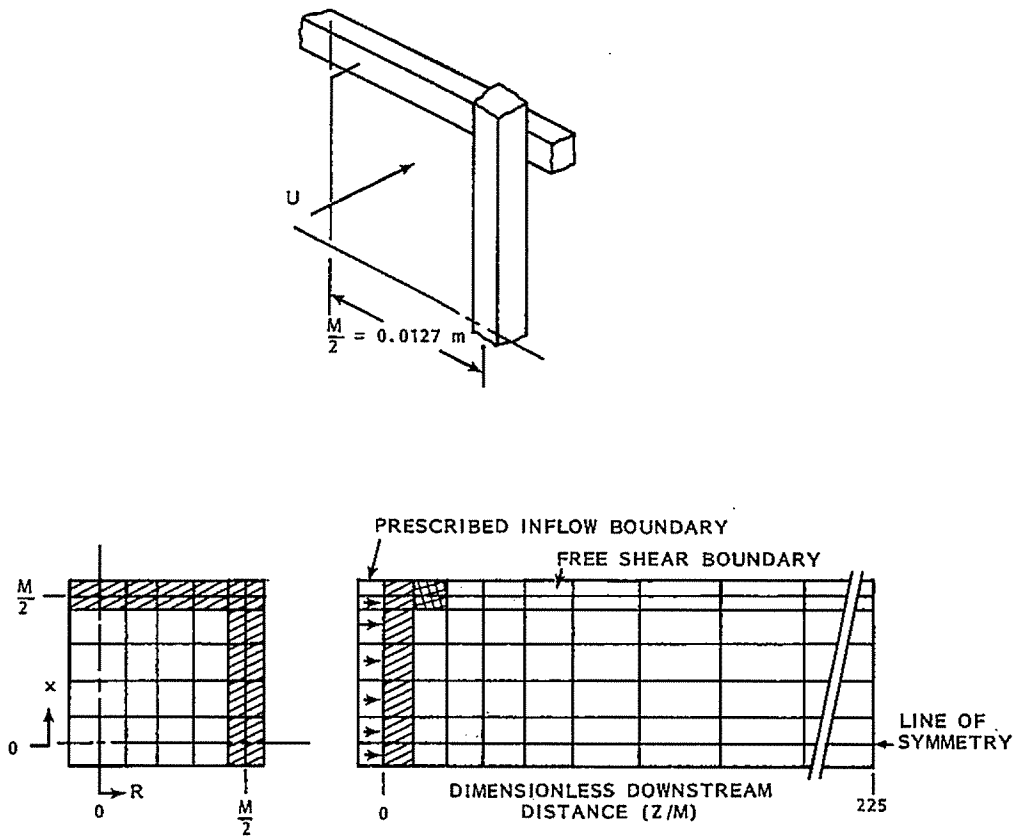


FIGURE 5.2. Square Rod, Square Mesh Grid and Computational Structure - Quarter-Section Symmetry

square rods being modeled in the simulation, and the decay results from dissipation of the turbulence as it is convected downstream.

5.1.4 Momentum Jets

Turbulent momentum jets are flows which have been investigated extensively. A wealth of information from experimental and analytical analyses is available for both planar and round jets issuing into various environments. The $k-\epsilon$ turbulence model has also been applied to jet flows and analyzed extensively.

TEMPEST simulations of planar and round jets were conducted. Comparisons were made to experimental and empirical results of Albertson et al. (1948), Gutmark and Wagnaski (1976), and Wagnaski and Fiedler (1970). Computed results of the TEACH code, which is a two-dimensional steady-state code with a $k-\epsilon$

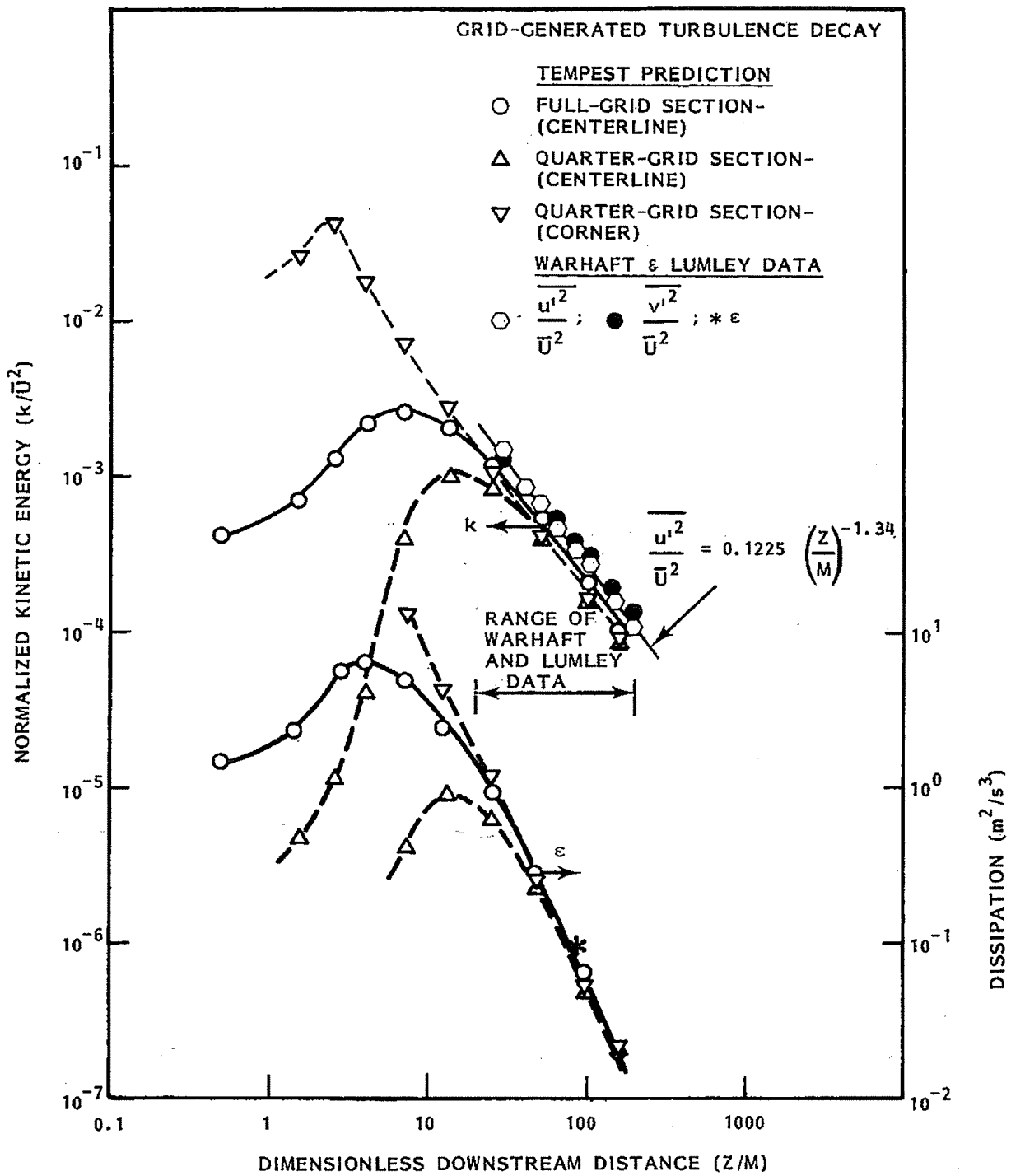


FIGURE 5.3. Comparison of TEMPEST-Predicted, Grid-Generated Turbulence with Data

turbulence model, were also compared. For the TEMPEST simulations, the $k-\epsilon$ model was utilized as coded, and no "knob turning" of model constants to improve results was done.

For both the planar- and round-jet simulations, symmetry was assumed. For the planar jet, symmetry with respect to the centerplane was used, and for the round jet, symmetry with respect to the centerline was used. For each case, 20 computational cells were used in the downstream direction and 20 computational cells were used in the cross-stream direction. Variable-spacing cell structure was also used with smaller cells concentrated in the high-shear regions and near the jet origin. Of the 20 lateral cells, only four were in the jet entrance. As discussed subsequently, four cells in the jet are probably not sufficient to adequately resolve the shear generation. Downstream, the modeled region was only 65 jet widths long.

Planar jet data of Gutmark and Wagnanski (1976) and round jet data of Wagnanski and Fiedler (1970) were used for comparison, as were the results of Albertson et al. (1948). These data were for jet Reynolds numbers greater than 10^4 . The data were obtained with low levels of inlet jet turbulence (less than 0.2 percent turbulence intensity).

Two sets of TEMPEST simulations were conducted to test the sensitivity of the predictions to inlet turbulence conditions. The first set was run with no inlet turbulence and a uniform inlet velocity profile. The second set was run with an inlet profile of turbulence and velocity. This profile was set as if the upstream geometry leading to the jet opening allowed for fully developed channel flow or pipeflow at the jet opening.

Comparison of the TEMPEST predictions of the dimensionless centerline velocity, V_{\max}/V_0 , is shown in Figure 5.4. For the plane jet, the axial distance is normalized to the slot width, B_0 . For the round jet, the jet diameter, D_0 , is used for distance normalization. Also shown in Figure 5.4 are the corresponding empirical correlations that correspond to approximate ranges of data reported.

The plane jet predictions agree reasonably well with the data and empirical curves, while the round jet results are underpredicted, especially in the

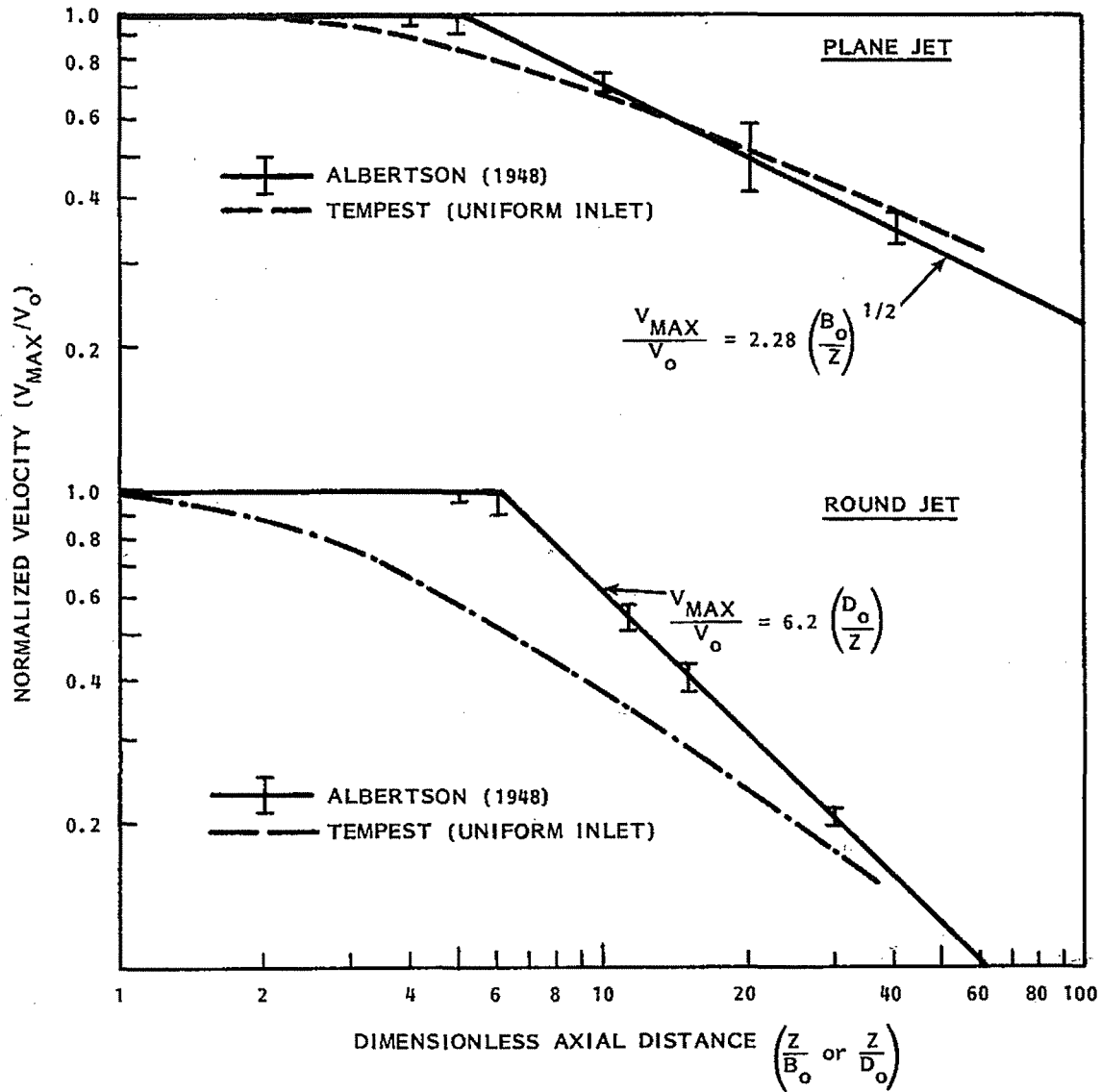


FIGURE 5.4. Momentum Jet Centerline Velocity

potential core region. Both predictions are approaching the asymptotic decay slope at large axial distances.

Figure 5.5 shows a comparison of normalized axial velocity profiles for both jet simulations. For the plane jet, results at two axial positions are shown, $Z/B_0 = 26$ and 52 . At the latter position, fairly good agreement exists between the predictions and Albertson's results. The round jet results show similar agreement at $Z/D_0 = 26$.

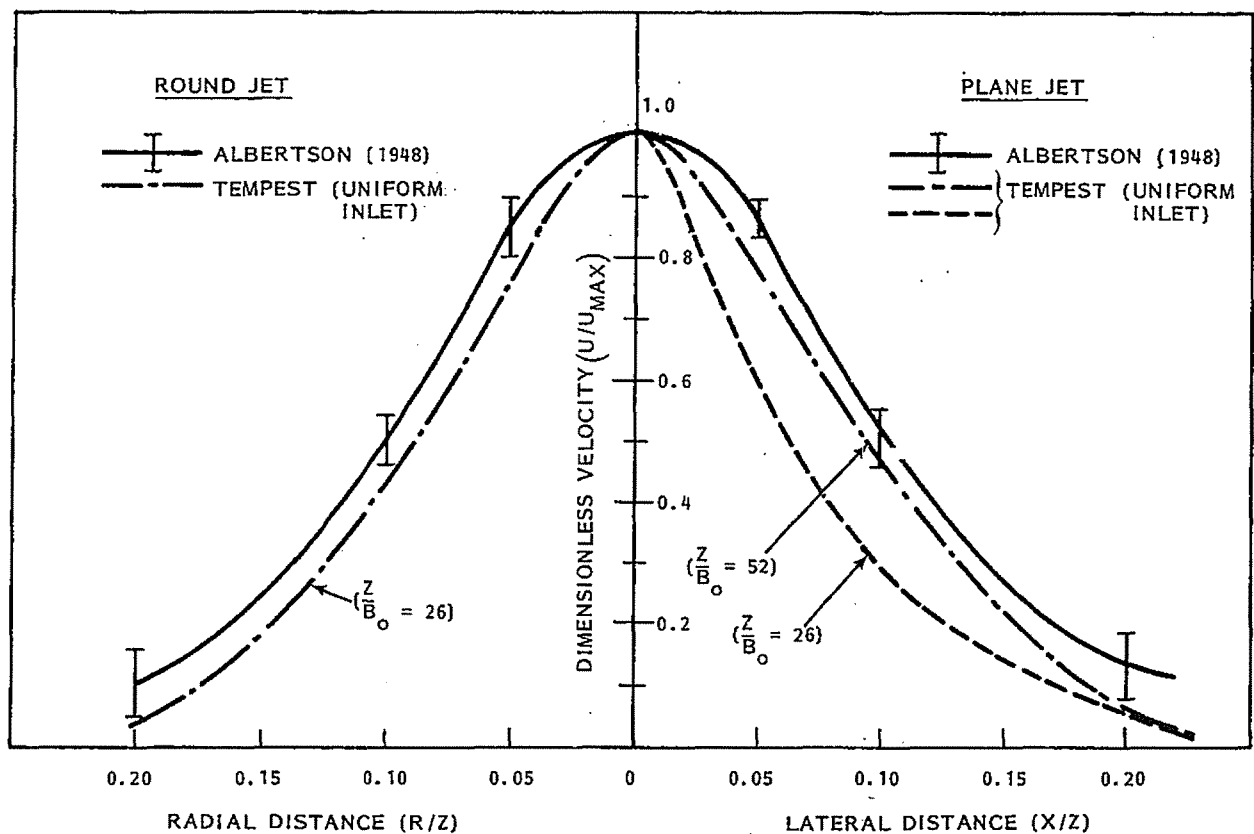


FIGURE 5.5. Momentum Jet Axial Velocity Profiles

The axial velocity profile results and the centerline decay results show the correct jet behavior. Discrepancies exist between the predictions and the data, however. These are most likely due to the node structure. Near the jet entrance, using only four computational cells to accurately model the jet half width does not provide sufficient resolution to model the growth of the shear layer at the jet boundary. This lack of sufficient resolution causes the potential core to be destroyed too quickly, as evidenced in Figure 5.4. The fact that the cylindrical jet core is degraded so rapidly follows directly from this lack of resolution. There is much more shear surface area relative to the jet flow area through which momentum is transferred laterally. Thus the potential core is degraded correspondingly. This same resolution argument applies to the lateral spread of the round jet.

Figure 5.6 shows an additional TEMPEST simulation compared to a TEACH code simulation for a case where inlet profiles of velocity and turbulence were

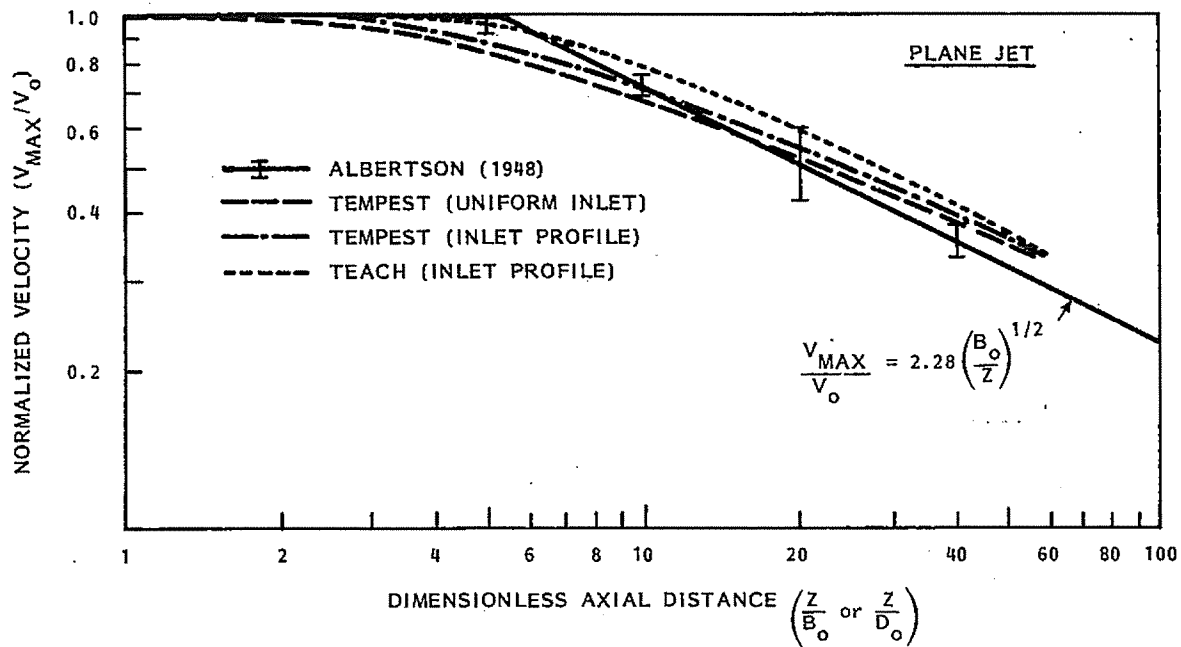


FIGURE 5.6. Decay of Centerplane Velocity Comparison

specified. The inlet conditions were determined based on assuming that the geometry caused the upstream jet to be a fully developed channel flow. The inlet profiles do have an effect on the predicted centerline decay.

Figures 5:7 and 5:8 show the TEMPEST-predicted axial and radial distribution of turbulence intensity in a round jet for the case of no inlet turbulence. Data of Wagnaski and Fiedler are also shown. TEMPEST results along the centerline show the expected peak as the shear layer penetrates the core at $Z/D \approx 6$. At larger axial distances, the predictions are in line with the data as far as the simulation was carried out. The radial profile shows further existence of the lack of node resolution as the turbulence is spread laterally more rapidly than the experimental data show.

5.1.5 Two-Dimensional Plane Channel Flow

Two-dimensional plane channel simulations were run. These simulations were used as a basis for checking turbulent law-of-the-wall-drag boundary conditions, turbulent heat transfer boundary conditions, and subgrid source terms. Hand calculations were performed to ensure that the logic was working

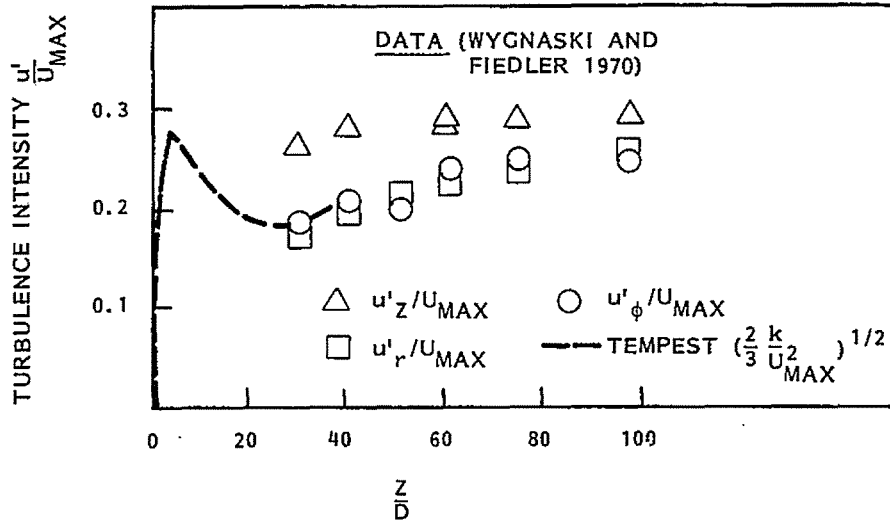


FIGURE 5.7. Axial Distribution of Turbulence Intensity in a Round Jet

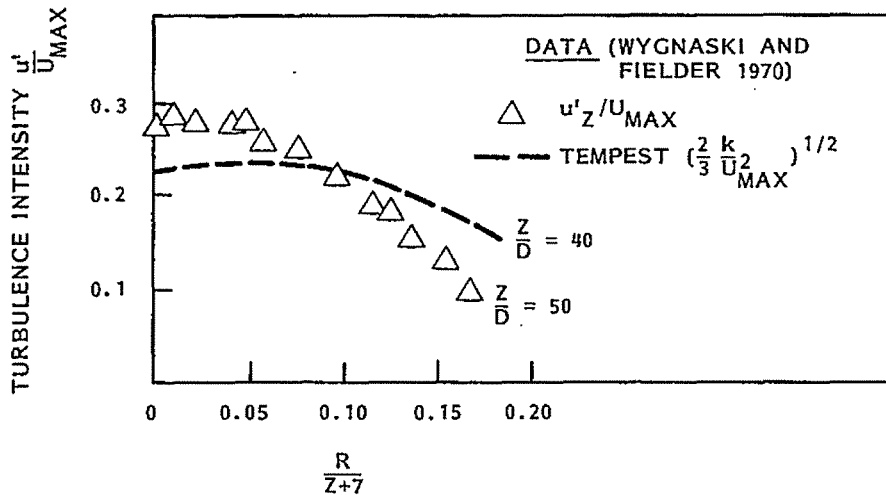
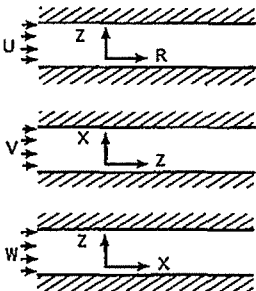
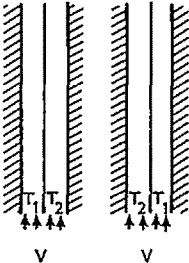
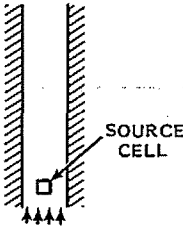
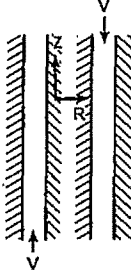


FIGURE 5.8. Radial Distribution of Turbulence Intensity in a Round Jet

correctly for combinations of cell types, boundary conditions, and coordinate directions.

Table 5.1 summarizes the two-dimensional test cases, which were computed with a 10x10 grid and a 10:1 aspect ratio channel. Three coordinate direction tests were run to check computed symmetry across the channel and to check coordinate direction consistency. An isothermal case and two heated cases were run with a centrally located zero-thickness plate. Symmetry, turbulence

TABLE 5.1. Summary of Two-Dimensional, Plane-Channel Test Cases

CASE	SIMULATION	LOGIC CHECKS
<p>COORDINATE DIRECTION TESTS 10 x 10 NODES 10:1 ASPECT RATIO</p>		<ul style="list-style-type: none"> • SYMMETRY • LAW-OF-WALL DRAG • WALL PRODUCTION • CONSISTENCY IN COORDINATE DIRECTION
<p>ZERO-THICKNESS PLATE 10 x 10 NODES 10:1 ASPECT RATIO</p>		<ul style="list-style-type: none"> • SYMMETRY • LAW-OF-WALL DRAG • TURBULENT HEAT TRANSFER
<p>SOURCES 10 x 10 NODES 10:1 ASPECT RATIO</p>		<ul style="list-style-type: none"> • MOMENTUM INJECTION SOURCE • THERMAL INJECTION SOURCE • TURBULENCE PRODUCTION SOURCE
<p>DATA COMPARISON 20 x 20 NODES 100:1 ASPECT RATIO Re ≈ 50,000</p>		<ul style="list-style-type: none"> • SYMMETRY • REVERSED GEOMETRY

boundary conditions, and heat transfer were checked for the plate. Source injection logic was checked for subgrid size momentum, thermal, and turbulence production sources.

A test case using a 20x20 grid in a 100:1 aspect ratio channel was computed for $Re = 50,000$. Constant cell spacing was used. The case was run with the specified flow boundary first on one end and then in the opposite direction on the other end to check the consistency of flow direction. Data from Laufer and Hossain as reported by Rodi (1980) are compared to the TEMPEST predictions in Figure 5.9. The predictions and data are in very good agreement.

The TEMPEST predictions in the 20x20 node simulation were exactly symmetric about the centerline over the whole flow field. A 20x20 node simulation of one-half the plane channel assuming a symmetry boundary was also run.

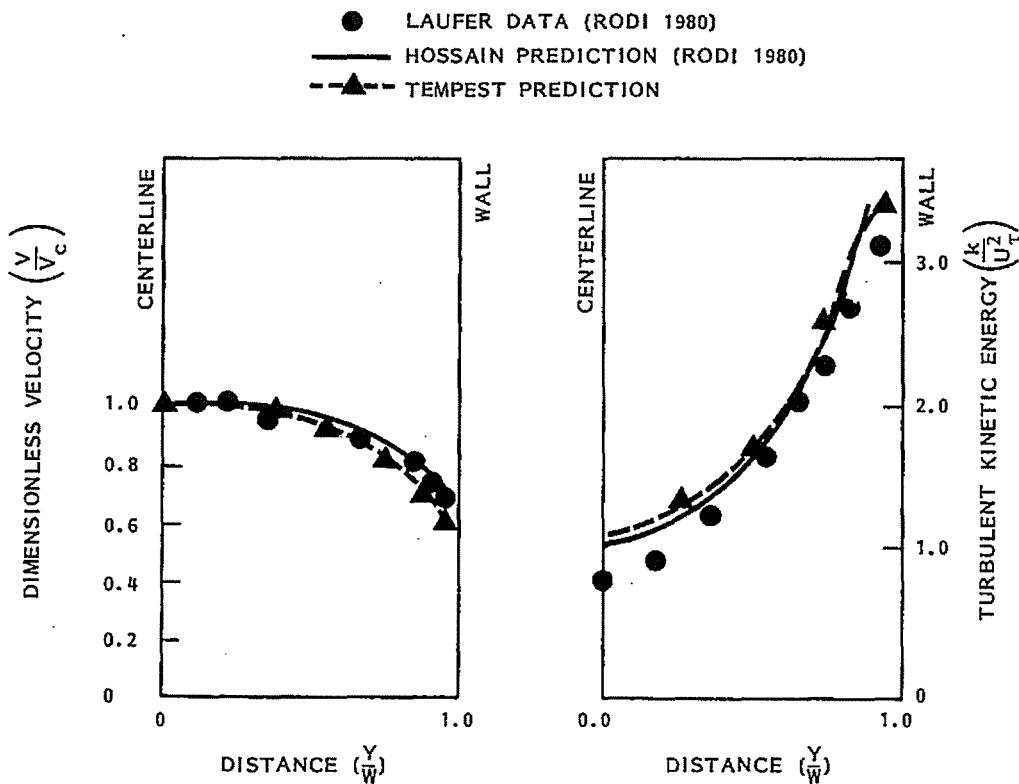


FIGURE 5.9. Comparison of Two-Dimensional, Turbulent-Plane-Channel Data and Predictions

Comparison of the full-channel-width simulation with the half-channel-width simulation is made in Figure 5.10. The two simulations show good agreement for velocity profiles with the centerline value being 0.8 percent different for the two noding structures.

The normalized turbulent kinetic energy profile is also presented in Figure 5.10. The full-channel simulation had eight computational cells in the half channel, and the half-channel simulation had 18 computational cells. Also included are the predicted results of Goldsmith (1981), which used 14 computational cells in a half-channel simulation. Goldsmith's results were compared to the experimental data of Hossain and Rodi (1977) and were found to consistently higher than the data by 10-20 percent except near the centerline. The TEMPEST results are very good agreement with Goldsmith's 14-node results and the data.

5.1.6 Two-Dimensional Pipe Flow

Two-dimensional pipe flow simulations were computed at $Re_0 = 50,000$ and $500,000$ (based on centerline velocity). Results were compared to Laufer's (1954) data for air flow in a pipe at the same Reynolds numbers. Pipe flow simulations at $Re_0 = 100,000$ (based on bulk velocity) were computed using water as the fluid. Data comparisons at this Reynolds number were compared to mercury data from Eyler (1978) and air data from Lawn (1977) at the same Reynolds number. Comparisons were also made with predictions made with the TEACH code and those made by Goldsmith (1981), both of which used a $k-\epsilon$ turbulence model similar to that in TEMPEST.

Figure 5.11 is a composite of the predicted air flow at $Re_0 = 50,000$ and $500,000$ and Laufer's data. Predictions and data for normalized velocities, turbulent viscosity, and turbulent kinetic energy are included in the figure. The TEMPEST predictions were computed using constant cell spacing with 18 radial nodes and 18 axial nodes. Each node had a cell aspect ratio ($\Delta R:\Delta Z$) of 1:200. The total computed L/D was 90. Results are presented at this length. Inlet conditions were specified as constant velocity and no initial turbulence.

To assess node spacing effects, two additional TEMPEST runs were made. One run used only eight constant-width nodes in the radial direction. The other

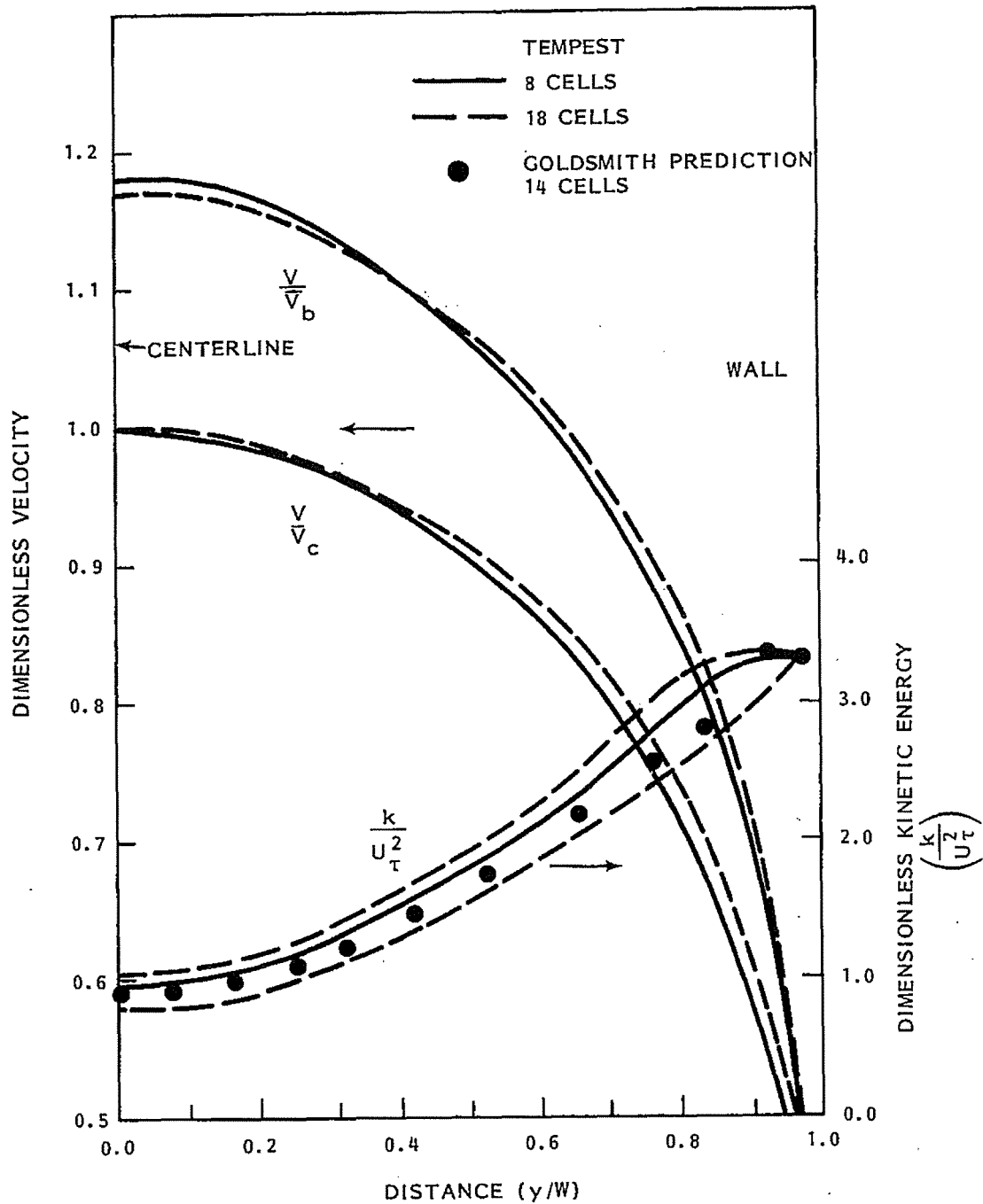


FIGURE 5.10. Two-Dimensional, Plane-Channel Velocity Profiles

used 18 constant-width nodes in the radial direction and variable spacing in the axial direction. The axial cell widths were gradually increased in the downstream direction. For this simulation at an $L/D = 90$, the computed

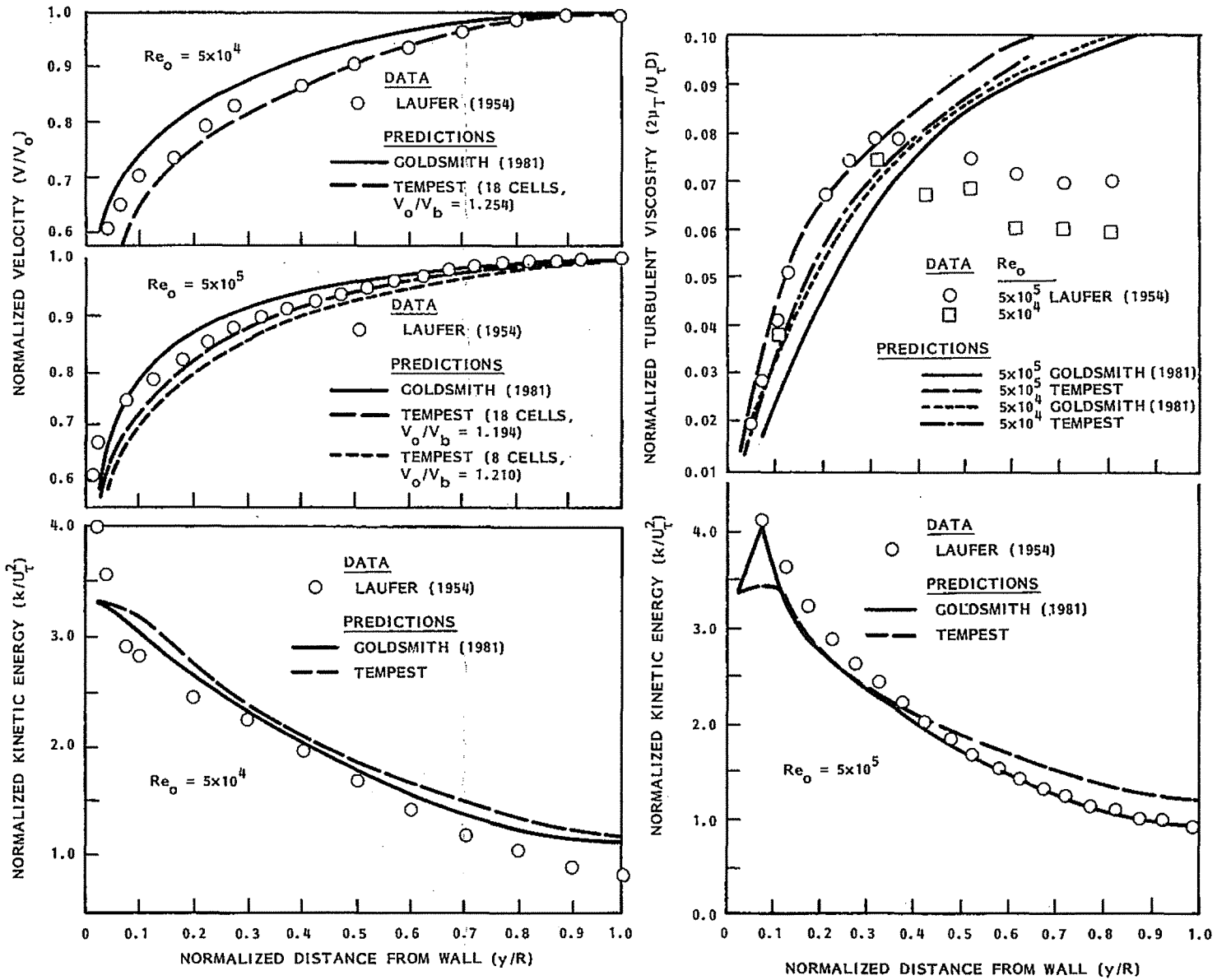


FIGURE 5.11. Comparison of Turbulent Air Flow in a Pipe at $Re_0 = 5 \times 10^4$ and 5×10^5

centerline velocity was identical (to four digits) to that of the case with constant axial cell spacing. In the developing entry length, there were computed differences in centerline velocities due directly to resolution. In the fully developed region, inlet conditions and entry length effects should not affect the radial profiles. This was confirmed by the agreement of the two axial-cell-spacing configurations.

In Figure 5.11, the TEMPEST predictions of the normalized velocity profile are in good agreement with Laufer's data for $y/R > 0.3$. Closer to the wall, the TEMPEST predictions fall below the data. Goldsmith's predictions consistently overpredict the data except very close to the wall at the higher Reynolds number. For the TEMPEST simulations with 8 and 18 radial nodes, there is less than a one-percent difference in the centerline velocity.

The TEMPEST predictions for turbulent viscosity are in good agreement with Laufer's data at both Reynolds numbers for $y/R < 0.5$. Near the centerline of the pipe, the turbulent viscosity is overpredicted. The turbulent kinetic energy profiles shown in Figure 5.11 are also in good agreement with the data.^(a) The predicted kinetic energy profiles at $Re_0 = 500,000$ deserve additional comment.

Goldsmith's prediction shows a marked peak at $y/R = 0.1$ which neither TEMPEST nor the data show. This peak is a direct consequence of the boundary conditions to the kinetic energy transport equation. Goldsmith did not solve the kinetic energy equation in the cell next to the wall. Rather, the value of turbulent kinetic energy was specified in that cell with the expression

$$\frac{1}{(C_\mu)^{1/2}} \left(\frac{\tau_w}{\rho} \right) \quad (5.1)$$

where τ_w/ρ was determined from a modified law-of-the-wall model based on local tangential velocity and turbulence quantities.

(a) Laufer's data for kinetic energy is the sum of measured components $\overline{u'^2}$, $\overline{v'^2}$ and $\overline{w'^2}$.

In early modeling efforts with TEMPEST the same approach was taken, and a very similar peak in the kinetic energy profile resulted. While this approach was satisfactory in a few flows, it was not generally applicable. TEMPEST computes kinetic energy in the wall cell using a sink term which is proportional to an integrated average of the local dissipation. This approach has been found to be much more general in its application, not only in TEMPEST but in other codes as well.

Additional pipe flow comparisons of TEMPEST and TEACH code predictions were made with the mercury pipe flow data of Eyler (1978) for $Re_b = 100,000$ and the average of data reported by Lawn (1977) for $3.5 \times 10^4 < Re_b < 25 \times 10^4$. A sample of results is included in Figure 5.12. Agreement between predictions and data is very good, which further supports the correctness of the logic solution algorithm and modeling approaches used in TEMPEST.

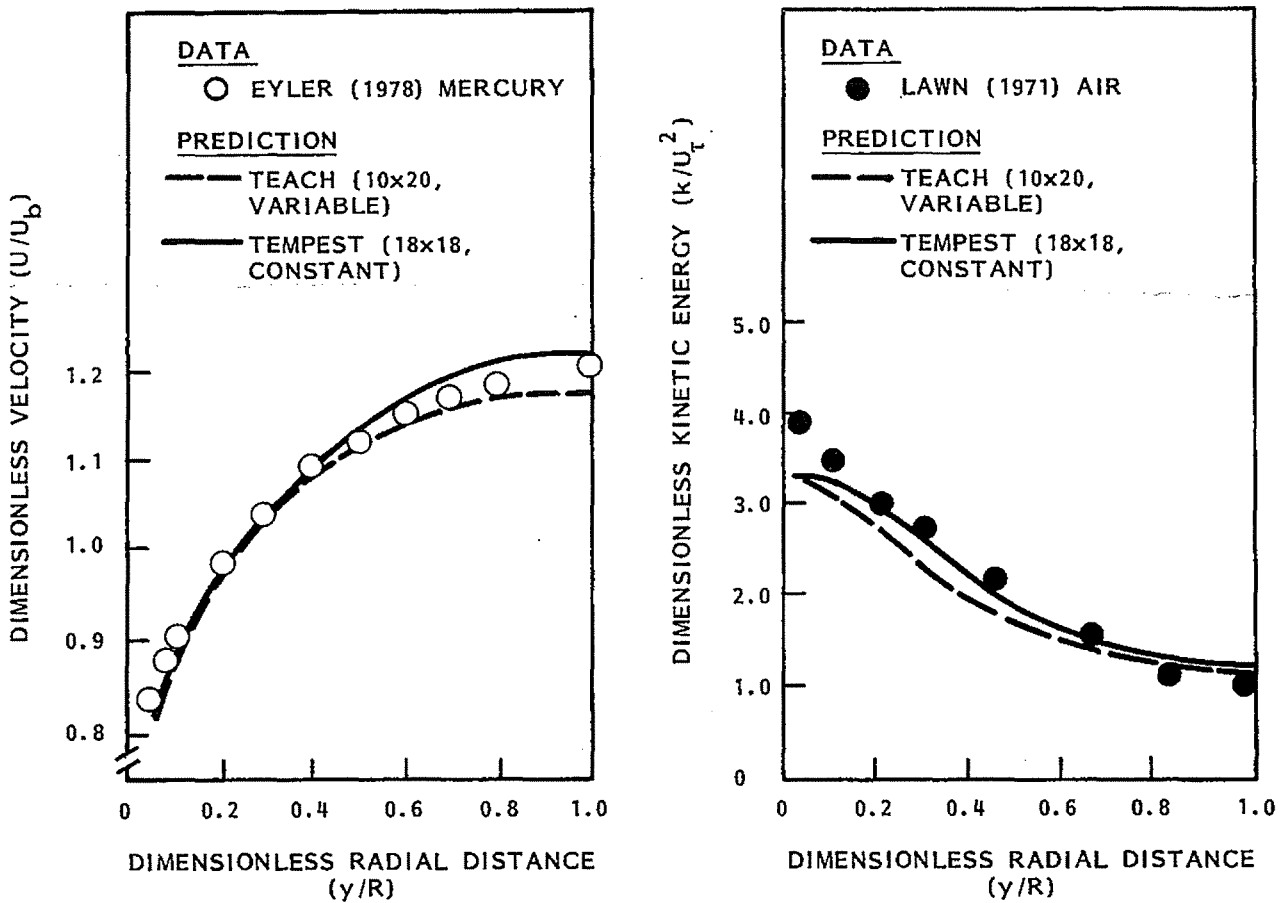


FIGURE 5.12. Turbulent Pipe Flow, Comparison of TEMPEST and TEACH Results

5.1.7 Three-Dimensional Scaled Breeder Reactor Upper Plenum Model

The TEMPEST code was used to conduct a numerical simulation of the steady-state flow conditions measured by Chen and Golay (1977) and Boyle and Golay (1980) in the Fast Flux Test Facility (FFTF) upper plenum model. Two- and three-dimensional (2D and 3D) simulations were conducted with constant and variable mesh spacing. Table 5.2 lists pertinent flow and numerical simulation parameters. A schematic of the test geometry is shown in Figure 5.13.

The node structure used for the simulations of the constant-mesh-spacing centerplane with the TEMPEST and TEACH codes is shown in Figure 5.14. Figure 5.15 shows the noding structure for the variable-mesh-spacing simulations used for the TEMPEST simulations. The 3D variable case used the same R-Z variable grid spacing as the 2D variable case. The X-direction noding is also shown in Figure 5.15. The constant mesh spacing was set up such that data measurement locations, indicated by the open circles in Figure 5.14, occurred at cell center locations where scalar quantities are predicted. In the numerical solution scheme, velocities are predicted at cell faces and, hence, are necessarily offset from the data measurement points. The structure of the variable mesh spacing was set up to better describe particular regions where velocity gradients are significant. These include the shear layer directly above the chimney wall and the channel walls.

A comparison of 2D, constant-mesh-spacing predictions with Chen and Golay's (1977) data is shown in Figures 5.16 and 5.17. In Figure 5.16, vertical velocity data, measured at horizontal planes $Z = 8.1$ cm and $Z = 17.6$ cm,

TABLE 5.2 FFTF Scale Model Flow and Simulation Parameters

<u>Data Source</u>	<u>Rev</u>	<u>Simulation</u>	<u>Nodes</u>	<u>Mesh</u>	<u>Code</u>
Chen and Golay (1977)	70,000	2D, Centerplane	18 x 26	Constant	TEACH
Chen and Golay (1977)	70,000	2D, Centerplane	18 x 26	Constant	TEMPEST
Boyle and Golay (1980)	70,000	2D, Centerplane	18 x 26	Constant	TEMPEST
Boyle and Golay (1980)	70,000	2D, Centerplane	18 x 26	Constant	TEACH
Boyle and Golay (1980)	70,000	2D, Centerplane	20 x 20	Variable	TEMPEST
Boyle and Golay (1980)	70,000	3D, Qtr Section	20 x 20 x 6	Variable	TEMPEST

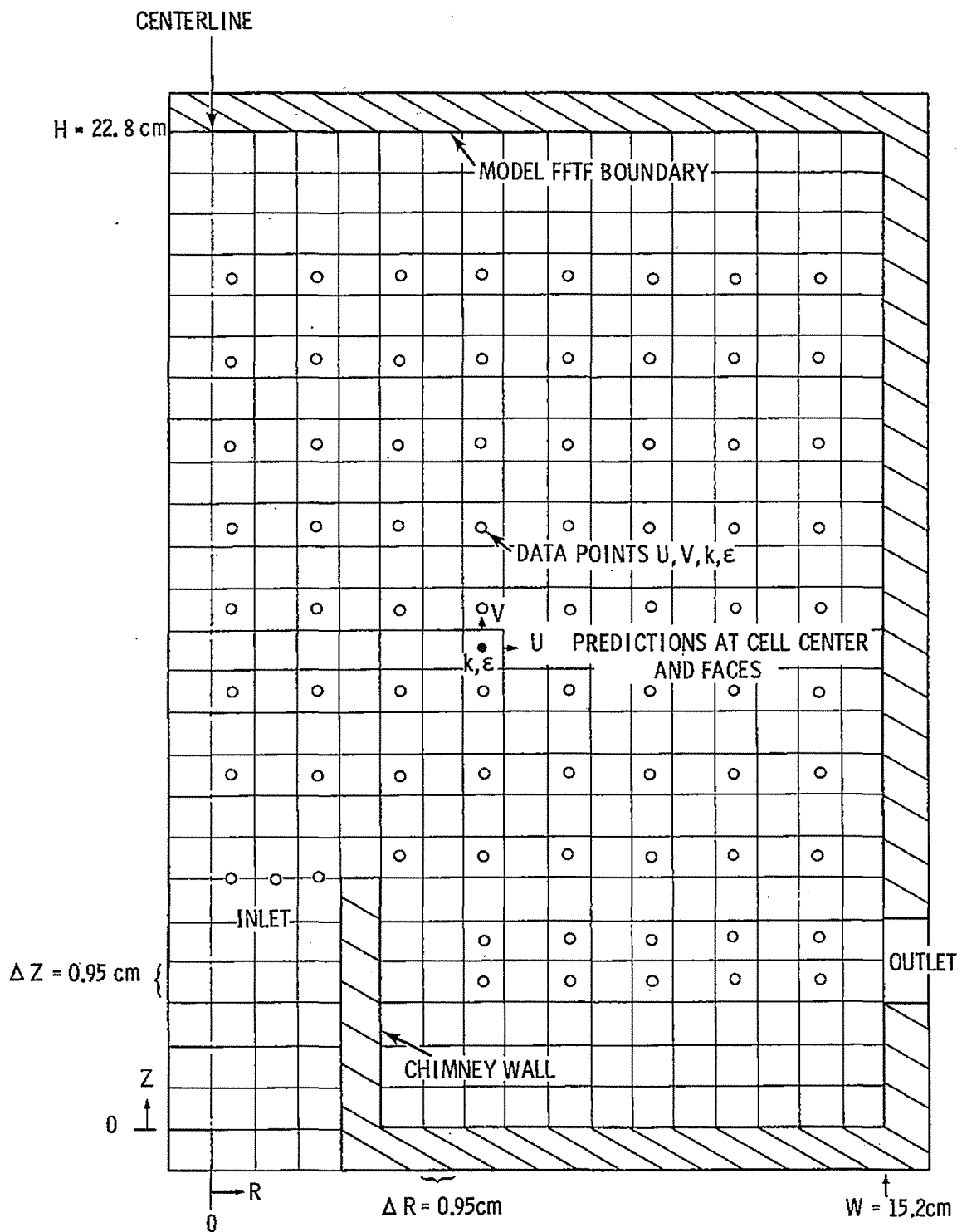


FIGURE 5.14. FFTF Scaled Model with Constant-Mesh Noding Structure

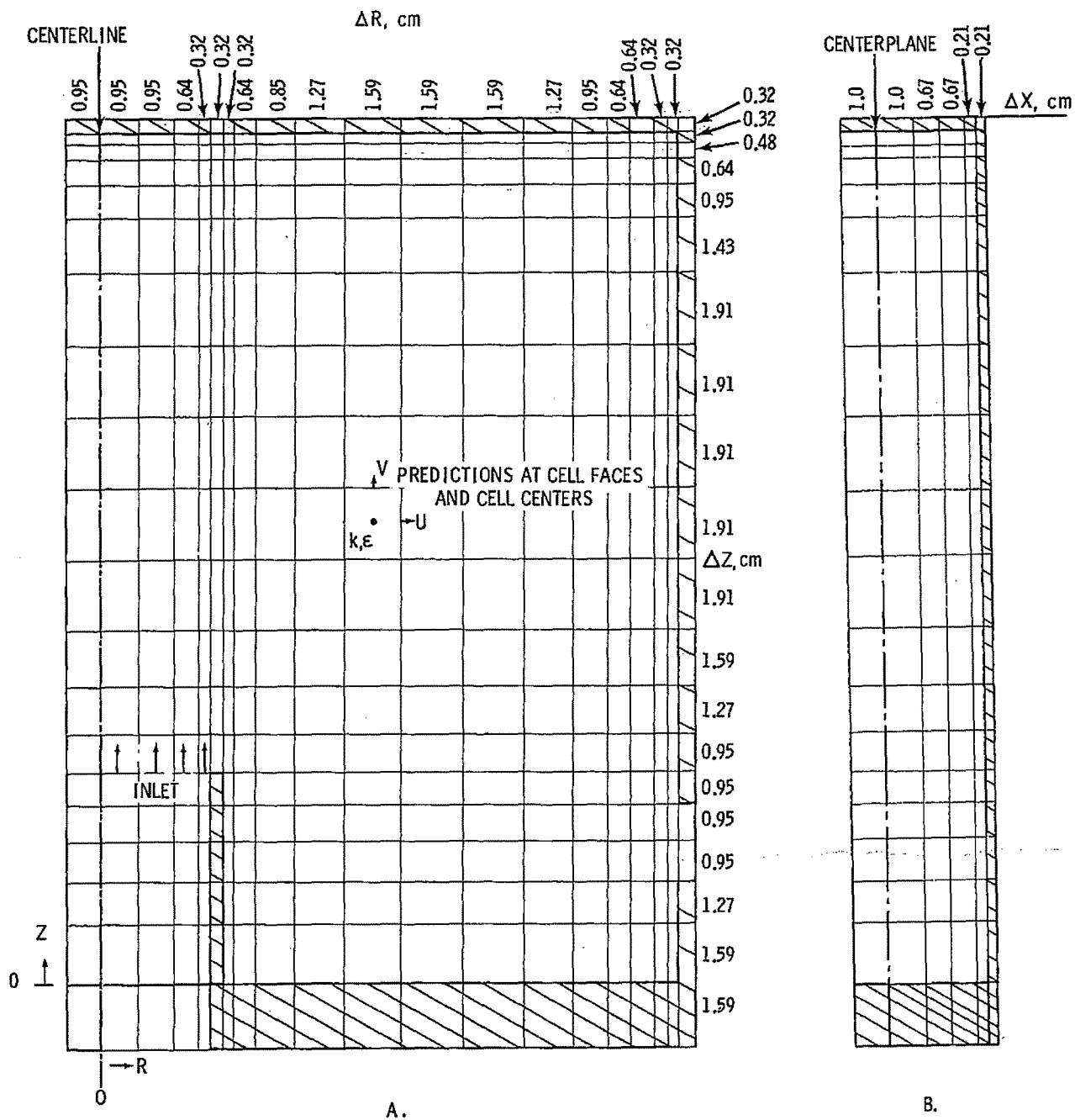


FIGURE 5.15. Variable-Mesh Noding Structure: A) 2D and 3D Centerplane, B) 3D Depth Plane

This observation is borne out by the magnitudes of the predicted horizontal velocity, which are almost linearly scalable along positions between the two measured data planes.

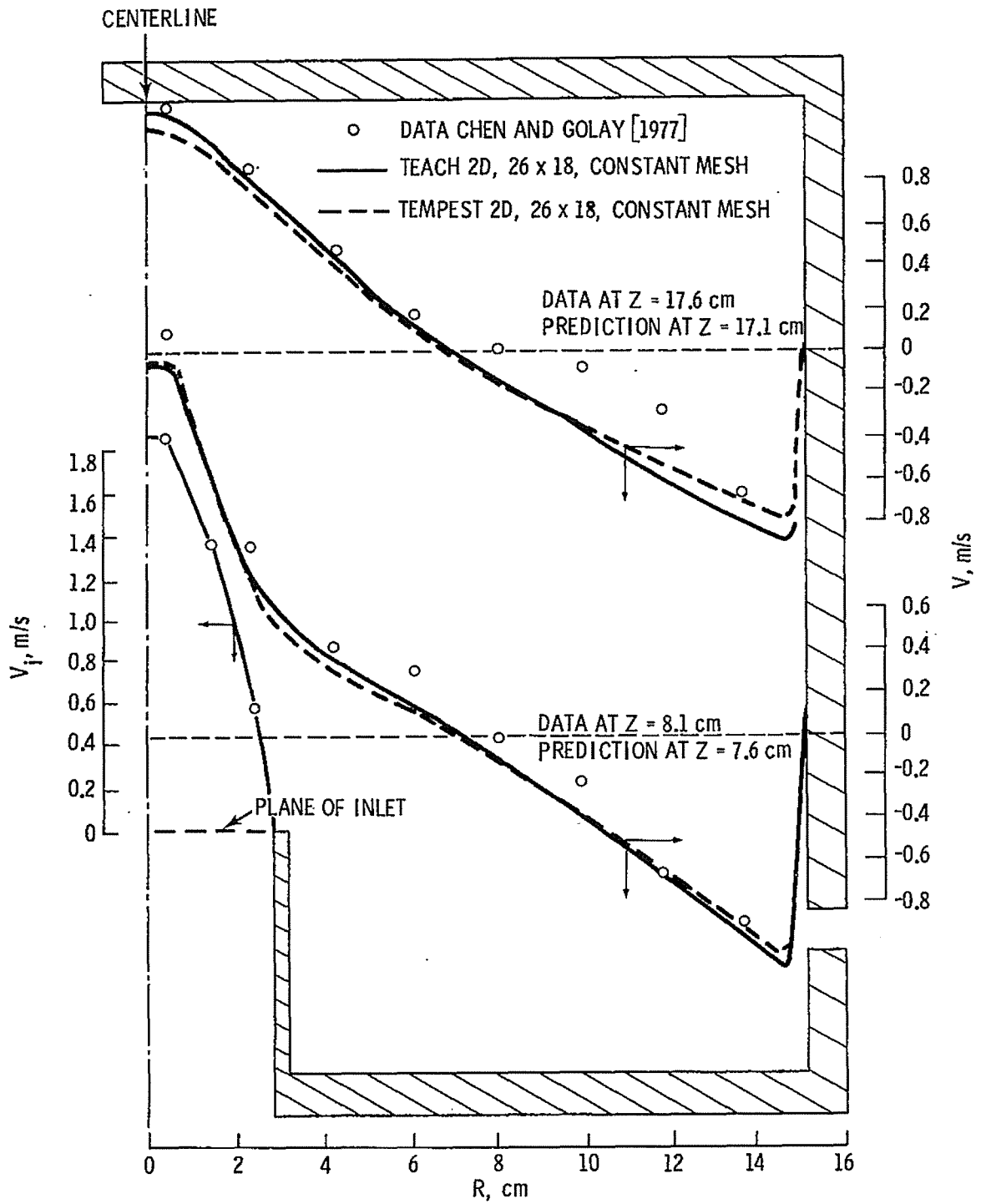


FIGURE 5.16. Mean Vertical Velocity at Two Horizontal Planes

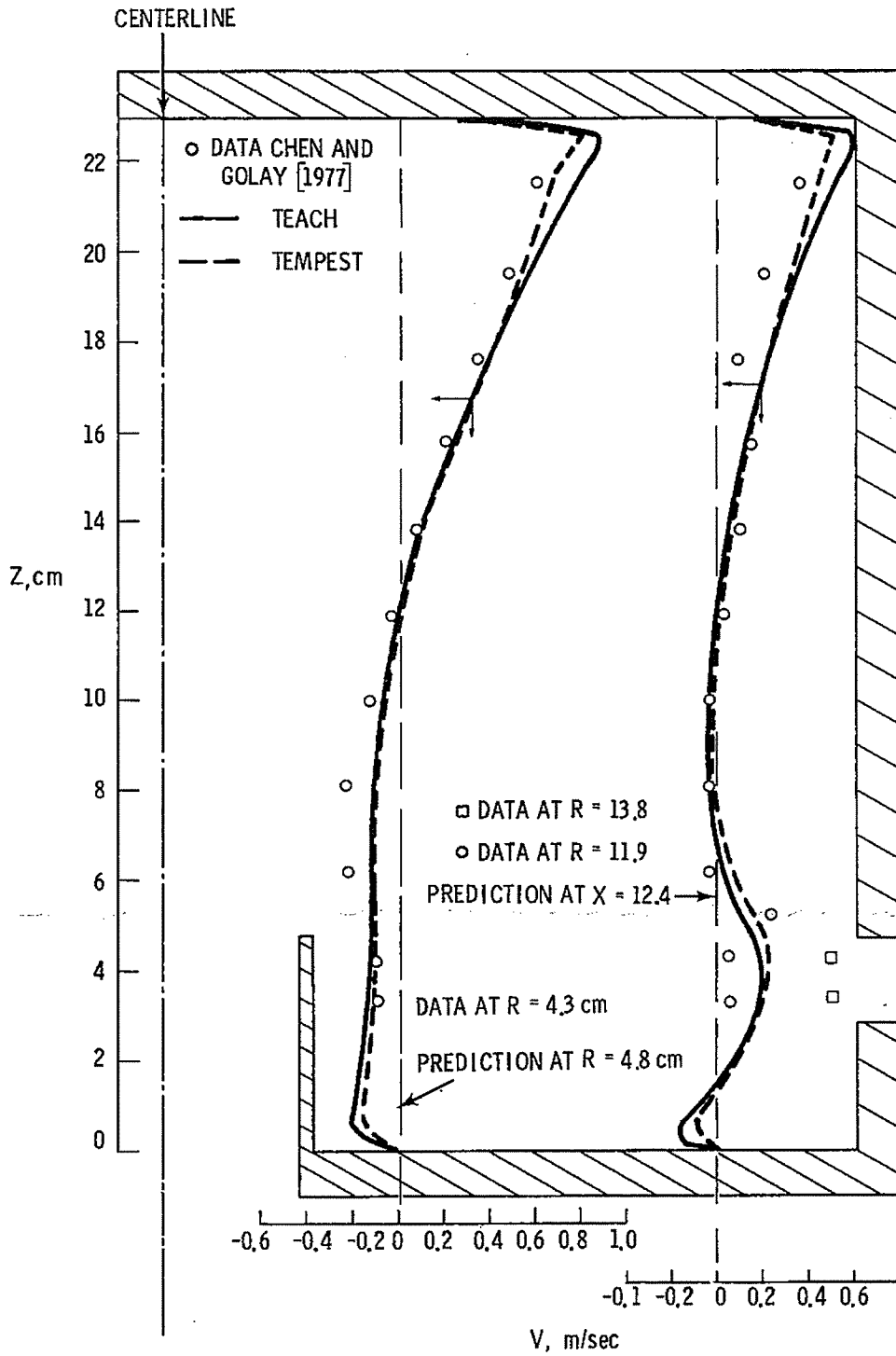


FIGURE 5.17. Mean Horizontal Velocity at Two Vertical Planes

The turbulent kinetic energy is compared in Figure 5.18 at two horizontal planes. These data and predictions are at the same horizontal plane positions, $Z = 8.1$ cm and 17.6 cm. It should be pointed out that Chen and Golay (1977) only measured two fluctuating components of the turbulent kinetic energy, u' and v' . They calculated the turbulent kinetic energy as

$$k = \frac{1}{2} (\overline{u'^2} + \overline{v'^2})$$

after making the assumption that the third fluctuating component was small, and neglecting it in calculating the kinetic energy would represent perhaps a 5% error in k .

The agreement between the two code predictions is very good, as shown in Figure 5.18. However, the predictions are not in very good agreement with the data. They significantly overpredict the turbulent kinetic energy over most of the flow field.

Available measured inlet conditions were used for inlet boundary conditions to the code predictions. This included the measured inlet vertical velocity distribution and inlet kinetic energy distribution. The horizontal velocity at the inlet was measured and was typically an order of magnitude less than the vertical inlet velocity. For the code predictions, it was assumed to be zero at the inlet plane. This assumption would have only a minor effect on the predictions, and would show up as a slightly altered spread rate of the jet region directly above the inlet chimney wall. In any case, the resolution (i.e., number and position) of the data in this region is insufficient for comparison with the predictions.

Dissipation was not measured by Chen and Golay (1977). Therefore, the code simulations used a uniform value based on an assumed equilibrium of production and dissipation at the inlet plane. However, as will be discussed subsequently, this assumption is not particularly valid for the experimental inlet configuration used.

Analysis of the measurements of Chen and Golay (1977) and the geometrical configuration of the experiment has led to several conclusions regarding the

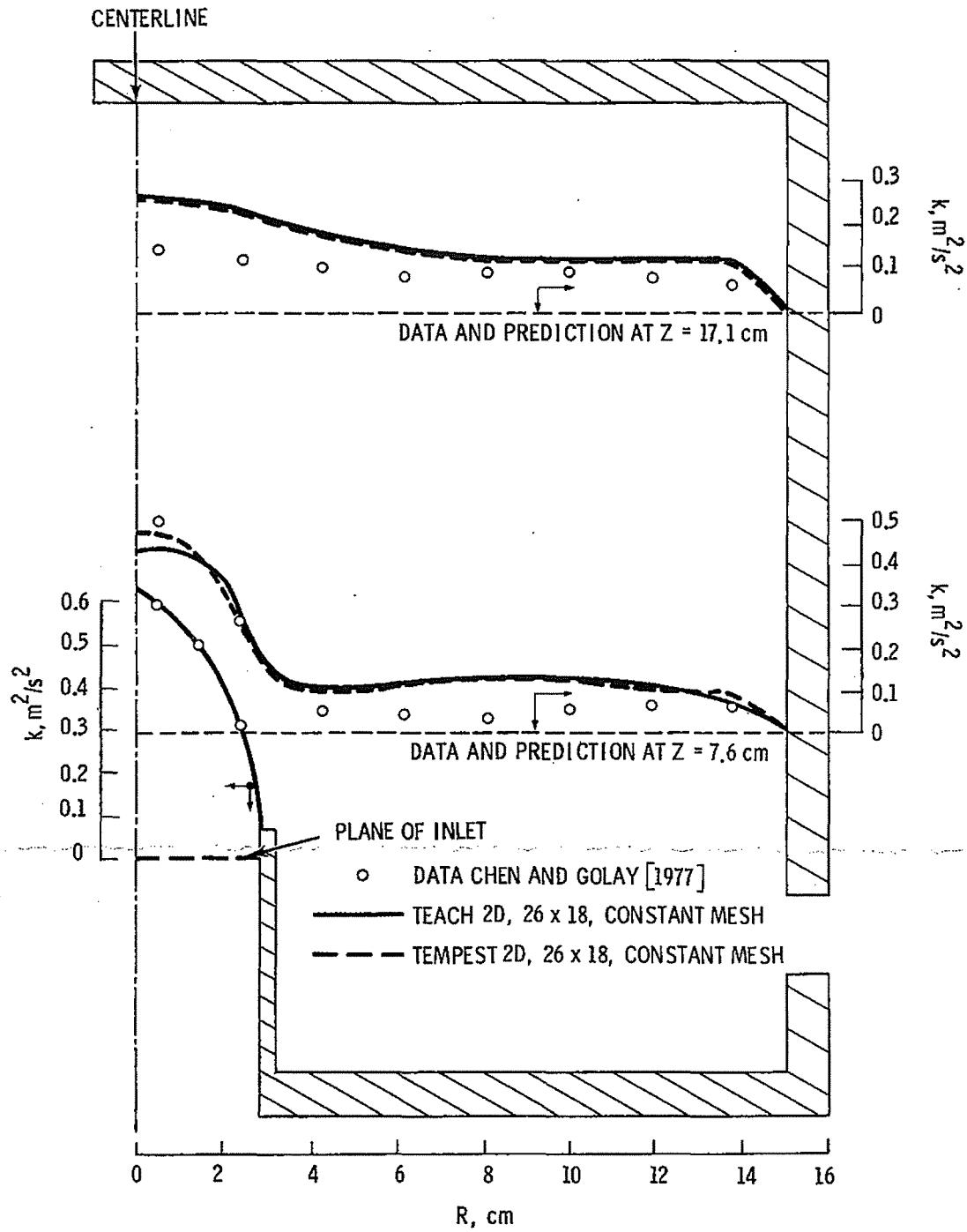


FIGURE 5.18. Comparison of Experimental and Predicted Data for Centerplane Kinetic Energy with Constant Grid Spacing

accuracy of the data. Principally, it can be concluded that the inlet geometry, which was a relatively short, parallel channel, did not allow for sufficient development of uniform inlet conditions. In addition, measurements were only made in the centerplane between the front and back walls, and mass balances at a given horizontal plane were not very good. This can be seen by the data shown at plane $Z = 17.6$ cm in Figure 5.17. Such mass balance errors, coupled with the nonuniform inlet distribution, raises the question as to how uniform the flow was dividing between the two reportedly symmetric valves of the test section. The measurements made were insufficient to answer these questions. Similarly, the measurements made were insufficient to quantify three-dimensional effects in the test section. These and other problems led Boyle and Golay (1980) to modify the flow system and test section, and to repeat a number of Chen and Golay's (1977) experiments.

The primary experimental modifications made included changing the inlet structure and incorporating flow equalization valves on the exit flow from either half of the symmetric test section. Modification of the inlet structure included putting screens in the lower inlet structure (see Figure 5.13) in an attempt to evenly distribute inlet flow and to provide a uniform turbulence field at the inlet plane at the top of the chimney. This modification was largely successful. Exit flow control valves were installed to provide uniformly split flow into each of the two symmetric test section valves. However, no flow meters were installed on each exit to ensure a uniform split. Rather, laser-Doppler anemometer (LDA) measurements of the horizontal velocity in the vertical centerplane were used to determine if a net zero flow existed at the plane.

It should also be pointed out that, as with the former work, Boyle and Golay (1980) only measured vertical and horizontal flow components. Measurements were made only in the centerplane between the front and back plates. The third component of fluctuating velocity was again assumed to be negligible in determining the kinetic energy. Dissipation was not measured. Even with these shortcomings, Boyle and Golay's data is very useful for comparing steady-state turbulence model predictions.

A more detailed computer simulation analysis of Boyle and Golay's data was conducted. This included determining the effect of the numerical grid spacing and the effect of modeling the flow field in two and three dimensions. A detailed analysis of the effect of specifying the level of inlet dissipation was also conducted. This latter effect was investigated first as it is perhaps the most significant with respect to adequately predicting the turbulence field values.

It was pointed out previously, as well as having been concluded by Chen and Golay (1977) and Boyle and Golay (1980), that the prescription of inlet conditions is very important to being able to predict the turbulent flow field. This is particularly true for the turbulent kinetic energy and the turbulent dissipation of kinetic energy. Since measurements of the inlet velocity and kinetic energy were made, these could be used as prescribed inlet conditions. However, use of the k - ϵ turbulence model also requires the specification of a boundary condition for inlet dissipation. The importance of its level can be seen in Figures 5.19 and 5.20.

In Figure 5.19, the predictions made using a 2D simulation with the TEMPEST code and constant mesh spacing are compared to measured kinetic energy values. The comparison is made for a vertical plane along the symmetry plane above the chimney. The magnitude of the kinetic energy is plotted on the horizontal axis, and the position is plotted on the vertical axis. The inlet kinetic energy is a measured value, and the expression used for inlet dissipation is:

$$\epsilon_i = \frac{0.08 k_i^{3/2}}{y_{wall}} \quad (5.2)$$

In this expression, which is reportedly valid for relating dissipation to kinetic energy in homogeneous flow, k_i is the inlet kinetic energy and y_{wall} is the distance from the chimney wall. It is apparent in Figure 5.19 that this expression significantly underpredicts the dissipation. This is evident from the predicted buildup or increase in kinetic energy above the chimney inlet. In the region directly above the inlet, where minimal velocity gradients occur, production of kinetic energy should be minimal and dissipation should be

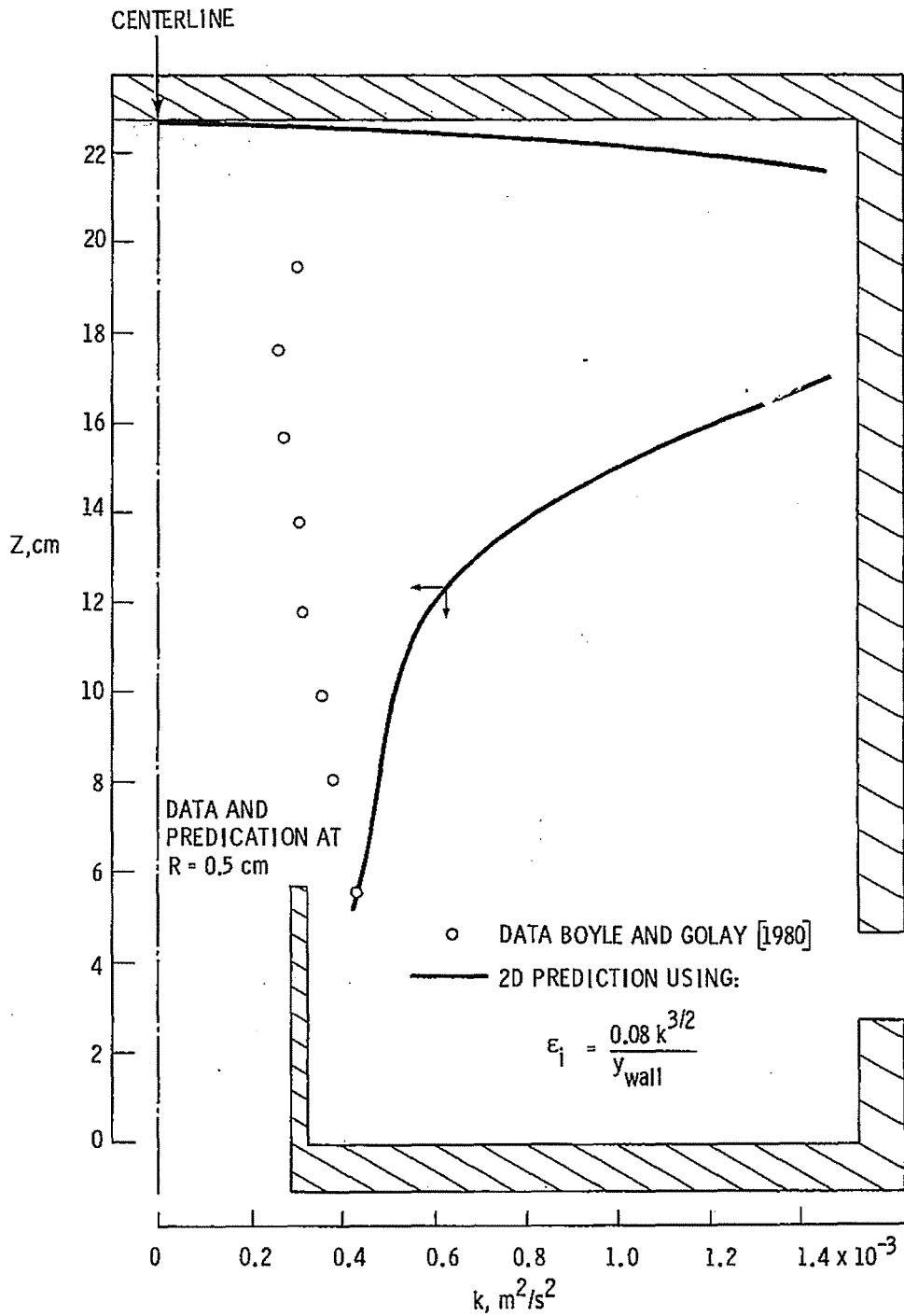


FIGURE 5.19. Vertical Profile of Kinetic Energy at the Centerline Above the Inlet Chimney

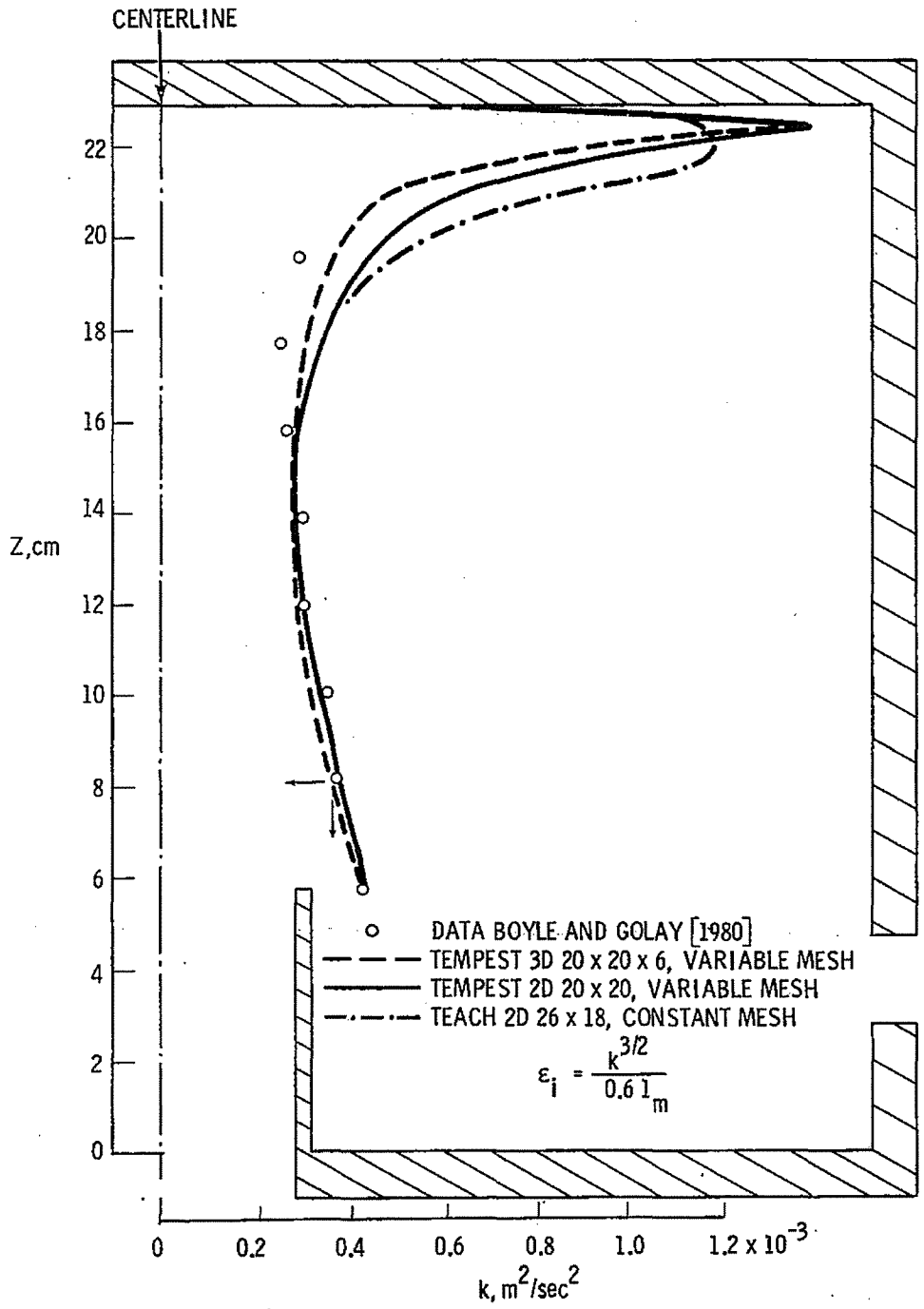


FIGURE 5.20. Vertical Profile of Kinetic Energy at the Centerline Above the Inlet Chimney

sufficient to decrease the level of turbulence. The data shows this decreasing trend.

The physical geometry of the test section is such that a decreasing kinetic energy trend is expected, since this region directly above the chimney inlet is similar to a decaying jet flow. The decaying trend might be expected to exist up to a point where turbulence production, due either to the mixing layer shear action caused by the chimney wall or the effect of the front and back plate, diffuses into the jet core.

Recognizing the deficiency of Equation (5.2), an alternate expression reported by Sha and Launder (1977) was used. Their expression is:

$$\epsilon_i = \frac{k^{3/2}}{C \ell_m} \quad (5.3)$$

where C is a constant equal to 6.0, and the length scale is essentially the Prandtl mixing length, or:

$$\ell_m = \text{MIN} \left\{ \begin{array}{l} 0.42 y \\ 0.1 \delta_{\text{wall}} \end{array} \right\} \quad (5.4)$$

Although prescribing inlet dissipation based on Equation (5.3) improved the comparison shown in Figure 5.19, it still was insufficient.

An alternative expression was finally used after analysis of the inlet structure led to the conclusion that no direct method existed for prescribing inlet dissipation. Thus, it was assumed that an expression like Equation (5.3) was valid but that the constant in the denominator must be varied. Ultimately it was found that, by using a constant of 0.6, sufficient dissipation could be prescribed to predict a decaying turbulent kinetic energy trend above the inlet.

Figure 5.20 shows the predicted results for the kinetic energy above the chimney using $C = 0.6$ (the rest of the results reported here were obtained using this value). Also shown are predictions using both 2D and 3D simulations with constant and variable mesh spacing. The data and predictions agree quite well. The 3D results appear to yield slightly better agreement near the uppermost measured data point. Unfortunately, no data were measured near

enough to the upper wall to compare with the peak in predicted kinetic energy there.

It should be noted that the variable-mesh-spacing cases shown in Figure 5.20 appear to provide significantly better resolution of the peak intensity near the upper wall. In the case of the constant mesh spacing, the maximum value occurs in the computational cell nearest the wall or boundary cell. In the variable mesh spacing cases, the maximum value is in the second cell into the fluid region, and the boundary cell is in the viscous sublayer. The fact that the magnitude of the peak for both the mesh cases is very nearly the same indicates that the modified log-law boundary condition commonly applied to the $k-\epsilon$ level of turbulence model works quite adequately for this case.

In Figure 5.21, the vertical velocity prediction is compared to data in the centerline symmetry plane above the chimney. Again, the 3D, variable-mesh-spacing case provides the best agreement with the data up to the uppermost point measured by Boyle and Golay (1980). Also shown in the figure is one additional data point, which was reported in the appendix of Boyle and Golay's report. This data point is one of a planar set of data at $Z = 21.4$ cm measured to determine the three-dimensional flow effects in the testing section. Unfortunately, this data point does not seem to follow the trend of the rest of the data. A discussion of the anomalous data point and three-dimensional flow measurements is presented subsequently in the section.

Other velocity field results for the constant- and variable-mesh simulations were found to be in very good agreement with data measured in the center-plane over most of the field. Two regions where the most disagreement occurred was in the mixing layer shear region directly above the chimney wall and in the fluid accelerating region near the exit. Because the data were measured in a uniform arrangement (see Figure 5.14), insufficient detail was available to determine which numerical simulation provided the best agreement. However, the variable-mesh-spacing results, qualitatively, seemed to resolve the regions of greatest discrepancy.

As far as predicting the turbulence field, the 3D variable mesh spacing generally provides the best agreement with data. Figure 5.22 compares several

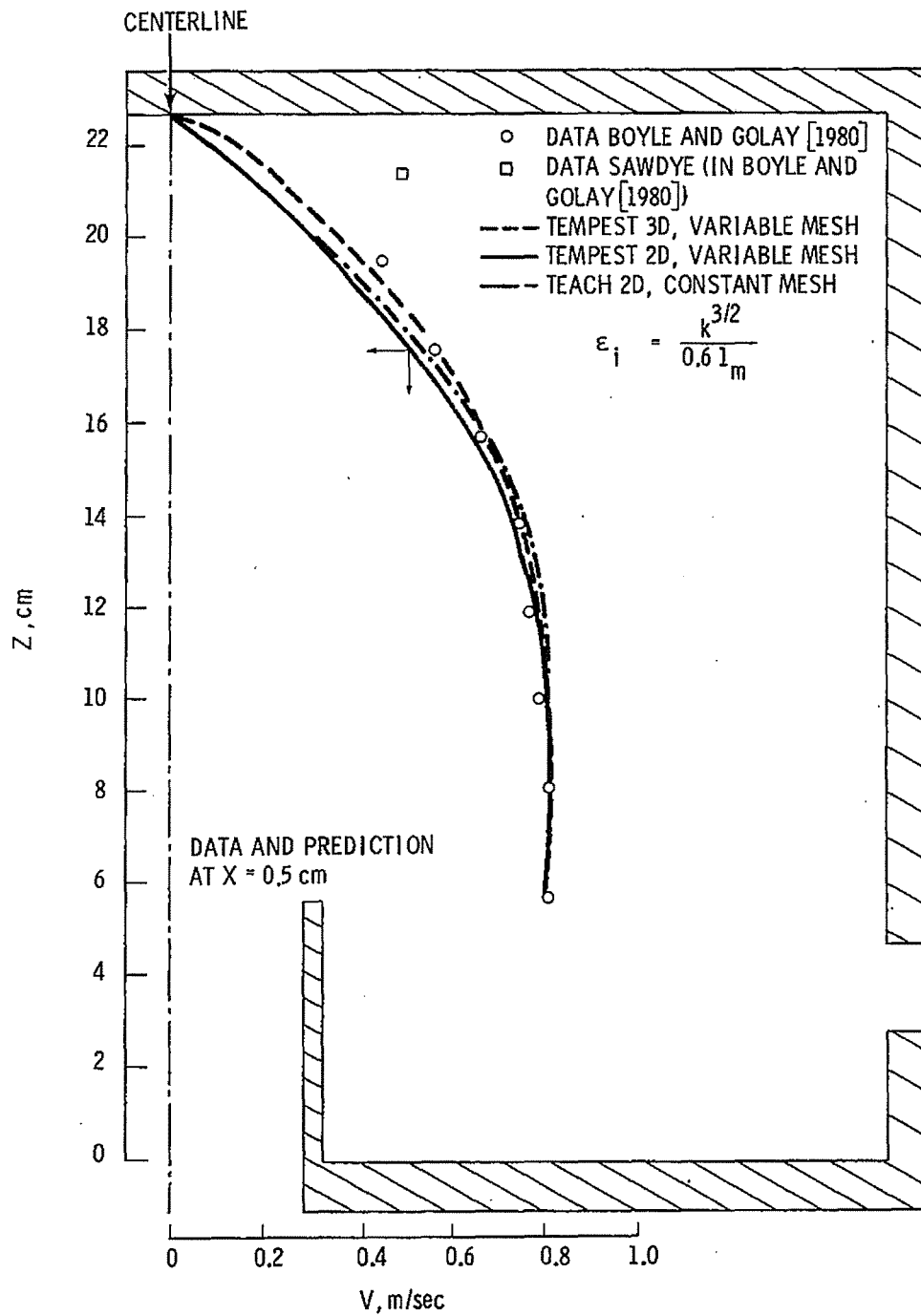


FIGURE 5.21. Vertical Profile of Mean Vertical Velocity at the Centerline Above the Inlet Chimney

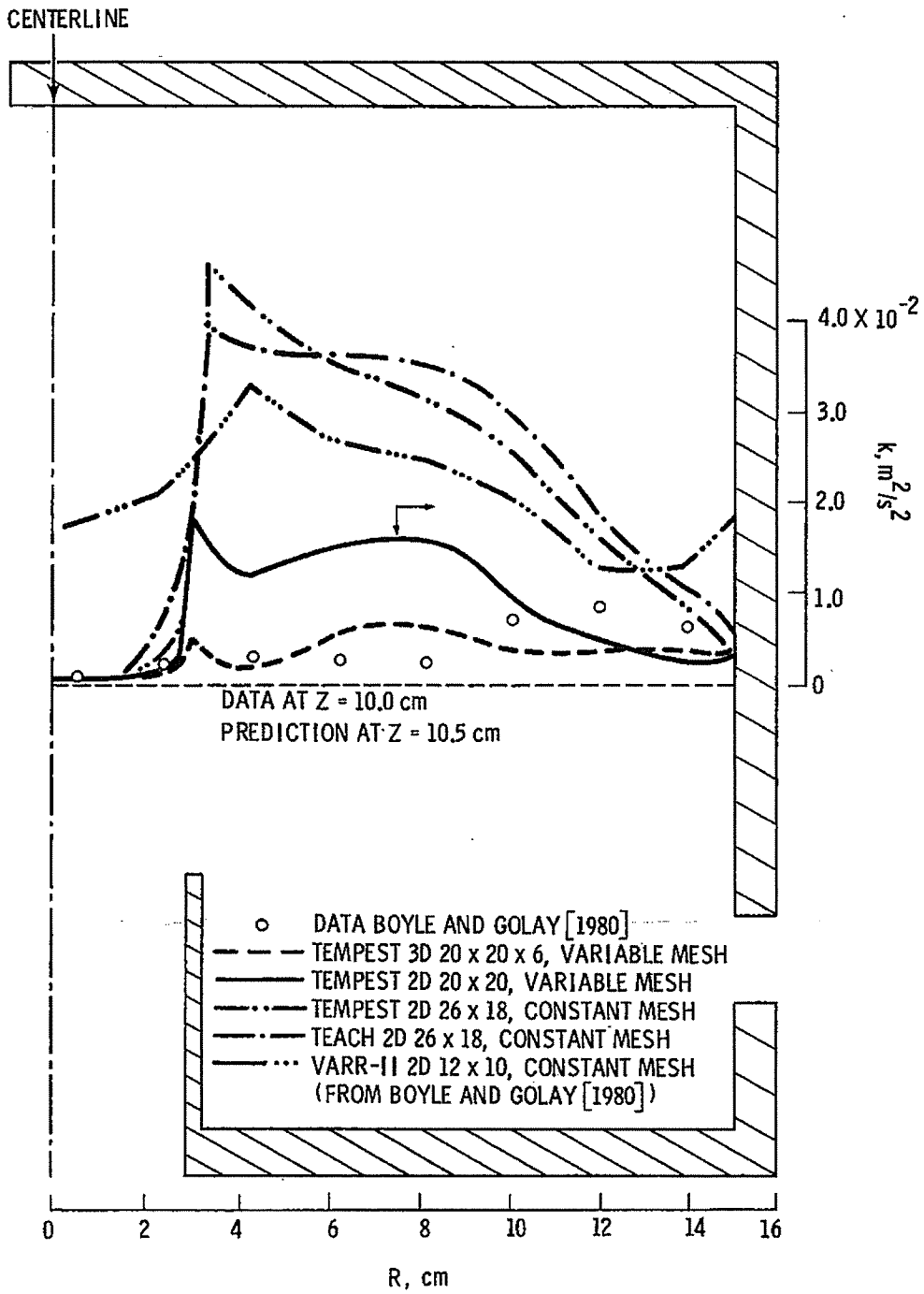


FIGURE 5.22. Comparison of 2D and 3D Kinetic Energy Predictions for Constant and Variable Mesh Spacing at Horizontal Plane Z = 10

simulations to kinetic energy data measured in the horizontal plane $Z = 10.0$. Included in Figure 5.22 is the computed results reported by Boyle and Golay (1980).

They used a code modified to simulate a $k-\epsilon$ turbulence model. Their 2D results for a 12×10 constant-spacing case are in general agreement with the 2D, constant-mesh-spacing simulations in this work. Two points are worth noting. First, coarseness of the computational mesh does not sufficiently resolve one of the most important flow regions--the mixing layer shear region above the chimney wall. Second, their predicted centerline value is nearly an order of magnitude too large, perhaps indicating that inappropriate inlet conditions were used. They allowed the code to initially generate inlet boundary values for kinetic energy instead of using experimental data. These values were more than two orders of magnitude greater than measured inlet values.

While the present 2D results agree well with the centerline kinetic energy and the finer constant-mesh-spacing cases appear to better resolve the shear layer, predicted values of kinetic energy are too high across the rest of the plane. The 2D, variable-mesh-spacing case shows better agreement, but the 3D, variable-mesh-spacing case still better predicts the magnitude of the data across the whole plane.

In Figure 5.23, turbulent kinetic energy comparisons are shown for data at two other planes, $Z = 6.2$ cm and $Z = 17.6$ cm. At the lower plane, the 3D case shows the best agreement with the data. At the upper plane, variance in the data makes it difficult to draw a conclusion.

It was pointed out earlier that the three-dimensional effects on the test section were measured and reported in the appendix of Boyle and Golay's (1980) report. Vertical and horizontal velocities in a plane at $Z = 21.4$ cm were measured, but kinetic energy was not. Measurements were made from the front to the back face at one-half of the test section. These results indicated that, indeed, significant 3D flow existed in the test section. In Figure 5.24, the vertical velocity data measured from the front to the back plate is compared to predictions. For the numerical simulation, variable mesh spacing was used and quarter-test-section symmetry was assumed.

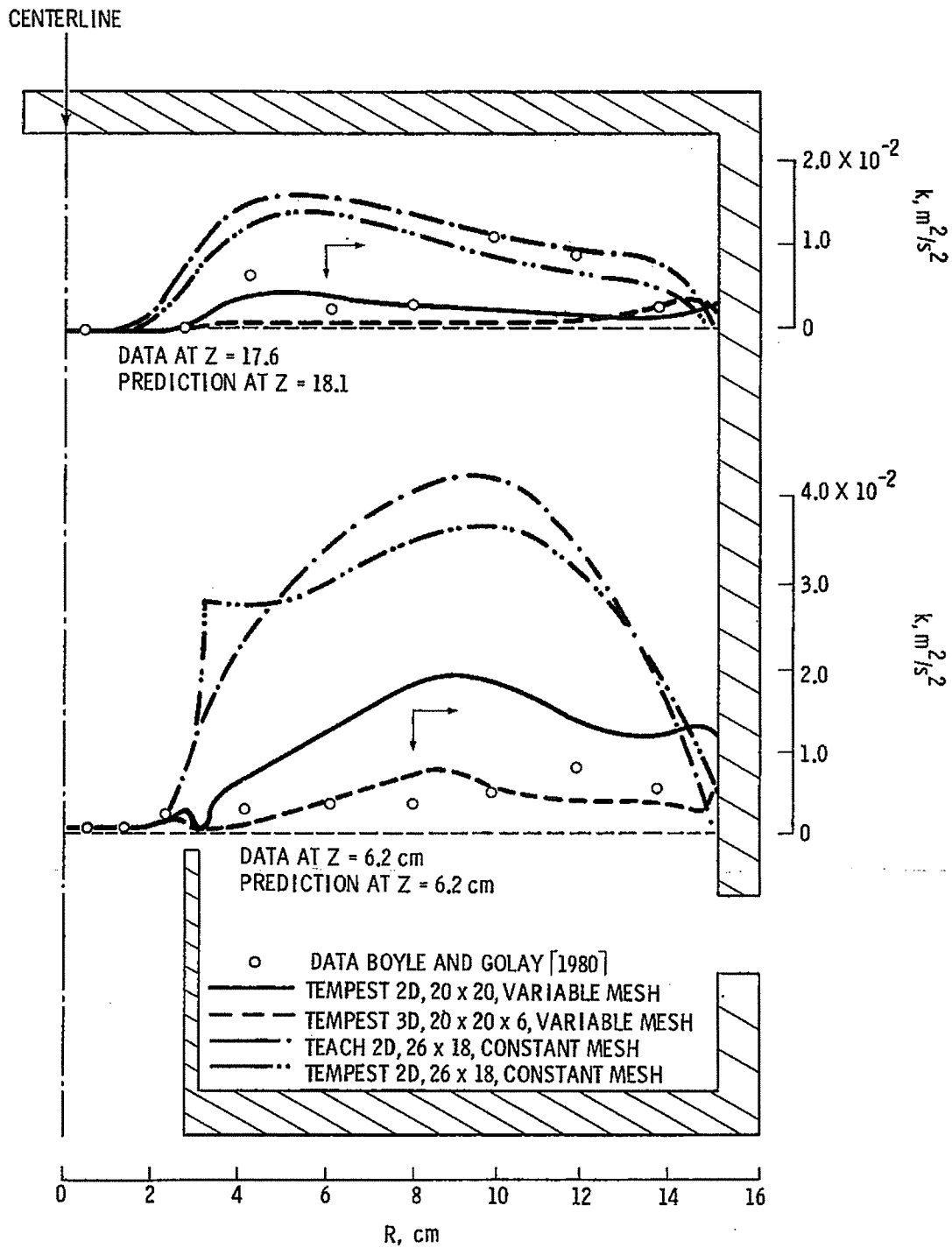


FIGURE 5.23. Comparison of 2D and 3D Kinetic Energy Predictions at Horizontal Planes Z = 6.2 and 18.1

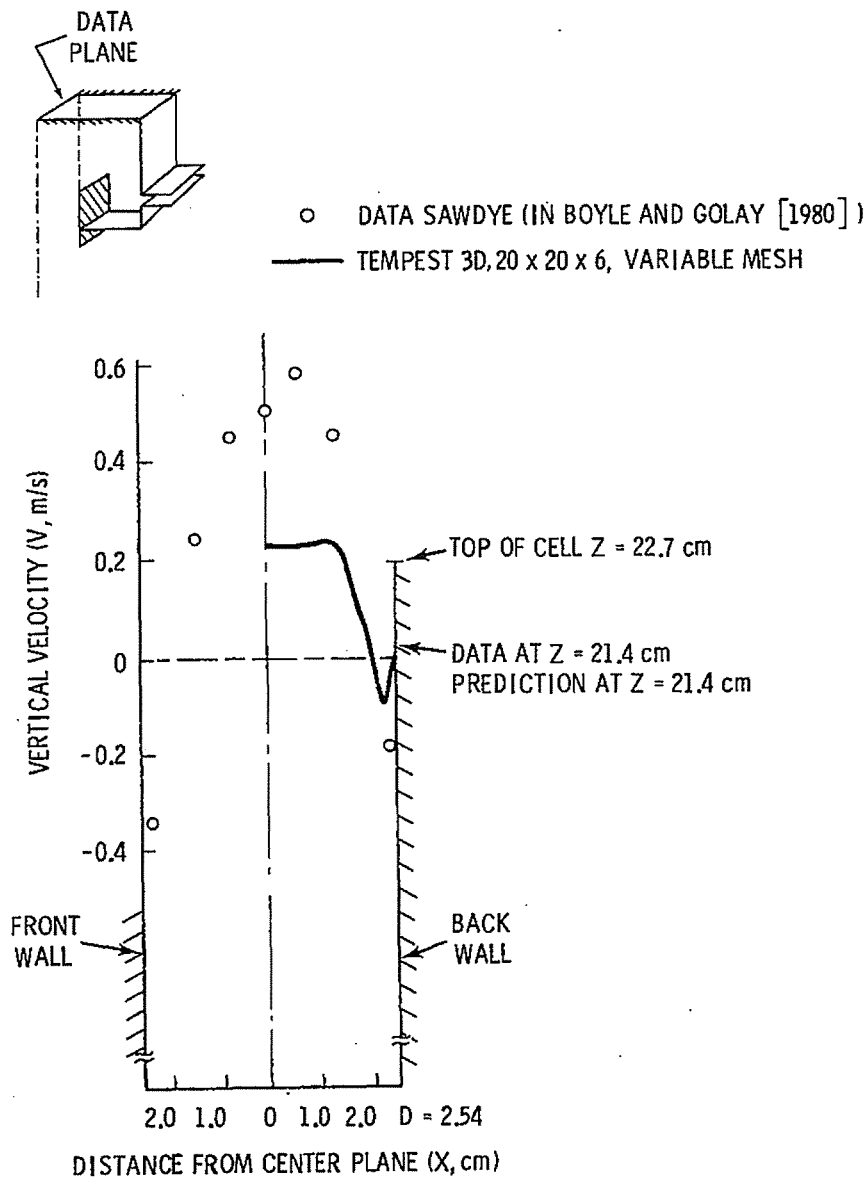


FIGURE 5.24. Comparison of Vertical Velocity Predictions and Data for 3D Flow

At first hand, the predictions do not appear to agree very well with the data, although the predictions do show a downflow along the back plate as do the data. It should be noted (see Figure 5.21) that the centerline data points appeared to be nearly a factor of two too large. In addition, the 3D-measured data show a significant degree of asymmetry from the front to the back plate. Unfortunately, even after numerous discussions with the experimenters, the discrepancy between the predictions and the data in this plane could not be

resolved. Neither could the discrepancy between the two data sets: those in the centerplane and those in the horizontal plane.

Summary of Scaled FFTF Plenum Model Results

Several conclusions can be drawn from the scaled FFTF plenum model results. Over a majority of the flow field, mean velocities and kinetic energy predictions with the $k-\epsilon$ model were in good agreement with the data when appropriate inlet conditions and 3D effects were accounted for. The velocity and kinetic energy data measured by Chen and Golay (1977) and Boyle and Golay (1980) were used in this work to compare steady-state, $k-\epsilon$ turbulence model predictions. Although certain deficiencies exist in the data, the data is generally useful for comparing the predictions of turbulence-model computer codes.

One deficiency in the data is an inadequate amount of data in the mixing layer shear region directly above the chimney wall and in the flow accelerating region near the exit. Similarly, the effect of 3D flow in the test section were not sufficiently documented by data. These deficiencies prohibit direct conclusions as to the detailed prediction capability of the turbulence model.

In the flow region directly above the chimney inlet, the typically decaying kinetic energy profile was predicted well when an appropriate level of dissipation was prescribed at the inlet boundary. Both 2D and 3D simulations predicted the reported data trend in this region. Over the rest of the flow region, the 3D simulation more closely predicted the measured turbulence data. Variable mesh spacing with finer noding in shear-generating regions improved the agreement between turbulence data and predictions as compared to coarser, constant mesh spacing.

5.2 TURBULENT FLOW WITH HEAT TRANSFER

Several turbulent flow simulations with heat transfer were computed with TEMPEST. These included buoyant, turbulent jets and plumes--and turbulent pipe flow with air, water, and sodium. These simulations were computed using two dimensions and were compared to data. Additional simulations of thermal mixing during high-pressure injection experiments in an LWR reactor 1/5-scale cold leg

and downcomer model were computed using three dimensions. Comparisons were made to temperature data measured during 200-second transients.

5.2.1 Buoyant, Turbulent Jets and Plumes

Two-dimensional, steady-state simulations of circular, buoyant, turbulent jets were conducted using the TEMPEST two-equation turbulence model (k, ϵ). Standard recommended coefficients for the model were used. The simulations consisted of warm fluid issuing into cooler quiescent fluid with free downstream boundaries and uniform inlet velocities without turbulence. A 20x20 variably spaced mesh, which assumed symmetry about the centerline, was employed.

To provide for two jets with significant levels of both inlet momentum and buoyancy, the densimetric Froude number at the inlet, defined as

$$F_o = V_o^2 / \left(\frac{\rho_\infty - \rho_o}{\rho_o} \right) g D_o$$

was maintained at 5 for both simulations. The Reynolds numbers at the inlets ($Re_o = V_o D_o / \nu_o$) were selected to reveal any sensitivity of the results to the level of turbulence. Thus, within the high-Reynolds-number jet ($Re_o = 3.6 \times 10^6$), the effective viscosity was essentially determined by the turbulent momentum transport, while within the lower-Reynolds-number jet ($Re_o = 1450$), the molecular viscosity could be a significant contribution to the effective viscosity.

Comparisons of TEMPEST results with data, semi-empirical analyses, and other numerical results for centerline behavior are given in Figures 5.25 and 5.26. It is seen in Figure 5.25 that the Abraham (1963) and Seban (1976) temperature data lie closer to the TEMPEST centerline temperature prediction using the lower Reynolds number, and that the computed values are within 30% for downstream distances less than 30 inlet diameters. TEMPEST results are also within 30% of those obtained by Seban with a numerical model that was specifically developed to calculate plumes and jets. The predicted results in Figure 5.25 also indicate a significant Reynolds number effect. At the lower Reynolds number, TEMPEST agrees very well with the data. At the higher Reynolds number, the temperature decay appears to be underpredicted.

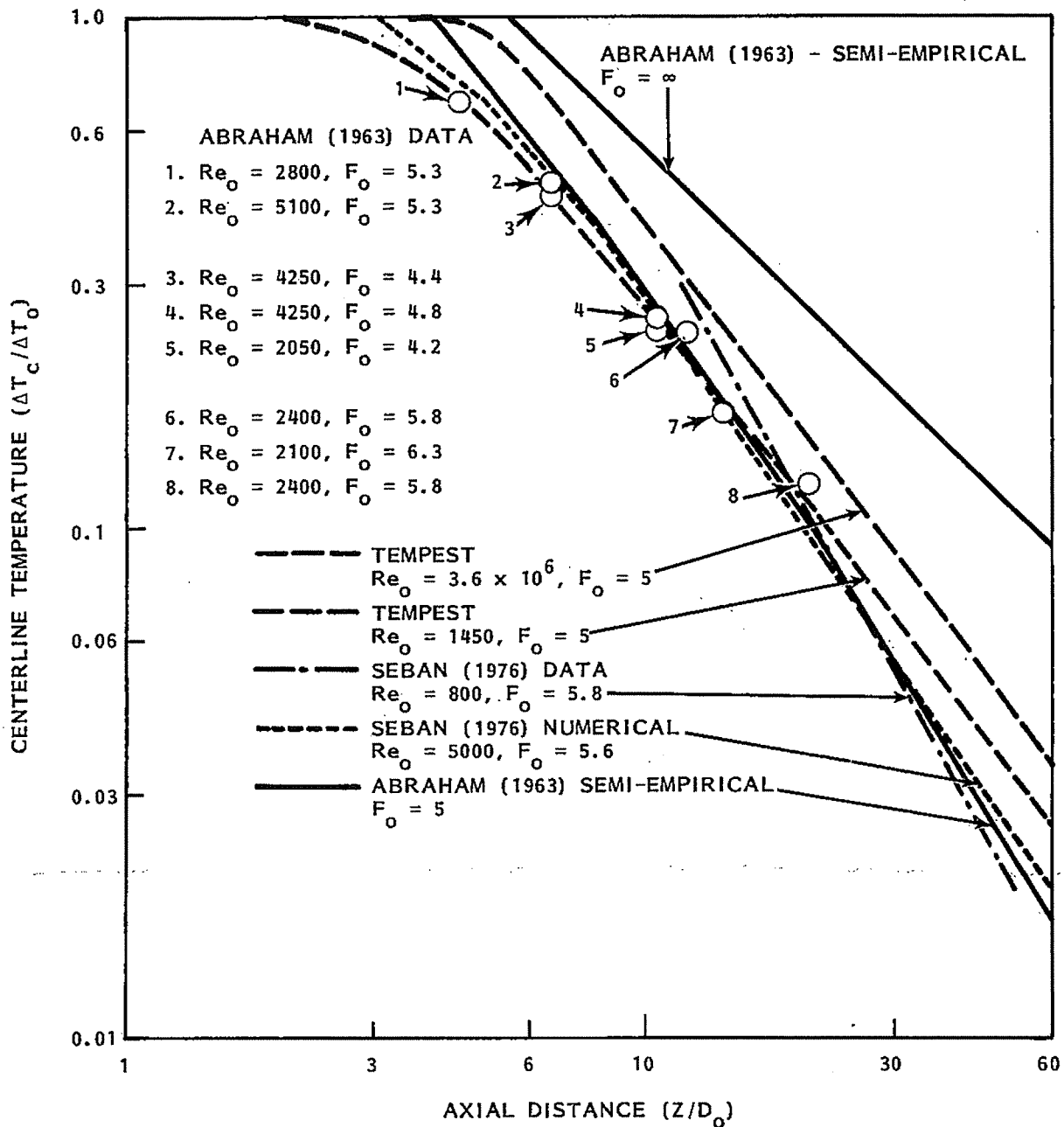


FIGURE 5.25. Centerline Temperature Results for Buoyant, Turbulent Jets

region of the buoyant jet. Both of the TEMPEST results are within 15% of the Seban velocity predictions, which are for a jet with an intermediate Reynolds number. The slopes of the two numerical curves and Abraham's semi-empirical curve for fully developed flow are almost identical and are approximately equal

The centerline velocity results are shown in Figure 5.26. The TEMPEST predictions indicate a significant Reynolds number effect on the developing to a $-1/3$ slope, with the high-Reynolds-number TEMPEST velocity curve having a slightly more negative slope. These results indicate that the effect of the Reynolds number is strongest over the developing region and that its influence on velocity, as well as temperature, gradually decreases with downstream distance.

A comparison of the TEMPEST predictions for velocity and temperature spreading in a fully developed, buoyant, turbulent jet with Gaussian profiles is shown in Figure 5.27. The Gaussian curves shown in Figure 5.27 were fit to the TEMPEST predictions at the "1/e-of-centerline-value" point. It is clear that the TEMPEST profiles are quite close to Gaussian curves (within 10%). The predicted thermal width is observed to be less than the momentum width, which

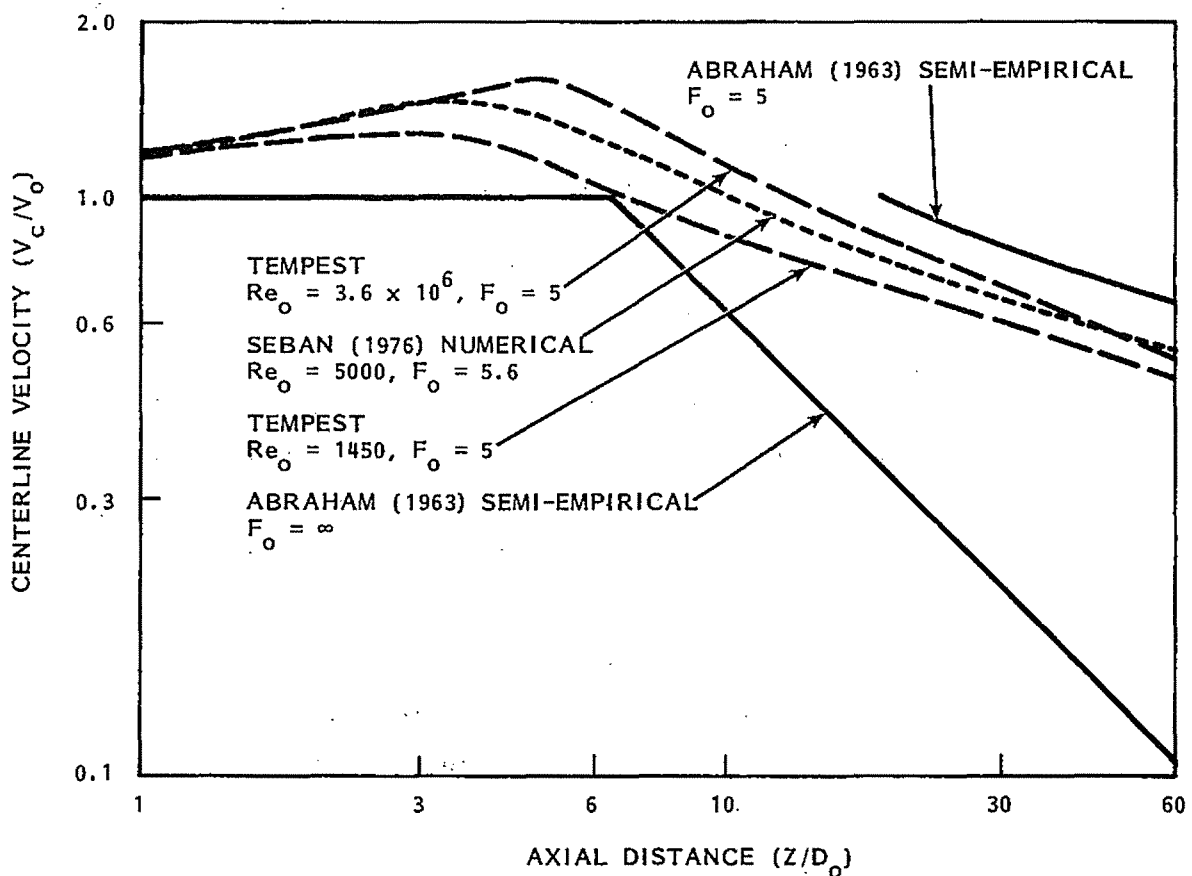


FIGURE 5.26. Centerline Velocity Results for Buoyant, Turbulent Jets

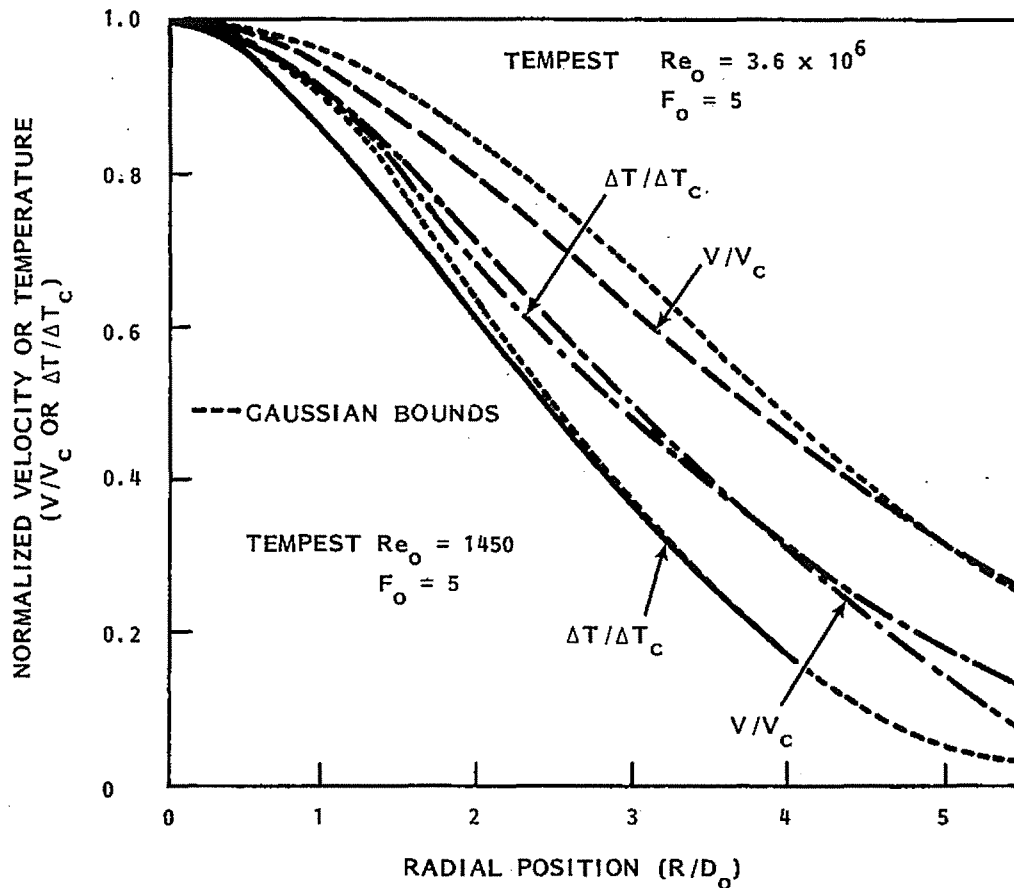


FIGURE 5.27. Velocity and Temperature Spread in a Buoyant, Turbulent Jet at $Z/D_0 = 35$

agrees with the numerical results of Seban for significantly buoyant jets ($F_0 > 5$). These velocity and temperature profiles are often assumed to be Gaussian in analyses of buoyant jets; thus these TEMPEST predictions can be seen as evidence of reasonable behavior of the turbulence model.

In conclusion, TEMPEST is capable of simulating buoyant, turbulent jets wherein significant initial momentum and buoyancy occur. The centerline temperatures are well predicted by TEMPEST, and, in general, the velocity and temperature predictions are comparable to the results of more specialized numerical treatment of 2D, buoyant, turbulent jets.

5.2.2 Turbulent Heat Transfer Boundary Condition Model and Pipe Flow Results

The turbulent wall heat transfer model incorporated in TEMPEST has been compared to data for heated pipe flows. The fluids used were water, air,

mercury, and sodium, which span Prandtl numbers from 7.0 to 0.005, respectively. Comparisons have been made with the data of Bremhorst and Bullock (1973), Eyler (1978), Lawn (1971), and Fuchs (1974). The results are summarized below.

The turbulent heat transfer boundary condition model in TEMPEST follows the basic approach of Jayatilleke (1969). A "universal" temperature profile

$$T^+ = \sigma_0 (U^+ + P) \quad (5.5)$$

is used to determine a local thermal resistance. In Equation (5.5),

$$\begin{aligned} T_0 &= \text{wall layer turbulent} \\ &\quad \text{Prandtl number} \\ U^+ &= \text{universal velocity} \\ P &= 9 \left[\left(\frac{\sigma}{\sigma_0} \right)^{0.75} - 1 \right]. \end{aligned}$$

The so called "P-function" models the added effect of a viscous sublayer.

Jayatilleke's model [Eq. (5.5)] is only valid for $Pr > 0.5$. A modification to the model is incorporated in TEMPEST which allows treatment of fluids with $Pr \ll 0.5$.

Heated Air Flow

A 2D pipe flow simulation of Bremhorst and Bullock's (1973) data was run. Ten nodes were used in the radial direction and twenty were used in the axial direction. Constant node spacing was used with a cell aspect ratio of 35. A constant wall heat flux was modeled by volumetric heating in a wall conduction cell.

Experimental flow conditions simulated were:

$$\begin{aligned} U_b &= 6.52 \text{ m/s} \\ Re_b &= 60,000 \quad (Re_{0a} = 34,700) \\ q_w'' &= 184.9 \text{ W/m}^2 \\ D &= 0.136 \text{ m} \end{aligned}$$

Other parameters include:

<u>Experimental</u>	<u>TEMPEST Predicted</u>
$U_{\tau} = 0.332 \text{ m/s}$	$U_{\tau} = 0.329 \text{ m/s}$
$T_{\tau} = 0.450^{\circ}\text{C}$	$T_{\tau} = 0.467^{\circ}\text{C}$
$T_w - T_o = 9.1^{\circ}\text{C}$	$T_w - T_o = 7.5^{\circ}\text{C}$

A comparison of computed temperature profile and turbulence intensity results are shown in Figure 5.28. The normalized profiles of temperatures versus radial position predicted by the TEMPEST code and Jayatilleke's constant-turbulent-Prandtl-number model are in very good agreement with the normalized data profile. Tempest's results for $T_w - T_o$ are 18% lower than experiment.

Predicted turbulence intensity from the $k-\epsilon$ model in TEMPEST shows expected trends when compared to measured anisotropic intensities. The results lie between $\sqrt{u'^2}$ and $\sqrt{v'^2}$ and tend toward the nearly isotropic centerline values as shown in Figure 5.28.

Heated Mercury Flow

A 2D vertically flowing heated mercury flow simulation was run. Constant mesh spacing was used with ten radial and thirty axial nodes. Flow parameters were:

<u>Experimental</u>	<u>TEMPEST</u>
$U_b = 0.315 \text{ m/s}$	0.306 m/s
$Re = 1.01 \times 10^5$	0.96×10^5
$q_w'' = 23.3 \text{ kW/m}^2$	22.9 kW/m^2
$\sigma = Pr = 0.024$	0.024
$U_{\tau} = 0.015 \text{ m/s}$	0.0149 m/s
$T_{\tau} = 0.89^{\circ}\text{C}$	0.813°C
$T_w - T_o = 8.77^{\circ}\text{C}$	9.06°C (at $\sigma_t = 1.5$)

A comparison of the temperature drop ($T_w - T$) is presented in Figure 5.29 for a turbulent Prandtl number, σ_t , of 0.9 and 1.5. For the latter value, the results agree well. A plot of dimensionless profiles, T^+ versus σy^+ , where σ is the molecular Prandtl number is shown in Figure 5.30. Again at $\sigma_t = 1.5$ the results are in good agreement.

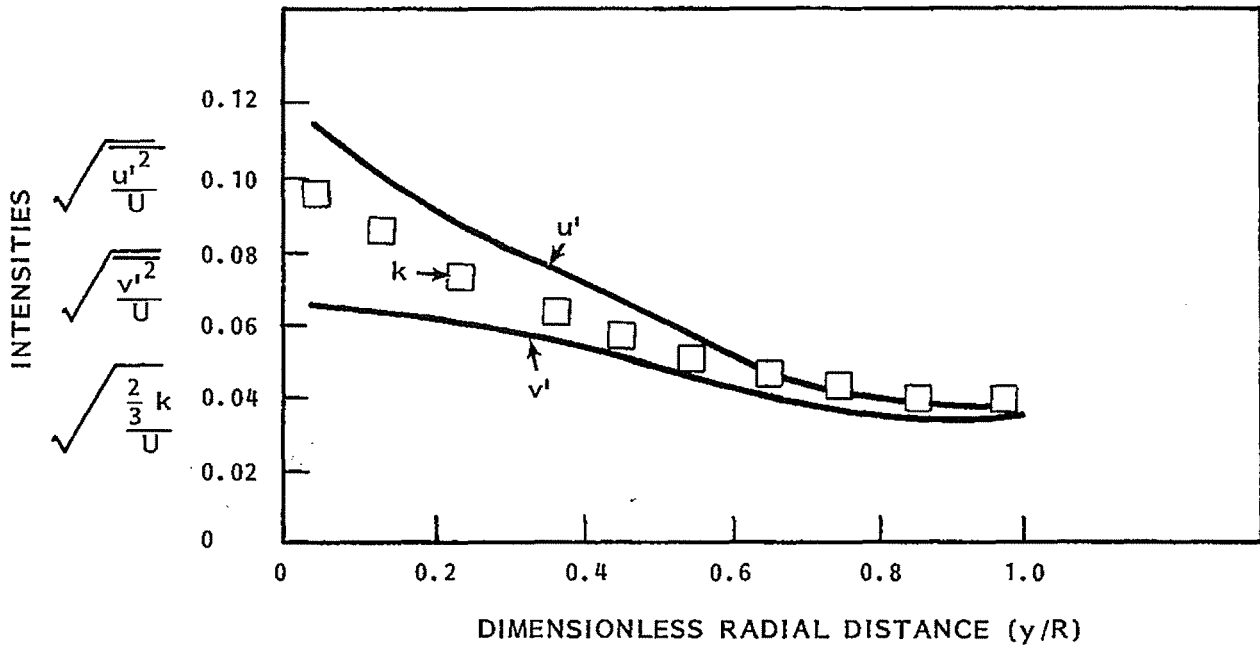
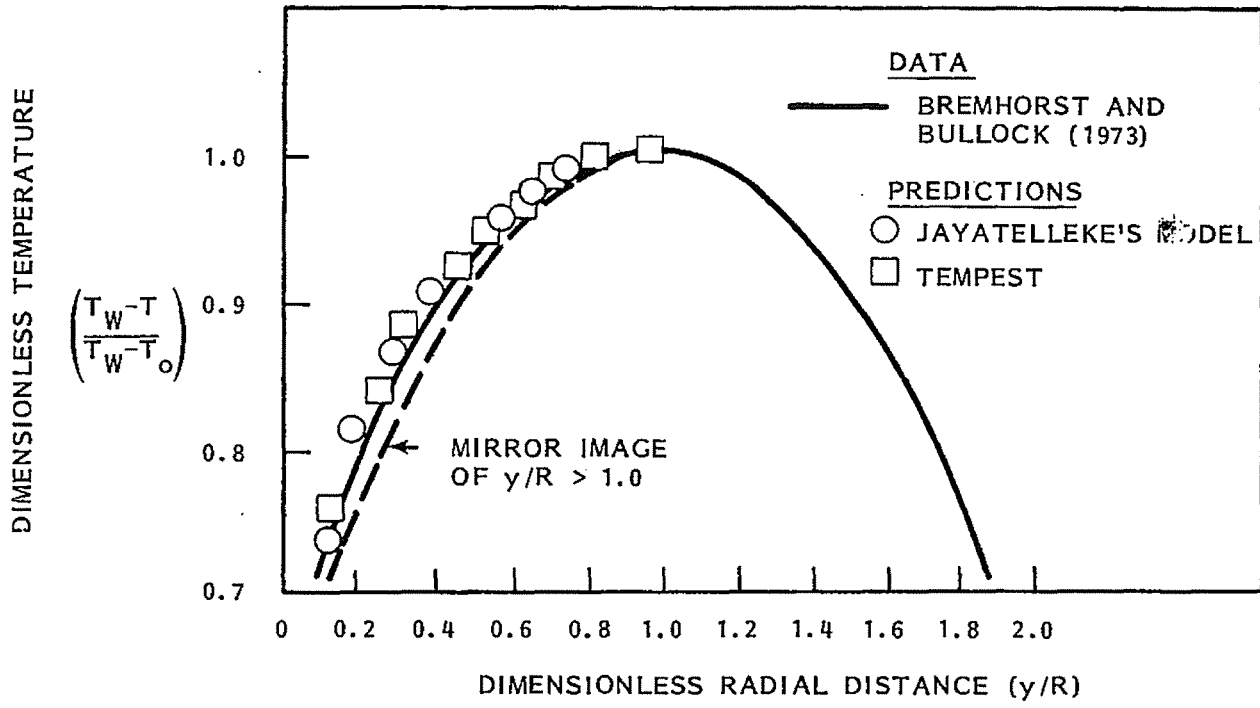


FIGURE 5.28. Heated Air Flow Temperature and Turbulence Profiles

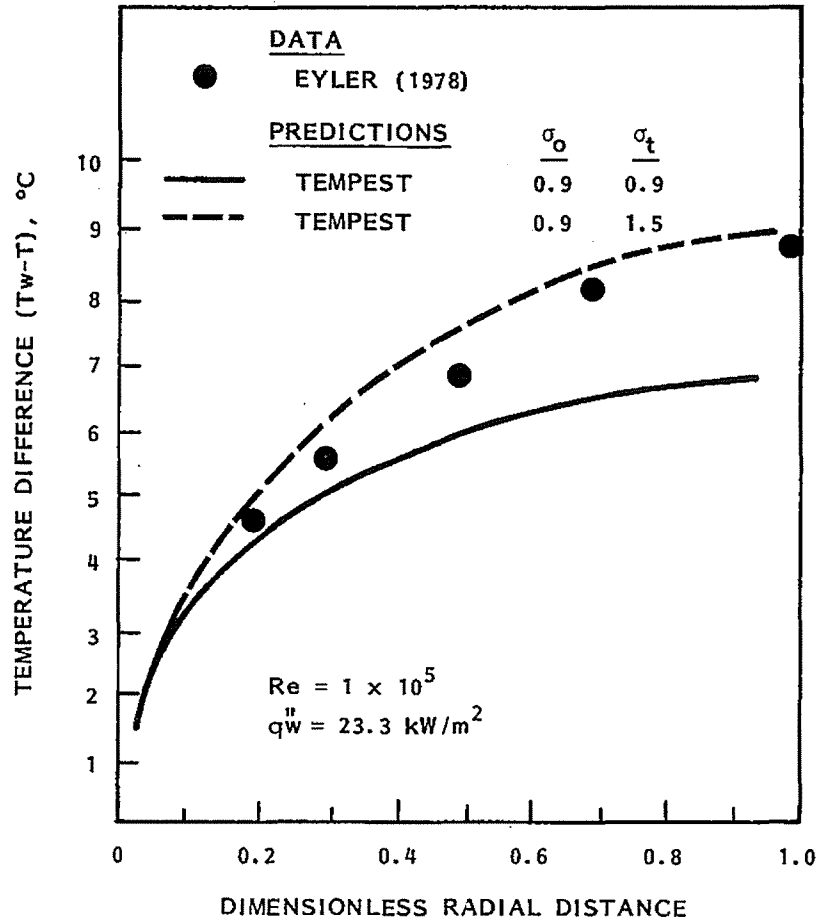


FIGURE 5.29. Mercury Pipe Flow Temperature Profile

Heated Sodium Flow

Heated sodium pipe flow simulations of Fuch's (1974) data were run for $Re = 5.6 \times 10^4$. Constant mesh spacing was used with ten radial and twenty axial nodes for cases with constant wall heat flux. Flow parameters were:

Experimental	TEMPEST
$T_b = 219^\circ\text{C}$	220°C
$U_b = (\text{not reported})$	$0.9\text{--}1.5 \text{ m/s}$
$Re = 4.2 \times 10^3 - 1.4 \times 10^5$	$5.6\text{--}8.6 \times 10^4$
$\sigma = Pr = 0.0071$	0.0072
$q_w'' = 19.6 \text{ kW/m}^2$	20.6 kW/m^2

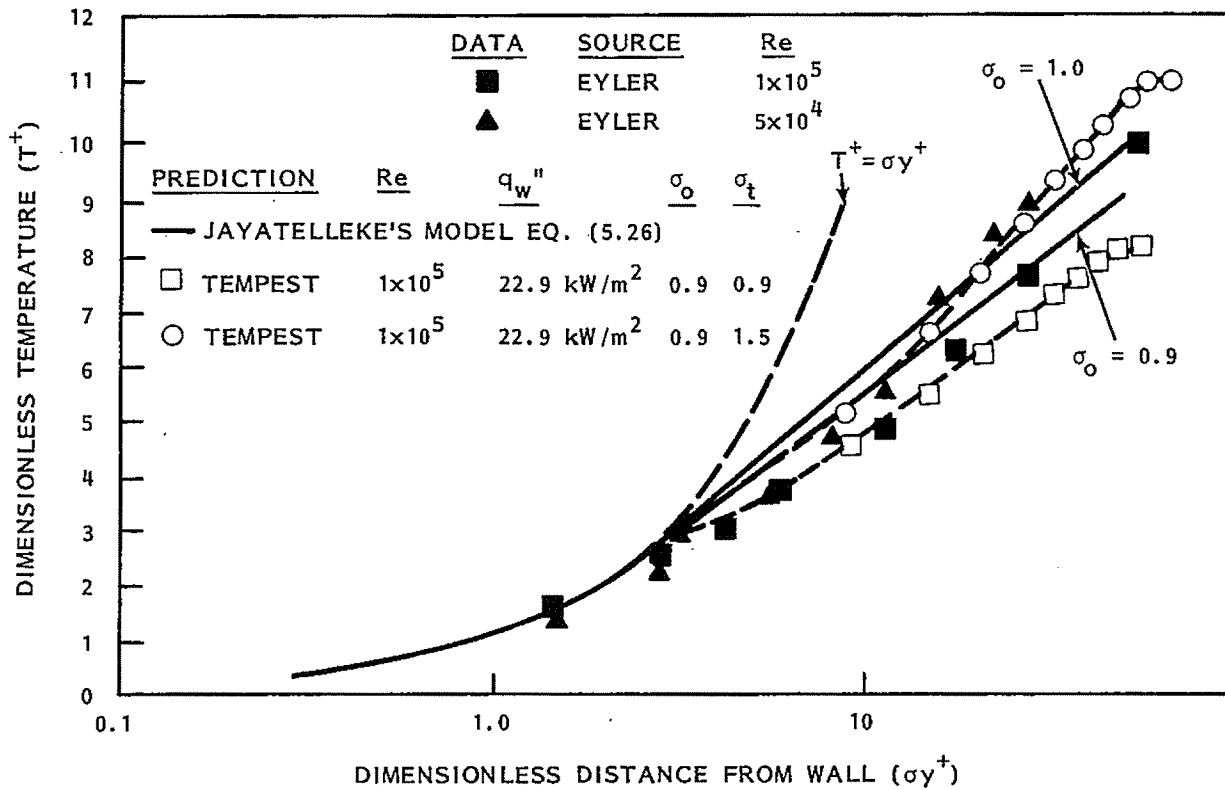


FIGURE 5.30. Dimensionless Mercury Pipe Flow Temperature Profiles

Several simulations were run using various turbulent Prandtl numbers from 0.9 to 2.5. In Figure 5.31, the predicted temperature drop ($T_w - T$) is compared to Fuch's data at $Re = 81,700$. The temperature drop is predicted very well with $\sigma_t = 2.5$. In Figure 5.32, dimensionless profiles are compared. The effect of σ_t on predictions is clearly evident as is the effect of flow Reynolds number.

Summary of Pipe Flow Results

Several conclusions can be drawn from these pipe flow results. These include:

- The model proposed by Jayatelleke (1969) can be used to prescribe a local heat transfer coefficient for computation in TEMPEST for Prandtl numbers above that for air.
- The model for local heat transfer coefficient modified to provide a computational boundary condition for low-Prandtl-number fluids works

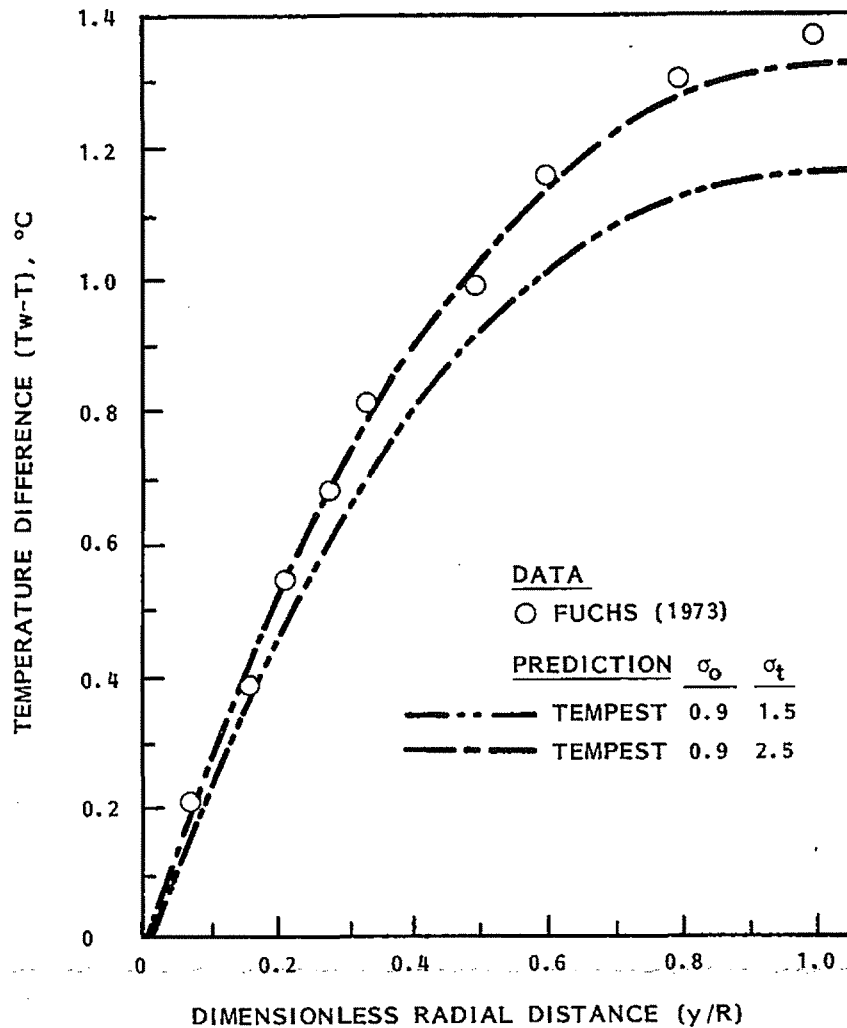


FIGURE 5.31. Experimental and Predicted Sodium Temperature Profiles (Re = 81,700)

quite well for near-wall cell locations that are in a purely conduction region and in the turbulent region.

- These results show that the boundary condition in the $k-\epsilon$ model works very well in heated pipe flows. This is evidenced by the friction velocities measured and predicted as shown in Table 5.3.
- The turbulent Prandtl number can have a marked effect on turbulent heat transport. A completely satisfactory method for predetermining the appropriate value to use for low-Prandtl-number fluids has not been confirmed.

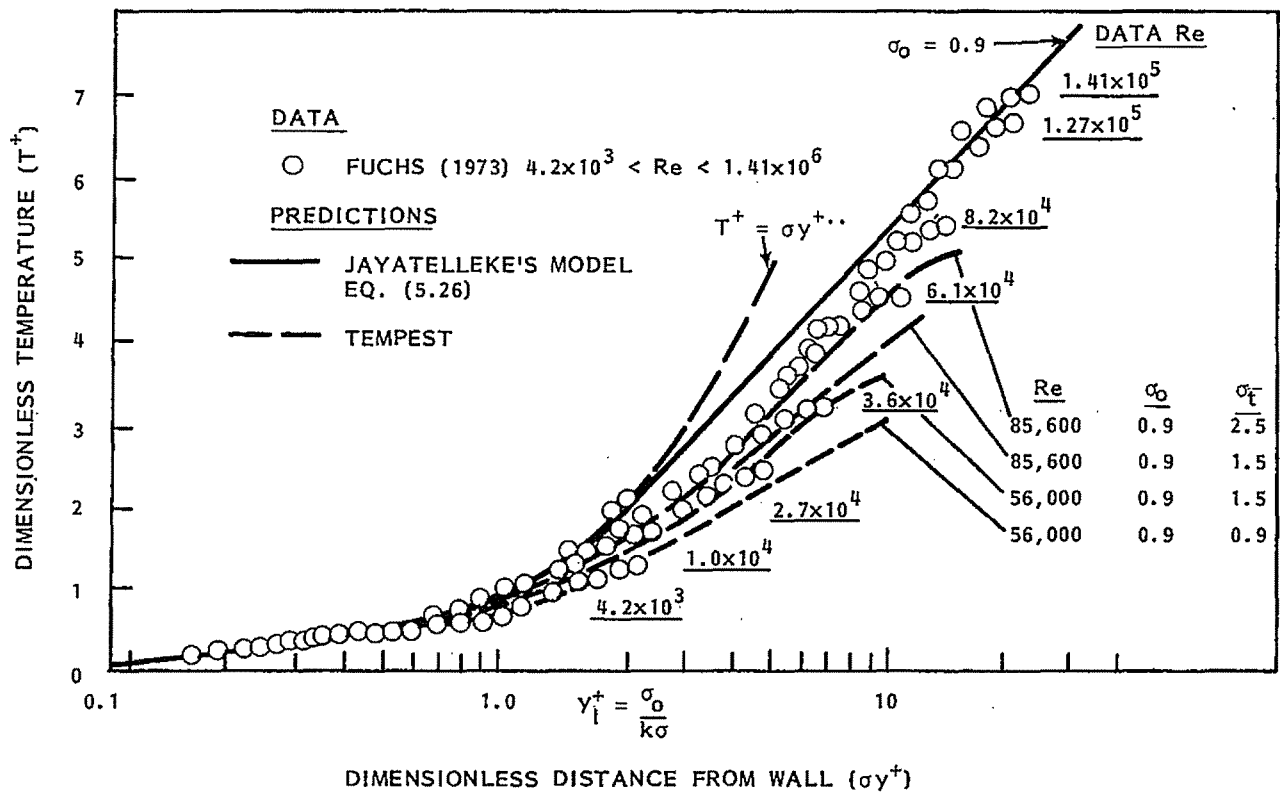


FIGURE 5.32. Experimental and Predicted Profiles of Dimensionless Sodium Temperature

TABLE 5.3. Friction Velocity Comparison in Heated Pipe Flows

Fluid	Re	Pr	$U^*_{\text{expr, m/s}}$	$U^*_{\text{Blasius, m/s}}$	$U^*_{\text{TEMPEST, m/s}}$
Air	6×10^4	0.72	0.332	0.328	0.329
Hg	1×10^4	0.016	--	0.0192	0.0196
Hg	1×10^5	0.024	0.015	0.0144	0.0149
Na	5.6×10^4	0.0072	--	0.046	0.045
Na	8.6×10^4	0.0072	--	0.065	0.065

U^*_{expr} = reported by experimenter

$$U^*_{\text{Blasius}} = U_b \sqrt{f/2}; f = \frac{0.0791}{\text{Re}^{.25}}$$

$$U^*_{\text{TEMPEST}} = \sqrt{\tau_w/\rho} = C_\mu^{1/4} k_p^{1/2}$$

5.2.3 Fluid and Thermal Mixing in a Model Cold Leg and Downcomer

A three-dimensional numerical simulation of fluid and thermal mixing in a cold leg and downcomer model was conducted. Results were compared to experimental data from a series of tests performed by Creare, Inc., for the Electric Power Research Institute. Results presented here are for Creare test number 61. A complete description of the experiment is given by Rothe, Ackerson, and Block (1982).

Creare test number 61 was performed in a geometrical configuration typical of a Westinghouse PWR (pressurized water reactor) cold leg and downcomer. This test was a no-loop-flow test with simulated high-pressure injection (HPI) issuing downward into the pipe through a small hole. Ambient fluid in the cold leg was 150°F and initially quiescent. Jet injection fluid was at 60°F.

TEMPEST was used to simulate the 200-second transient in both the cold leg and the downcomer. Predicted transient temperatures were in very good agreement with the data over the whole transient.

Experiment

The experimental facility in which the cold leg and downcomer fluid and thermal mixing tests were conducted was a ~1/5th-scale, 90° sector of Westinghouse and Combustion Engineering PWR designs. Details of the facility are given by Rothe, Ackerson, and Block (1982). Only a brief description is given here. Figure 5.33 shows a schematic of the pertinent geometry and thermocouple locations.

The cold leg was an acrylic pipe with a 5.62-in. ID and a 3/16-in. wall. On the coolant pump end of the horizontal cold leg pipe, a perforated plate was positioned approximately 5 ft from the downcomer to model resistance to flow through the pump. Approximately 1 ft from the downcomer, the pipe had a 30° bend (elbow) in the horizontal plane. At the downcomer end of the pipe, a diffuser expanded to a 7.46-in. diameter.

5.51

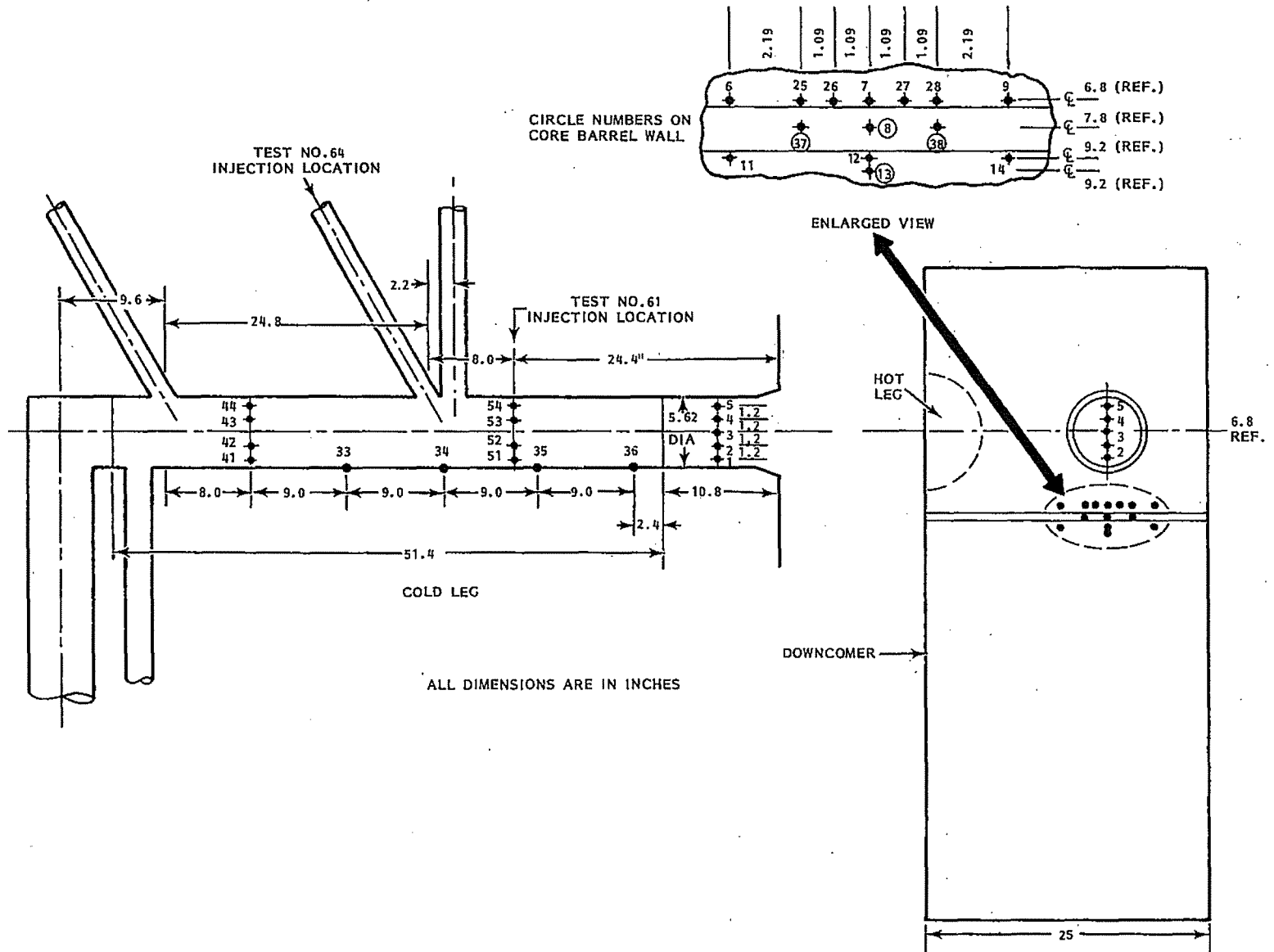


FIGURE 5.33. Schematic of Cold Leg and Downcomer Mixing Test Model.

The downcomer was made of acrylic sheet and measured 5 ft high by 2 ft wide. The distance between the pressure vessel side and core barrel side was 2 in. The centerline of the cold leg was 15.11 in. below the top of the downcomer and 4 in. off center. A hot leg penetration was in the downcomer. At the bottom of the downcomer, flow exited through eight 1.5-in. holes that were evenly spaced along the width. Numerous thermocouples were located throughout the apparatus, as indicated in Figure 5.33.

Conditions for Creare test number 61 are given in Table 5.4. This was a no-loop-flow, thermal mixing test. The injector was located 24.4 in. from the downcomer. It had a 0.273-in. inner diameter (ID) and was oriented at an angle of 90° to the cold leg pipe axis. The injection, location, and orientation is typical of a Westinghouse PWR design, though not scaled exactly.

Initial steady-state loop temperatures ranged from a reported 147°F at thermocouple number T2 to 151°F at thermocouple T1. High-pressure injection temperature was constant at 62°F. The HPI flow rate was 0.62 gal/min, which corresponds to an injection velocity of 3.4 ft/sec through the 0.273-in. injector. The HPI Reynolds number was 48,000.

The test was conducted by monitoring the loop thermocouples to ensure steady-state thermal conditions initially. The HPI was commenced abruptly, and temperatures throughout the loop were monitored for 200 seconds. Red dye in

TABLE 5.4. Conditions for Creare Test No. 61

Test Conditions

Injector Positions.....	Near Small
Injector Angle.....	90°
Density Ratio (no salt).....	0.018
Froude Number.....	0.015
Loop Flow Rate.....	0.000
HPI Flow Rate.....	0.62 gal/min
HPI Temperature.....	62°F
Initial Loop Temperature (nominal).....	150°F

the HPI allowed the mixing to be observed during the transient. Nominal time zero was defined at the time the red dye first entered the cold leg at the injection port.

TEMPEST Model

The TEMPEST computer code was used to numerically simulate the flow and thermal mixing experiments in the cold leg and downcomer. The numerical simulation was conducted in two parts. The first part consisted of computing the mixing in the cold leg pipe, and the second part consisted of computing the mixing in the downcomer. The two parts were coupled by using the pipe outlet results as inlet boundary conditions to the downcomer simulation.

The simulations were conducted in two parts to maintain the computational grid in the natural geometry of the pipe and the downcomer. The pipe was computed using cylindrical coordinates, and the downcomer, having a rectangular box configuration, was modeled using Cartesian coordinates. The 30° bend in the cold leg pipe was not modeled. The pipe was assumed to be straight.

A total of 1520 computational cells were used to model the cold leg pipe. A 180° segment was computed assuming a vertical plane of symmetry through the centerline. In the pipe, 5 radial cells were used from the centerline to the pipe wall, 10 cells were used in the azimuthal direction, and 26 cells were used in the axial direction. Figure 5.34 outlines the noding structure.

On the pressure vessel end of the cold leg pipe, a partial downcomer was modeled. This was done to provide a correct boundary condition effect of the downcomer and, in particular, of the core barrel wall. Fluid that was entrained at this boundary was assumed to be at the nominal downcomer temperature of 150°F. This assumption is valid if fluid above the cold leg in the downcomer does not mix sufficiently.

For test number 61, all walls of the pipe and downcomer were modeled as adiabatic walls. In this test, the thermal cooldown transient was not severe and thus the thermal capacity and conduction effects in the acrylic sheet did not contribute significantly to the thermal energy balance.

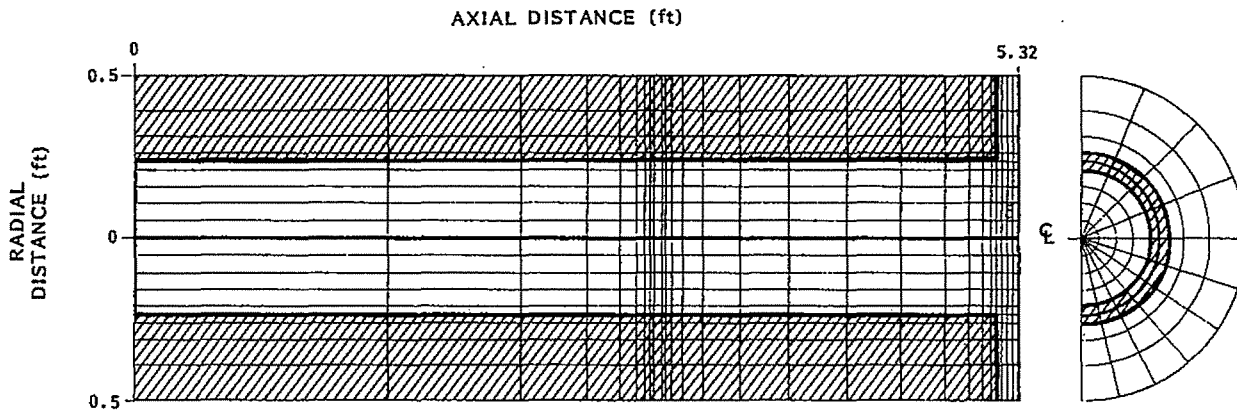


FIGURE 5.34 Cold Leg Pipe Noding Structure

In the experiments, a perforated plate existed in the cold leg pipe on the coolant pump end. The lower third of this plate was solid. Uniformly spaced, 3/16-in. holes existed in the upper two-thirds area. The total open (flow) area was only 27% of the plate area. In the computer simulations, this end of the pipe was assumed to be completely closed off, which is a conservative assumption. It is conservative because closing it off forces any colder fluid reaching that end to remain in the pipe rather than allowing it to be replaced by warmer fluid in the vertical downpipe.

Thermal mixing in the downcomer was computed using Cartesian geometry. A total of 1698 computational cells were used. The vertical height of 5 ft was modeled with 22 cells, and 15 cells spanned the 2-ft width. There were four computational cells in the 2-in. distance between the core barrel and the pressure vessel walls. The cold-leg diffuser was also modeled on the inflow boundary. Figure 5.35 exhibits the computational cell structure. Inflow boundary conditions to the downcomer were specified as transient boundary condition tables. These tables were generated at a corresponding plane in the pipe simulation by integration, which conserved mass and energy. All walls of the downcomer model were treated as adiabatic.

In the experiments, the outflow at the bottom of the downcomer was through eight uniformly spaced holes. Because these holes could not be modeled directly in the numerical simulation, this boundary was modeled as a computed

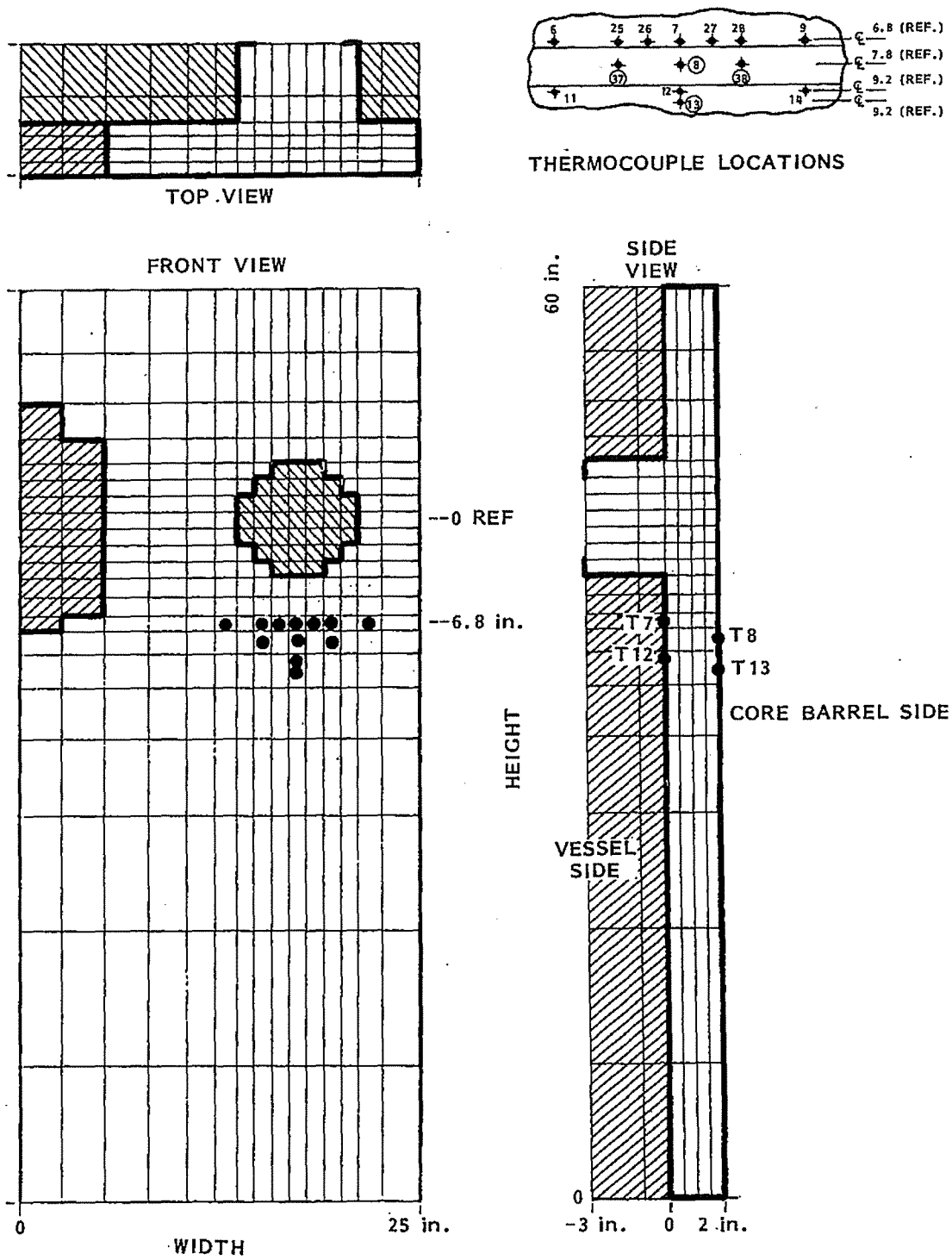


FIGURE 5.35. Downcomer Noding and Relative Thermocouple Locations

outflow boundary. A drag coefficient was specified at the outflow to simulate a constant pressure condition.

Test number 61 is a thermal mixing test consisting of cold-leg HPI through a 0.273-in.-ID pipe located 2.4 in. from the downcomer. Thermocouples located throughout the cold-leg and downcomer were monitored continuously in the test. While most thermocouples were mounted on the walls, two thermocouple rakes were located in a vertical line in the cold leg (see Figure 5.33).

Figure 5.36 shows time-temperature data and TEMPEST predictions at thermocouple rake locations in the cold leg. On the pressure vessel end of the cold leg (thermocouples T1 to T5) TEMPEST predictions are in good agreement with the data. Near the bottom of the pipe where colder fluid is flowing toward the downcomer, the predictions are typically 2 to 3°F less than the data. Near the top of the pipe, the predictions are 2 to 3°F above the data. At the pump end of the cold leg, the predictions are in excellent agreement with the data over the whole transient.

Figure 5.37 includes data and predictions at four locations along the bottom of the cold-leg pipe. Because the TEMPEST simulation assumed the pipe wall to be adiabatic, the predictions are for fluid temperatures in the first computational cell, which is a distance of 0.15 in. from the wall. Again the data and predictions are in excellent agreement.

In the downcomer, thermocouples were located on the pressure vessel and core barrel walls. Figure 5.38 is a comparison of vessel wall results. Figure 5.39 shows core barrel wall results. In both figures, TEMPEST results are fluid temperatures at the center of the first computational cell located 0.25 in. from the walls. The results are in good agreement, although the predictions tend to be 3 to 4°F higher than the data at some locations.

The injection of cold HPI into the pipe and the subsequent thermal mixing transient involve several flow phenomena. The HPI jet entrains fluid before it impinges on the pipe wall. The vigorousness of the mixing resulting from impingement is not sufficient to maintain a completely mixed condition in the pipe. Thermal stratification thus develops as the colder fluid spreads in both

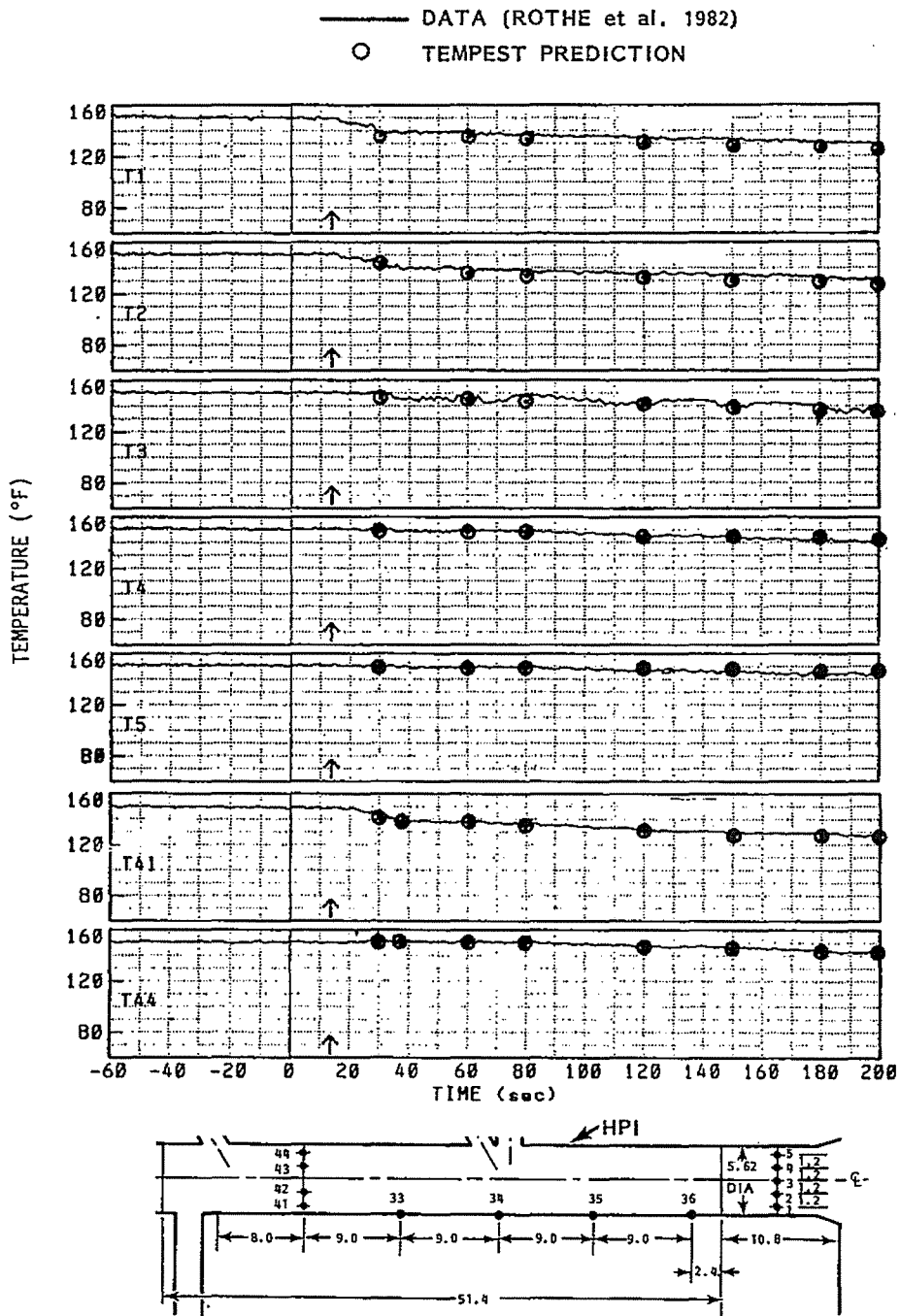


FIGURE 5.36. Transient Cold Leg Pipe Temperatures

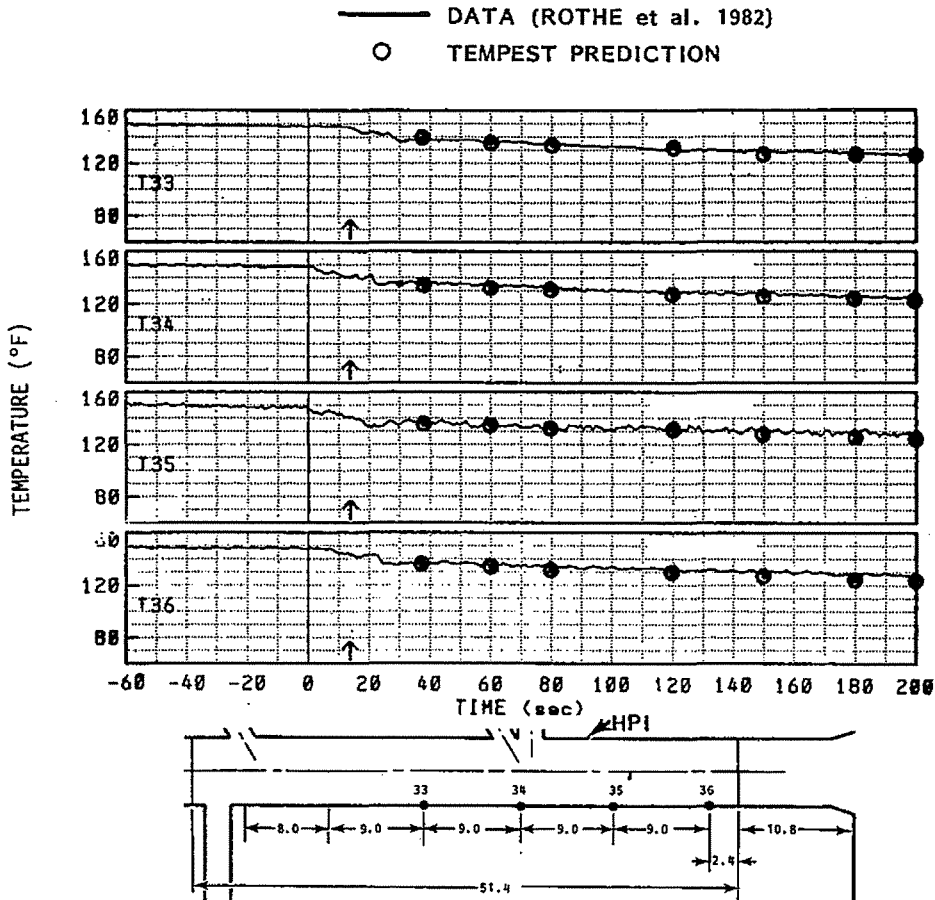


FIGURE 5.37. Data and Predictions for Cold-Log Temperatures in Creare Test Number 61.

directions along the pipe bottom. Fluid that travels toward the pump will eventually return to be reentrained in the jet. Fluid that travels toward the downcomer will mix with entrained fluid from the upper portion of the pipe. This fluid in the upper portion of the pipe is nominally the temperature of the upper region of the downcomer, from which the fluid is entrained.

As the colder fluid in the lower portion of the pipe reaches the diffuser, it slumps and accelerates as it flows over the lip into the downcomer. Once in the downcomer, the colder fluid falls toward the bottom. As it falls, it mixes with ambient downcomer fluid. Also in the downcomer, a countercurrent upward

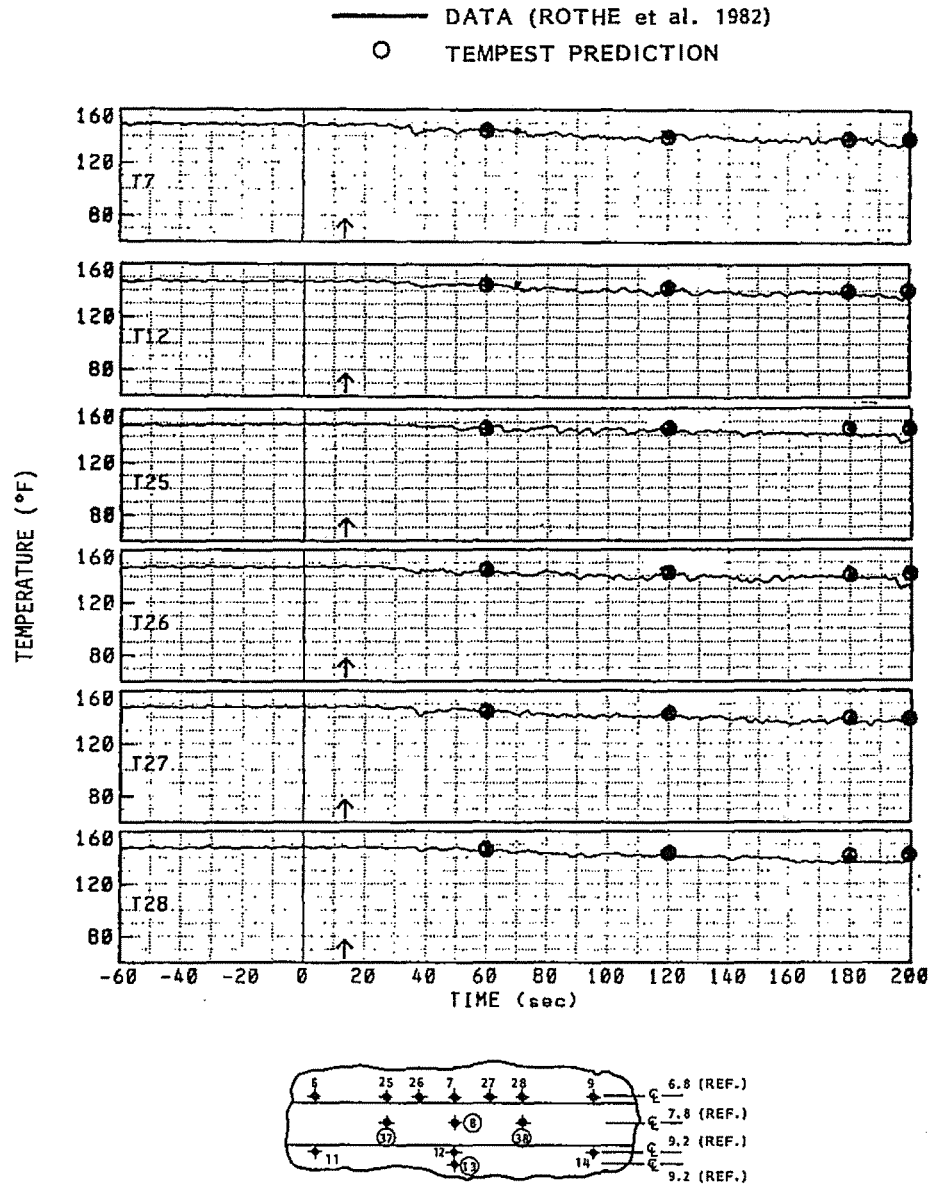


FIGURE 5.38. Downcomer Vessel Wall Temperatures

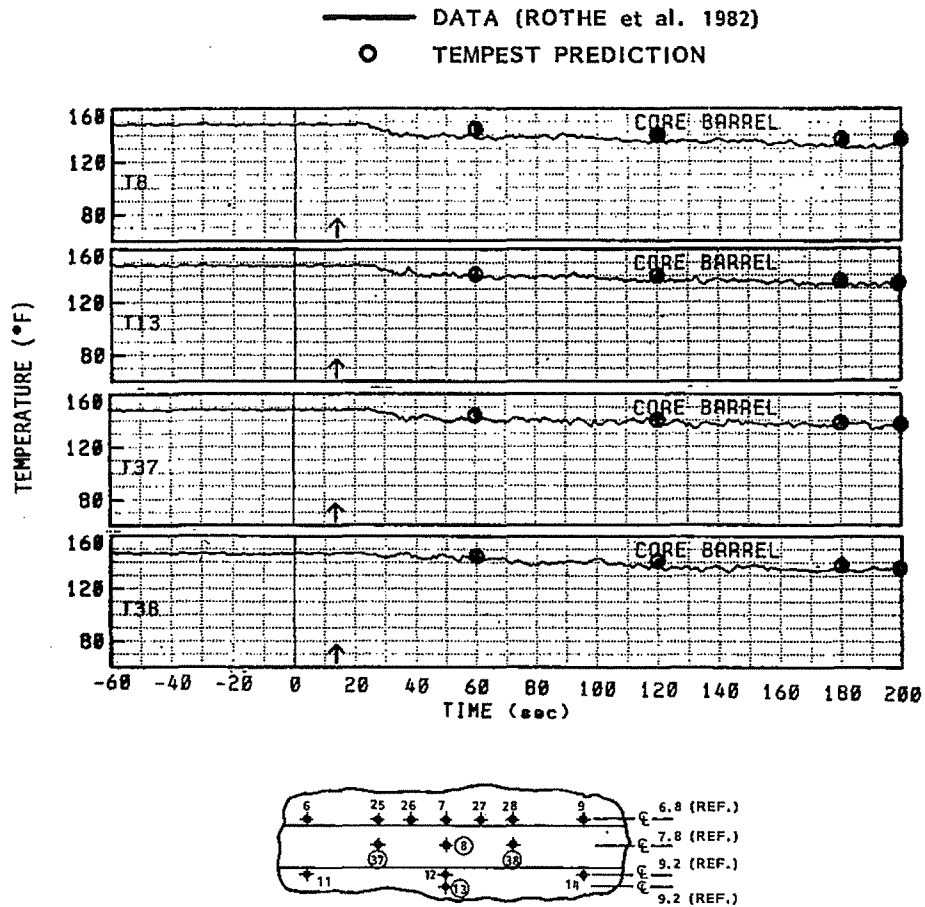


FIGURE 5.39. Downcomer Core Barrel Wall Temperatures

flow exists on either side of the falling colder fluid. This upward-flowing fluid is then entrained either back down or back into the cold leg pipe.

These basic flow phenomena were predicted in the TEMPEST simulation. Figure 5.40 presents TEMPEST-predicted isotherms that exhibit the aforementioned mixing phenomena. Entrainment occurs near the HPI injection location, and stable stratification occurs as flow diverts upstream and downstream in the pipe.

Note that the fluid being entrained from the downcomer back into the pipe is approximately 2°F cooler than the assumed entrainment temperature of 150°F. This may in part explain the 2 to 3°F overprediction of downcomer wall temperatures in Figure 5.38.

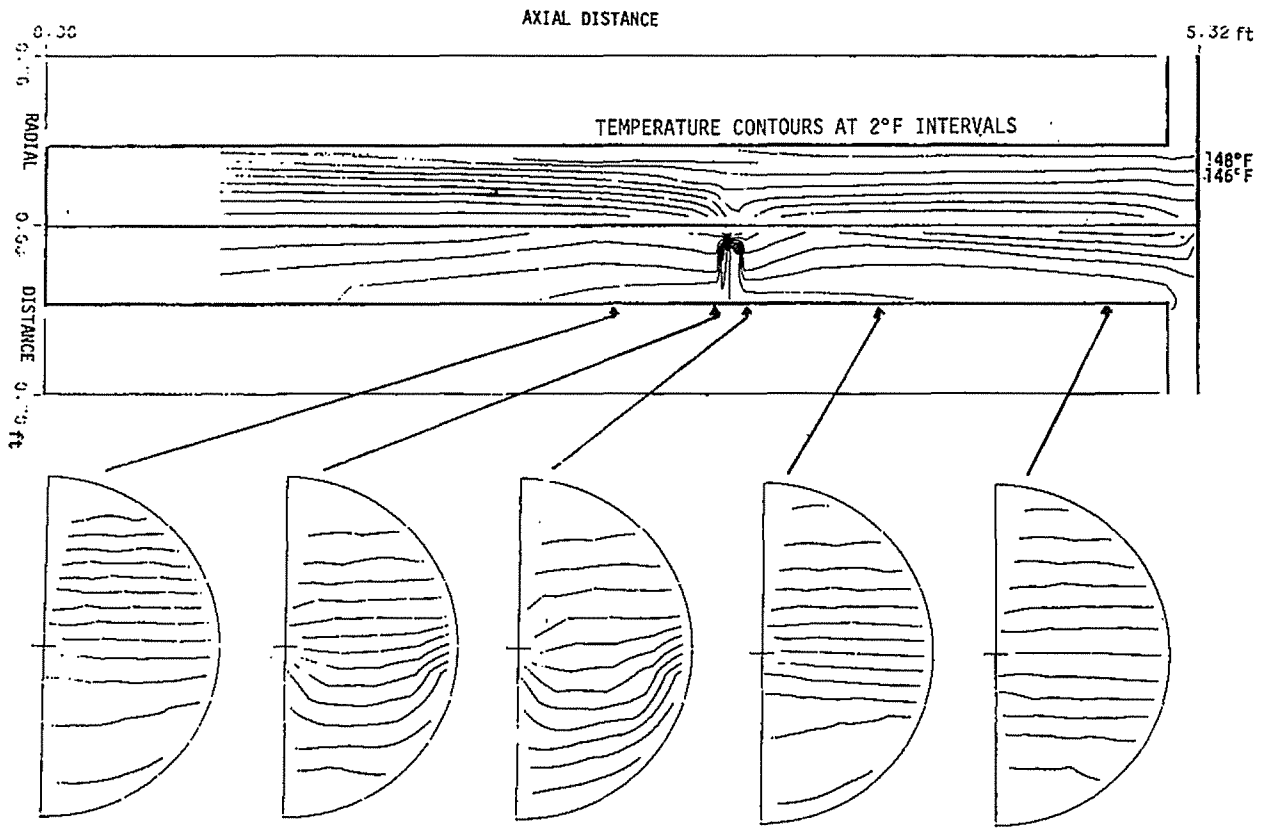


FIGURE 5.40. Temperature Contours at 200 sec

Note that the fluid being entrained from the downcomer back into the pipe is approximately 2°F cooler than the assumed entrainment temperature of 150°F. This may in part explain the 2 to 3°F overprediction of downcomer wall temperatures in Figure 5.38.

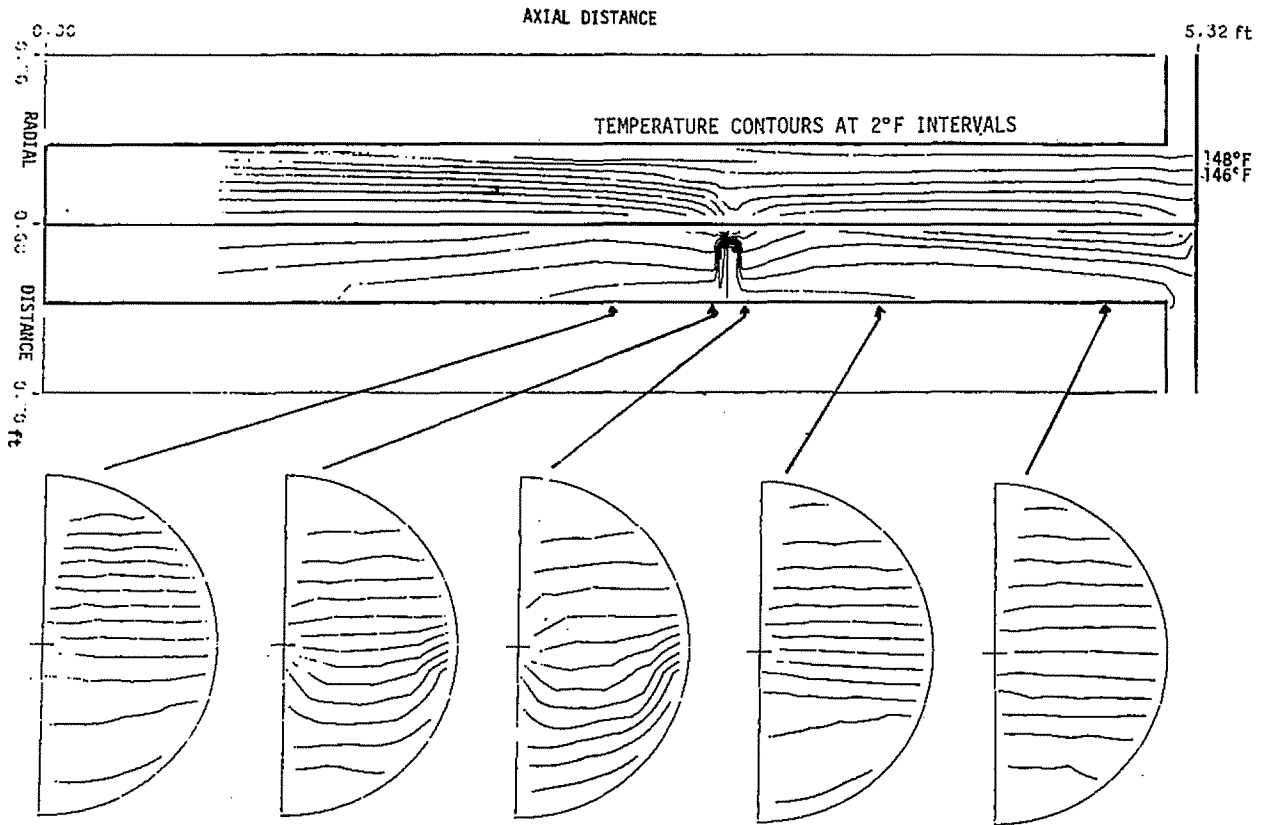


FIGURE 5.40. Temperature Contours at 200 sec

6.0 ADDITIONAL SIMULATIONS

In the three previous chapters of this report, computed results were compared to data, analytical solutions, and other code predictions for the purpose of assessing and verifying code predictions. Numerous other simulations conducted by PNL were designed to confirm an operating mode, a boundary condition, a computational capability, etc., or to show a particular application. Several such simulations are described in this chapter.

6.1 LAMINAR CONVECTION

Laminar convection simulations computed and presented for additional confirmation of operating modes and applications include:

- vertical, closed-end thermal siphon (designed to test computed boundaries)
- natural convection about a horizontal cylinder (designed to test computed boundaries completely encompassing a flow region)
- full-polar convection in an enclosed region (designed to test periodic boundary conditions)
- transient, two-region, coupled convection (designed to test thermal conduction coupling of different fluid regions).

The results of these simulations are presented below.

6.1.1 Vertical, Closed-End Thermal Siphon

A vertical, closed-end thermal siphon was modeled to demonstrate TEMPEST's computed boundary logic for computed inflow/outflow cells in a buoyancy-induced flow. Figure 6.1 includes a schematic of the modeled system. Fluid in an 8-ft-high, 1-in.-ID, vertical pipe communicates at the bottom with fluid in a constant-temperature reservoir. The top is closed. The pipe wall was modeled with a linear temperature gradient which varied from the 200°F reservoir temperature at the bottom to 140°F at the top. This wall temperature gradient cools fluid near the wall, causing the fluid to fall. Warm fluid entrained from the lower reservoir rises along the centerline. The computed boundary thus entails both inflow and outflow in the same plane.

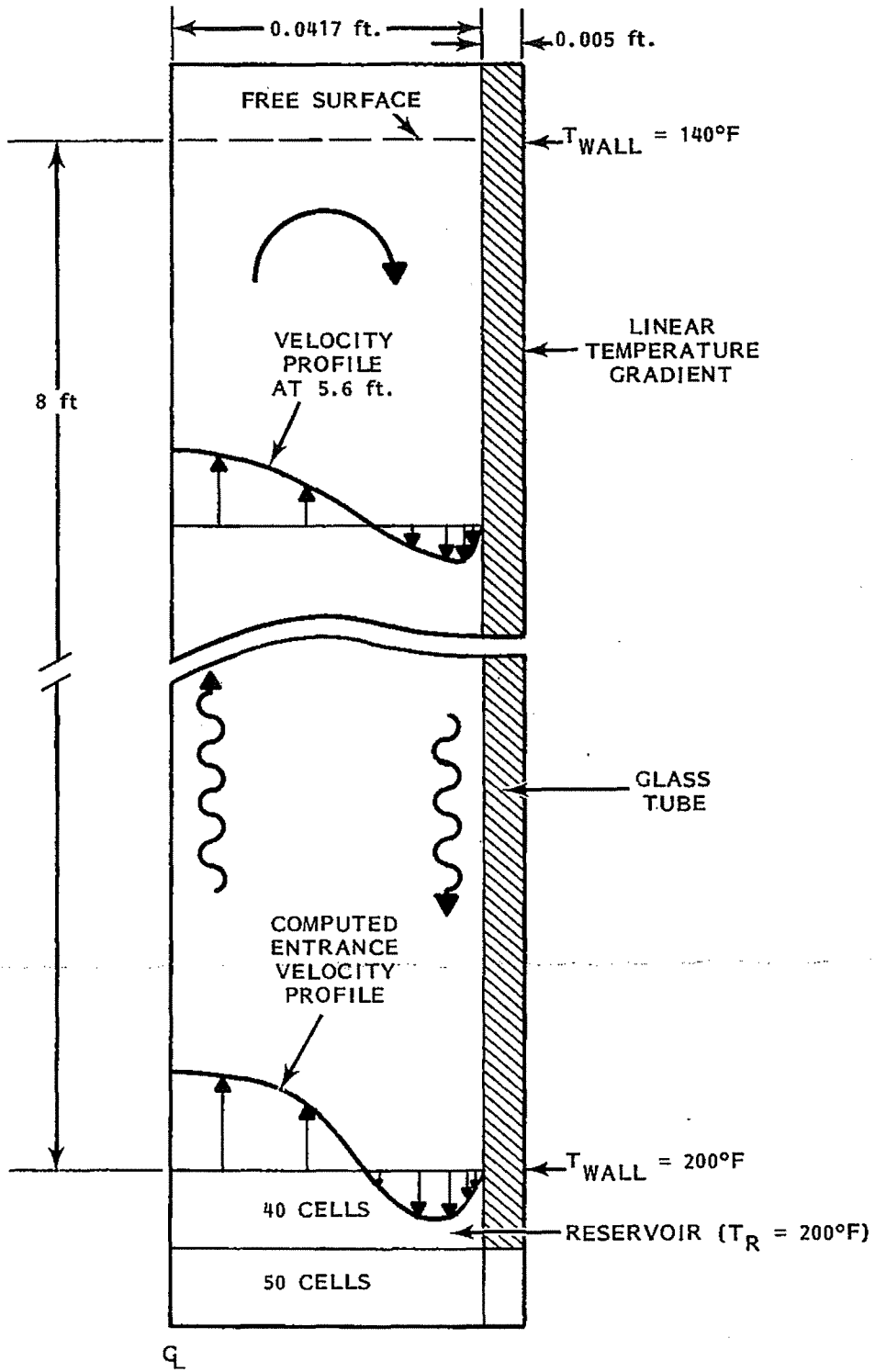


FIGURE 6.1. Vertical, Closed-End Thermal Siphon

A steady-state flow was not achieved in this simulation. Rather, a cyclic, chugging behavior was observed. Although no data were available for comparison, the computed boundary condition logic was determined to be working correctly during the cyclic variations.

6.1.2 Natural Convection About a Horizontal Cylinder

A problem involving natural convection about a horizontal cylinder was used to test the behavior of TEMPEST when the entire external boundary is a free boundary. For this simulation a two-dimensional slice was taken through the pipe, and the circulation of fluid within the pipe was also computed. Figure 6.2 illustrates the induced flow field (velocity vectors) and thermal plume developed above the cylinder (isotherms). An important aspect of this problem is that the Boussinesq approximation is very useful in eliminating the need for hydrostatic pressure boundary conditions at the periphery of the modeled region.

6.1.3 Natural Convection in a Full-Polar, Cylindrical Region

The periodic boundary condition logic in TEMPEST was tested by simulating free convection flow in a cylindrical pipe cross section. The noding structure used is shown in Figure 6.3. Portions of the interior wall surface were modeled as adiabatic, while portions were modeled as constant-temperature boundaries. The periodic boundary was set up to be along a plane normal to the gravitational vector.

This geometry represents a severe test of the logic associated with full-polar, cylindrical coordinate convection for several reasons. With the periodic boundary located normal to the gravitational vector, small convergence errors encountered in the pressure solution iteration can lead to asymmetric flow prediction. To achieve a symmetric flow, it was necessary to reduce the convergence criteria in TEMPEST to 10^{-9} ft³/ft³-sec. This convergence is considerably tighter than that required to achieve a converged steady solution in a similar geometry that assumes vertical centerplane symmetry.

Three separate cases were run with sodium as the convecting fluid. In each case, symmetric boundary conditions were specified to test the periodic

6.4

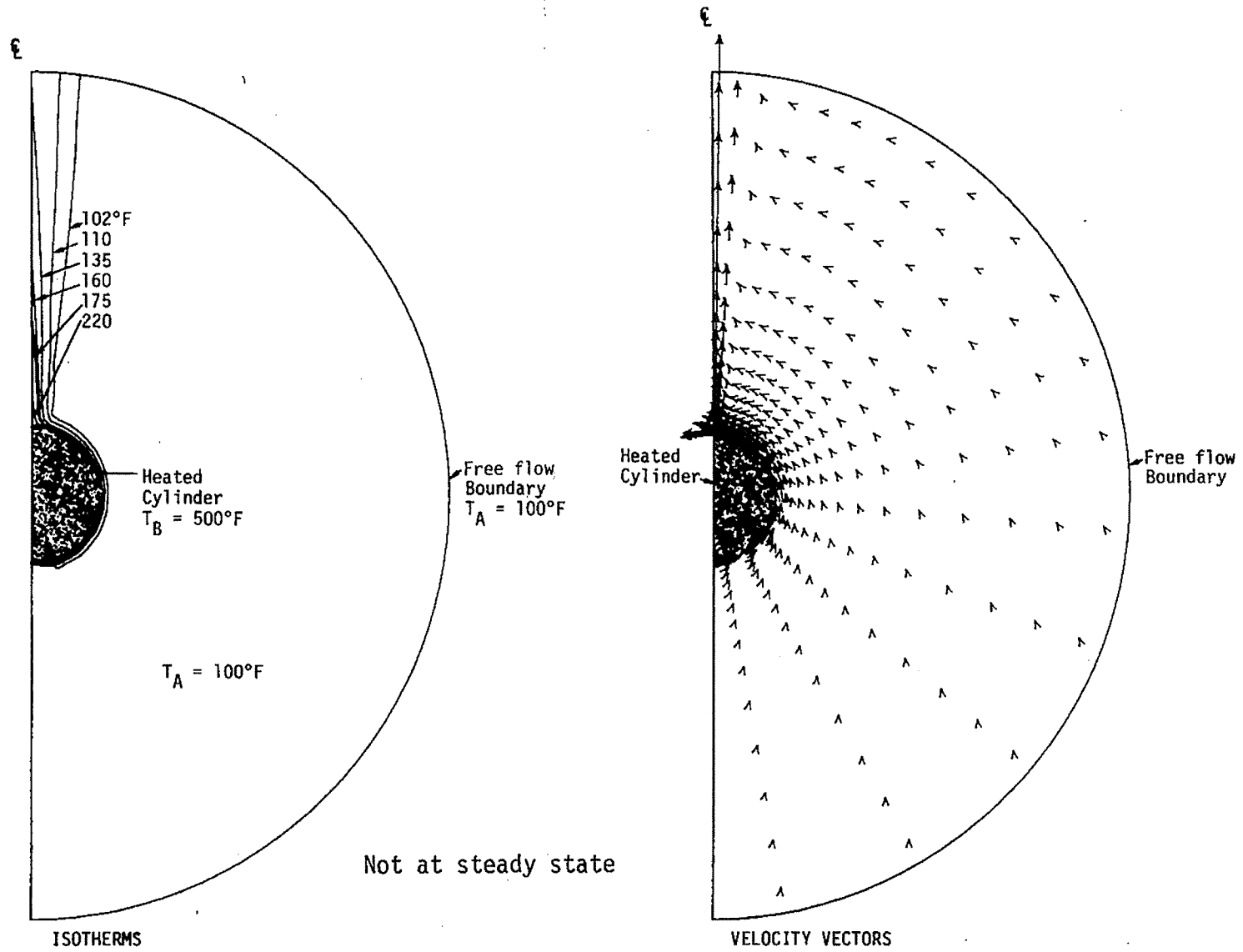


FIGURE 6.2. Natural Convection about a Heated Horizontal Cylinder Located in a Free Environment, Isotherm and Velocity Vectors

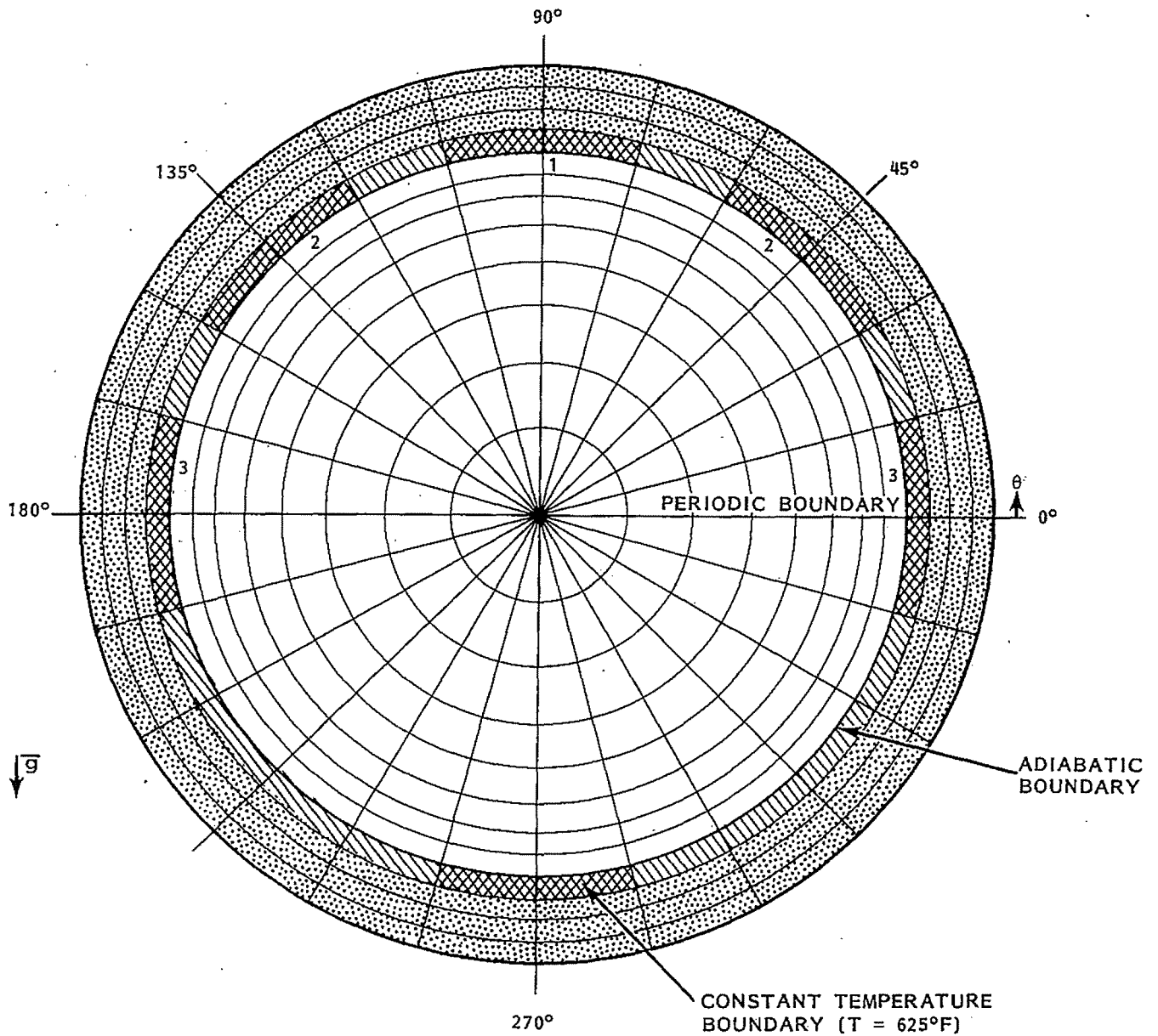


FIGURE 6.3. Grid Structure for Full-Polar, Cylindrical Pipe Convection

boundary condition logic. Fluid in the pipe was initialized to be 600°F. Cold surface temperatures were set to 575°F, and hot surface temperature were set to 625°F. In all three cases, the cold surfaces were above the level of the hot surfaces. This configuration causes buoyancy-induced flow to occur.

The location of the prescribed temperature surfaces is presented in Figure 6.3. In the first case, with a single cold surface at 90° (top) and the hot surface at 270° (bottom), two planes of symmetry exist; one along the vertical plane and one along the horizontal plane. In the second and third cases, each with two symmetrically located cold surfaces, the flow must be symmetric about the vertical plane only.

Figure 6.4 shows the predicted results for the vertical velocity component along the vertical and horizontal planes for the three cases. In case 1, there is symmetry about two planes, and identical circulation flows occur in each quadrant. The vertical velocity is upward along the lower half of the vertical plane because of the hotter surface and positive buoyancy. Correspondingly, the vertical velocity is downward along the upper half of the vertical plane. Vertical velocity is zero along the horizontal plane through the center.

In case 2, a warm, buoyant plume rises from the bottom and uniformly splits into each side near the top. In this case, as well as case 3, the vertical velocity profiles intersect at the centerpoint, $r/R_0=0$. This is important to note because a velocity at the centerline is not computed directly. The correct intersection of the curves in both cases supports the correctness of the polar coordinate differencing and the periodic boundary condition logic.

6.1.4 Transient, Two-Region, Coupled Convection in Cylindrical Coordinates

A transient, two-region, natural-convection simulation was run to test coupling of solids conduction and buoyant convection in cylindrical coordinates. The configuration and noding structure is shown in Figure 6.5. It consists of an 180-degree cross-section sector of two concentric pipes. Sodium exists in the central pipe, and nitrogen exists in the annular gap. A heat transfer coefficient was specified on the exterior of the outside pipe.

Initial conditions were set at time $t = 0$. These were:

Sodium temperature	= 500°F
Stainless steel wall	= 800°F

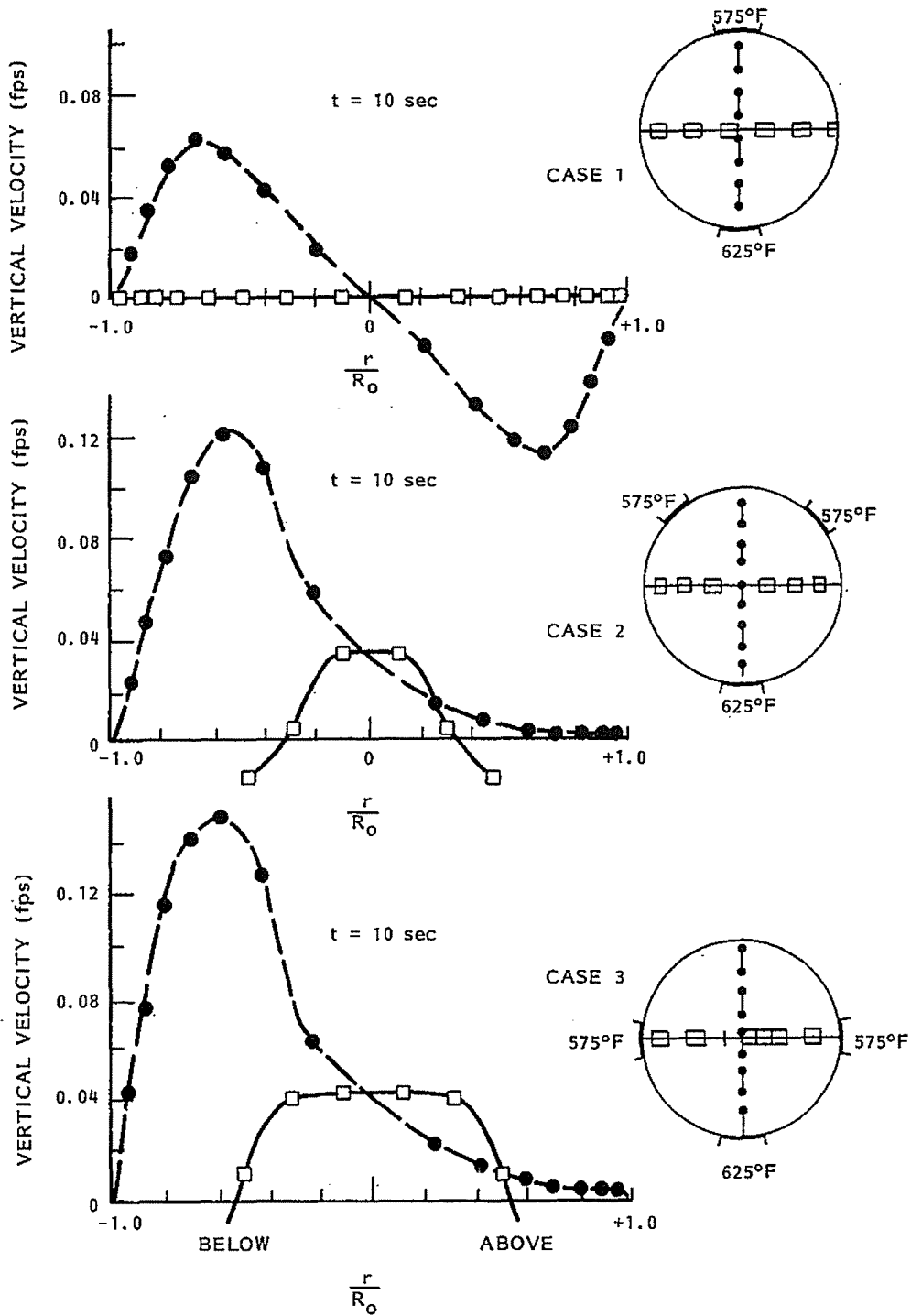


FIGURE 6.4. Vertical Velocity Profiles for Full-Polar, Cylindrical Pipe Convection

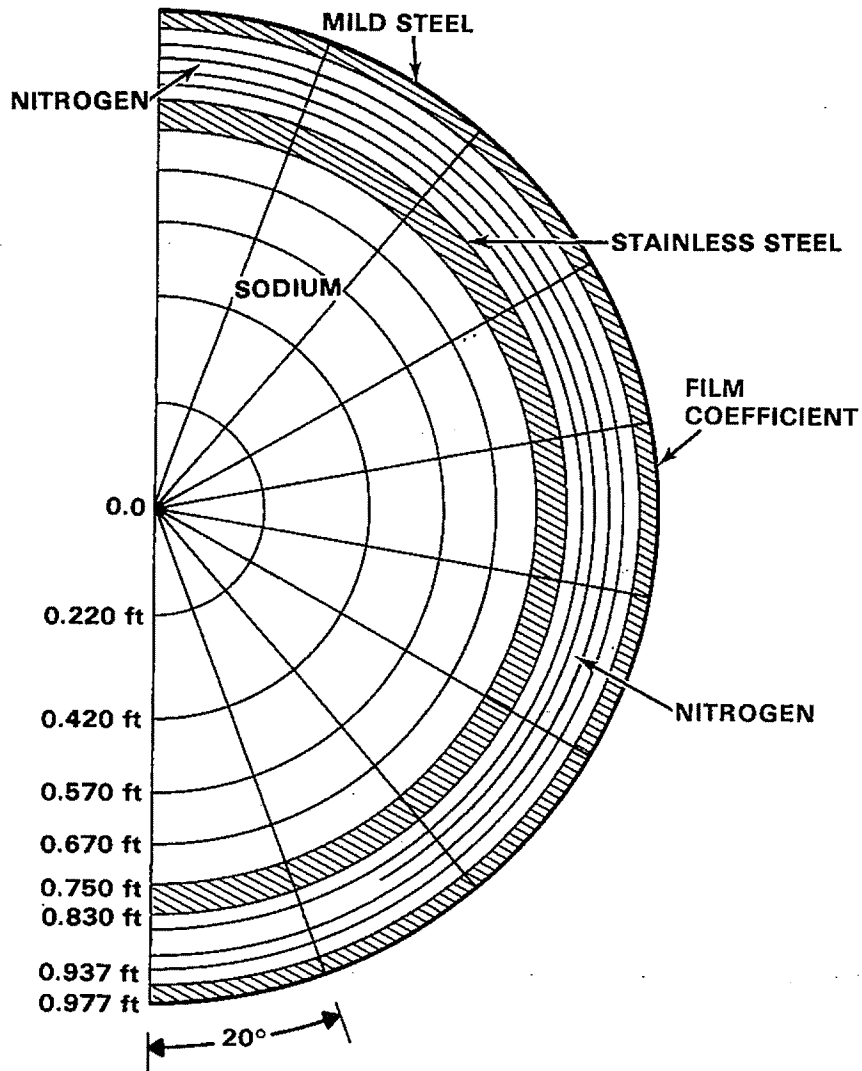


FIGURE 6.5. Description of the Heat-Transfer-Coupled Two-Region Model

Nitrogen Temperature	= 800°F
Mild Steel Wall	= 800°F
Ambient Temperature	= 100°F

Material properties of the two fluids were determined with the property library functions in TEMPEST. The pipe wall material properties were specified on input cards.

Figure 6.6 shows the time-temperature history of three points on the pipe walls. The temperature on the outer surface of the inner pipe initially was less than that on the inner surface of the outer pipe. This happened because the sodium cools the inner pipe faster than the heat transfer to the ambient environment cools the outer pipe. Consequently, the nitrogen initially flows

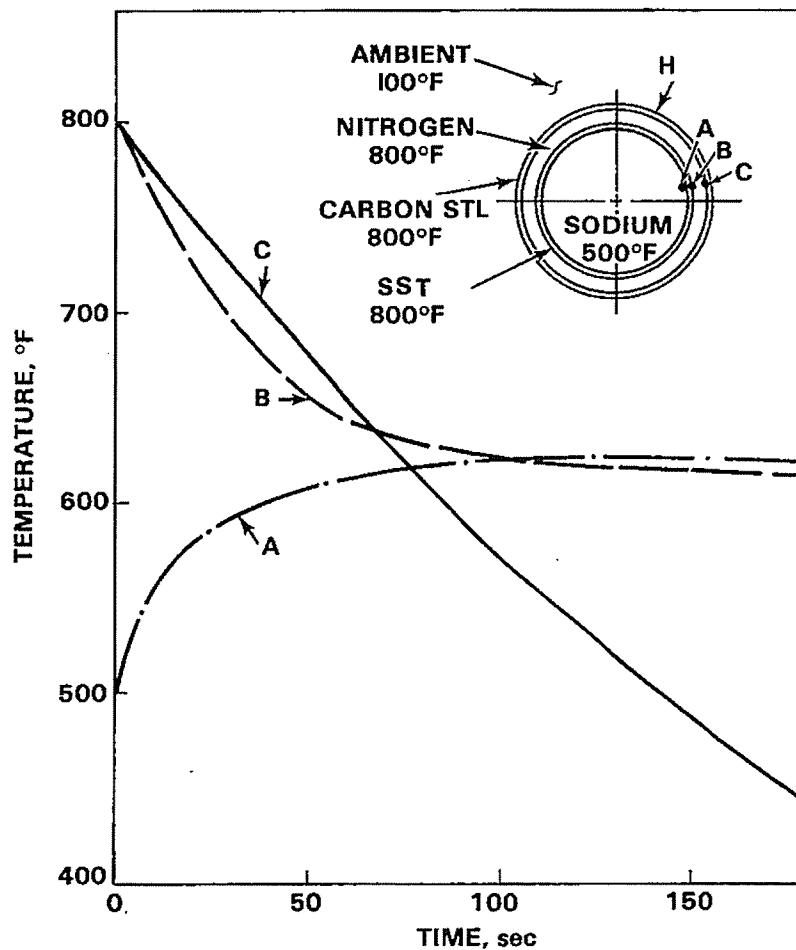


FIGURE 6.6. Temperature History of the Two-Region Problem

down the inner wall and up the outer. Further into the transient, the exterior cooling causes the outer wall temperature to fall below that of the inner wall, and the nitrogen reverses its flow direction.

No data were available for comparison with this simulation. It was used to further test the coupled heat transfer logic in cylindrical coordinates.

6.2 TURBULENT CONVECTION

Turbulent convection simulations conducted to confirm an operation mode or a capability include:

- cooling tower inlet structure with flow diverter vanes
- buoyant river plume
- large-scale prototype breeder (LSPB) inlet torus.

Results of these simulations are presented below.

6.2.1 Cooling Tower Inlet Structure with Flow Diverter Vanes

A schematic of a large cooling tower inlet structure designed to provide a uniform upward flow is shown in Figure 6.7. The design requirement of uniform upward flow was based on a need to provide uniform flow entering an augmented cooling tower test section. The proposed inlet structure design, which included several vertically oriented flat plates located in the elbow, was analyzed with TEMPEST to determine if the vanes would suffice. Zero-thickness plates were included in the simulation to model the vanes.

The velocity field predicted with TEMPEST using the turbulence model is detailed by velocity vectors in Figures 6.7 and 6.8 for the cases of vanes present and absent, respectively. In the former case, the zero-thickness plates modeling the vanes do tend to divert the flow in a manner such that shortly downstream a uniform profile exists.

In the case without vanes (Figure 6.8) typically expected behavior is predicted. There is a large separated recirculation zone downstream of the corner. At the outlet, a significantly distorted velocity profile exists. A smaller recirculation also occurs in the lower corner.

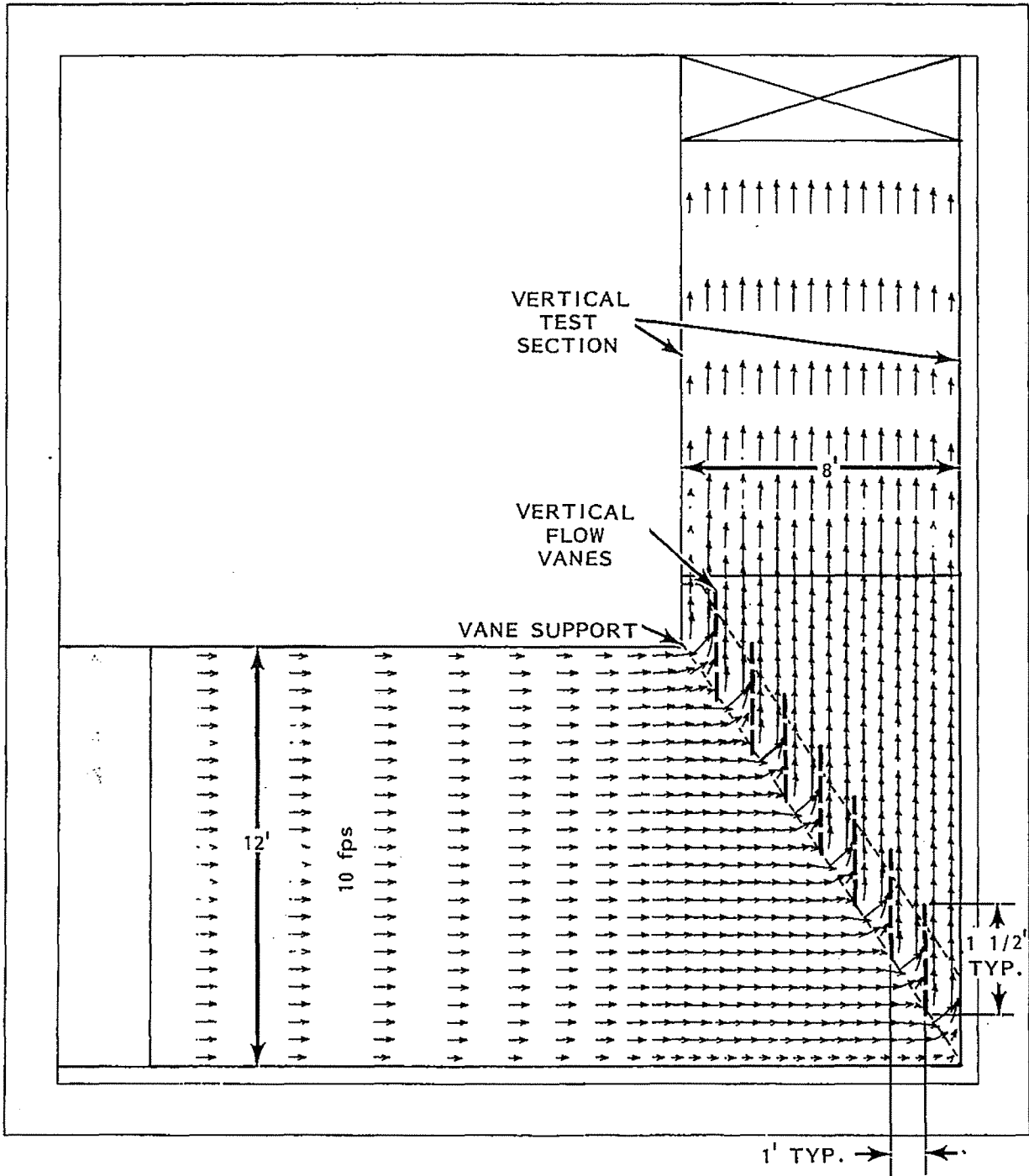


FIGURE 6.7. Cooling Tower Inlet Structure with Turning Vanes

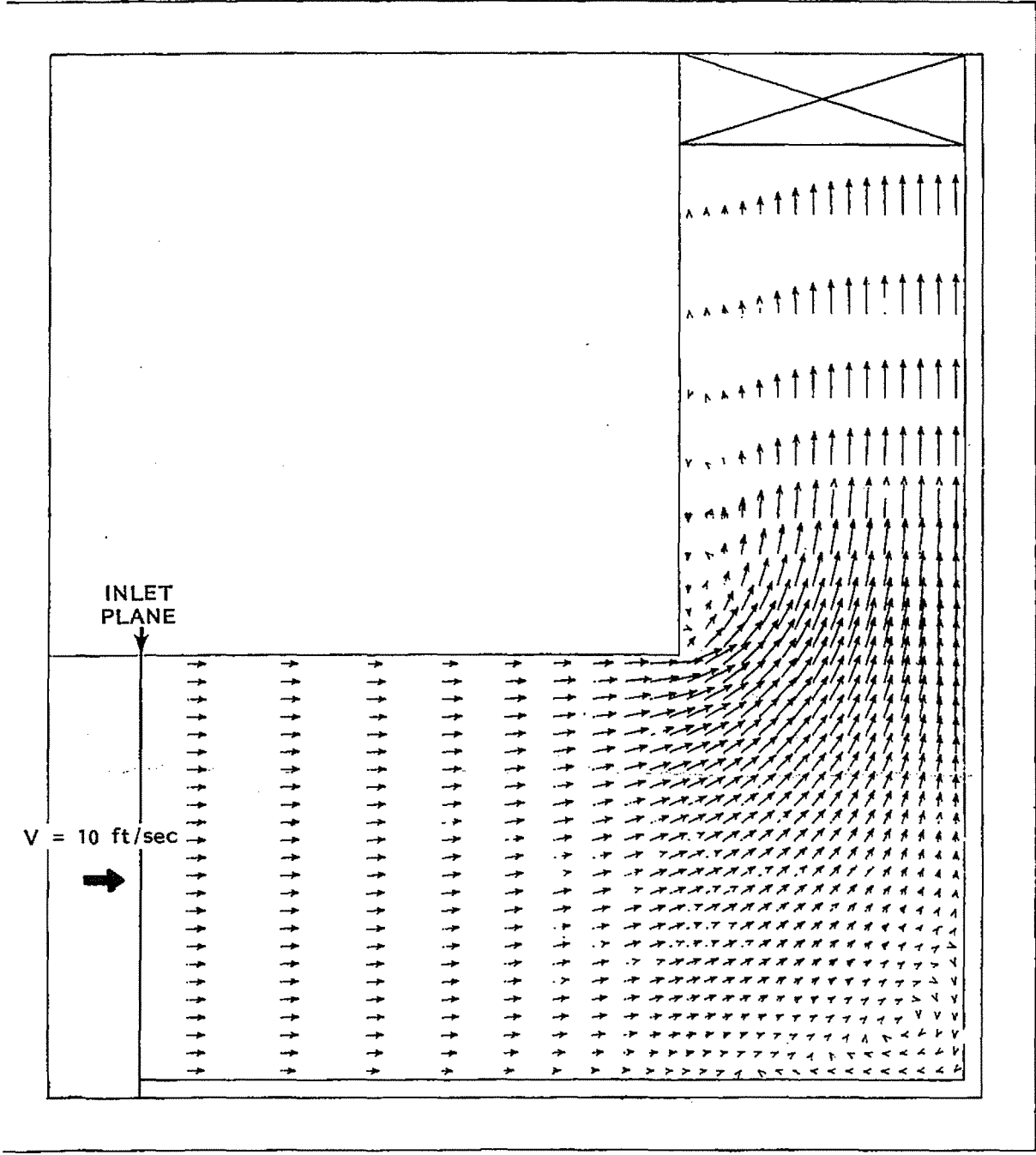


FIGURE 6.8. Cooling Tower Inlet Structure with No Turning Vanes

6.2.2 Positively Buoyant Thermal Outfall Plume Injected at the River Bottom

The TEMPEST computer code was used to simulate the mixing characteristics of a positively buoyant thermal plume injected into the bottom of a river. The objective of the simulation was to investigate the spread of the thermal plume and to predict excess temperatures (above the river's ambient temperature) at the bottom and surface of the river. Only a brief summary of the analysis and results is presented herein.

Two simulations of the near-field mixing region of the plume were modeled. The first modeled the plume effect from a distance of 40 ft upstream of the injection point to a distance of 1400 ft downstream. The lateral distance was 160 ft from the plume centerline. The second simulation was a refinement of the initial plume mixing region. It spanned the region from 40 ft upstream to 180 ft downstream. The lateral width was 50 ft from the plume centerline. For each of the two simulations both a coarse and a fine node structure were used.

River and outfall flow and thermal conditions were assumed. At the upstream boundary of the simulation, the velocity of the river was assumed to be constant in the lateral direction. The velocity varied with depth according to an assumed profile. It was assumed that the depth was 28.5 ft and that the ambient river temperature was 70°F. The outfall was flush with the river bottom and had a 13 ft diameter. A flat, circular diverter plate was located 6 ft above the outfall exit plane. The outfall flow rate was 1.3 percent of the total river flow rate and entered the river at an initial excess temperature of 70°F.

Predictions for the larger of the two mixing region simulations were computed for two different node structures. The first one used 1458 computational nodes and the second one used 2160 nodes. In the latter case the additional nodes were used to refine the computational region directly surrounding the outfall injection location. Predictions for the smaller of the two mixing region simulations were computed with four different node structures--one coarse and one fine were of a two-dimensional vertical centerplane region, and one coarse and one fine were of a three-dimensional region.

Results for the predicted river bottom excess temperature are presented in Figure 6.9. Results for river surface excess temperature are presented in Figure 6.10. Several observations can be made from the results. The two-dimensional simulations with coarse and fine node structures show marked differences from the three-dimensional results. This is a direct consequence inability of the two-dimensional simulations to adequately model the actual mixing phenomenon. The three-dimensional models allow correct interaction of the lateral plume spread caused by the director plate and by turbulent mixing. Resolution differences of the coarse and fine node structure are not pronounced. There is an apparent resolution effect, though. The results in the two figures are only of the overlapped region of the two simulation cases. The simulating the larger field mixing region shows an enhanced cooling of the river bottom temperatures in the very near field region (less than 40 ft from the outfall). The river surface excess temperature shows very little deviation in the overlapped simulation regions.

Results of these simulations have not been verified because experimental data for the assumed conditions was not available. Analysis of the predicted flow and thermal field results did indicate that basic physical phenomena were being predicted, including buoyancy effects and pronounced lateral turbulent mixing. The $k-\epsilon$ model in TEMPEST was used without adjusting constants for these simulations.

6.2.3 Large-Scale Prototype Breeder Inlet Torus B10-A Transient

A three-dimensional simulation of the inlet torus of the large-scale prototype breeder (LSPB) was computed. The geometry of the inlet torus is like a doughnut. The major diameter of the torus is 24 ft 10 in., and the minor diameter is 4 ft 4 in. At four equally spaced azimuthal intervals, 32-in. primary coolant pipes enter through the top of the torus and have 90° elbows directing the flow tangentially in the direction of the major circumference. There are 12 horizontal, equally spaced, 20-in. transfer pipes that connect the torus to the inlet plenum under the core.

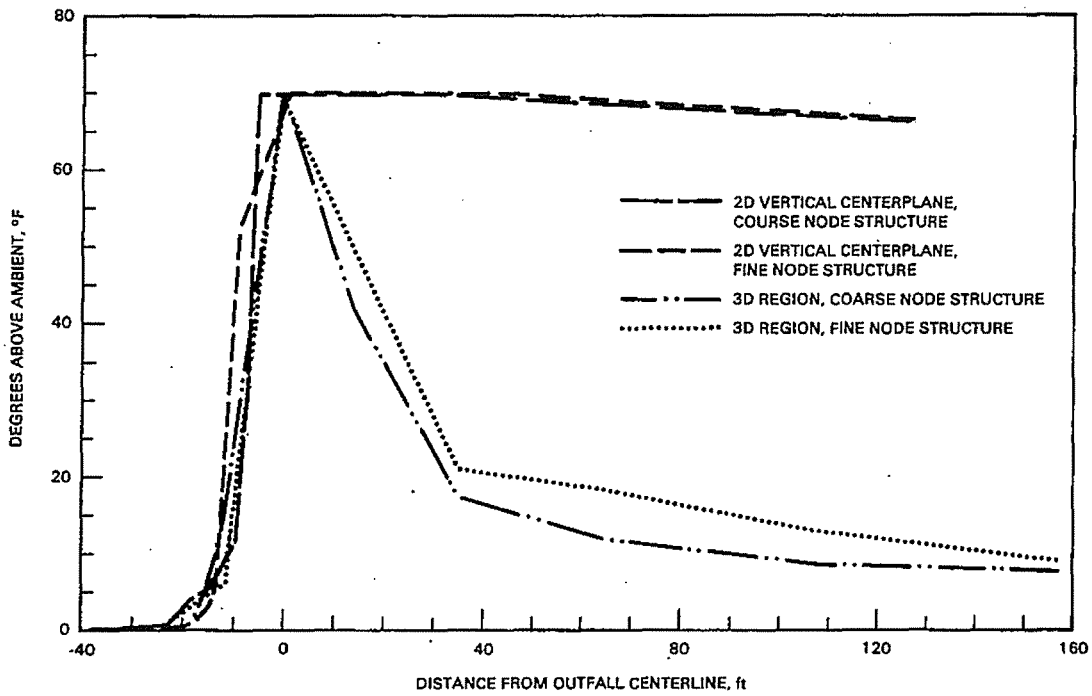


FIGURE 6.9. Predicted River Bottom Excess Temperature as a Function of Distance from Outfall Centerline

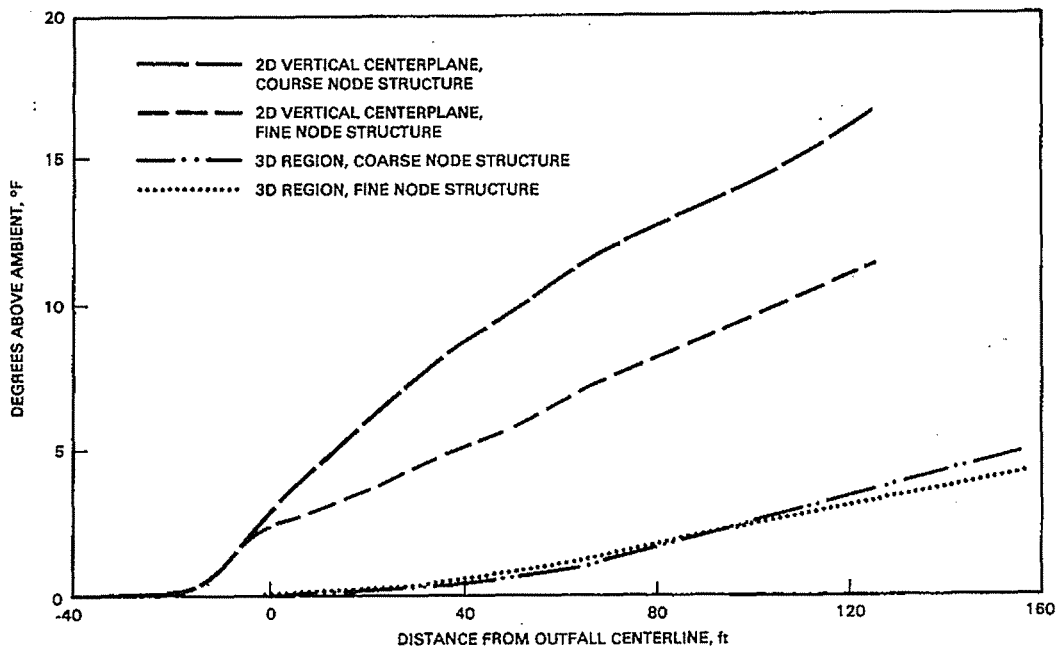


FIGURE 6.10. Predicted River Surface Excess Temperature as a Function of Distance from Outfall Centerline

The B-10A design transient is one in which primary sodium in one of the four coolant loops enters the torus at a nominal temperature several hundred degrees Fahrenheit above the nominal temperature in the other three coolant loops. This temperature difference may lead to degraded system cooling in a natural-convection mode. The maximum transient temperature difference also affects the thermal stress design of the torus.

The objective of the TEMPEST simulation was to investigate the flow and mixing in the torus during the transient. This was done by modeling the torus in three dimensions. The periodic boundary capability in TEMPEST was used in the azimuthal direction to model the 360° sector. Transient inflow boundary conditions were modeled at locations corresponding to the inlet pipe elbows, and computed outflow boundaries were modeled at the transfer pipe locations. The B-10A design transient was computed out to 1000 sec.

Figure 6.11 presents the predicted transient temperatures at four locations around the minor circumference of the torus cross section. These results are in the quadrant which the hotter coolant is entering. In the other three quadrants, there was a much smaller temperature differential from top to bottom. Figure 6.12 presents the predicted temperatures as a function of angular position at $t = 1000$ sec. It is apparent that significant thermal stratification is present in the affected quadrant. Interquadrant mixing is inhibited by the presence of the inlet pipe in the torus. This is evidenced by the marked temperature differences around the top of the torus.

These results were computed using sodium as a test fluid, and the $k-\epsilon$ turbulence model was used. No data were available for comparison, so the results cannot be verified for accuracy. The periodic boundary condition was shown to work properly in this complex geometry. The simulation also demonstrates that TEMPEST is capable of computing the thermal-hydraulic behavior in this component of an LSPB without undue difficulties either in the solution convergence or in the model set up.

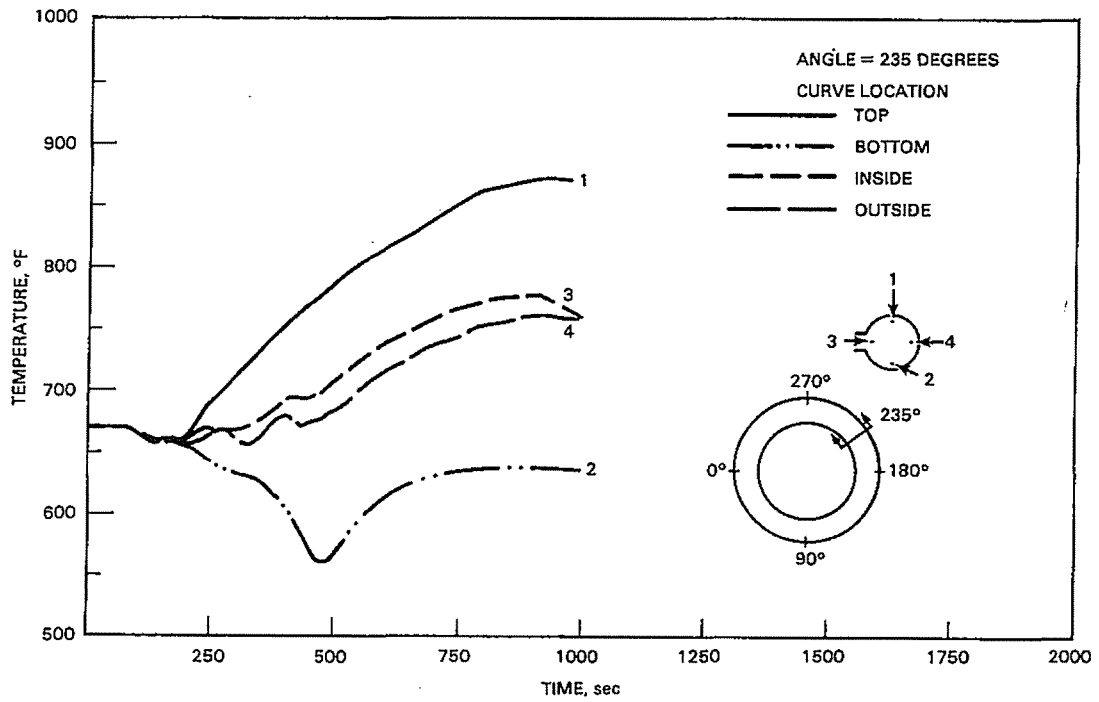


FIGURE 6.11. B10-A Transient Torus Temperatures

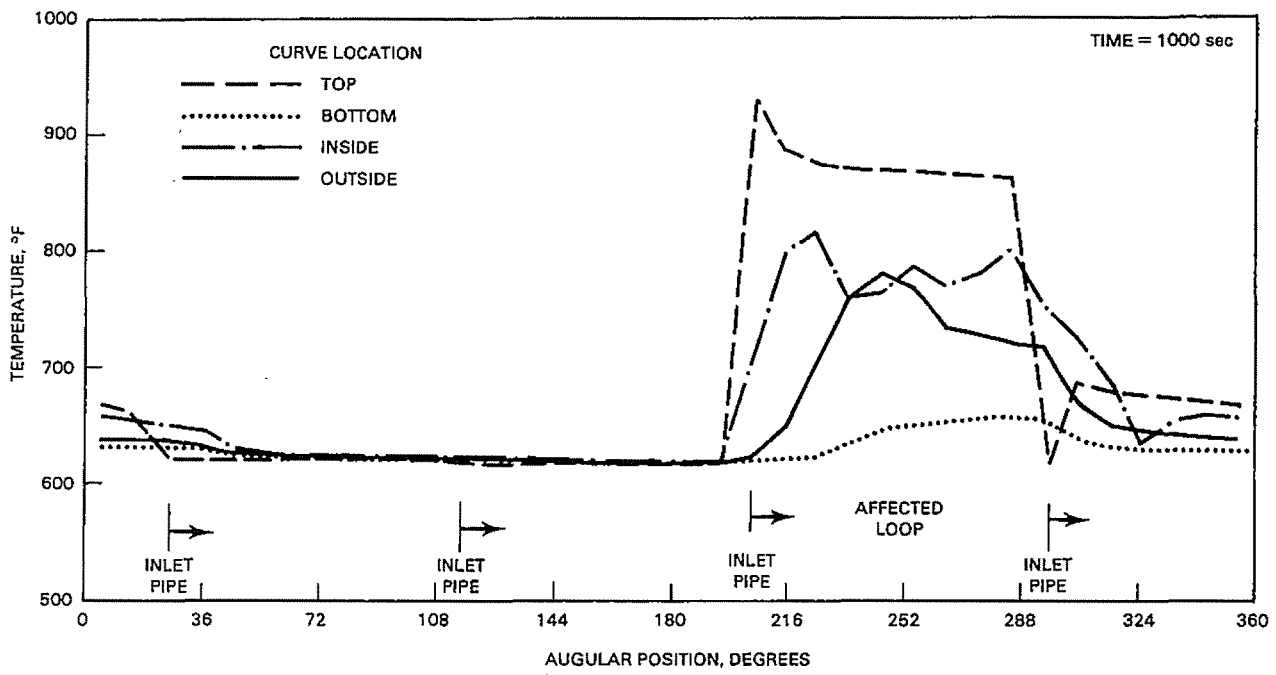


FIGURE 6.12. B10-A Torus Temperatures at $t = 1000$ sec.

REFERENCES

- Abraham, G. 1963. Jet Diffusion in Stagnant Ambient Fluid. Publication No. 29, Delft Hydraulics Laboratory, Holland.
- Albertson, M. L., Y. B. Dai, R. A. Jensen and H. Rouse. 1948. "Diffusion of Submerged Jets." Proc. Am. Soc. Civil Engrs., 74:571.
- Anderson, R., and A. Bejan. 1981. "Heat Transfer through Single and Double Vertical Walls in Natural Convection: Theory and Experiment." Int. J. of Heat and Mass Transfer. 24(10):1611-1620.
- Boyle, D. R., and M. W. Golay. 1980. Transient Effects in Turbulence Modeling." DOE/ET/37240-83TR, Massachusetts Institute of Technology, Cambridge, Massachusetts.
- Bremhorst, K., and K. J. Bullock. 1973. "Spectral Measurements of Turbulent Heat and Momentum Transfer in Fully Developed Pipe Flow." Int. J. of Heat and Mass Transfer. 16:214-2154.
- Carslaw, H. S., and J. C. Jaeger. 1959. Conduction of Heat in Solids. Second Edition, Oxford University Press, London, England.
- Chen, Y. B., and M. W. Golay. 1977. Coolant Mixing in the LMFBR Outlet Plenum. C00-2245-44TR. Massachusetts Institute of Technology, Cambridge, Massachusetts.
- deVahl Davies, G., and I. P. Jones. 1983. "Natural Convection in a Square Cavity - a Comparison Exercise." In Numerical Methods in Thermal Problems. Vol. II., pp. 552-572, Pineridge Press, Swansea, U.K.
- Eckert, E. R. G., and W. O. Carlson. 1961. "Natural Convection in an Air Layer Enclosed Between Two Vertical Plates with Different Temperatures." Int. J. of Heat and Mass Transfer. 2:106-120.
- Edwards, A. L. 1972. TRUMP: Computer Program for Transient and Steady-State Temperature Distribution in Multidimensional Systems. UCRL-14754 (Rev. 3).
- Eyler, L. L. 1978. Turbulent Structure Measurements and Transport Modeling in Liquid Metals. Ph. D. Thesis, Purdue University, West LaFayette, Indiana.
- Farouk, B., and S. I. Güçeri. 1982. "Laminar and Turbulent Natural Convection in the Annulus Between Horizontal Concentric Cylinders." J. of Heat Transfer. 104:631-636.

- Friedmann, M., J. Gillis and N. Liron. 1968. "Laminar Flow in a Pipe at Low and Moderate Reynolds Numbers." Applied Scientific Research. 19:426-438.
- Fuchs, H. 1974. Warmeübergang an Stromendes Natrium. Doctorale Thesis, Eidgenössischen Technischen Hochschule, Zurich, Switzerland.
- Goldsmith, M. ed. 1981. Comparisons of Turbulent-Flow Calculations with Experiment. WAPD-TM-1473, Bettis Atomic Power Laboratory, West Mifflin, Pennsylvania.
- Goldstein, R. J., and D. K. Kreid. 1967. "Measurements of Laminar Flow Development in a Square Duct Using a Laser-Doppler Flow Meter." J. of Applied Mechanics. Vol. 34, Trans. ASME, 89:813-818.
- Gutmark, E., and I. Wygnanski. 1976. "The Planer Turbulent Jet." J. of Fluid Mechanics. 73:465-476.
- Hinze, J. O. 1976. Turbulence. McGraw-Hill Book Co., New York, New York.
- Hjelm, R. L., and T. E. Donovan. 1979. "Numerical Investigation of Electric Field Effects on Unsteady Buoyant Molten Glass Flows." Paper presented at the ASME/AIChE 18th National Heat Transfer Conference, 79HT-98, August 6-8, 1979, San Diego, California.
- Hossain, M. S., and W. Rodi. 1977. As reported by Rodi, W. 1980. In Prediction Methods for Turbulent Flows, W. Kollmann, ed., pp. 254-350, Hemisphere Publishing Co., New York, New York.
- Jaeger, J. C. 1942. Philosophical Magazine, Ser. 7, 33(222)
- Jayatillaka, C. L. V. 1969. "The Influence of Prandtl Number and Surface Roughness on the Resistance of the Laminar Sublayer to Momentum and Heat Transport." In: V. Giguil and E. Hahne (editors), Progress in Heat and Mass Transport 1. Pergamon Press, New York.
- Jones, W. P., and B. E. Launder. 1972. "The Prediction of Laminarization with a Two-Equation Model of Turbulence." Int. J. of Heat and Mass Transfer, 15:301-314.
- Kollmann, W., ed. 1980. Prediction Method for Turbulent Flows. Hemisphere Publishing Co., New York, New York.
- Kreid, D. K. 1967. "Measurements of Developing Laminar Flow in a Square Duct Using a Laser-Doppler Flow Meter." J. of Applied Mechanics. Vol. 34, Trans. ASME, 89:813-818.
- Kuehn, T. H., and R. J. Goldstein. 1976. "An Experimental and Theoretical Study of Natural Convection in the Annulus Between Horizontal Concentric Cylinders." J. of Fluid Mechanics. 74(4):695-719.

- Laufer, J. 1954. Structure of Turbulence in Fully Developed Pipe Flow. NACA Report 1174.
- Lauder, B. E. 1975. "On the Effects of a Gravitational Field on the Turbulent Transport of Heat and Momentum." J. of Fluid Mechanics. 67(3):569-581.
- Lavin, Z., and A. A. Fejer. 1966. Investigation of Swirling Flows in Ducts. Illinois of Technology Research Institute Technical Report on Contract No. AF33(615)-2122.
- Lawn, C. J. 1971. "The Determination of the Rate of Dissipation in Turbulent Pipe Flow." J. of Fluid Mechanics. 48(3):477.
- Lawn, C. J. 1977. "Turbulent Temperature Fluctuations in Liquid Metals." Int. J. of Heat and Mass Transport. 20:1035-1044.
- Lis, J. 1966. "Experimental Investigation of Natural Convection Heat Transfer in Simple and Obstructed Horizontal Annuli." Proceedings of the 3rd International Heat Transfer Conference. pp. 196-204.
- McDonald, J. W., V. E. Denny and A. F. Mills. 1972. "Numerical Solutions of the Navier-Stokes Equations in Inlet Regions." Transactions of the ASME, J. of Applied Mechanics, No. 72-APM-DD.
- Morton, B. R. 1960. "Laminar Convection in Uniformly Heated Vertical Pipes." J. of Fluid Mechanics. pp. 227-240.
- Richtmyer, R. D., and K. W. Morton. 1967. Difference Methods for Initial Value Problems. Interscience Publishers, 2nd Edition.
- Rodi, W. 1980. In Prediction Methods for Turbulent Flows, W. Kollmann, ed. pp. 259-350, Hemisphere Publishing Co., New York, New York.
- Rothe, P. H., M. F. Ackerson and J. A. Block. 1982. Fluid and Thermal Mixing in a Model Cold Leg and Downcomer with Loop Flow. EPRI NP-2312, Electric Power Research Institute, Palo Alto, California.
- Schlichting, H. 1968. Boundary-Layer Theory. 6th Edition. McGraw-Hill Book Company, New York, New York.
- Seban, R. A., and M. M. Behnia. 1976. "Turbulent Buoyant Jets in Unstratified Surroundings." Int. J. of Heat and Mass Transfer. 19(10):1197-1204.
- Sernas, V., and E. I. Lee. 1978. "Heat Transfer in Air Enclosures of Aspect Ratio Less than One." J. of Heat Transfer. 103(4):617-622.
- Sha, W. T., and B. E. Launder. 1977. A General Model for Turbulent Momentum and Heat Transport in Liquid Metals. ANL-77-78, Argonne National Laboratory, Argonne, Illinois.

- Trent, D. S. 1973. A Numerical Model for Two-Dimensional Hydrodynamics and Energy Transport. (VECTRA code), BNWL-1803, Pacific Northwest Laboratory, Richland, Washington.
- Trent, D. S., L. L. Eyler and M. J. Budden. 1983. TEMPEST A Three-Dimensional Time-Dependent Computer Program for Hydrothermal Analysis Volume I: Numerical Methods and Input Instructions. PNL-4348, Pacific Northwest Laboratory, Richland, Washington.
- Turner, W. D., D. C. Elrod and I. I. Siman-Tov. 1977. HEATING-5 An IBM-360 Heat Conduction Program. ORNL/CSD/TM-15, Oak Ridge National Laboratory, Oak Ridge, Tennessee.
- Viskanta, R., and D. W. Lankford. 1981. "Coupling of Heat-Transfer Between Two Natural Convection Systems Separated by a Vertical Wall." Int. J. of Heat and Mass Transfer. 24(7):1171-1177.
- Warhaft, Z., and J. L. Lumley. 1978. "An Experimental Study of the Decay of Temperature Fluctuations in Grid-Generated Turbulence." J. of Fluid Mechanics. 88(4):659-684.
- Wynaski, I., and H. Fiedler. 1970. "The Two-Dimensional Mixing Region." J. of Fluid Mechanics. 41:327.



Pacific Northwest
NATIONAL LABORATORY

*Proudly Operated by **Battelle** Since 1965*

902 Battelle Boulevard
P.O. Box 999
Richland, WA 99352
1-888-375-PNNL (7665)
www.pnnl.gov



U.S. DEPARTMENT OF
ENERGY